Cranfield University

Francesca Bortolani

Synthesis and development of lead zirconate titanate inks for direct writing

School of Applied Science

PhD Thesis
2010

Supervisors
Dr Robert A Dorey
February 2010

Cranfield University
School of Applied Science

PhD Thesis
2010

Francesca Bortolani

Synthesis and development of lead zirconate titanate inks for direct writing

Supervisors
Dr Robert A Dorey
February 2010

Abstract

The work presented in this thesis is focused on the development of a novel low processing temperature PZT (lead zirconate titanate) ink for direct writing of functional microsystems. The work examines both the synthesis of PZT powder for use in the ink as well as the formulation of the ink. Two different routes were investigated for the powder synthesis: electro hydrodynamic atomisation (EHDA) and molten salt synthesis (MSS). EHDA is a technique that leads to the formation of small and spherical droplets that, after drying, result in solid particles. Several process parameters were investigated in order to determine their influence on particle size. PZT sols with concentrations up to 0.6 *M* were electrosprayed under different conditions: the flow rate was varied from 0.2 to 0.6 $ml\,h^{-1}$ and the distance between the needle and the bottom electrode was increased from 20 to 40 *mm*. The solvent was dried by the use of a focused lamp with temperature between 200 and 680^oC. It was determined that, in order to reduce the size of the PZT particles, low concentration and low flow rate were needed. The needle-electrode distance was found not to have a strong effect on size. However an increase in the focus temperature to a threshold of 520^oC led to a reduction of the particle diameter. A further increase of the degree of heating led to the formation of big and irregular particles. Small PZT particles with diameter of $\sim$260 *nm* were obtained under the following conditions: flow rate of 0.2 $ml\,h^{-1}$, sol concentration of 0.2 *M*, needle-electrode distance of 30 *mm* and drying temperature of 520^oC. The synthesised powder was spherical in shape, that made it suitable for IJP, but the yield was very low.

In order to overcome the problem associated with the low yield of EHDA, MSS was investigated. Also in this case process parameters were studied with the purpose to reduce particle size. The optimum synthesis conditions were found to be 1 hour at 850^oC, with a ramp rate of 3.3$^oC\,min^{-1}$. Under these circumstances, PZT particles with a mean diameter of $\sim$340 *nm* were synthesised. From the investigation it came to light that long times and higher temperatures led to an increase in particle size due to coarsening process. Short times and low temperatures led instead to an incomplete reaction between the starting oxides. A reaction mechanism for the formation of PZT is also proposed: fully dissolved Pb reacts with the insoluble TiO_2 to form $PbTiO_3$. Then ZrO_2 reacts with PT and the remaining Pb to form PZT.

Composite inks were formulated from the powders synthesised by both the routes. In the case of EHDA however the formulation was hampered due to a low amount of powder available. This resulted in a quick powder sedimentation that led to nozzle clogging during printing. Inks composed of MSS powder were formulated with different solid loadings to identify under which conditions the nozzles were clogging. Two different patterns were printed on the substrate: a 20x20 drops for the identification of the ink behaviour on the wafer, and a line array pattern to determine in which conditions printing quality was enhanced.

Happiness only real when shared.

CHRISTOPHER MCCANDLESS

Acknowledgments

First of all I would like to thank my supervisor Dr. Rob Dorey, for his endless support and experience. I also wish to thank my colleagues from the Microsystems and Nanotechnology Centre. In particular Dr. Steve Dunn and Joe for the nice chats about food, mountains and gardening, and Dr. Paul Jones, Andy, Mark, Matt, Matthew, Divya, Tatiana, Harrison and Sabina. Thanks also to Enza, our spectacular secretary.

A special thank goes to all my friends in UK, that made me feel at home since the first moment: Laura, Geppo, Jenny, Harry, Mehdi, Jahan, Marco, Silvia, Alessio, Barbara, Giuseppe, Julian, Peter, Alice, Dario, Malaika, Oscar, Nenad, Jorgina and Cesar.

I also want to express my gratitude to my friends that gave their support from far away: Amalia, Silvia, Michela, Rosa, Teresa, Giulia e Sara.

Last but not least, I thank my parents and my sister's family, with particular regard to Checco and Gaia, for all the fun I have with them.

Thank to Andrea for being there, always.

Publications

Published

- R. A. Dorey, S. A. Rocks, F. Dauchy, D. Wang, F. Bortolani, E. Hugo, *Integrating functional ceramics into microsystems*, Journal of European Ceramic Society, 28 (7) 2008, 1397-1403
- F. Bortolani, D. Wang, R. A. Dorey, *Micro direct writing of ceramics*, Whittles Publishing, 2009, pp. 293
- F. Bortolani, R. A. Dorey, *Synthesis of spherical lead zirconate titanate (PZT) nanoparticles by electrohydrodynamic atomisation*, Advances in Applied Ceramics, 108 (6) 2009, 332-337

Submitted

- F. Bortolani, R. A. Dorey, *Molten salt synthesis of PZT powder for direct write inks*, submitted to Journal of European Ceramic Society

Oral presentations

- *Nanoparticulate PZT ink for direct writing of MEMS*, Royal Academy of Engineering Research Fellowship final review, Cranfield University, Cranfield, 4 August 2008
- *Nanoscale synthesis of piezoelectric direct writing inks*, Piezo 2009, Belvedere Hotel, Zakopane, Poland, 1-4 March 2009
- *PZT for direct writing*, Electronic ceramic department (K5), Jozef Stefan Institute, Ljubljana, 29 March - 9 April 2009

Poster presentations

- Development of PZT nano-particulate inks for direct writing of functional MEMS devices, Ferroelectrics UK 2007, West Park Centre, Dundee, 20-21 August 2007

Attended seminars

- European training action on ceramic nanocomposites, Consejo superior de investigaciones cientificas (CSIC), Madrid, 23-27 February 2009
- Bottom-up synthesis of nanocomposites for molecular building blocks, Jozef Stefan Institute, Ljubljana, 29 March - 9 April 2009
- Energy-conscious mechanichemical processes for electroceramics, Jozef Stefan Institute, Ljubljana, 29 March - 9 April 2009
- Introduction t piezo technologies, Industrial training from the Piezo Institute, National Physical Laboratory (NPL), London, 1 September 2009

Contents

List of Figures

List of Tables

Nomenclature

β	Maximum spreading
ΔX	Printing mismatch
δ	Density
η	Viscosity
γ	Surface tension
π_η	Droplet size-liquid properties correlation parameter
θ	Contact angle
ε_o	Permittivity of free space
ε_r	Relative permittivity
${C^*}_{max}$	Supersaturation
${C^*}_{min}$	Nucleation concentration
C_o	Capacitance of air
C_s	Saturation treshold
E_c	Coercive field
P_r	Remnant polarisation
P_s	Spontaneous polarisation
Q_R	Rayleigh charge limit
r_{max}	Maximum droplet radius
T_C	Curie temperature
T_{MP}	Melting point temperature
T_R	Reaction temperature
V_x	Cartridge velocity
V_z	Firing velocity
A	Top electrode area
C	Capacitance
c	Composite layer

CMO Conventional mixed oxides
Conc Sol concentration
D Electrical dispacement
d Piezoelectric coefficient
DoD Drop on demand ink jet printer
dpi Dots per inch
E Electric field
EG Ethylene glycol
EHDA Electro hydrodynamic atomization
EPD Electrophoretic deposition
IJP Ink jet printing
K Conductivity
KNN Sodium potassium niobate
M Molar concentration
m Mass
MEMS Micro electromechanical systems
MPB Morphotropic phase boundary
MSS Molten salt synthesis
Nd Normalised droplet diameter
Np Normalised particle diameter
PFN Lead ferrite niobate
PLZST Lead lanthanum zirconate titanate stannate
PMN Lead manganese niobate
PT Lead titanate
PZ Lead zirconate
Q Liquid flow rate
R Resistance
r Radius
Re Reynolds number
S Mechanical strain
s Sol infiltration
SEM Scanning electron microscope
T Temperature
t Sample thickness

TLD	Through lens detector
v	Ink velocity
We	Weber number
X	Applied stress
XRD	X-Ray diffraction
Z	jettability of a fluid
z	Acoustic impedance

Chapter 1

Introduction

Piezo micro electromechanical systems (MEMS) are electronic devices that convert a mechanical stimulus into an electrical signal and/or vice versa. The main constituent of a piezo MEMS is the active material, a film of ceramic with piezoelectric properties. Piezoelectricity is the ability of a material to interconvert mechanical and electrical energy [1, 2]. Other functional constituents of the systems are substrate, mechanical elements and electrical connections [3, 4]. Typical MEMS applications are force or pressure sensors, actuators, ignition systems and ultrasound transducers [5, 6]. Among the materials showing piezoelectric behaviour, lead zirconate titanate (PZT) is the most widely used. PZT is a hazardous material due to its lead content and currently there is research effort to minimise use of or develop of lead free materials [6]. However, the excellent piezoelectric properties of PZT [7] are still unmatched. One challenge of research is to minimise the amount of PZT used [6], primary through reducing material wastage during production. Miniaturisation can also play a role in this by reducing the overall amount of material used [6].

The current manufacturing techniques for the deposition of ceramic films for MEMS production include screen printing, electrophoretic deposition and spin coating [3, 8–13]. These methods have been designed for the deposition of large volumes of film. The drawbacks of

such techniques range from the toxic substances used for etching and the high amount of wasted PZT [14], to the high cost of mask manufacturing, low resolution capability and limited adaptability [3]. The little adaptability of these processes is particularly important for R&D applications requiring fast prototyping and small volume/high cost products such as medical transducers.

The current challenges in the field of PZT MEMS manufacturing are device miniaturisation, fast prototyping and reduction of the use of hazardous materials [6]. The limitations of the standard deposition methods have stimulated the development of new techniques. Direct writing is a group of high-resolution computer-controlled deposition methods [15], which are potentially able to address these needs. Direct writing includes micropen writing, robocasting, fused deposition and ink jet printing. Among these, ink jet printing (IJP) is a non-contact droplet-based technique, while the others are filament-based. This leads to the fabrication of three dimensional structures with the smallest feature size in the direct writing group [15]. Other key advantages are fast and economic prototyping and no wastage of material.

1.1 Aim and objectives

The aim of this work is the development of an ink suitable for ink jet printing for the production of microscale PZT structures for piezo MEMS.

The common approaches to the deposition of thick films of ceramic use suspensions of PZT powder. This work will explore the use of powder suspensions in sol carrier fluids to yield a low temperature processing route compatible with MEMS materials. The first objective of this work will be the synthesis of PZT powder compatible with the IJP process. This means a particle dimension in the submicron range, ideally 200 *nm* or less. Different routes have been used in the past, such as hydrothermal and sol-gel [16–24]. These techniques are time consuming and require multiple steps. Additionally the resulting particles agglomerate,

leading to dimensions bigger than 1 μm. Dangerous materials, such as 2-methoxyethanol, are also needed for the synthesis [22]. Two alternative routes will be investigated for the production of PZT: electro hydrodynamic atomisation (EHDA) and molten salt synthesis (MSS). These techniques have been used successfully to prepare ceramic particles in the submicron range [25–28].

The second objective is to achieve control of the relics on the substrate during printing. A PZT ink has to be carefully formulated in order to maximise stability and resolution. In this work viscosity and surface tension of the ink will be formulated to an optimal range through the use of additives. Moreover, by the use of additives the powder will be stabilised to reduce the risk of sedimentation and agglomeration and subsequent nozzle clogging.

The final objective will be to investigate the printing parameters and optimise them to obtain a ceramic film with the desired characteristics. The ink behaviour on the substrate will be evaluated in terms of spreading and printing quality.

1.2 Thesis structure

This thesis is structured as seven chapters, of which this *Introduction* is the first.

In Chapter two the *Literature review* is presented. The first section of this chapter covers piezoelectric materials, with particular attention on PZT, MEMS and their applications. The second and third sections concern direct writing and ink jet printing, highlighting the ink related aspects. In the fourth section the features connected to the synthesis of ceramic powder by EHDA and MSS are discussed, with special regard given to the parameters influencing particle size and shape.

Chapter 3, *Experimental procedure*, contains a description of the methodologies adopted in this work.

Preparation of micro-nanoparticles by EHDA, is the subject of Chapter four. The process

parameters influencing the droplet size, such as sol concentration, liquid flow rate, temperature and distance from the electrode are investigated. This chapter has been adapted from a published journal paper as part of this PhD [29].

Preparation of micro-nanoparticles by MSS is discussed in Chapter five. The effect of processing parameters, such as time, temperature and heating rate on the final powder size and shape is examined and a reaction mechanism proposed. Finally the piezoelectric properties of the powder are evaluated.

Chapter six, *PZT ink development and printing*, concerns the formulation of a PZT ink for IJP. The aspects related to particle stabilisation and determination of the physical properties of the ink are examined. Inks with different solid loadings are prepared and different patterns are printed on silicon substrates to determine the printing quality.

The thesis ends with the *Conclusions and Further work* chapter which summarises the major conclusions of this work and suggests actions for future research.

Chapter 2

Literature review

2.1 Piezoelectric materials

2.1.1 Piezoelectricity and ferroelectricity

Piezoelectricity was first discovered in single crystals of quartz by Jacques and Pierre Curie in 1880 [5]. It is the ability of some materials to develop an electrically charged surface when subjected to a mechanical stress (direct piezoelectric effect), or to change in dimension when an electrical field is applied (converse piezoelectric effect) as shown in figure 2.1 and it has been described in several books [1, 2].

The equations related to the piezoelectric effects are reported below. Direct piezoelectric effect is defined by equation 2.1:

$$D = d\,X \tag{2.1}$$

where D is the electrical displacement in $C\,m^{-2}$, X is the applied stress in $N\,m^{-2}$ and d is the piezoelectric coefficient in $C\,N^{-1}$. Converse piezoelectric effect is defined by equation 2.2:

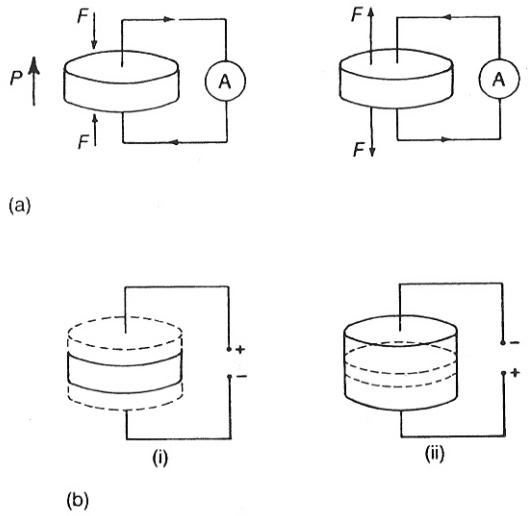

Figure 2.1: The direct (a) and converse (b) piezoelectric effects: (i) contraction and (ii) expansion. From [1].

$$S = d\,E \tag{2.2}$$

where S is the mechanical strain and E is the electric field in $V\,m^{-1}$.

In nature 32 point groups exist, of which 11 have a centre of symmetry. Of the remaining 21, 20 exhibit piezoelectricity and of these 10 are polar as shown in the chart in figure 2.2.

Beside piezoelectricity, two other phenomenon have to be mentioned: pyro- and ferroelectricity. In pyroelectric materials it is possible to change the degree of the spontaneous polarisation by simply changing their temperature. Ferroelectricity instead is the ability to change the direction of polarisation by applying an external electric field. The polarisation direction is maintained even if the field is removed. The first material discovered that shown this phenomenon was barium titanate, $BaTiO_3$.

These phenomenon are connected to the crystal structure of the material. In order to exhibit piezoelectricity, a material crystal structure must not posses a centre of symmetry, i.e. be non-centrosymmetric. To exhibit pyroelectricity, the material has to be polar. Since all

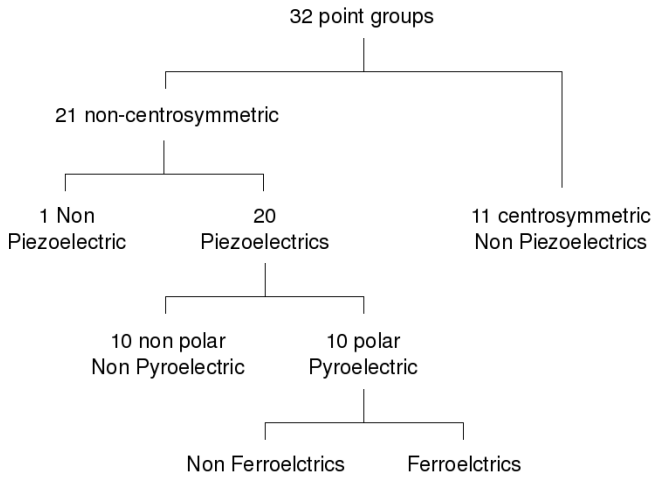

Figure 2.2: Flow chart showing the connection between materials.

polar materials are non-centrosymmetric, they are also piezoelectrics. Piezoelectric crystals can be polarised by applying a stress or an electric field. All ferroelectrics are pyroelectrics and piezoelectrics, but not all piezoelectrics are pyro- or ferroelectrics.

Materials such as lead zirconate titanate (PZT) or $BaTiO_3$ possess a crystal structure called perovskite. The perovskite phase, minimal formula ABO_3, takes its name from calcium titanate, $CaTiO_3$ named after the mineralogist who discovered it. In this structure A represents a big cation (Pb^{2+} or Ba^{2+}) at the corners of the unit cell and O represents the oxygens in a faced centred cubic structure, positioned at the centre of each face of the unit cell. B represents a smaller cation (Ti^{4+} or Zr^{4+}) in the centre of the octahedron cage formed by the oxygen ions. Each A cation is surrounded by 12 oxygen ions. Each B cation is instead surrounded by 6 oxygen ions. In this way the oxygen octahedron shields A and B cations from each other. Figure 2.3 represents the perovskite structure of barium titanate. Since B is small compared to the oxygen cage it can be moved slightly off its centre leading to the appearance of piezoelectric properties. These materials switch from non-ferroelectrics to ferroelectrics depending on temperature. The threshold at which this transformation occurs is the Curie

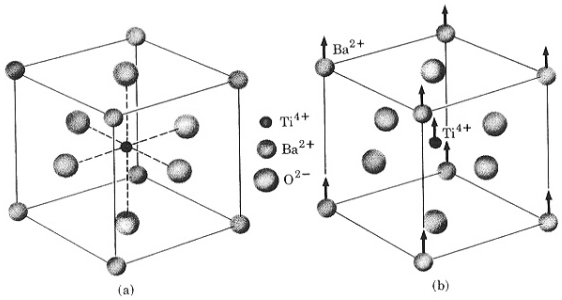

Figure 2.3: Barium titanate cubic perovskite structure (a). Below the Curie temperature (b) the structure is slightly deformed, developing a dipole moment. From [30].

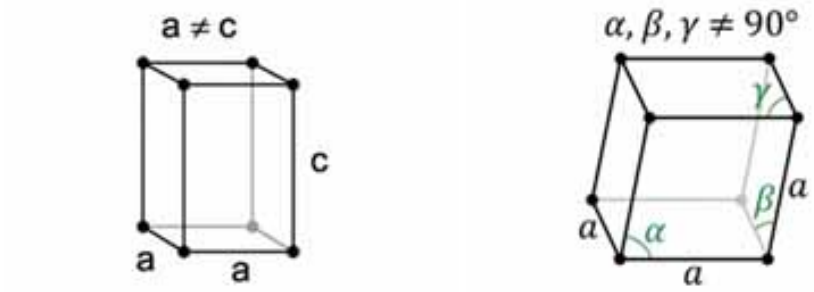

(a) **(b)**

Figure 2.4: Non-cubic crystal structures: (a) tetragonal and (b) rhombohedral.

temperature, T_C. It is characteristic to every material and it is composition dependent. At temperatures higher than T_C they are non-ferroelectric, at temperatures lower than T_C the structure becomes non cubic, such as tetragonal or rhombohedral, as shown in figure 2.4, and polar (ferroelectric).

In the cubic structure the B cations are in the centre of the octahedrons, while in the other structures they are shifted off the centres. When the B cation is displaced from the centre of the octahedrons, a change in the cell dimension occurs and hence in the crystal structure of the material. This situation leads to the creation of oriented dipoles (spontaneous polarisation, P_s), that can be switched by applying an external electric field as the ferroelectric domains, defined below.

In a ferroelectric material there are some regions in which the dielectric poles are aligned,

but in other regions the poles may be directed in a different direction. These region are called ferroelectric domains and groups of domains occur in individual crystallographic grains. In a ferroelectric ceramics the grains are randomly oriented and the material is not piezoelectric. In order to develop piezoelectricity a poling process is necessary. It is done by applying an external field (with simultaneous heating) high enough to align the domains in the direction of the applied field. The external field is maintained until the material is cooled down. This behaviour is described by the hysteresis loop, as shown in figure 2.5. By applying an electric field (E) to the material, the domains orientate, resulting in a increase of the polarisation, up to a maximum value (saturation polarisation). When the field is reduced, the polarisation does not go back to zero, but it falls to the remnant polarisation (P_r), because some domains remain oriented. In order to reduce the polarisation to zero, an electric field of a determine strength has to be applied. It is called coercive field (E_c). Figure 2.6 represent a schematic

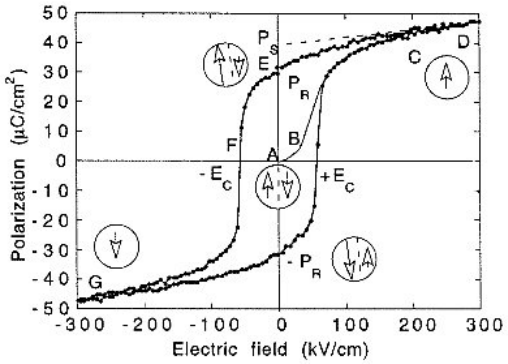

Figure 2.5: Schematic representation of the ferroelectric hysteresis loop. From [31].

of the poling process. In the unpoled material (left) the net polarisation is zero. After poling the domains are aligned with the electric field, the remnant polarisation is non-zero and the material is piezoelectric.

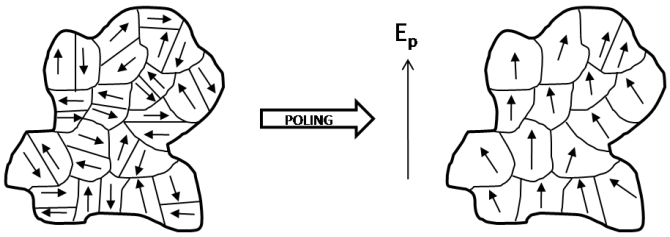

Figure 2.6: Schematic representation of the poling process.

2.1.1.1 Lead zirconate titanate

Barium titanate was the first piezoelectric ceramic studied (1946) followed by lead zirconate titanate (PZT) [1], first reported in 1954 by Jaffe and co-workers [32]. Since then many studies have been conducted on PZT, that replaced $BaTiO_3$ due to its higher operating temperature and better piezoelectric and ferroelectric properties [7].

PZT, $Pb(Zr_xTi_{1-x})O_3$, is a solid solution of lead zirconate (PZ) and lead titanate (PT). The dependence of crystal structure on the temperature is shown in figure 2.7.

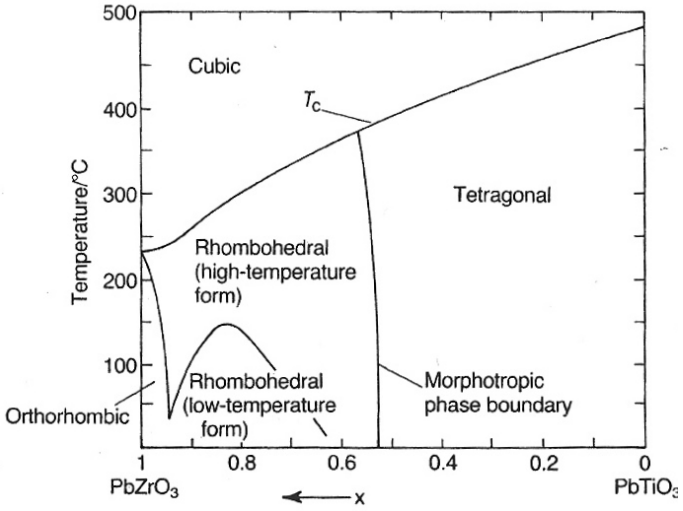

Figure 2.7: PZT phase diagram. From [1].

At high temperatures, above the T_C, the material is cubic and non polar, while at temperatures lower than T_C it can show different polar behaviours depending on the composition. At high PZ content the cubic structure elongates along a diagonal forming a rhombohedral

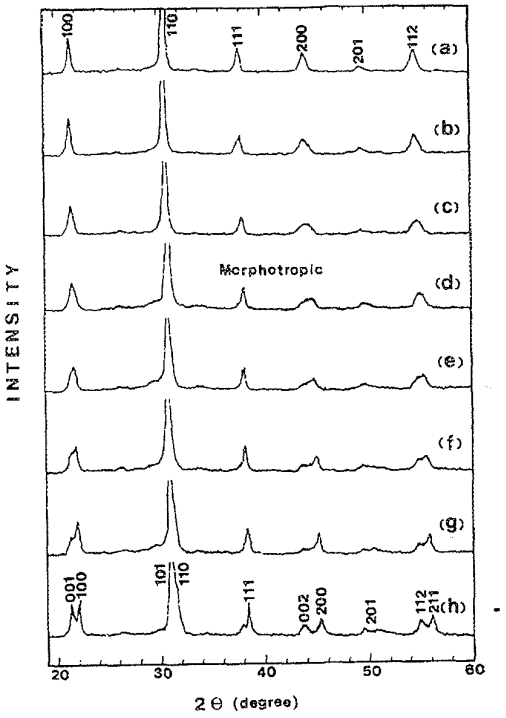

Figure 2.8: XRD patterns for PZT films with different Zr/Ti ratios: a) 64/36, b) 60/40, c) 56/44, d) 53/47, e) 52/48, f) 48/52 g) 44/56 and h) 40/60. From [33].

symmetry. When PT is predominant, the cubic structure elongates along an edge leading to the formation of the tetragonal symmetry. In figure 2.8 the phase change as a function of composition in PZT films (fired at 450^oC) is shown. At low Zr content tetragonal phase is obtained after firing. As the Zr content increases (figure 2.8 h to f), the splitting of the tetragonal peak at 2θ = 45^o is less pronounced, indicating the substitution of Ti ions with Zr ions, leading to a reduction of the tetragonal distortion [33]. Above 60 *mol%* of Zr (figure 2.8 a and b) the phase is rhombohedral, characterised by the unsplit peaks [33]. At Zr content between 52 and 60 *mol%* (figure 2.8 e to c) the two phases coexist and the XRD patterns are characterised by broad peaks. There is a region called morphotropic phase boundary (MPB) at which a transition between these two phases occurs at constant temperature. At the MPB composition, $x \simeq 0.52$ at room temperature, PZT shows the best characteristics, such as the highest piezoelectric coefficient (d_{33}), dielectric constant and mechanical coupling factor.

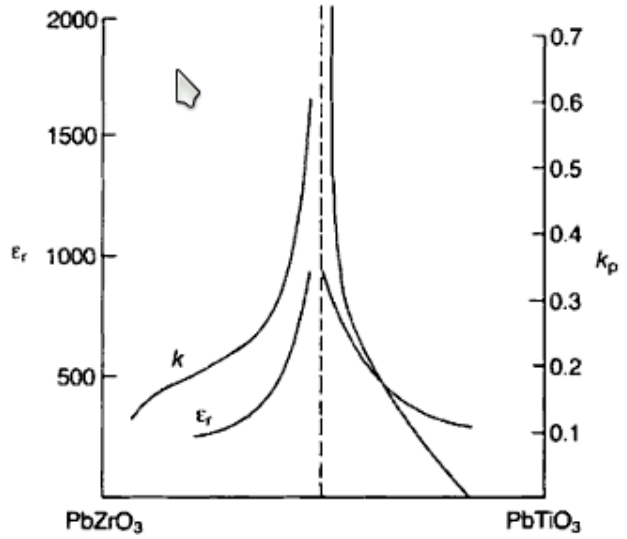

Figure 2.9: Coupling coefficient, k_p and permittivity values as a function of the composition of PZT. From [1].

Typical material properties for PZT close to the MPB composition are reported in table 2.1.

Table 2.1: Characteristic data of PZT close to the morphotropic phase boundary (Pz26). From [34].

Parameter	Symbol	Value
Curie temperature, ^oC	T_C	> 330
Piezoelectric coefficient, $pC\,N^{-1}$	d_{33}	290
Dielectric constant	K	1300
Dielectric loss	tanδ	0.003
Mechanical coupling factor	k_p	0.57

Since the piezoelectric coefficient reflects the electrical charge produced for an applied mechanical stress, it is an important parameter because it gives an indication of the sensitivity of a piezoelectric device [35]. An example of the dependence of properties on composition is shown in figure 2.9. It can be seen that both relative permittivity and coupling coefficient trends have a maximum in correspondence to the MPB.

Dopants effect The role of dopants in ceramics is to improve their properties, according to the final application. The doping effect is obtained by introducing substitutionals on the

A or B sites in the ABO_3 structure. The introduction of the doping agents, with typical concentration from 0.05 to 5 *at%* [1], lead to the formation of Pb or oxygen vacancies. Two different types of doping agents can be distinguished: donor or acceptors. Donor dopants are agents with a higher charge than that of the ions they replace, e.g. La^{3+} for Pb^{2+}. Acceptor dopants instead have a charge lower than that of the ions they replace [1], e.g. Na^{+} for Pb^{2+}.

When acceptors are used, oxygen vacancies are formed and hard doping is obtained. The oxygen vacancies form reorientable dipoles with the doping agent, that align creating internal fields. These fields stabilise the domains reducing the mobility of domain walls. Dielectric constant, dielectric losses and piezoelectric constant are decreased while mechanical quality factor is higher [2]. Hard doped PZT finds applications ranging from high voltage generators to high power ultrasonics (i.e. ultrasonic bath) [34]. On the other hand, when donors are used the charge is compensated by cation (Pb) vacancies [1] and soft doping is obtained. In this case the mobility of domain walls is enhanced [2]. Properties such as piezoelectric coefficient and permittivity are increased while the mechanical factor is reduced [2]. Soft PZT ceramics are used for pressure sensors applications and for transducers for medical and flow measurements [34].

In their work, Hizebry et al. [36] demonstrate the role of K and Nb doping in crack propagation in PZT (54/46) ceramics. Depending on the doping agent used, different behaviours were obtained. When Nb was introduced in the ABO_3 structure, crack growth resistance was observed. In the case of K doping, the behaviour was similar to that of the undoped ceramic. The authors attributed this difference to the nature of the doping agent. The substitution of Pb^{2+} with Nb^{5+} induces Pb vacancies. In this condition the domain mobility increases, leading to material reinforcement. On the contrary, when K was introduced in the structure, oxygen vacancies were created, that restrict domain motion [36]. Niobium-doping was also found to improve piezoelectric properties of PZT ceramics (53/47) when 1 *mol%* of Nb was introduced in the structure [37].

2.1.2 Application of piezoelectric materials

2.1.2.1 General applications

Piezoelectric ceramics in the form of thin or thick films are used in different devices. The application can be based on the direct or the converse piezoelectric effect or even on both of them.

Devices based on the direct piezoelectric effect convert mechanical energy into electrical energy. Application of this phenomenon range from ignition systems to sensor, such as force or pressure sensors [5]. However, the most known application of the direct piezoelectric effect is ignition systems, commonly used in lighters. In these systems two piezoelectric cylinders are compressed mechanically (i.e. by pressing a button). This compression generates a spark that can ignite a combustible gas. Highly volatile liquids are used for this purpose, such as butane or naphtha, in order to have flammable vapour to ignite. Piezoelectric crystals utilised in such ignitors have dimensions of about 3-5 *mm* in diameter and 5-8 *mm* in length [5].

When a device converts electrical energy into mechanical energy it is based on the converse piezoelectric effect. Devices based on this effect are actuators, ink jet printheads (see subsection 2.1.2.2), sound and ultrasound transducers and sensors. An example of piezoelectric actuator is described in the work of Zinck et al.[38], where the fabrication of membranes is shown. They showed that 800 nm PZT thin film was a good piezoelectric actuator for the fabrication of these membranes, that were suitable for microfluidic application, such as micro-pumps or micro-valves.

Recently the attention of piezoceramics has moved towards an application in the medical field [6, 39–41] as ultrasonic imaging for the detection of organs and skin. This technology is based on the propagation of sound waves at the interface between two media, with different acoustic impedance (z) [42]. This parameter describes the propagation of the sound waves in two media and it is frequency dependent. The propagation of these acoustic waves is

maximum between media with equal z. The waves are generated by a transducer and they travel between media with different z. When the waves encounter a media with different impedance, some of them are reflected back (generation of the echo) and some continue to travel. The echoed waves reach the transducer and generate a voltage proportional to the difference in acoustic impedance between the media. The transmitted waves will encounter other interfaces, repeating the process [5]. The received signals are then elaborated and the image is obtained.

2.1.2.2 Ink jet printheads

Ink jet printheads are a common example of device that works on the base of the converse piezoelectric effect. In printheads, a piezoelectric film (PZT) is situated on top of the ink chamber, in correspondence of each nozzle.

At the beginning (standby position) the piezoelectric crystal is slightly deformed (figure 2.10 a). The voltage applied is reduced to zero volts. This brings the crystal into a flat, relaxed position (figure 2.10 b) that corresponds to the maximum chamber volume. In this phase the ink is sucked into the chamber. By the application of a determined voltage (higher than the initial one) the PZT film is deformed again. This deformation is larger than the deformation obtained in the initial stage and it leads to a pressure increase in the chamber that results in the ejection of a droplet from the nozzle (figure 2.10 c). While the droplet is travelling toward the substrate, the piezoelectric crystal relaxes to the standby position and the chamber is refilled by the ink reservoir (figure 2.10 d). The droplet reaches the substrate and the cartridge is ready for the next cycle.

2.1.3 Micro electromechanical systems

Piezoelectric materials are commonly used in the fabrication of micro electromechanical systems. Micro electromechanical systems (MEMS) are electronic devices composed of an ac-

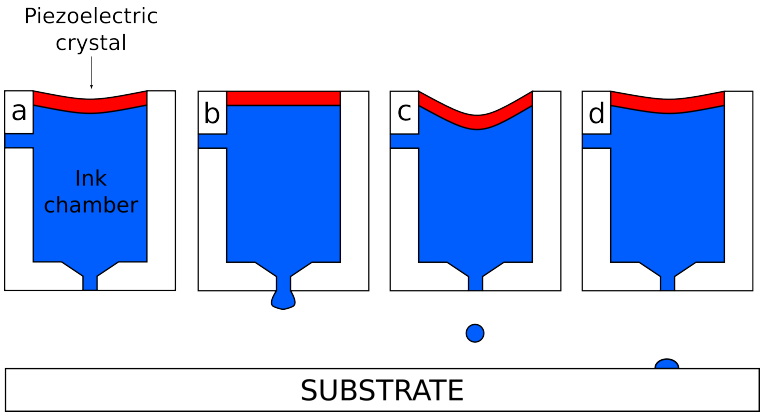

Figure 2.10: Ink jet print head based on the converse piezoelectric effect.

tive material (piezoelectric), mechanical elements and electrical connections, deposited onto silicon, polymer or metal substrates [3, 4]. The use of ceramics, such as PZT, as the active material has several advantages because, besides outstanding piezo-properties, they exhibit superior mechanical and functional properties, such as heat resistance, hardness and corrosion resistivity [43].

Techniques commonly used to deposit ceramic films on the substrate are screen printing [8, 9, 12], electrophoretic deposition [3] and spin coating [3, 10, 11] and they will be examined in the next subsections. A patterning process, photolithography, is also reported.

2.1.3.1 Ceramic films

Depending on the application, such as sensors, actuators or transducers, thick or thin films of ceramic are required to obtain the desired properties [3]. In recent years the attention has been focused on the application of PZT in thick films preparation [15, 44, 45] and its integration on silicon substrates.

The thickness of thick films can range between 10 μm to 100 μm [3, 44] but a single layer thickness depends on composition and properties, such as rheology and density, of the active material to be deposited. For these reasons the ink formulation is fundamental in order to obtain the desired properties of the final film.

During the fabrication of thick films problems related to the formation of cracks, the reaction between the substrate and the active film and pores formation can occur. Processing of ceramic films requires high temperatures and in presence of the substrate. In the case of PZT sintering process take place at 1200-1400^oC [46]. This can result in several problems, such as interfacial reactions between the film and the substrate (i.e. Pb and silicon), lead volatilisation, shrinkage, appearance of cracks and consequently lack of performances.

During sintering of PZT on silicon wafer it was noted that a reaction between Pb species and SiO_2 occurred [3]. The product of the reaction is a lead silicate compound that results in a loss of mechanical properties, such as delamination and presence of porosity. This problem can be solved by the use of diffusion barriers, such as ZrO_2, MgO or TiO_2, which are commonly deposited on silicon wafer [3].

In order to overcome problems related to the high sintering temperature, the combined use of powder and solution of the same material can be used. This leads to the creation of a composite system, slurry or ink, i.e. of PZT powder and PZT sol.

The presence of solid particles in the film results in several advantages. First of all it helps to reduce the crystallisation temperature, and hence all the connected problems. For example, in their work Wu et al. [47] compared the perovskite phase formation in films prepared with zero powder loading and with 1 wt% of PZT ceramic seeds. In the first case perovskite phase was formed at 600^oC, while in the case of seeded solution the phase formation temperature was 550^oC. Moreover the dielectric and ferroelectric properties were increased. The reduction of the crystallisation temperature can also lead to a reduction of the interdiffusion of species between the film and the substrate and also in lead volatilisation [48].

Another advantage that can be achieved by the presence of the powder within a fluid of the same material is a reduction in cracks formation in the film. Cracks are formed by the internal stress [11]. This stress is caused by the differential strain between the substrate and the ceramic film [10]. Barrow et al. [49] discovered that the deposition of a ceramic powder

dispersed in a sol gel solution resulted in a crack free layer. PZT and other ceramic films have been fabricated using this method. PZT ceramic (5 wt%) was mixed with PZT sol gel solution and deposited on the substrate by spin coating. Each layer was pyrolized to evaporate the organic solvent. Once the desired thickness was attained, the film was sintered to develop the perovskite phase. Using a dispersion of PZT powder in a solution of the same material resulted in a film with properties comparable with those of the bulk material. The formation of a crack free film was attributed to the presence of strong bounds between the PZT sol, the PZT powder and the substrate created by the sol. Moreover the presence of powder reduces the shrinkage because the sol amount is limited.

However, the presence of solid particles in the film can lead to the development of porosity due to interstitial gaps and packing defects. This can result in a lower values of dielectric constant. In order to reduce the formation of pores, sol infiltrations or the addition of sintering aids (e.g. Cu_2O-PbO) can be done. In the first case the sol fills the porosity of the existing layers. In the second case Cu_2O-PbO acts as a sintering aid, forming a liquid phase at low temperature that leads to a higher density of the final ceramic film [48].

Composite systems have been successfully used to create thick films [40, 46, 48], overcoming the main problem linked to pure sol-gel method (limited film thickness) [49]. Using this technique, Zhang et al. [40] fabricated a high frequency transducer with a PZT thickness of 13 μm. A 50 wt% of PZT powder was mixed with a sol-gel PZT precursor and deposited on silicon substrate by spin coating. The final transducer was suitable for high frequency imaging applications. In addition, by controlling solid loading and composite physical properties, such systems can be also used in direct writing applications.

2.1.3.2 Screen printing

Screen printing is the deposition technique most used for the fabrication of thick films [3]. The process is composed of several steps [35]. Initially the ink is spread on a screen posi-

tioned above the substrate, but not in contact with it. A squeegee is drawn across the screen forcing it in contact with the substrate. At the same moment the ink is forced to pass through the fine mesh of the screen. Finally, after the squeegee passage, the screen returns to the initial position, leaving the ink deposited on the substrate. Further layers can be printed to obtain the desired thickness, once the previous layer has dried. A final sintering process is required to eliminate the organic components and to densify the film [3].

Ink suitable for screen printing should be able to pass through the mesh when the squeegee forces it to do so, but retain its shape when the screen returns to the original position [35]. Moreover it has to produce a homogeneous layer, without the formation of bubbles or cracks [9]. The ink is usually composed of four constituents: active material, binder, vehicle and modifiers [3]. The active material is the material to be deposited on the substrate. The binder is a phase that helps to hold the active material together and to bind it to the substrate. The vehicle is a solvent that works as a carrier for the active material and the binder. Finally modifiers are substances added to the ink in order to obtain the desired rheological properties.

With screen printing the pattern is deposited directly on the substrate, but its main limitation is the resolution achievable, which depends on the size of the mesh [3]. The minimum resolution achievable is around 200 μm [35]. For this reason screen printing is not suitable to obtain small features.

2.1.3.3 Electrophoretic deposition

Electrophoretic deposition (EPD) is a technique used for obtaining thick or thin ceramic films or microstructures. EPD comprises two steps: electrophoresis and deposition [13]. In the first step, charged particles dispersed in a solvent move to an electrode (substrate) of opposed charge because of the presence of an electric field. As a second step the particles deposit onto the electrode [13] forming the desired pattern. An extra sintering stage is also needed to densify the film.

The particle stabilisation is very important in the suspension formulation as it affects the particle deposition on the electrode [13]: sedimentation degrades the quality of the layer. For this reason electrostatic (pH control) or electrosteric (absorption of of polyelectrolytes on particle surface) stabilisation is used to maintain the particles in suspension [3] and avoid sedimentation. The electric field is applied through constant current density because the field is maintained constant and hence a constant deposition rate is obtained [50].

With EPD it is possible to coat complex geometries [50], but the substrate needs to be conductive or coated with an electrode. This limits the use of EPD as a technique for MEMS fabrication because often there is a need to cover non-conducting areas with the ceramic film [3]. Another problem related to EPD is the difficulty in maintaining large particles in suspension, particularly in the case of lead based compounds [3].

2.1.3.4 Spin coating

Spin coating is a process used to deposit thin films on flat substrates [10, 11] and it is usually adopted as deposition technique for photolithography processes [51].

Prior the deposition, the substrate (i.e. silicon wafer) is cleaned with acetone and isopropanol in order to remove dust or debris on the substrate surface. The steps of the spin coating process can be summarised as follows [52]. The wafer is placed in the spin coater and an excess of a solution or suspension of the material to be deposited is placed on top of it. The wafer is then spun. During spinning, the solution is spread, eliminating the unwanted material, and dries leaving a thin film on the substrate. Spin speed, spin time and concentration of the solution determine the thickness of the resulting film [53]. Typical speed and duration are 2000-3000 rpm and 30-60 seconds, respectively, but higher values are also used [10]. The film is than baked at low temperature (100-200^oC) to eliminate the organic components and then pyrolysed. All these steps are repeated until the desired thickness of film is reached.

Since an excess of material is required, high waste is present in this process.

2.1.3.5 Photolithography

Photolithography is a patterning process, composed of multiple step [54]. The steps can be summarised as follows [51]. The first step is the photoresist deposition after deposition of the material to be patterned on the substrate (silicon wafer). The photoresist is deposited on it by spin coating, forming an uniform layer. The excess of solvent is removed by heating the wafer at a temperature that depends on the photoresist utilised. Two types of photoresists are used: positive and negative. The first ones (more common) become soluble in the developer after exposion. The negative type becomes insoluble. The dried wafer is subjected to UV light through a mask (that limits the resolution) containing the desired pattern. A developer is then used to develop the photoresist revealing the pattern. A chemical agent (typically acid, e.g. HF or HCl) is then used to remove the material in the areas not protected by photoresist (etching). Finally the remaining photoresist is removed using a solvent revealing the desired patterned ceramic film.

This process is suitable for the fabrication of large volumes of devices [14]. However its big limitation is related to the low feature diversity and the big amount of wasted material [14]. Moreover it is a energy consuming process [55] and dangerous materials are used in the etching step, leading to health and safety issues.

2.1.3.6 New trends

The key factor in the design of new devices is usually the cost of their components [6]. This depends on the quality, the amount and the environmental impact of raw materials. Regarding PZT, the biggest drawback is given by the toxicity of lead. To reduce the lead effect on the environment, studies have been done in order to eliminate Pb or reduce its content in the product [6]. Nowadays the trend is to use less of the hazardous materials (i.e. Pb) and to miniaturise. In small devices, the amount of dangerous material is reduced, but material properties have to be enhanced in order to make miniaturised devices competitive

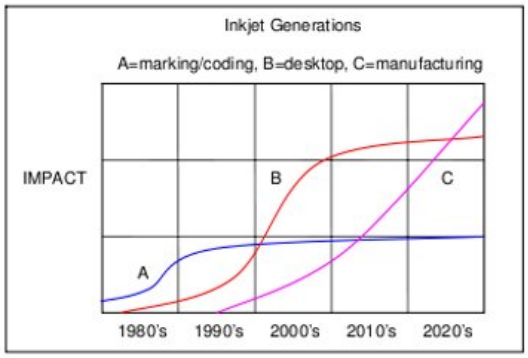

Figure 2.11: Development of the ink jet printing application. From [58].

with traditional devices [6]. Lately lead-free materials have become of interest [6]. Potassium sodium niobate (KNN) received considerably attentions as a lead-free ceramic. However its poor sinterability [56] and its low properties, compared to traditional PZT ceramics, leave it under study.

The trend for miniaturisation has been the driving force for the development of ink jet printing. At the beginning of the 1960s the first printers (continuous method) were developed and they were commercialised a decade later by IBM. In the same period the first drop on demand printers were invented and produced later by Siemems and Canon [57]. Nowadays, drop on demand are the most commonly used ink jet printers for every day applications. In figure 2.11, the development of ink jet applications is shown. Initially, in the 1980s, ink jet found space in applications for marking and coding and later office and home printers were commercialised [58]. Recently the increased sophistication of electronics has led to the improvement of ink jet printing technology with the origin of new applications (curve C in figure 2.11), including the fabrication of displays, actuators, transducers and in-situ synthesis of DNA [14].

2.2 Direct writing techniques

The need for miniaturisation and the need to overcome the disadvantages of the common deposition techniques led to the development of a new group of technologies, called direct writing. Micropen writing, robocasting, fused deposition and ink jet printing represent the techniques embraced in the group. These approaches can be divided into two groups: droplet-based, such as ink jet printing, and filament-based, like robocasting, fused deposition and micropen writing. In table 2.2 the minimum printed feature size for all of these techniques is reported. It can be seen that among direct writing techniques, ink jet printing is the one that leads to the smaller printable feature size. This makes it suitable for the fabrication of miniaturised devices.

Table 2.2: Minimum printed feature size for the direct writing techniques. Adapted from [15].

Technique	Minimum feature size (μm)
Ink jet printing	20 (lateral)
Robocasting (in air)	500 (diameter)
Fused deposition	100 (diameter)
Micropen writing	25 (diameter)

2.2.1 Filament-based techniques

In these techniques, highly concentrated colloidal inks [59] are squeezed through an orifice forming a continuous filament at its outlet. Its deposition on the substrate is computer controlled. The main advantage of the filament-based techniques is that 3D structures with unsupported elements can be created. Since the filament is continuous, the start-stop steps have to be minimised in order not to interrupt the ink flow [15]. For this reason the pattern design is more complicated compared to ink jet printing. An ink suitable for filament-based techniques usually contains significant levels of additives which have to be removed by heat treatment [15]. Moreover a sintering step is needed. The filament diameter is related to the

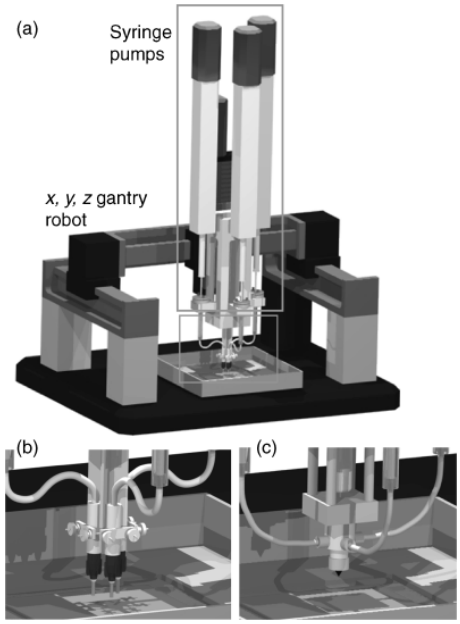

Figure 2.12: schematic representation of the robocasting deposition technique: a) vertical structure, b) discrete nozzle array and c) mixing nozzle. From [60].

nozzle diameter, ink rheology and the printing speed. Robocasting, fused deposition and micropen writing will be discussed in the next subsections.

2.2.1.1 Robocasting

Robocasting, as well as fused deposition, is typically used for the assembly of 3D ceramic components [15]. A schematic representation of this technique is shown in figure 2.12. The ink is loaded into one or more syringes (if different inks have to be printed on the same pattern) and it is extruded through the nozzle. A determined pressure is required to maintain the desired flow conditions [15]. In order to avoid or reduce the risk of cracking and shrinkage during the drying process, the inks suitable for robocasting are formulated with high solid contents, up to 64 *vol%* [15]. An example of a structure obtained by robocasting technique is represented in figure 2.13.

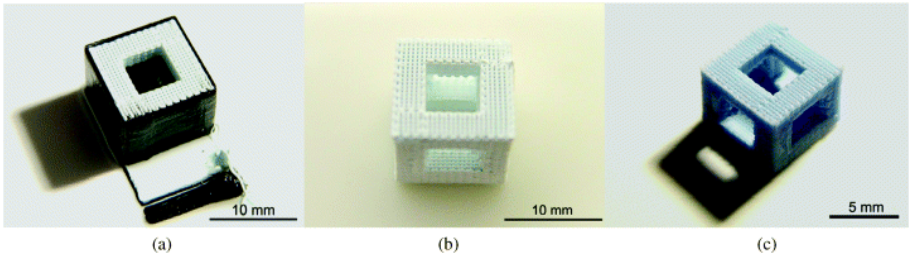

Figure 2.13: Hollowed cube obtained by robocasting of a concentrated hydroxyapatite ink, using a carbon black ink as a fugitive support: a) after printing, b) after carbon black removal and c) after sintering. From [15].

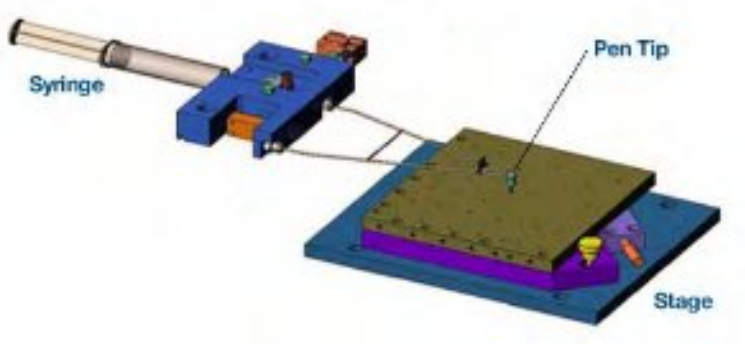

Figure 2.14: Schematic representation of the micropen writing deposition technique. Adapted from [55].

2.2.1.2 Fused deposition

Fused deposition is a technique similar to robocasting. The main difference is that the ink is usually composed of a colloid-filled polymer that is molten due to the extrusion at elevated temperatures and solidify on the substrate after cooling [15]. These kinds of ink need high binder contents to create uniform consistency. In order to remove the binder a burnout step is required and it can lead to the formation of defects such as blisters [15].

2.2.1.3 Micropen writing

As in the previous techniques, the ink, in the form of a paste, is extruded through an orifice [43]. The ink is loaded into a syringe and it is compressed at high pressures through a micro-capillary tip on the substrate, as shown in figure 2.14. The major advantage of this technique

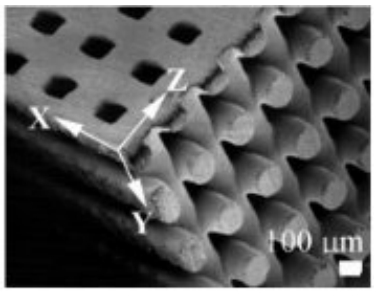

Figure 2.15: 3-D structure of silica colloid fabricated by micropen writing. Adapted from [43].

is the possibility of deposition onto non-planar or curvilinear substrates [55]. Micropen writing is suited for the production of thick film devices [15]. An example of type of structure that can be obtained with this approach is shown in figure 2.15.

2.2.2 Droplet-based techniques

Ink jet printing (IJP) is a droplet-based direct writing techniques. It is a non-contact process that allows the creation of thin or thick structures under computer control [15, 43, 59, 61].

Several advantages can be achieved by the use of IJP. First of all, it is a non-contact technique. This reduces the material contamination, possible in the contact deposition techniques. Since the pattern is created by computer control a change in the design is easy to obtain, without the use of expensive masks such as in the case of screen printing. This results in a fast and economic prototyping process. The pattern can be directly printed on the substrate and on a wide variety of substrates. An example of an antennae printed on a flexible substrate is shown in figure 2.16.

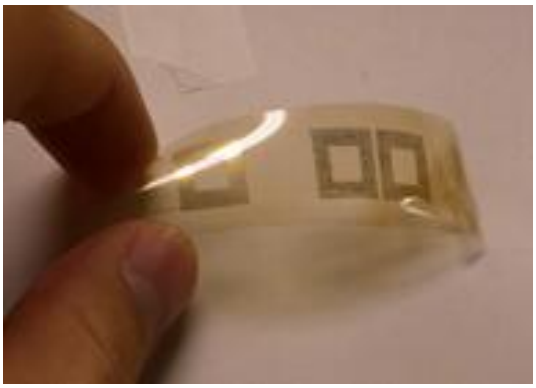

Figure 2.16: Antennae printed on plastic. From [14].

Moreover the wastage of material is very low, the printing speed is high and the resolution achievable is better compared to many traditional thick film deposition techniques and to the other direct write approaches, as shown in table 2.2.

Ink jet printing is under development and in recent years has been extended to other applications, e.g. in the biomedical field, like medical imaging and drug delivery, optic and electronic [59, 62] and it will be discussed in the next section.

2.3 Ink jet printing

Two different categories of ink jet printer exist and they can be distinguished depending on the ink delivery mode: continuous and drop-on-demand (DoD) [3, 14, 15, 59, 63–65]. These will be examined in subsections 2.3.1 and 2.3.2, respectively.

2.3.1 Continuous

In continuous ink jet printing, schematically represented in figure 2.17, the ink is forced by a high pressure to pass through an orifice forming a jet at the outlet. The ink flow breaks up into single droplets which are first charged by electrodes and then deflected by deflecting plates [15] to be deposited at desired positions. The droplet deposition on the substrate is controlled

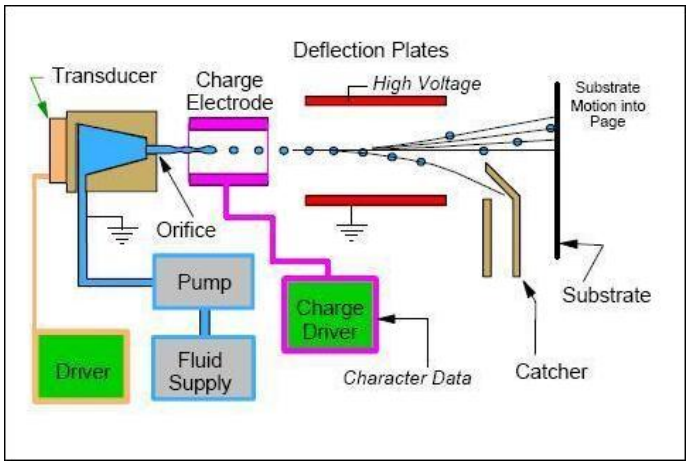

Figure 2.17: Schematic representation of a continuous ink jet printer. From [66].

by their level of charge and plate charge [58]. For this reason the ink must be conductive, which limits its use with ceramics unless a conductive ceramic or carrier is used. Not all the ejected droplets are deposited on the substrate because they are not needed for the creation of the pattern. Since it is a non-contact technique, these unprinted droplets can be recirculated through an ink recovery system [14, 15].

The droplets produced are uniform [65] and with a size approximately double that of the orifice diameter in a range of 20-150 μm [14]. This technique also offers a higher speed process compared to the DoD technology and allows large areas to be patterned in shorter periods of time [63, 65].

2.3.2 Drop-on-demand

A schematic representation of DoD printer is shown in figure 2.18.

The main difference from continuous printing is that in DoD the droplets are ejected only when required. As with the continuous method, DoD is a non contact method, but ink recirculation is not necessary in this case because the droplets are ejected from the orifice only when required. The droplet positioning on the substrate is controlled by the movement of the printhead across it [3]. This technique is better suited for the accurate deposition of

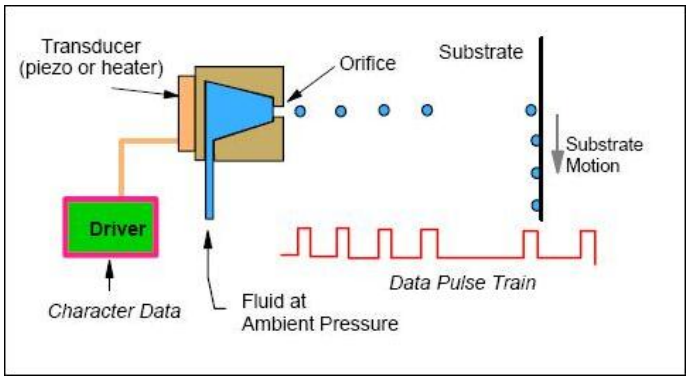

Figure 2.18: Schematic representation of a drop-on-demand ink jet printer. From [66].

small amounts of material [3, 15, 65]; the diameter of the drops produced is in the range 20-150 μm [14].

The droplet is obtained by a pressure pulse that acts on the ink reservoir [15, 64]. This pressure pulse can be created by heating the liquid chamber to create a vapour bubble (thermal DoD) or by exciting a piezoelectric actuator at a determined frequency (piezo DoD, see figure 2.10) [15]. Of the two systems, the latter one is the most common [64]. The pressure pulse travels through the chamber and when it reaches the orifice a drop is ejected [14].

2.3.3 Nozzles and resolution

The resolution achievable using IJP is related to the number of resolved drops that can be printed in a given space (namely dpi, dots per inch) [67]. However other factors can also influence the final resolution, including liquid viscosity and surface tension [68]. In order to print small but resolved patterns, like patterns for MEMS application, a high resolution is needed. Since the resolution corresponds to the number of droplets deposited in a linear inch, it is connected to the droplet size, which is related to feature size. A typical droplet is double the size of the nozzle used to eject it and ranges between 20 and 150 μm [14]. The control of the droplet spreading on the substrate is also important for the obtainment of resolved pattern.

Ink jet printing of ceramics involves the use of solid particles dispersed in a carrier fluid.

To prevent nozzle clogging and to degrade the final printed area the particles dispersed in the liquid media should be $\frac{1}{100}$ the size of the nozzle diameter. Since this dimension can be as small as 21 μm, the powder should be around 200 nm in size. This leads to a requirement for the synthesis of powders in the submicron range and their stabilisation in carrier fluids in order to prevent nozzle clogging as a consequence of sedimentation or agglomeration (see section 2.3.5). If nozzles are partially blocked due to clogging or due to the formation of dried ink film at their outlet, resolution, accuracy and precision will be compromised. Even if with ink jet printing the droplets are directed on the substrate with high accuracy, partial clogging can cause a deviation of few microns in the droplet deposition [67]. This results in ink placement where it is not required, therefore a poor pattern reproduction is obtained.

2.3.4 Printing parameters

The quality of a pattern depends on both the ink properties and printer setting. The printer parameters that affect the quality of the printing for the printer used in this work are summarised as follow:

2.3.4.1 Drop Spacing (DS)

It represents the centre-to-centre distance from one drop to the next in X and Y directions. It is adjustable from to 5 to 254 μm. Changes in the drop spacing dimension means a change in the pixel dimension.

2.3.4.2 Firing Voltage (V)

It is the voltage applied to the piezoelectric crystals situated at each nozzle. The application of this voltage results in a deflection of the crystal and a droplet is ejected from each active nozzle. The voltage ranges between 1 and 40 V. High values of firing voltage lead to the ejection of bigger drops due to the generation of higher pressure in the print chamber.

2.3.4.3 Cartridge Print Height (CPH)

It is defined as the distance between the substrate and the printhead during printing. By decreasing the CPH it is possible to improve the printed area, because the droplet mismatch on the substrate is reduced (see subsection 2.3.7), but contact between the cartridge and the film is more likely to happen. It can be adjusted from 0.25 to 1.5 mm.

2.3.4.4 Tickle control

This controls the movement of the ink meniscus at the nozzle opening and is achieved by applying a sub-ejection oscillating voltage to the piezo element in the printhead. It is adjustable from 1 to 100 *kHz* and helps to maintain the nozzles clean from the formation of dried ink film at them outlets.

2.3.5 Inks for ink jet printing

Several types of ink can be printed by IJP, i.e. dye or pigment inks, water [69, 70], solvent [61, 62, 71–73], or wax based [74, 75] inks depending on the application. For example, dye inks are not commonly used for thick film deposition because of the small thickness achievable for each layer. For this purpose pigment inks are usually employed. High solid loading are preferable because the desired film thickness can be printed quickly and shrinkage during solvent evaporation is reduced, but typical solid loadings are lower than 5 vol% [3, 59] in order to obtain a printable ink. The printability of the ink depends on several factors and properties, including viscosity and surface tension, as described below.

The fluid dynamics of drop-on-demand drop formation has previously been reported [70, 74]. A dimensionless number Z represents the possibility that a fluid will be ejected by a DoD ink jet printing and it is given by the following equation [15, 64]:

$$Z = \frac{Re}{\sqrt{We}} = \frac{\sqrt{\gamma\,\delta\,r}}{\eta} \tag{2.3}$$

where Re is the Reynolds number ($Re = \frac{v\,r\,\delta}{\eta}$), We is the Weber number ($We = \frac{\delta\,v^2\,r}{\gamma}$), v is the ink velocity, γ, δ and η are the surface tension, density and viscosity of the ink, respectively and r is the nozzle orifice radius. A droplet can be ejected by the printer if Z is in the range 1-10, as shown in figure 2.19. If Z is too small (<1) the viscous forces are dominant and high pressure is required to eject a droplet. If Z is too high (>10, figure 2.19) a column of liquid is formed from the nozzle before droplet formation [75], this phenomena can lead to the creation of satellite drops. Satellite drops are drops that follow the main drop after its ejection, as shown in figure 2.20. Their formation is common in ink jet printing [58], and is an unwanted phenomena as it results in loss of quality. They appear when the ligament of ink behind the main drop breaks up, forming one or more small drops. Three different types of satellites can be distinguished [58]. In most cases satellites merge in the main drop (forward- or backward-merging), recombining with it after a certain period of time. The third type is represented by the so-called infinite satellites, where the satellites do not merge with the main drop but travel behind it until they reach the substrate. This is the case in which the quality of printing is reduced as shown later in figure 2.24 b.

For these reasons ink properties have to be controlled within determined ranges. For example, with the Dimatix DMP-2831, it is possible to jet a wide variety of fluids with viscosities in the range 2-30 $mPa\,s$ and surface tensions up to 60 $mN\,m^{-1}$. But at the operating temperature the fluid characteristic ranges shrink down to 10-12 $mPa\,s$ for viscosity and 28-33 $mN\,m^{-1}$ for surface tension.

The viscosity increases rapidly with the solid loading. However it is possible to print suspension with concentration higher than 5 vol%. Through the control of particle size, dispersant level and type of solvent Wang and Derby [64] have been able to print a suspension

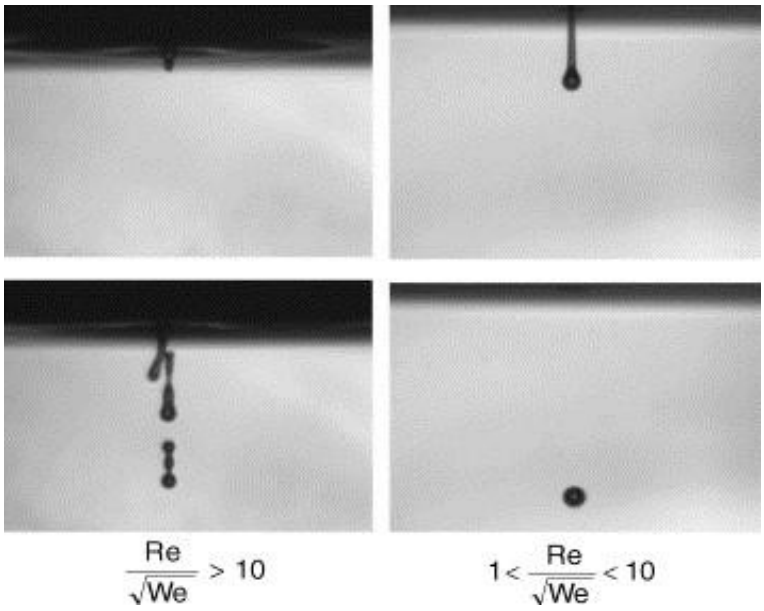

Figure 2.19: Images of ejected droplets of inks with Z > 10 (left) and 1 < Z< 10 (right). From [76].

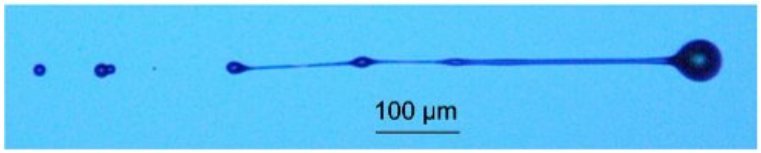

Figure 2.20: Formation of satellite drops after the breaking of the ink ligament ejected from the nozzle (Z>10). From [58].

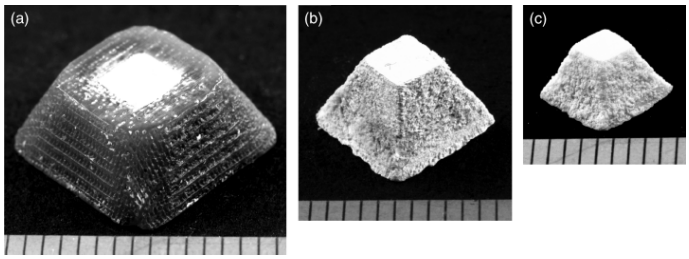

Figure 2.21: Images of printed objects (scale divisions indicates 1mm): (a) as-printed ceramic object showing external support structure, (b) ceramic/wax object after removal of support structure, and (c) printed ceramic object after sintering illustrating shrinkage. From [64].

of 35% by volume of PZT in a 60/40 paraffin oil/wax vehicle by ink jet printing (figure 2.21).

In order to minimise nozzle clogging dispersants are included in the ink formulation to improve the stability of the ceramic particles suspended in the solvent. The amount of dispersant required is a function of the effective surface area of the particles dispersed in the liquid. The smaller the particle size, the higher the surface area, and hence the larger the area for the dispersant to cover. Therefore a decrease in the particle size means a higher amount of dispersant. This amount can vary from 0.1 to 0.6 wt% of the powder but larger quantities have also been used [77]. The presence of humectants, such as ethylene glycol (10-20 vol%), is also common in ink formulation to prevent clogging by reducing the drying rate of the ink [78].

Since inks undergo solidification by solvent evaporation [59], the drying stage can be considered as a critical process and its rate must be controlled in order to maintain high resolution. If the drying rate is too high, nozzle clogging occurs; if it is too low the ejected drops will spread on the substrate causing a loss of resolution [3, 59, 65].

2.3.6 Fluid spreading on substrate

After impact on the substrate, the drop spreads which influences the layer thickness and the lateral resolution. Understanding the fluid spreading on a substrate is important to obtain

the desired pattern. The requirement for printed circuits are smoothness, narrow and straight lines; for organic LEDs, film uniformity is mandatory to achieve uniform emission [79]. Different equations have been proposed to determine the droplet spreading on a surface. For example Lewis [59] suggests an estimation of the maximum spreading of a droplet by the following equation:

$$\frac{r_{max}}{r} = \sqrt{\frac{We^2 + 12}{3\ (1 - cos\theta) + 4\ \frac{We^2}{\sqrt{Re}}}} \tag{2.4}$$

where r_{max} is the maximum droplet radius after impact, *r* is the droplet radius and θ is the contact angle between the droplet after impact and the substrate. This equation represents the upper limit of spreading because it does not consider the drying stage [59]. A simplified estimation of the drop spreading is proposed by Gong [80]. He represented the droplet impact on a smooth surface as a drop that spreads with a shape of an ice hockey puck, as shown in figure 2.22. The author elaborated an equation that identify the maximum spreading (β) of a droplet on a smooth surface, valid for $We \gg \sqrt{Re}$, as shown in equation 2.5:

$$\beta = 1.351\ Re^{\frac{1}{8}} \tag{2.5}$$

β represents the maximum diameter of the hockey puck scaled by the initial droplet diameter [80]. The spreading factor increases with both increasing Reynolds and Weber numbers.

In their study Soltman and Subramanian [79] examined the effect of temperature and drop spacing on the droplet deposition on a smooth surface. The ink used in the study was a suspension of a conductive polymer in water, used for organic LEDs. In figure 2.23 the different morphologies obtained after printing are shown. Individual drops (figure 2.23 a) are obtained at large drop spacing. Under this condition the droplets are too far to interact to each other, independently from the temperature. At low temperature and DS the droplets merge

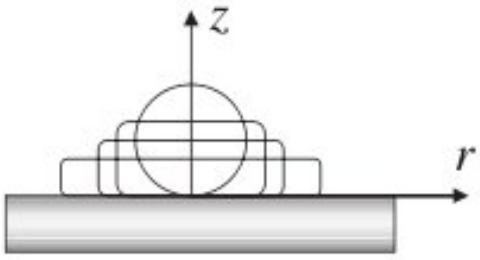

Figure 2.22: Schematic representation of droplet spreading on a solid smooth surface. From [80].

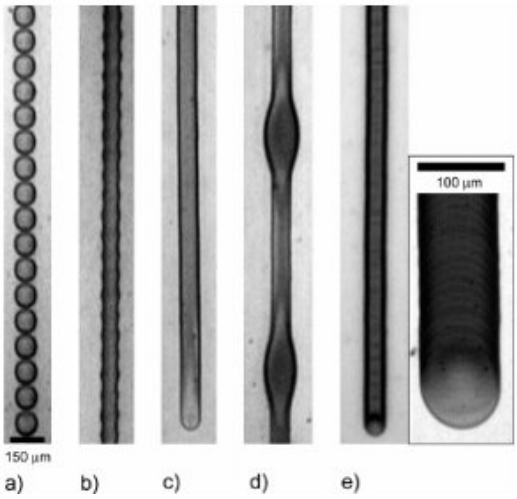

Figure 2.23: Examples of printed lines behaviours: a) individual drops, b) scalloped line, c) uniform line, d) bulging line and e) stacked coins. From [79].

in a scalloped line, characterised by the rounded contact lines (figure 2.23 b). This pattern is narrower than the individual drops because the spreading of the fluid on the substrate is decreased by the merging between the droplets. The best printed line (uniform line in figure 2.23 c) is obtained by further decrease of the DS. If the DS is reduced too much the bulging behaviour appears (figure 2.23 d). Finally, when the temperature is increased to a value at which the evaporation of a drop is faster than the jetting frequency, stacked coin behaviour is obtained. At this temperature each drop will dry before the next drop is deposited, avoiding droplets from merging.

2.3.7 Defects

The quality of the printed pattern is connected to the formation of defects, both macro and microscopics. In order to obtain a good quality printed area the formation of such defects has to be limited and eventually avoided. In their work, Song and Nur [62] explained the defect formation and prevention in ceramic deposition by ink jet printing as discussed below.

Macroscopic defects, such as satellite drops and ink spray formation result in erroneous droplet deposition. These defects can be attributed to the ink properties. Microscopic defects, instead can be considered as internal voids and craters and are due to solvent boiling or impact of the droplet on the substrate.

2.3.7.1 Macroscopic defects

Macroscopic defects are associated with the formation of spray, satellite drops and the printing distance. Ink spray arises when a dried film of ink obstructs the outlet of the nozzle. This situation is common in solvent based inks and can be reduced by cleaning the nozzle tip (i.e. enabling the tickle control or cleaning the nozzle on a pad). Another cause of nozzle clogging is the presence of agglomerates or debris. Their presence can be reduced by milling and filtering the ink but in long printing processes the formation of agglomerates is likely to happen. In figure 2.24 a, the effect of spray formation is shown. It can be seen that the area surrounding the pattern is covered by fine droplets resulting from the break up of the main drop during printing.

Another cause for the presence of macroscopic defects in the pattern is the formation of satellite drops. They are formed when the liquid jet breaks-up, leading to the formation of a primary drop and many other small drops behind it. As a consequence of their formation the droplet relic will be no longer circular, but distorted (figure 2.24 b), because the deposition of the primary drop is followed by the deposition of the satellites behind it. The ink viscosity can be increased in order to reduce the probability of satellites drop formation.

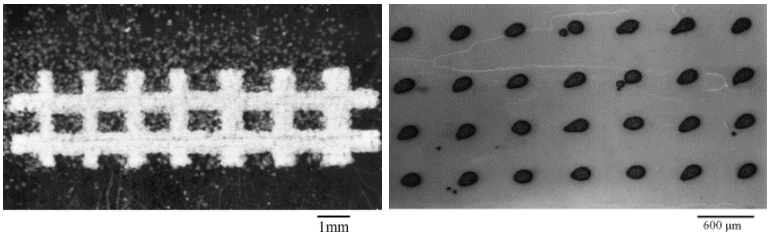

(a) **(b)**

Figure 2.24: IJP defects. (a) An example of grid pattern printed on acetate using a PZT ink showing the effect of ink spray on line definition. (b) Dot array printed using an organic gold ink showing the effect of satellite drop on the elongated shape of relics and occasionally fine droplets are detached from the main droplet. Adapted from [62].

The distance between the printhead and the substrate (CPH) can also have an effect on the quality of the printed pattern. An increasing in the CPH can results in a mismatch (ΔX) in the droplets deposition, as shown in figure 2.25. A correlation between the CPH and two printing velocities (equation 2.6) can be given by:

$$\Delta X = CPH \, \frac{V_x}{V_z} \tag{2.6}$$

where V_x is the cartridge velocity during printing and V_z is the firing velocity. V_x is constant for each printer and V_z can be also considered constant for a given ink and cartridge as it depends on the ink properties and power of the piezoelectric crystal. So as the CPH increases, the mismatch in droplet deposition (ΔX) increases as well. The effect of CPH is more important when thick films are printed. An increment in the film thickness during printing leads to a reduction of the distance between the printhead and the deposited material, meaning an effective reduction of the CPH. In this condition the droplet deposition is no longer in the desired place, that results in a loss of printing quality. In addition the risk of contact between the cartridge and the deposited material is increased.

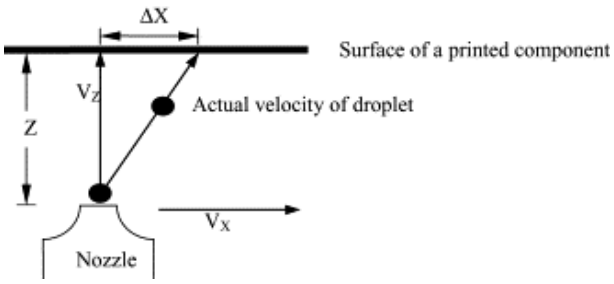

Figure 2.25: Schematic representation of the effect of the distance between the substrate and the cartridge (Z corresponds to the CPH). From [62].

2.3.7.2 Microscopic defects

Microscopic defects are associated with the printing process. Voids or craters can be created when droplets are printed on a existing layer if it is not dried or hard enough to resist the penetration of the subsequent droplets. The drying rate is a key point in the reduction of void formation. An increment in the drying rate can result in the liquid to solid conversion of the top surface of the deposited layer of ink, reducing the penetration of subsequent droplets. This is achieved by increasing the printing temperature or by the use of volatile solvents, but it can also lead to nozzle clogging or to the stacked coins behaviour.

If the deposited layer is not dried enough, craters will be formed as a new drop impacts on it. In this case the surface tension tends to reduce the surface area associated to the crater, resulting in a recovery of the defect. When these conditions are present, such as in the case of ink formulated with high quantity of additives, the drying rate should not be increased as it may result in the formed crater not self healing.

Several other factors can influence the final quality of the printed pattern such as nozzle diameter, the presence of surfactants, the atmospheric conditions and ink spreading on the substrate [67]. Several studies have been done on droplet spreading on different substrates [67, 75, 81, 82]. A typical ink drop of 60 μm can produce, after contact with the substrate, a feature with a diameter of 600 μm and a height of 1 μm [3, 59], but the droplet size is related to the nozzle size, so the orifice diameter represent a limitation in the ejection of small

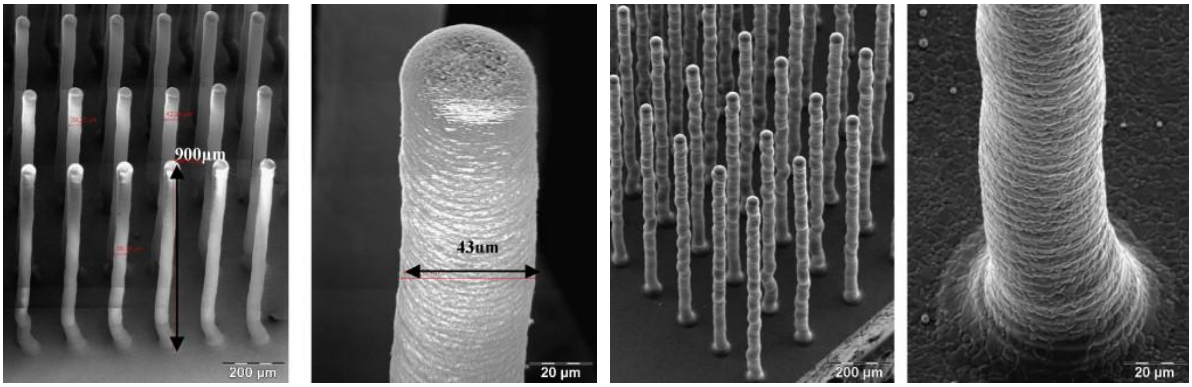

(a) **(b)**

Figure 2.26: SEM micrographs of micro-pillar arrays of a) PZT and b) TiO_2. From [83].

droplets [82]. For all of these reasons the control of ink properties and process parameters is very important for obtaining defect free, small printed features.

2.3.8 Application of ink jet printing

In their work, Lejeune et al. [83] describe the fabrication of ceramic micro-pillar arrays of PZT for medical imaging probes and TiO_2 for photocatalytic devices. A drop-on-demand IJ printer with nozzle diameters of 52 or 60 μm was used for the experiments. The ceramic suspensions were adjusted in order to reach the values of viscosity and surface tension of 5-20 $mPa\,s$ and 30-35 $mN\,m^{-1}$, respectively. Different inks were formulated with diverse amounts of binder and solid loading. Successful micro-pillar arrays were built with inks described as follow: 10 *vol%* PZT powder, high molecular weight binder and ceramic to binder ratio of 60/40 for the PZT suspension and 15 *vol%* of TiO_2 powder, high molecular weight binder and ceramic to binder ratio 75/25 for the TiO_2 suspension, as shown in figure 2.26. Both the inks were printed with a 52 μm aperture print head.

Ink jet printing allows the fabrication of complex geometries without the need of expensive masks. This characteristic of IJP is useful when the pattern has to be changed several times. In fact the new pattern design can simply be uploaded into the printer program. Cappi

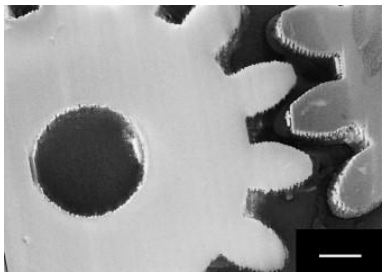

Figure 2.27: SEM micrographs of the Si_3N_4 gearwheel after sintering for 2 hours at 1780^oC . Scale bar 1 *mm*. From .

et al. [84] successfully printed a complex shape with Si_3N_4 suspension by ink jet printing. 30.2 *vol%* of Si_3N_4 powder with mean particle diameter of 0.4 μm was dispersed in aqueous medium. Ethanol and ethylene glycol were added to adjust physical properties and an organic additive was used to avoid flocculation. A drop-on-demand IJ printer equipped with two bubble-jet print heads was used for the experiments. In figure 2.27, the Si_3N_4 gearwheel printed by IJP is shown. It can be seen that after sintering no lamination occurred and a complex geometry was printed.

2.4 PZT micro-nano powder synthesis

Several techniques have been used to synthesise PZT submicron and nanopowder, including hydrothermal [19, 21], chemical [85, 86], milling co-precipitation [87] and sol-gel [16–18, 20, 22–24]. These techniques are usually long and complex processes and result in agglomerated particles or big particles. The use of toxic and hazardous solvent, such as 2-methoxyethanol or HF, may also be needed [22].

In hydrothermal synthesis the need to expensive teflon autoclaves is necessary and the procedure can lead to the formation of large cubic particles as shown in figure 2.28. The micrograph represents PZT powder synthesised by hydrothermal method as described in [19]. Starting materials have reacted for 4 hours at 160^oC.

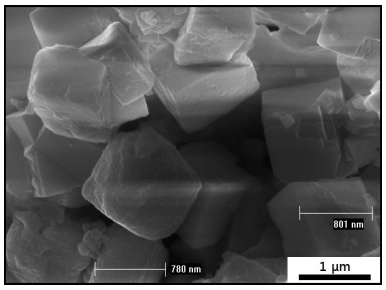

Figure 2.28: SEM micrograph of PZT powder synthesised by hydrothermal method.

In chemical routes, such as the one described by Bose and Banerjee [85], several steps are needed to synthesise the desired powder. A precursor solution of $Pb^{2+}$was prepared by dissolving $Pb(NO_3)_2$ in water. Zr^{4+} and Ti^{4+} precursor solutions were prepared by dissolution and precipitation steps, with the use of HNO_3, NH_4OH and HF. The precursor solutions were mixed together with the addition of sucrose solution. Different heating steps were used in order to remove first water, then carbon and to develop perovskite phase.

Sol-gel is a widely used technique to synthesise ceramic powder, but the process is usually long, as with the process described by Linardos et al. [16]. In figure 2.29 the synthesis of PZT powder by sol-gel method is described. PVP was added to the PZT-PVP gel (i) to obtain a new PZT-PVP gel (ii). This was then dried at 60^oC for 144 hours and heat treated at different profiles to obtain PZT powder. It can be noted that several heating and stirring steps are needed for long periods of time.

Electro hydrodynamic atomisation and molten salt synthesis represent two alternative and simple routes for the production of ceramic particles in the submicron range (micro-nanoparticles) and they will be discussed in the next subsections of this chapter.

2.4.1 Electro hydrodynamic atomisation

Electro hydrodynamic atomisation (EHDA), also known as electrospray, is an alternative technique that allows the production of nanopowder [25, 26] or the deposition of ceramic

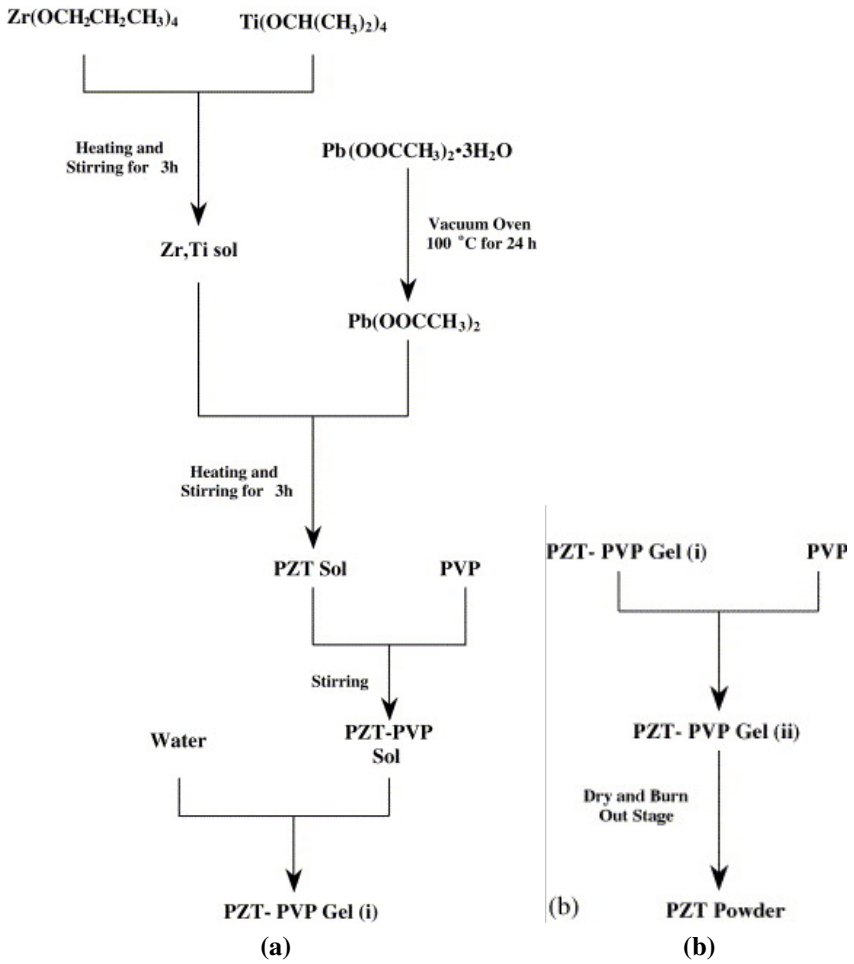

Figure 2.29: Synthesis of PZT powder by sol-gel method: preparation route of a) PZT-PVP gel and b) PZT powder. Adapted from [16].

films onto substrates [88–91]. In some cases the films were composed of nanopowders [90, 91].

EHDA is a process that atomises liquids due to an applied electrical force. The liquid flows into a needle and a meniscus is obtained at its outlet. The meniscus elongates forming a jet and disintegrates into fine droplets due to the applied electric field [92–94]. The deformation and the disintegration of the jet are caused by a balance between electrical and physical forces [95]. This can be explained by the Rayleigh charge limit, expressed by equation 2.7 [96]:

$$Q_R = 8\,\pi\,\sqrt{\gamma\,\varepsilon_o\,r^3} \tag{2.7}$$

where Q_R is the Rayleigh charge limit, γ is the surface tension of the liquid to be atomised, ε_o is the permittivity of the free space and r is the droplet radius. The formation of a charged droplet happens when Q_R is exceeded.

The shape of the meniscus determines the formation of different spraying modes, as described in the subsection 2.4.1.1. Several advantages can be distinguished in electrospray:

- the droplet size can be varied from tens of nanometres to microns and their distribution can be very narrow depending on the spray mode;
- the droplet size can be controlled by varying the process parameters;
- the electrically charged droplets are self-dispersing in air. This reduces the risk of agglomeration during flight;
- since the droplets are charged, it is possible to deflect their trajectory [94, 97].

Once the droplets are obtained, the solvent has to evaporate to form the powder. Figure 2.30 represents schematically the steps involved in the powder production from sprayed liquids (solutions or suspensions).

Many parameters influence the jet formation and its subsequent atomisation and it is not

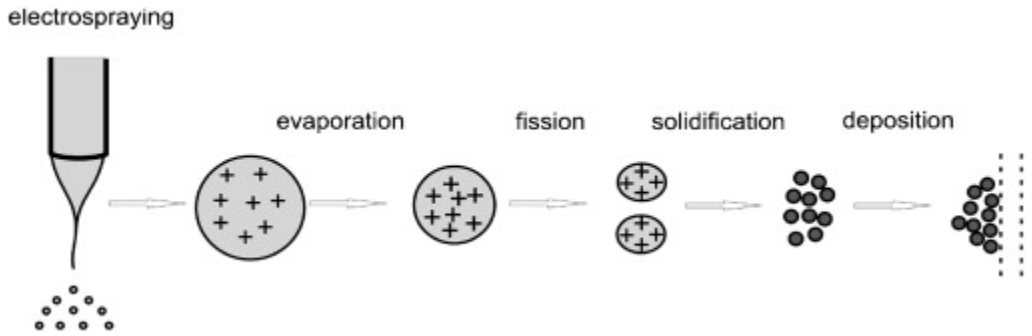

Figure 2.30: Schematic representation of powder production by EHDA. From [94].

simple to predict the conditions required to obtain a determined spray mode [93]. The parameters that influence the atomisation process can be distinguished into physical properties of the liquid (viscosity, surface tension, density, electrical conductivity) and process parameters (liquid flow rate, applied voltage, capillary diameter) [89, 93]. An overview of the effects of these variables on droplet formation will be given in the subsection 2.4.1.3.

2.4.1.1 Spraying modes

The formation of a spray mode depends on the behaviour of the jet and how it disintegrates into droplets. Two categories of spraying mode are possible, dripping and jet modes. A schematic representation of the described modes is shown in figure 2.31.

1. *Dripping modes.* In this group of modes, the liquid is detached from the needle as a fragment (top row in figure 2.31). If the fragment has the shape of large drops, dripping mode is created. A reduction in the drop size leads to microdripping mode, and if the drops have a spindle shape spindle or multi spindle modes are generated. Ramified-meniscus mode is also possible.

2. *Jet modes.* This group comprises all the modes in which the liquid elongates in a form of a continuous jet and disintegrates into droplets at a distance from the outlet of the needle (bottom row in figure 2.31). When the jet is stable it is possible to distinguish the cone-jet mode. This jet can split into a few jets to create the multi-jet mode. The jet

is not always stable but can rotate or oscillate around the needle axis. In the first case precession mode is obtained and in the second case oscillating mode [92, 94].

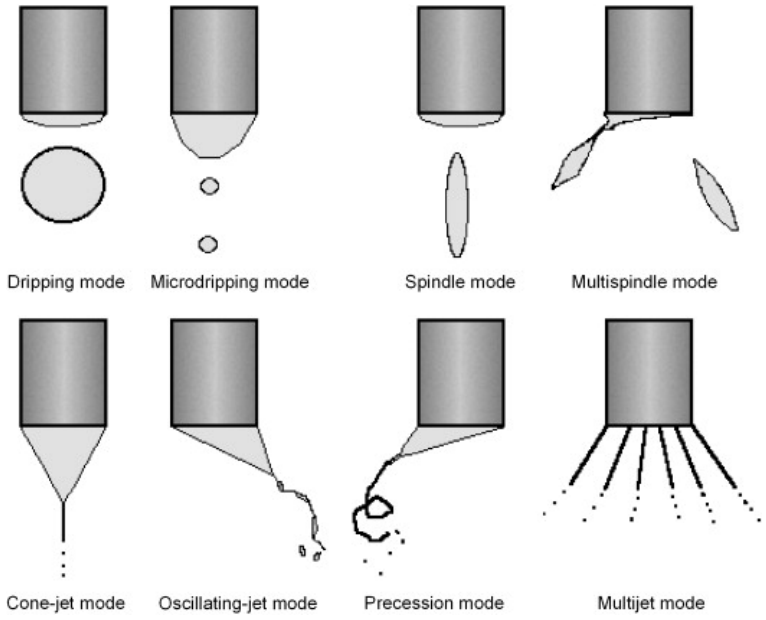

Figure 2.31: Schematic representation of different spraying modes in EHDA. Dripping modes (top) and jet modes (bottom). From [94].

2.4.1.2 Cone-jet mode

The cone-jet is the most used mode for the production of nanoparticles [25, 97–101] because it produces droplets and hence relics with a narrow size distribution [98].

It is formed when the meniscus assumes the shape of a cone (known as Taylor cone) and a jet (< 100 μm in diameter) is extended at its apex. The end part of the jet undergoes instabilities (Rayleigh instability) and breaks up forming the droplets [89, 92–94]. Two types of instabilities are known: varicose and kink. In the first case the jet breaks up into droplets due to waves generated on its surface and it does not move from its linear position. The formed droplets are equal in size. In the second case the jet moves laterally off the axis of the needle and breaks up due to electrical and inertial forces [92, 93].

The length and the diameter of the jet depend on the physical properties of the liquid

and on process parameters. According to Cloupeau and Prunet-Foch [92] an extended jet is created with high viscosity and resistivity values and with higher flow rate. The jet diameter depends on the conductivity (K) and on the flow rate. For a determined value of K, in the cone-jet mode, the jet diameter decreases with decreasing flow rate.

Some variants can be possible in the cone-jet mode and their appearance depends on the applied field. If the voltage is slightly lower than the one required for a stable cone, a pulsed cone-jet is formed. By increasing the field after the formation of a stable jet, the cone depth decreases until it is too small for the needle and this results in a lateral displacement of the cone. In this condition the jet splits creating one or more jets (multijet mode) [89, 92].

2.4.1.3 Effect of different variables on droplet formation

Since it is the most studied mode, the attention will be focused on cone-jet mode and the effect of several properties and parameters on the atomisation process will be examined.

Several studies have been done on EHDA in order to determine the influence of the liquid properties, including viscosity [102] electrical conductivity [103], and process parameters, such as applied voltage and flow rate [89], nozzle geometry [91] and size of dispersed particles [104]. For example, an increase in viscosity led to an increase in the droplet size and wider size distribution [102].

All of these parameters and properties have an effect on EHDA, but not all of them influence the droplet size. According to Rosell-Llompart and De La Mora [105] the main variables that have an effect on the droplet diameter are the liquid flow rate and the the liquid physical properties, such as electrical conductivity, viscosity, surface tension, density and dielectric constant. For the cone-jet mode, several scaling laws have been used to predict the droplet size or to determine which parameters have an effect on it [105–108]. For example equation 2.8 [89, 102] represents a correlation between droplet size and liquid physical properties:

$$\pi_\eta = \frac{\sqrt[3]{\gamma^2\,\rho\,\varepsilon_r\,\varepsilon_0}}{\eta} \tag{2.8}$$

where γ is the surface tension, δ is the density, ε_r is the relative permittivity, ε_0 is the permittivity if the free space and η is the viscosity. The droplet size depends on the dimensionless parameter π_η. Equation 2.8 is valid only if $\pi_\eta \ll 1$, when the droplet size increases with the viscosity.

Equation 2.8 represents the influence of liquid parameters on the droplet size but it does not predict it. Two different equations can instead be used to predict the droplet diameter in EHDA. According to Hartman et al. [106] for $\varepsilon_r \ll 1$ droplet size is directly proportional to the cube of the flow rate and inversely proportional to the conductivity and the surface tension (equation 2.9):

$$d_d \propto \left(\frac{Q^3\,\varepsilon_0\,\delta}{\gamma\,K}\right)^{\frac{1}{6}} \tag{2.9}$$

where Q is the flow rate and K is the electrical conductivity.

For $\varepsilon_r \gg 1$ Ganan-Calvo elaborated another equation [108]:

$$d_d \propto \varepsilon_r^{\frac{1}{6}} \left(\frac{Q\,\varepsilon_0}{K}\right)^{\frac{1}{3}} \tag{2.10}$$

In figure 2.32 the effect of the liquid flow rate on the particle size obtained by EHDA is shown. It can be seen that an increment in the flow rate leads to the formation of bigger particles.

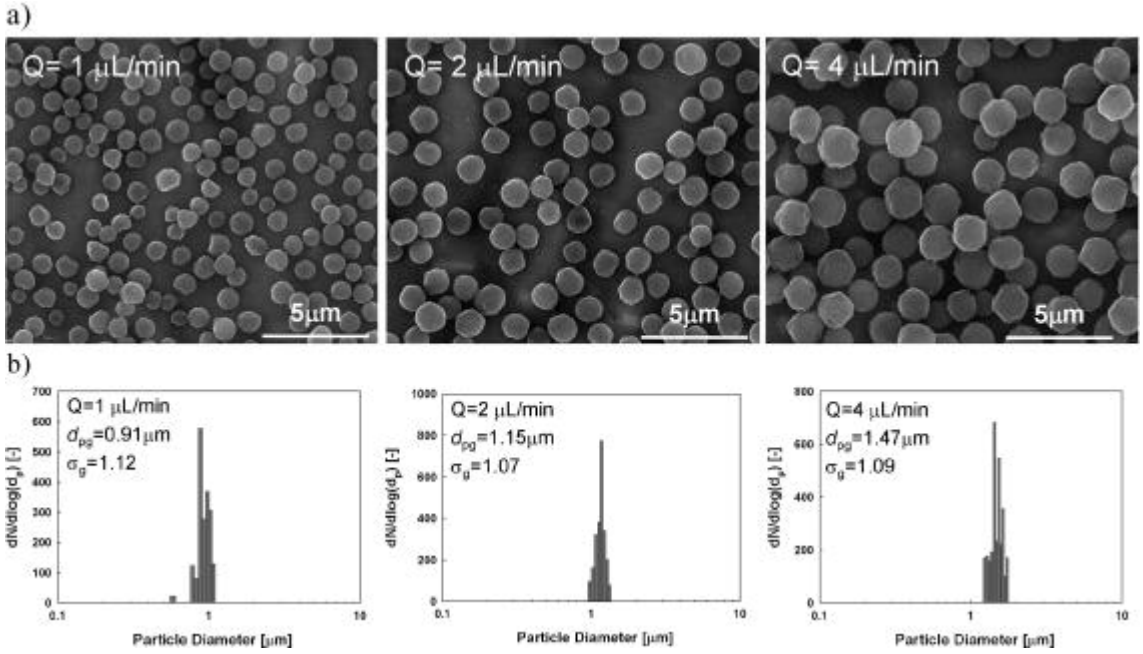

Figure 2.32: Effect of liquid flow rate in the production of poly(methyl methacrylate)-pigment nanoparticle composites. (a) FE-SEM micrographs and (b) particle size distribution (d_{pg}= geometric mean diameter; σ_g= standard geometric deviation). From [101].

2.4.2 Molten salt synthesis

Molten salt synthesis (MSS) is a simple process that yields large amounts of ceramic in short periods of time. In this technique starting materials are mixed together with a salt or a mixture of salts and then heat treated at a temperature higher than the melting point of the salt. The starting materials are commonly oxides, but oxalates, nitrates and carbonates have been also used as precursors [27, 28, 109, 110]. A schematic representation of the steps of the molten salt synthesis is shown in figure 2.33.

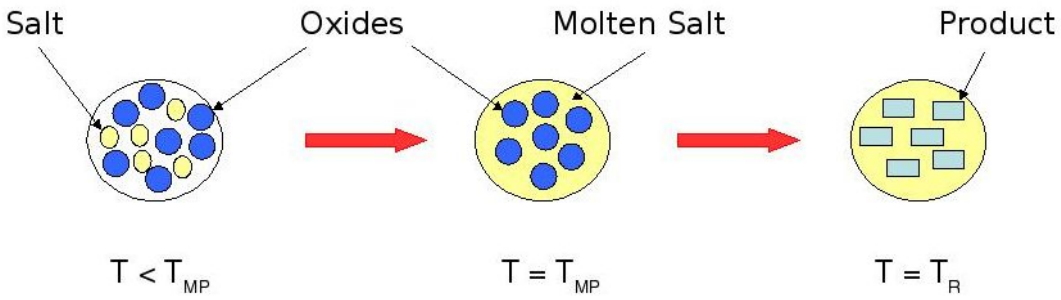

Figure 2.33: Schematic representation of molten salt process.

At a temperature lower than the salt melting point (T<T_{MP}) the oxides are mixed together. When the temperature reaches T_{MP}, the salt becomes molten. By further heating at the reaction temperature (T_R), the oxides react in the molten salt and the product is obtained.

Several factors have an effect on the size and shape of the final product, such as type of salt, solubility of raw materials in the salt, morphology and chemical composition of the starting materials, salt melting point, salt-to-reactant ratio and process parameters, such as temperature, heating ramp and reaction time [27]. In table 2.3 a summary of the effect of different parameters on molten salt synthesis is given.

Table 2.3: Effects of different parameters on particle size and shape and on reaction rate. The symbols indicate a strong influence (★) and a weak influence (-). Adapted from [111].

Processing parameter	Reaction rate	Particle size	Particle shape
Temperature	★	★	★
Time	-	★	★
Amount of salt	-	★	-
Type of salt:			
- Anion size	-	★	★
- Solubility	★	★	★
Ratio between salts (in mixture)	★	-	-
Excess of PbO	-	-	★

The difference between MSS and conventional mixed oxides (CMO), or solid state reaction, is the presence of salt (flux) that acts as a solvent for the reaction. For this reason the

salt selection is very important. For example, in the synthesis of PZT in NaCl-KCl flux, the atom mobility is 10^{10} times higher than in CMO [112]. This means that the reaction can be completed in a shorter period of time. To synthesise PZT by solid state reaction, high temperatures and long times (900^oC and 3-6 hours, respectively) are needed [113, 114].

2.4.2.1 Salt

As stated before, the salt plays an important role in MSS and it has to be chosen depending on the synthesis. It affects the product formation through its melting point, its viscosity and by the solubility of the staring materials in it. The salt must therefore have some specific characteristics in order to be used in the synthesis:

- it must not react with the starting materials, intermediate compounds or the final product;
- it should be very soluble in water. In this way it will be simpler to remove after synthesis by washing with hot deionised water;
- it should have a relatively low melting point [110–112, 115].

The temperature can be further reduced by using a eutectic mixture. For example the use of NaCl-KCl instead of pure NaCl reduces the melting point from 801 to 657^oC, as shown in figure 2.34.

In a salt with a lower viscosity, the starting materials can diffuse quickly and lead to the final product in a shorter time. An early product formation in terms of time and/or temperature is also achieved if the reactants are more soluble in the molten salt.

The salt-to-reactant ratio also has an effect on the final product. The salt amount should be enough to cover the particle surfaces and fill the interstices [112]. A typical ratio is 1:1 by weight [56, 109, 112, 117–121] but higher amounts of salt have been used as well [115, 122]. It was noticed [27, 111, 123] that a higher ratio led to bigger particles. As stated above the salt is removed from the final mixture by washing with hot deionised water. So a smaller

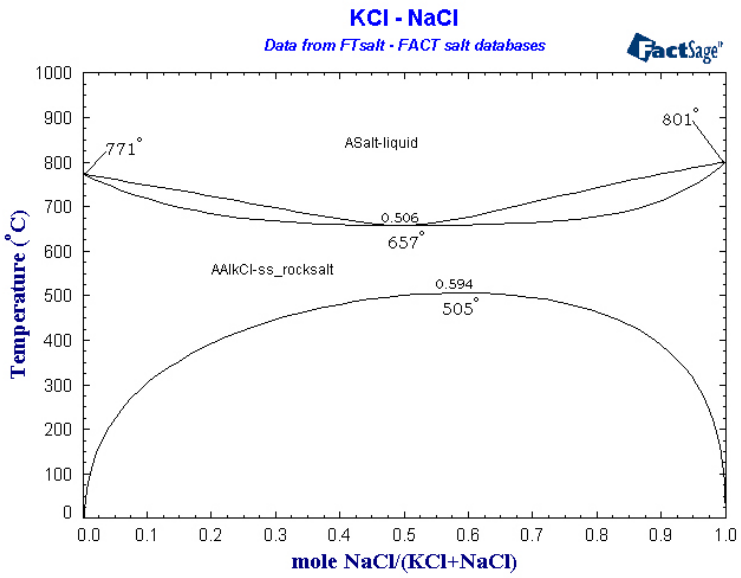

Figure 2.34: NaCl-KCl phase diagram. From [116].

quantity of salt is also advantageous because is simpler to remove.

Different types of salts have been used for this kind of synthesis, such as chlorides [27, 56, 109, 111, 112, 115, 117–120, 122, 124–127], sulphates [109, 117, 118, 123] and hydroxides [27, 28] singles or in eutectic mixtures in order to reduce the melting point.

Zeng et al. [56] synthesised sodium potassium niobate, $K_xNa_{1-x}NbO_3$ (KNN) perovskite powder in different alkali chlorides such as KCl, NaCl and their eutectic mixture. They found that the salt plays an important role on the powder morphology and shape. It was noted that under the same conditions (synthesis at 900^oC, for 90 minutes, heating and cooling rate of 10 and $5^oC\,min^{-1}$, respectively) cubic particles were obtained. The powder dimension gradually increased by changing the flux from KCl, to NaCl and the eutectic mixture (melting points 776, 801 and 657^oC, respectively), as shown in figure 2.35. This was due to different diffusion rates of K^+ and Na^+ ions in the molten salts. The ion diffusion rate in the NaCl-KCl mixture at 900^oC is very high, which led to an increase in the particle size.

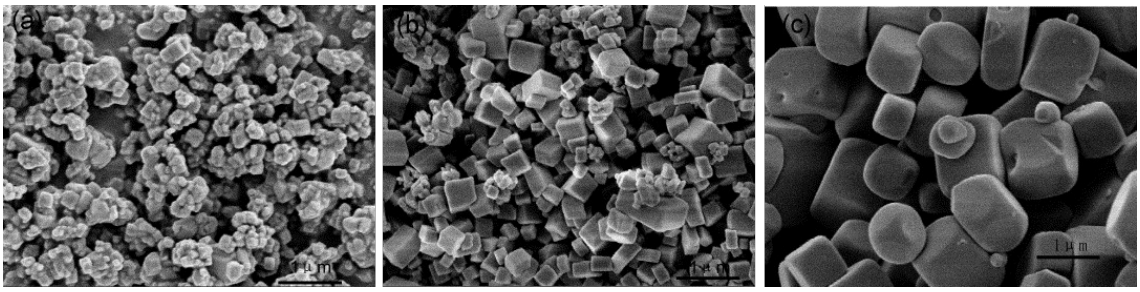

Figure 2.35: SEM micrographs of KNN powders synthesised at 900^oC in different fluxes: a) KCl, b) NaCl, c) NaCl-KCl eutectic mixture. Scale bars 1 μm. Adapted from [56].

In their study Zhao et al. [117] investigated the effect of different types of salt on the synthesis of lead lanthanum zirconate titanate stannate powder (PLZST). The powder was synthesised in sulphates (Li_2SO_4/Na_2SO_4) and chlorides (NaCl-KCl) fluxes. It was discovered that single perovskite phase was developed at different temperatures depending on the flux used. In sulphates a temperature of 850^oC was needed, but in chlorides the perovskite phase was formed 50^oC below this (in the same conditions of heating rate and isothermal time). To confirm this behaviour the temperature was increased at 900^oC and the powders were synthesised for different period of time. Again, in the sulphate flux perovskite phase was not developed before 30 minutes but in chlorides a time of 15 minutes was sufficient. This is due to a difference in the mobility of species in the fluxes. The viscosity of molten chlorides is lower than that of sulphates because of the the smaller size of Cl^-ions compared to the $SO_4{}^{2-}$. This is reflected on the species mobility in the fluxes. Lower viscosity means larger mobility and hence quicker reactions.

2.4.2.2 Effect of time

Two different processing times can be distinguished in molten salt synthesis, as shown in figure 2.36: the isothermal time and the overall reaction time.The first one corresponds to the dwell time. The second is the time during which the flux is liquid, and it can be identified as the sum of the isothermal time and the time taken to reach the required temperature starting

from the melting point of the salt (T_{MP}).

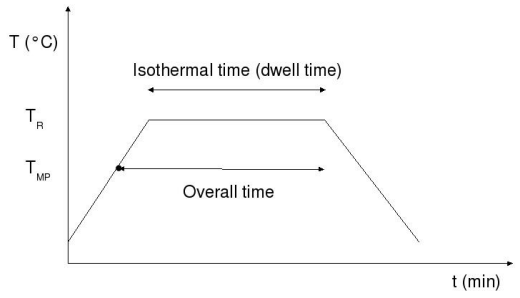

Figure 2.36: Schematic representation of the isothermal and overall reaction times.

To obtain small particles, a short isothermal time is needed [27, 28, 111]. On the other hand this can reduce the purity of the final product.

The mechanism that regulates the formation of the product can be explained by using LaMer's diagram [128] as shown in figure 2.37. It represents the change of the product concentration during time. The concentration of the product increases with time until a critical supersaturation degree is reached (${C^*}_{max}$). At this point nucleation occurs and the solid product is formed. The nuclei tend to grow and this leads to a decrease in the product concentration below a determined value (${C^*}_{min}$). After this point no more nuclei are generated and the particles grow by diffusion process until a saturation threshold (C_s) is reached.

In their study on $BaZrO_3$, Zhou et al. [27, 28] noted that cubes of the desired product were first formed. The particle size gradually increased with increasing isothermal time. Moreover a shape change from cubes to spheres was noted. Cubic particles of $BaZrO_3$ were obtained by heating precursors and flux at 720^oC for 30 minutes and subsequent quenching the mixture to room temperature. A mixture of cubic and spherical particles was obtained

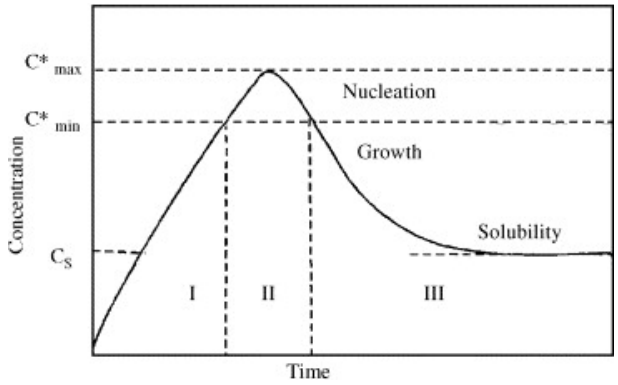

Figure 2.37: Representation of LaMer diagram. From [129].

(in the same conditions) by increasing the isothermal time. The amount of spherical particles increased with increased isothermal time. Spheres were instead synthesised at 720^oC for 3.5 hours letting the mixture cool down into the furnace. In all the cases the heating ramp rate was set at $5^oC\,min^{-1}$. A representation of this behaviour is shown in figure 2.38. From the experimental data, it was hypothesised that the formation of barium zirconate started with cubes. These gradually converted into spheres once a critical particle size had been reached.

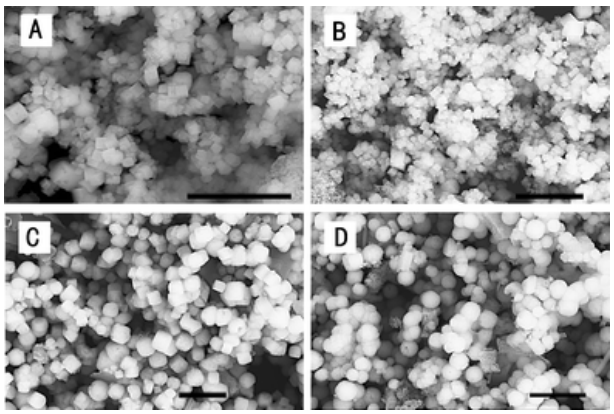

Figure 2.38: SEM micrograph of $BaZrO_3$ particles synthesised at 720^oC for different isothermal times: a) 30, b) 60, c) 120, d) 210 minutes. All samples were heated at a rate of $5^oC \cdot min^{-1}$ and quenched to room temperature after the isothermal time was completed. Scale bars = $1\mu m$. From [28].

2.4.2.3 Effect of temperature

Compared to CMO synthesis, MSS results in product formation at lower temperature due to the presence of the molten salt. For example, $CaZrO_3$ can be synthesised in molten salt at least 250^oC below the required temperature for CMO (>1300^oC) [130]. This can be achieved because of the higher mobility of the species in the liquid flux than in CMO [112]. However the reaction temperature, as well as the isothermal time, affects the final product in terms of purity, size or morphology.

Higher temperatures help to obtain a purer product and to increase the formation of nuclei [28, 127] which means a higher number of seeds. On the other hand it also results in an increase in the particle size [27, 111, 118] because of the higher material transport rate.

In the synthesis of $Pb(Fe_{0.5}Nb_{0.5})O_3$ (PFN) [127] it was noted that the percent of perovskite was enhanced by higher temperature, as well as time and amount of excess PbO. At 700^oC pure PFN was not obtained for all the combination of time and excess of PbO. Pure perovskite phase of PFN was instead obtained at 900^oC after 60 minutes of reaction without any PbO excess.

2.4.2.4 Effect of heating ramp

According to Yoon et al. [111], particle dimensions can be modified by changing the heating velocity. They discovered that the size can be reduced by increasing the rate of heating to the required temperature. In their study, the synthesis of $Pb(Mg_{\frac{1}{3}}Nb_{\frac{2}{3}})O_3$ (PMN) particles using different heating rates is shown. PMN size was reduced from $\sim$ 1.5 μm to $\sim$ 0.5 μm by increasing the velocity from 5 to $150^oC\,min^{-1}$.

From all the previous observations it is possible to assume that to obtain small particles by MSS a short time, low temperature and fast heating rate are needed. A small flux quantity should be also used.

2.4.2.5 Dissolution-precipitation and template formation mechanisms

Size and morphology of the starting materials affect size and shape of the final product. This is connected to their solubility in the molten salt [115, 119, 123, 130]. Two different cases can be distinguished. If the reactant solubilities in the salt are comparable, the product will be formed in a short time and its morphology will not depend on the morphology of the starting materials (dissolution-precipitation mechanism). The second case appears when one of the reactants is more soluble than the other (template formation mechanism). The more soluble reactant dissolves and diffuses through the salt to the less soluble one, where the reaction occurs at the surface. In this situation the product morphology will be similar to that of the less soluble reactant that has acted as a template.

In figure 2.39 an example of this behaviour is shown. Two different sources of TiO_2, spherical and rod-shaped, were used to synthesise lead titanate (PT) at 900^oC for 2 hours [119]. It can be seen that changing the shape of the TiO_2 led to PT with different morphologies: when spherical TiO_2 was used, spherical PT particles were obtained (figure 2.39 a and b). When the shape of TiO_2 was rod-like, the PT resulting from the reaction had a rod-like morphology (figure 2.39 c and d). Since PbO is more soluble than TiO_2 in alkali chlorides [111, 119], this result confirms the template formation mechanism.

Needle-like $TiZrO_4$ and PbO powders were used to prepare PZT with the same morphology [118]. The reaction was complete at 750^oC after 30 minutes but secondary phases were observed. Increasing the temperature helped to reduce this composition variability. Moreover the aspect ratio of needle-like PZT particles was also reduced in comparison to the powder synthesised at 750^oC.

In the case of lead based compounds, the amount of PbO excess also has an influence on the product formation. It was noted that an extra quantity of this oxide helps to reduce the final particle size [111]. It was also found that an excess of PbO led to a higher amount of perovskite phase [127].

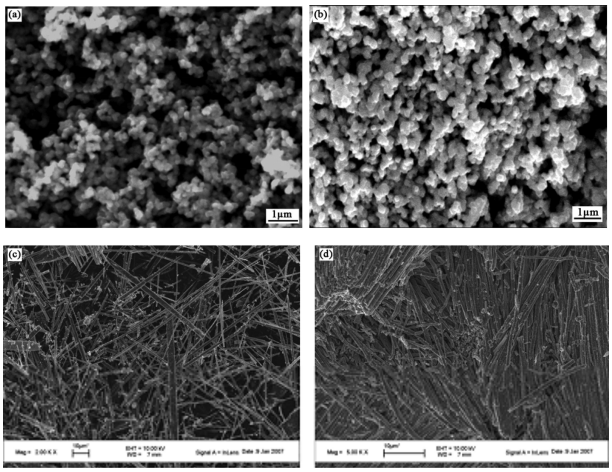

Figure 2.39: SEM micrograph of TiO_2 and $PbTiO_3$ from different titanium sources: a) spherical TiO_2, b) spherical PT, c) rod-shaped TiO_2, d) rod-shaped PT. From [119].

In order to obtain the product with desired size and shape, the solubility of the starting materials in the liquid salt should be high to facilitate their dissolution and migration and speed up the product formation.

Chapter 3

Experimental procedure

In this chapter the experimental procedures are described. First the preparation of the PZT sol and powders by different methods, such as electro hydrodynamic atomisation and molten salt synthesis, will be illustrated. Then the attention will move to the characterisation of the samples in terms of particle dimension, viscosity, surface tension and other features.

3.1 PZT sol

Stoichiometric amounts of titanium IV isopropoxide (3.42 *g*) and zirconium IV propoxide, 70 wt% solution in propanol (5.62 *g*), were mixed together in a glove box under nitrogen atmosphere. After stirring, 5 *ml* of glacial acetic acid and 10 *ml* of 1-propanol were added. Then lead acetate trihydrate (9.95 *g*) was mixed with the Ti/Zr mixture and refluxed for approximately 30 minutes while heating and stirring. The solution was diluted to 0.6 *M* by further addition of glacial acetic acid and 1-propanol (10 and 11 *ml*, respectively). The final ratio of the metal ions was Pb 1.1 : Zr 0.5 : Ti 0.5. All the health and safety procedures were checked.

Titanium isopropoxide, zirconium propoxide and 1-propanol were obtained from Sigma

Aldrich while lead acetate and glacial acetic acid were obtained from Fisher.

3.2 Synthesis of PZT powder

In this section the methodology used for the PZT powder synthesis by EHDA and MSS is given, without the addition of any dopant. The powders prepared by these methods were used to prepare PZT inks as described in section 3.3.

3.2.1 Electro hydrodynamic atomisation

Starting from the 0.6 *M* PZT sol described in the previous section, 5 different solutions with concentrations between 0.1 and 0.5 *M* were prepared by dilution with a 1-propanol : acetic acid mixture (1.1:1 by volume).

The EHDA setup was equipped with a stainless steel needle (outer and inner diameter of 1.2 and 0.8 mm, respectively) held in epoxy resin, connected to a syringe pump (Kd Scientific, model 789100) using a silicone rubber tube. As a bottom electrode and to collect the powder, an aluminium substrate was used. The needle was connected to a high voltage supply (Glassman high voltage, Inc., Series EH) while the substrate was held at ground potential. In figure 3.1 a schematic representation of the EHDA apparatus is given. The sol flow rate and

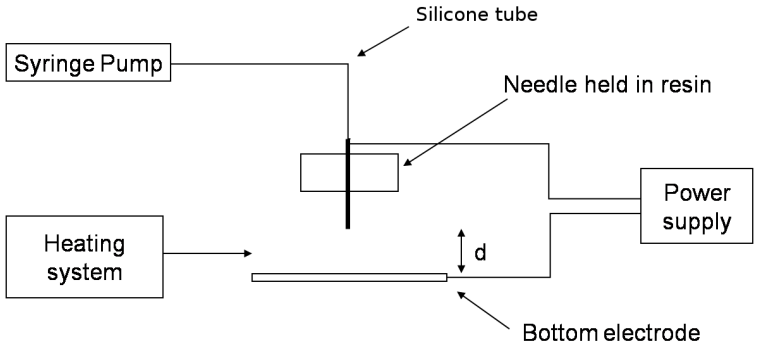

Figure 3.1: Schematic representation of the EHDA apparatus.

the distance between the the needle and the bottom electrode (d) were varied from 0.2 to 0.6 $ml\,h^{-1}$ and from 20 to 40 mm, respectively.

Two different approaches were used to produce the powder: gas heating, in which the spray was dried in a hot gas flow, and direct heating, where a focused lamp was used to dry the spray as it passed through the beam of light.

In the gas heating setup the needle-substrate distance was set at 20 mm and a nitrogen flow, set to 0.5 $l\,min^{-1}$, was used to heat the spray chamber. The gas was heated by passing through a tube furnace (Carbolite, MTF 10/25/130) set at 450^oC. The nitrogen temperature in the spray area was 60^oC as determined by the use of a thermocouple.

The direct heating configuration is shown in figure 3.2, where a focused lamp (Osram, 64635 HLX) was used to heat the spray directly as it passed through the light beam. The temperature was changed by varying the applied current. In the vertical axis the lamp was

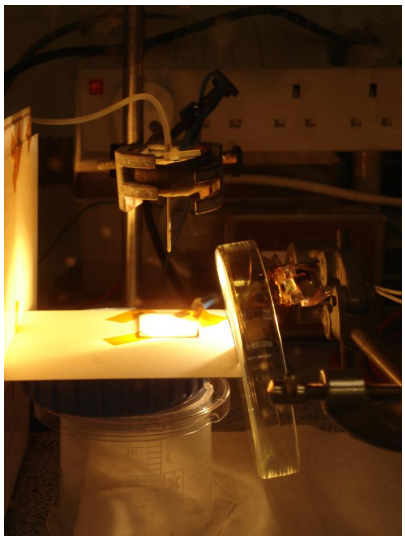

Figure 3.2: Direct heating setup.

placed halfway between the needle mouth and the aluminium foil. In the longitudinal axis the lamp distance was set in order to direct the focus spot on the spray area. A quartz glass slide was placed in front of the lamp to protect the bulb from the spray. The focus temperature was determined before the tests by directing the beam of light onto an alumina sheet and

recording the temperature as a function of the applied current with a thermocouple. The field applied was varied between 4 and 7.5 kV in order to obtain a stable cone jet spraying mode. This was done by visually checking the shape of the cone.

Heat treatments of the sprayed powder were conducted in a box furnace (Carbolite, ELF 11/6B) at temperatures between 200 and 650^oC with a heating ramp rate of 5$^oC\,min^{-1}$ and a dwell time of 20 minutes.

3.2.2 Molten salt synthesis

To synthesise PZT powder by molten salt method PbO, ZrO_2 and TiO_2 starting materials were used. All the starting materials were used as received without any further purification. ZrO_2 and TiO_2 were supplied by Sigma Aldrich (purity higher than 99%), lead oxide (98%) was supplied by BDH.

The oxides were mixed in the Pb:Zr:Ti proportion of 1:0.5:0.5 (mixture A). An eutectic mixture (B, 1:1 molar) of sodium and potassium chloride (the flux) was prepared. The mixtures A and B were mixed in the proportion 1:1 by weight and ground with an agate mortar and pestle. The new mixture and 200 g of zirconia grinding media were placed in a 250 *ml* borosilicate glass bottle. Ethanol was added as carrier in a quantity high enough to cover the powder and zirconia balls and the content was ball milled for 24 hours.

After milling, the slurry was filtered using a funnel with a perforated borosilicate glass plate to remove the zirconia balls. The balls were washed with ethanol to ensure all the oxide/salt mix was collected. The filtered slurry was collected in a beaker and it was kept at 100^oC overnight to remove the solvent. The resulting powder was ground by mortar and pestle and heat treated in alumina crucibles using the conditions listed below (table 3.1).

Table 3.1: Molten salt synthesis conditions.

T ramp rate ($^oC\,min^{-1}$)	Temperature (^oC)	Dwell time (min)
3.3 - 5 - 10 - 20 - 70	750 - 800 - 850	30 - 60 - 120

After synthesis, the flux was removed by washing with lukewarm deionised water until no Cl^- ions in the filtered water were detected through the addition of $AgNO_3$ solution. The filtered powder was dried overnight at 80^oC and then ground with a mortar and pestle to break up the agglomerates resulting from the water evaporation.

3.3 Ink formulation

The viscosity of PZT sol was adjusted by adding ethylene glycol (99.8%, Sigma Aldrich) to reach a value of approximately 10 $mPa\,s$. The PZT powder was added to the resulting sol in different loadings, from 1 to 5 *vol%*, forming the PZT ink.

In order to make the ink stable and maintain the particle in suspension, a dispersant (KR-55, Kenrich Petrochemicals, Inc.) was added to the ink. The determination of its optimum amount was carried out by adding different quantities of KR-55 to a 5 *vol%* PZT suspensions. The amount was varied from 0.5 to 5 *wt%* (with respect to the powder amount). For each sample the viscosity was determined as described in subsection 3.5.1. The viscosity values were plotted against the dispersant quantities: the minimum of the curve corresponded to the optimum amount of dispersant.

Two different routes were used to disperse the ink components: ball milling and the use of an ultrasonic horn. In the first case the ink was ball milled for 24 hours in a borosilicate glass bottle with 200 g of zirconia balls. In the second procedure an ultrasonic horn (Sonics, Vibracell) was used to break up agglomerates eventually formed and to disperse the ink. In this case powder, sol and ethylene glycol were mixed together for 2 minutes at 60% of amplitude (100% of amplitude corresponds to the maximum ultrasonic vibrations at the probe tip). The mixture was ultrasonicated again for 30 seconds at 20% of amplitude after the dispersant was added.

An ink with higher solid content (16 *vol%*) was prepared by mixing PZT sol, PZT powder

synthesised by MSS and the dispersant (1.5 *wt%*) and was dispersed using the ultrasonic horn.

3.4 Powder characterisation

Prior to all characterisation, the powders were first ground with an agate mortar and pestle in order to break up large agglomerates.

3.4.1 Scanning electron microscopy

A scanning electron microscope (SEM, SFEG XL30 FEI) was used to observe the particle shape and dimension.

A conductive carbon tape was stuck to an aluminium stub and the powder was deposited on top of the tape. The SEM parameters used for imaging were: through lens detector (TLD), working distance of 5 mm, spot size of 2 *nm*, and acceleration voltage of 10 kV.

The powder composition was determined in parallel to SEM imaging by SEM-EDX analysis. In this case the working distance was set at 6 mm, spot size of 4 nm and acceleration voltage of 20 kV.

3.4.2 Particle size evaluation

The particle size of the synthesised powder was determined by using an image analysis program, ImageJ (version 1.38).

From the SEM micrograph of each sample (at the same magnification) the size of at least 30 particles per sample was measured manually as shown in figure 3.3. Mean particle size and standard deviation were automatically calculated by the program.

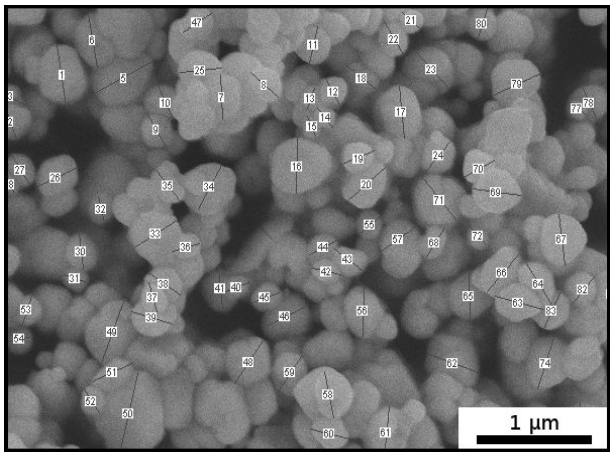

Figure 3.3: Example of the particle size measurement. Average dimension 344 $\pm$ 22 *nm*.

3.4.3 X-Ray diffraction

X-Ray diffraction (XRD, Siemens D5005) analysis of the powder produced was done in order to determine the presence of the perovskite phase and eventually the presence of secondary phases.

The powder was deposited on carbon tape attached to a glass slide. The scans were conducted in the range 20-60 2θ with a step size of 0.05^o and a time per step of 1 s.

3.5 Inks and sol characterisation

3.5.1 Rheology

Viscosity measurements were conducted using a rheometer (Bohling Instrument, Ltd.) fitted with a concentric cylinder geometry (C14, cup inner diameter and bob outer diameter of 15.4 and 14 *mm*, respectively). On a 3 *ml* sample, a pre-shear of 200 s^{-1} was applied for 30 s, followed by an equilibration time of 60 s. The viscosity was measured at 25^oC at a single shear rate of 100 s^{-1}as the average of 5 consecutive measures. The measurement was repeated 3 times for of each sample.

3.5.2 Surface tension determination

The weight of 50 drops of deionised water was measured. With the same, dried, pipette, 50 drops of sample were weighted. The sample surface tension was calculated using equation 3.1:

$$\gamma = \gamma_{H_2O} \frac{m}{m_{H_2O}} \tag{3.1}$$

where γ_{H_2O} and m_{H_2O} represent the surface tension and weight of the droplets of water at the operation temperature, respectively and m represent the weight of 50 drops of sample fluid. Typical values of water surface tension are reported in table 3.2.

Table 3.2: Value of water surface tension at different temperature. From [131].

Temperature (^oC)	Surface tension ($mN\,m^{-1}$)
0	76
25	72
50	70
100	59

The same procedure was repeated 3 times for each sample.

3.5.3 Permittivity and electrical conductivity

Permittivity and electrical conductivity were measured for sols of different concentrations and for the 1.1:1 (by volume) propanol : acetic acid mixture.

The permittivity of the samples was measured with a Solartron SI1260 frequency-gain analyser with a interdigitated comb electrode (GIA, Pearson Panke) immersed in the sample. The lower frequency limit was determined by the presence of electrode polarisation at 10^4 *Hz*. The upper limit was selected as 10^6 *Hz*, collecting five points per decade. The observed values were almost constant over the whole frequency range for all the samples and an average value of C and *R* (parallel equivalent circuit) was therefore used for data elaboration. The permittivity ε_r was calculated using equation 3.2:

$$\varepsilon_r = \frac{3.93\,C}{C_0} - 2.93 \tag{3.2}$$

where C is the measured capacitance of the sample and C_o is the capacitance of air measured with the same electrode. The geometrical constants of the fringing electric field, 3.93 and 2.93, have been previously reported in [132]. The value of conductivity was calculated by equation 3.3:

$$K = \frac{3.93\,\varepsilon_o}{R\,C_o} \tag{3.3}$$

where *R* is the measured resistance of the sample and ε_o is the permittivity of free space.

3.6 Ink jet printing

PZT sol and PZT inks prepared as described in sections 3.1 and 3.3, were used to print different patterns composed of dots or lines with a DoD Fujifilm Dimatix DMP-2831 ink jet printer, shown in figure 3.4. The inks or sol were printed on a 530 μm thick substrate

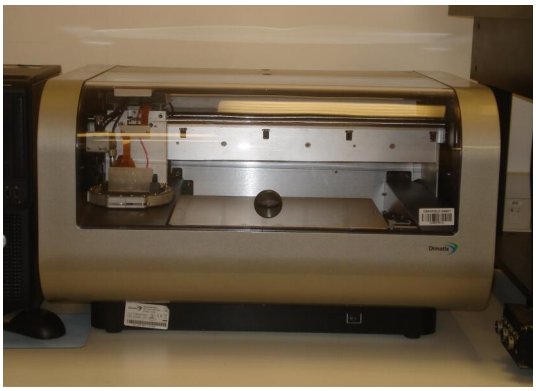

Figure 3.4: Fujifilm Dimatix DMP-2831 ink jet printer.

composed of silicon, Ti adhesive layer ($\sim$10 *nm*) and platinum electrode ($\sim$100 *nm)*. Ti/Pt was selected as this is typical for final device.

Disposable cartridges (DMC-11610, figure 3.5) were filled with 1 ml of sol or ink and

left with the nozzles facing down for 30 minutes prior the printing process.

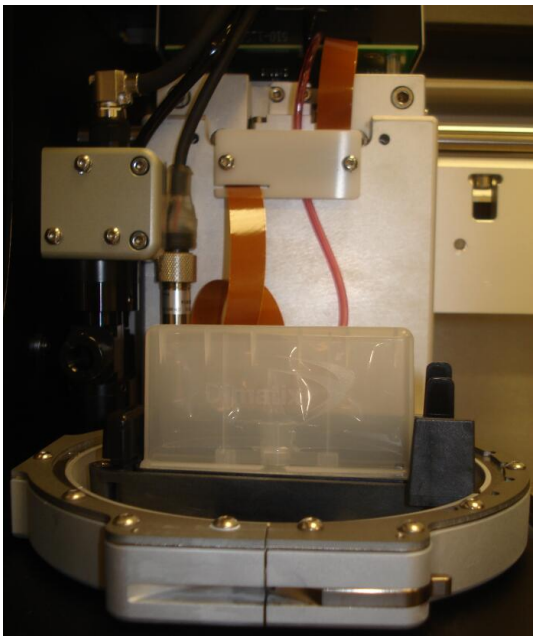

Figure 3.5: Fujifilm Dimatix DMC-11610 cartridge installed in the printer.

In the printing process several parameters were investigated to determine their influence on the print quality. The drop spacing (DS) was kept fixed at 25 μm for all the experiments. A test pattern was initially printed on a silicon wafer in order to determine if printing was possible. It was composed of a square of 10x10 pixels and it was printed a CPH of 0.35 *mm* and at a voltage of 25 V. A pattern composed of 20x20 drops (figure 3.6 a) was printed at different cartridge printer height, from 0.3 to 0.5 *mm*, and at different voltages (15, 16, 18, 20, 23, 25, 28 and 30 *V*) using 1, 4 or 16 nozzles. This pattern was used to determine the ink behaviour on the substrate (e.g. droplet spreading on the surface). The distance between two droplets (centre to centre) in a row or in a column was 50 μm (2 DS). Relic dimension was determined by using an image analysis program, ImageJ. The line array pattern (figure 3.6 b) was printed under the same conditions but at 15, 20 and 25 *V*. It represents a square and lines of different thickness in the X and Y directions. By printing this pattern it will be possible to determine the resolution in both the printing direction and in the transverse direction.

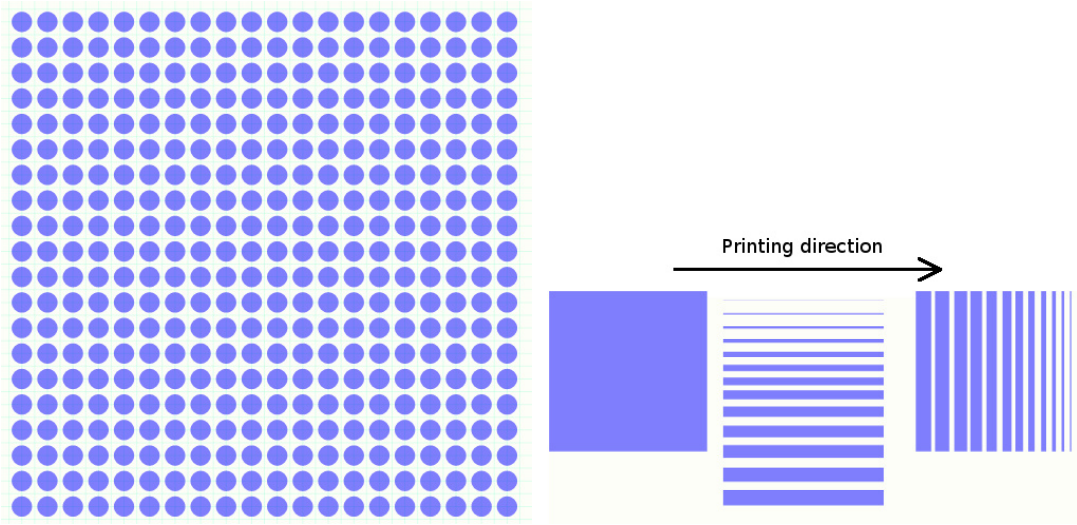

Figure 3.6: Patterns printed with the ink jet printer: a) 20x20 drops and b) line array.

3.7 PZT film deposition

In order to determine piezo and ferroelectric properties of the PZT powder/PZT sol system, PZT films were deposited on the previously described platinised silicon wafer, by spin coating. The ink utilised for this purpose was a 16 *vol%* ink, as described in section 3.3.

Prior to the deposition, the wafers were washed with acetone and isopropanol and then heated for 30 seconds at 200^oC in order to evaporate any residual solvent. Every layer was deposited by spinning the ink at 2000 rpm for 30 seconds. Then the organic components were removed by heating the wafer at 200^oC for 60 seconds, and the film was then pyrolized at 450^oC for 30 seconds. To infiltrate the sol into the PZT layer, PZT sol was spin coated following the same steps described before. The films were built up by depositing several layers and by infiltrating them with PZT sol. The number of sol infiltrations was kept constant to 1 to allow the effect of film thickness to be evaluated. Different PZT films were obtained by depositing 1, 2, 3 or 4 PZT layers, respectively. A single PZT film (without any sol infiltration) was also prepared.

All the films were sintered at 720^oC for 20 minutes to develop the perovskite phase. Prior

to the sintering stage, a small area of PZT was removed in all the samples by mechanical abrasion, in order to reveal the back electrode (platinum) and allow the electrical measurement to be done.

3.8 Optical microscopy

To observe the morphology of printed dots and lines a reflective light optical microscope (Nikon Optiphot 2) was used. The microscope was equipped with a QImaging, Micro Publisher 3.3 RTV digital camera. The presence of microscopic cracks was investigated as well. A confocal scanning laser microscope (Olympus Lext OLS3100) was used to check profiles and thicknesses of the printed patterns.

3.9 Determination of film properties

To characterise the electrical properties of the films, circular Cr-Au top electrodes (radius of 1 and 0.5 *mm*) were evaporated on the surface of the films using Edwards coater, E480. The vacuum chamber contained chromium and gold filaments underneath a sample holder, and a thickness detector. Cr and Au were loaded in the chamber. The desired mask was placed and fixed on top of the samples and loaded in the vacuum chamber with the samples facing down. The layers deposition was conducted at chamber pressure of $5 \cdot 10^{-6}$ *mbar*. At this point Cr and Au layers were evaporated on the samples by applying a current at each filament (25-28 *A*). The final thickness of the layers were approximately 25 *nm* for Cr and 100 *nm* for Au.

3.9.1 Poling

In the poling process, each sample was placed on a hot plate and two probes were connected to the top and bottom electrode. The films were heated to 200^oC. At this temperature an electric

field of 8 $V \cdot \mu m^{-1}$ was applied between the two electrodes for 10 minutes. The sample was cooled down and the applied voltage was maintained until the temperature reached a value lower than 75^oC. The probes were then disconnected and the sample removed from the hot plate.

3.9.2 Piezoelectric and dielectric measurements

The piezoelectric coefficient, d_{33} was measured with a piezometer system (Berlincourt method). The sample, in the correspondence to the poled electrode, was positioned in between two probes. The d_{33} value was obtained by applying an oscillating force between the probes and measuring the resultant charge. For each top electrode 3 measurements were registered.

Capacitance and dielectric loss were measured with a precision component analyser (Wayne Kerr, 6425) at frequencies ranging from 1 to 100 *kHz*. Top and bottom electrode were connected to two probes. An AC field of 100 mV was applied at different frequencies and the value of capacitance and loss registered. From the capacitance values, the relative permittivity, ε_r, was calculated using equation 3.4:

$$C = \frac{\varepsilon_o \, \varepsilon_r \, A}{t} \tag{3.4}$$

where *C* is the capacitance, *A* is the top electrode area (3.14 mm^2 for the big electrode and $7.85 \cdot 10^{-1}$ mm^2 for the small electrode) and *t* is the sample thickness.

3.9.3 Ferroelectric hysteresis measurements

Ferroelectric hysteresis loop was determined with a Radiant Technology interface (RT66A) connected to a high voltage power supply (Trek, 610E). Two probes were connected to the top and bottom electrode and different voltages were applied to the sample. The voltage was increased with a step of 1 $V \, \mu m$ from 21 to 297 *V* to observe the evolution of the hysteresis

loop.

Chapter 4

Preparation of PZT micro-nanoparticles by electro hydrodynamic atomisation

4.1 Introduction

Small and spherical PZT particles are needed for the development of an ink suitable for ink jet printing purposes. Since the particle dimension should be around 200 *nm* in diameter, attempts were made to synthesise PZT powder within this size range (micro-nanoparticles). In this chapter the synthesis of PZT particles by electro hydrodynamic atomisation of precursors PZT sols is described. In this technique PZT sol is atomised and sol droplets are created. The droplets are allowed to dry, hydrolyse and partially pyrolyse during their flight before they reach the bottom electrode. Individual unagglomerated powder particles are obtained at the end of the process. Several parameters were changed in order to investigate their influence on the final size and shape of particles, such as the sol concentration, the liquid flow rate, the drying temperature and the distance between the needle and the bottom electrode.

Table 4.1: Properties of precursor sols. The concentration 0 *M* corresponds to the 1-propanol-acetic acid mixture 1.1:1 by volume used to dilute the sols.

Sol concentration *M*	Density $kg\,m^{-3}$	Viscosity $mPa\,s$	Surface tension $mN\,m^{-1}$	Relative permittivity	Electrical conductivity $mS\,m^{-1}$
0	921	2.6	23.2	14	0.2
0.1	943	2.7	23.4	16	1.8
0.2	956	3.0	22.6	18	2.3
0.3	973	3.2	21.1	19	3.4
0.4	1017	3.7	20.9	20	3.9
0.5	1039	4.2	20.8	21	4.1
0.6	1061	4.8	19.3	22	4.1

4.2 Study of EHDA parameters on size and shape of PZT particles

4.2.1 Effect of sol concentration

The effect of sol concentration on the size and shape of PZT particles was determined by spraying PZT sols of 0.1, 0.2, 0.3, 0.4, 0.5 and 0.6 *M* in the gas heating setup as described in 3.2.1. Liquid flow rate and needle-substrate distance were 0.2 $ml\,h^{-1}$ and 20 *mm*, respectively. In table 4.1 the rheological and electrical properties of PZT sols are reported. It can be seen that the values of density, viscosity, relative permittivity and electrical conductivity increase steadily with the sol concentration. The values of surface tension decrease with increasing sol concentration.

The voltage applied during EHDA was set at 5 kV and the formation of a stable jet was visually checked.

Figure 4.1 shows the particle shape for different sol concentrations as the powder was collected on the aluminium foil, and the average particle dimension is shown in figure 4.2. At low sol concentration 0.1 *M*, disc-shaped particles were formed (figure 4.1 a). Increasing the concentration to 0.4, 0.5 or 0.6 *M* led to the formation of large particles within the spray.

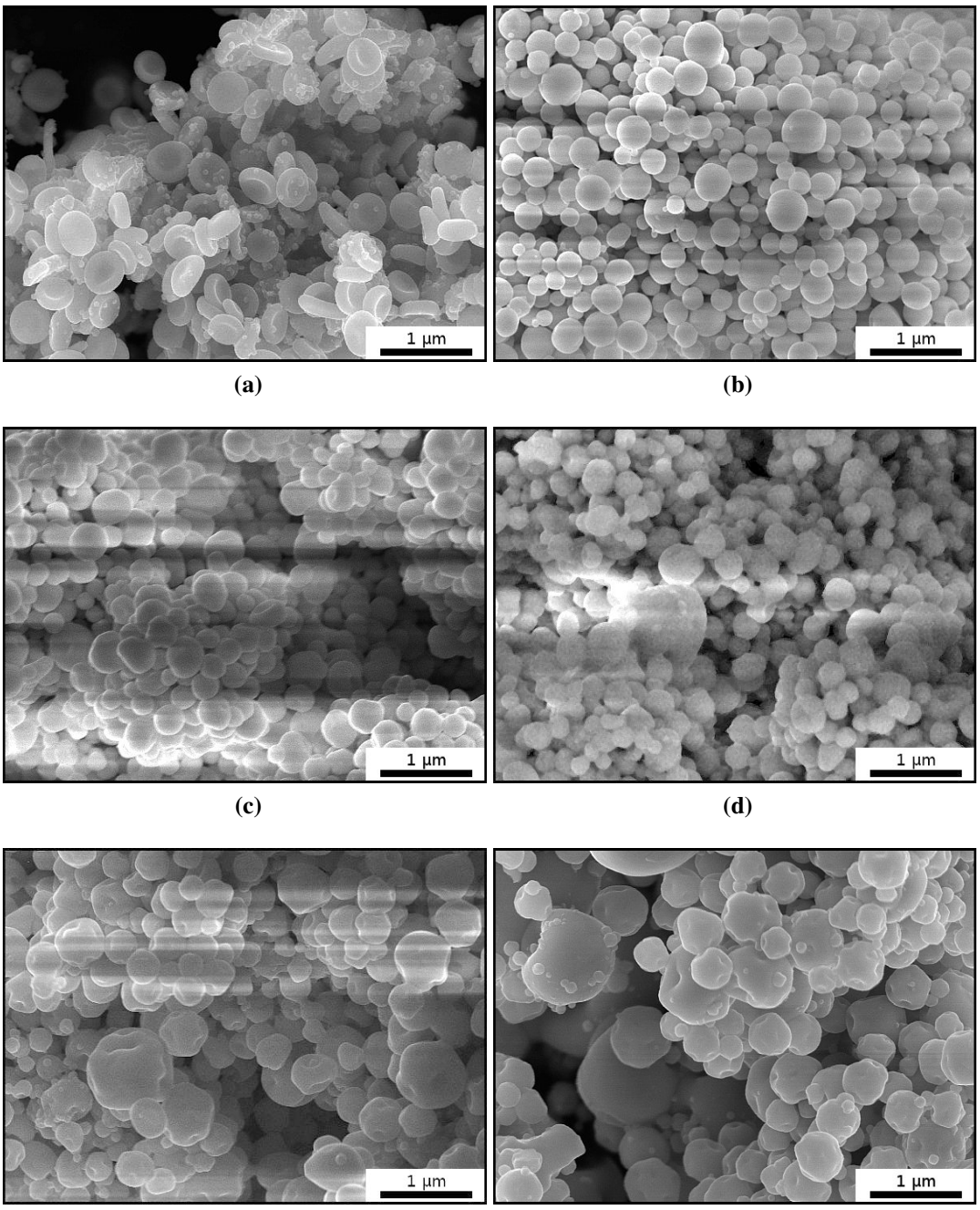

Figure 4.1: SEM micrographs representing PZT powders synthesised in the gas heating setup from different sol concentrations: a) 0.1, b) 0.2, c) 0.3, d) 0.4, e) 0.5 and f) 0.6 *M*. Flow rate, needle-electrode distance and applied voltage were set at 0.2 $ml\,h^{-1}$, 20 *mm* and 5 kV, respectively.

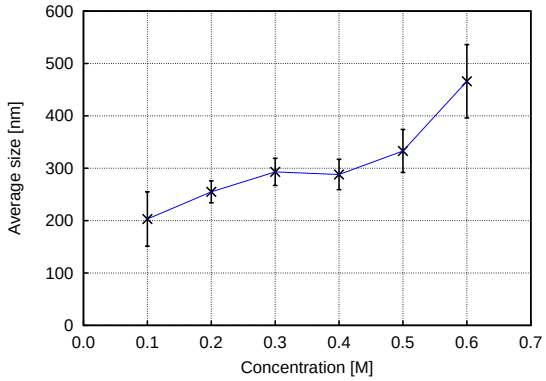

Figure 4.2: Variation of particle size with the sol concentration for the powders synthesised in the gas heating setup. Flow rate of 0.2 $ml\,h^{-1}$, needle-electrode distance of 20 *mm* and applied voltage of 5 *kV*.

The powders synthesised from 0.2 and 0.3 *M* sols were spherical and contained no larger particles. In all the cases the powder collected on the bottom electrode was white and uniform in colour and appearance.

The formation of disc-shaped particles at low sol concentration (0.1 *M)* is in agreement with results from sprayed polycaprolactone by Xie et al [133]. They showed that a change in the polycaprolactone concentration had an effect on the particle size and morphology (figure 4.3). Particle size decreases with the polymer content and the shape changed from spherical to biconcave (disc-shape, figure 4.3 b) to irregular.

In order to predict the droplet and particle size produced by EHDA, several studies have been done, as described in section 2.4.1.3. From the properties of the sols listed in table 4.1 is it possible to calculate the dimensionless parameter π_η (equation 2.8) as reported in table 4.2. π_η does not predict the droplet diameters, but it gives an indication on the influence of the viscosity on their formation. The viscosity is known to have an effect on the droplet size if $\pi_\eta \ll 1$, when the droplets increase their size with the viscosity. In our case π_η is only slightly lower than 1. This means that increasing the viscosity by increasing the sol concentration could lead to an increment in the droplet size and hence in the particle dimension. However,

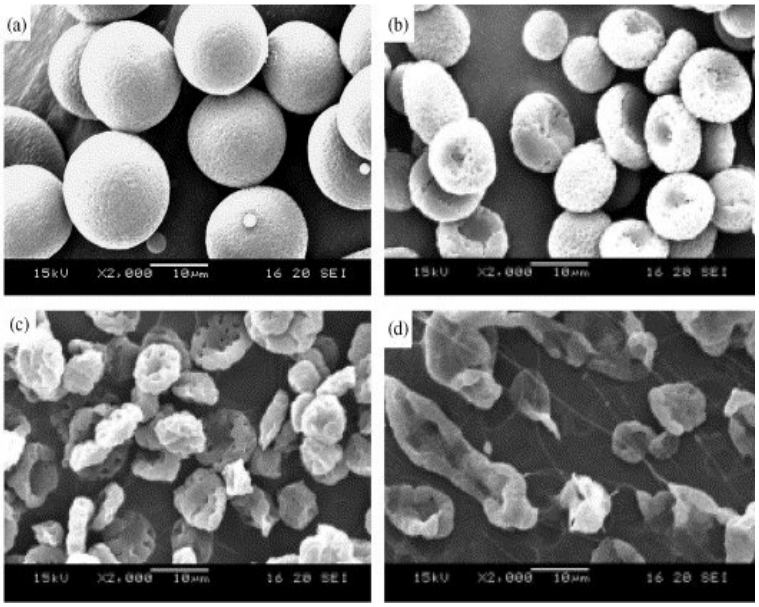

Figure 4.3: SEM micrographs of particles of polycaprolactone synthesised under different polymer concentration at flow rate of 3 $ml\,h^{-1}$: a) 6%, b) 3%, c) 1% and d) 0.5% of polycaprolactone. Adapted from [133].

Table 4.2: Dependence of the parameter π_η from the sol concentration.

Sol concentration, M	π_η
0.1	0.16
0.2	0.14
0.3	0.13
0.4	0.12
0.5	0.11
0.6	0.09

π_η is relatively close to 1, so it is possible that the viscosity does not have a significant effect. Since the target of the synthesis was to obtain small and spherical PZT particles a prediction of their dimension was needed. Equations 2.9 and 2.10 correlate the droplet diameter with liquid properties and process parameters and they are valid for $\varepsilon_r \ll 1$ and $\varepsilon_r \gg 1$, respectively. The same equations have been proposed by Ganan-Calvo et al. [107]. They reported that for liquid with a very low viscosity and electrical conductivity equation 2.9 was valid. For liquid with a very large viscosity and electrical conductivity, equation 2.10 was valid instead. Since the relative permittivity of the sols are larger than 1, but the viscosity

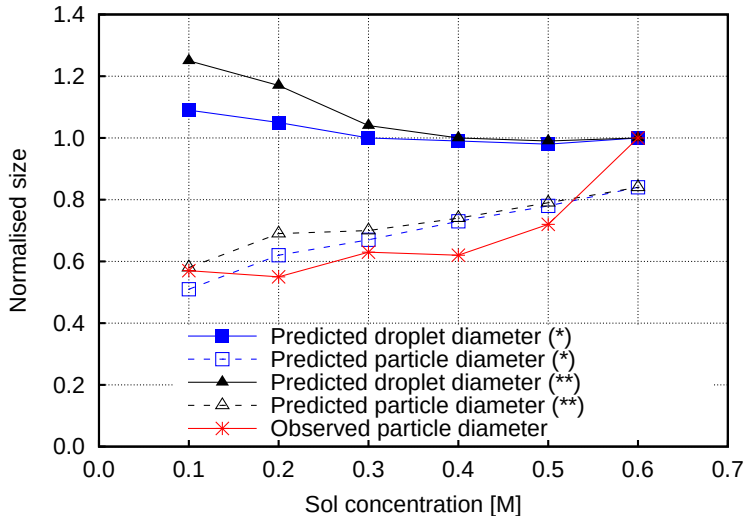

Figure 4.4: Predicted relative droplet and particle size as a function of the sol concentrations, normalised at 0.6 *M*. The symbols * and ** correspond to the equation 2.9 and 2.10, respectively.

and the conductivity are very small, both equations will be considered.

The relative particle size of the synthesised powder versus sol concentration is plotted in figure 4.4 (observed particle diameter line) and the values are normalised at 0.6 *M*. The predicted relative droplet sizes based on equations 2.9 and 2.10 are also plotted as a function of the sol concentration (solid lines, symbols * and **, respectively). It can be seen that the measured particle size increases with the sol concentration, but both equations predict that droplet size should decrease with increasing sol concentration. Although the equations predict the droplet size and not the final particle size, a correlation between droplet and particle size can be made by considering the concentration of the sol, where more concentrated systems will shrink less due to the lower solvent content. For this reason a modified predicted particle size trend has been calculated for both the equations by assuming a volumetric shrinkage term (cube root of the sol concentration) as shown in equation 4.1:

$$Np = Nd\,\sqrt[3]{Conc} \tag{4.1}$$

where *Np* is the normalised particle diameter, *Nd* is the normalised droplet diameter (from

equations 2.9 and 2.10) and *Conc* is the sol concentration. The new trends are also plotted in figure 4.4 (dashed lines, symbols * and **). It can be noted that the observed particle diameter trend is in agreement with the predicted particle diameter trends: the size increases with the concentration. However, for the 0.6 *M* system a different behaviour can be noticed experimentally. Here the value appears to deviate from the predicted trend. This can be attributed to the influence of the viscosity, because for this concentration the value of π_η is the lowest and the increase in viscosity may have a larger effect on particle size due to the production of larger droplets.

4.2.2 Effect of flow rate

Based on the results of the previous tests, a sol concentration of 0.2 *M* was chosen to study the effect of liquid flow rate on particle size and shape. It was carried out by spraying 0.2 *M* PZT sol at 0.2, 0.4 and 0.6 $ml\,h^{-1}$ in the gas heating setup . The needle-substrate distance was fixed at 20 *mm* and the applied voltage at 5.5 *kV*. The powders obtained under these conditions are compared in figure 4.5. It is possible to note that the particle size increases with the flow rate. The image analysis of the SEM micrographs (figure 4.5) shows that the particle size increased from 256 *nm* (for a flow rate of 0.2 $ml\,h^{-1}$) to 478 and 523 *nm*. This is in general agreement with the predictions of equations 2.9 and 2.10, where the droplet size increases with the flow rate. The observed particle size as a function of the flow rate is plotted in figure 4.6 along with the particle size predicted using equations 2.9 and 2.10.

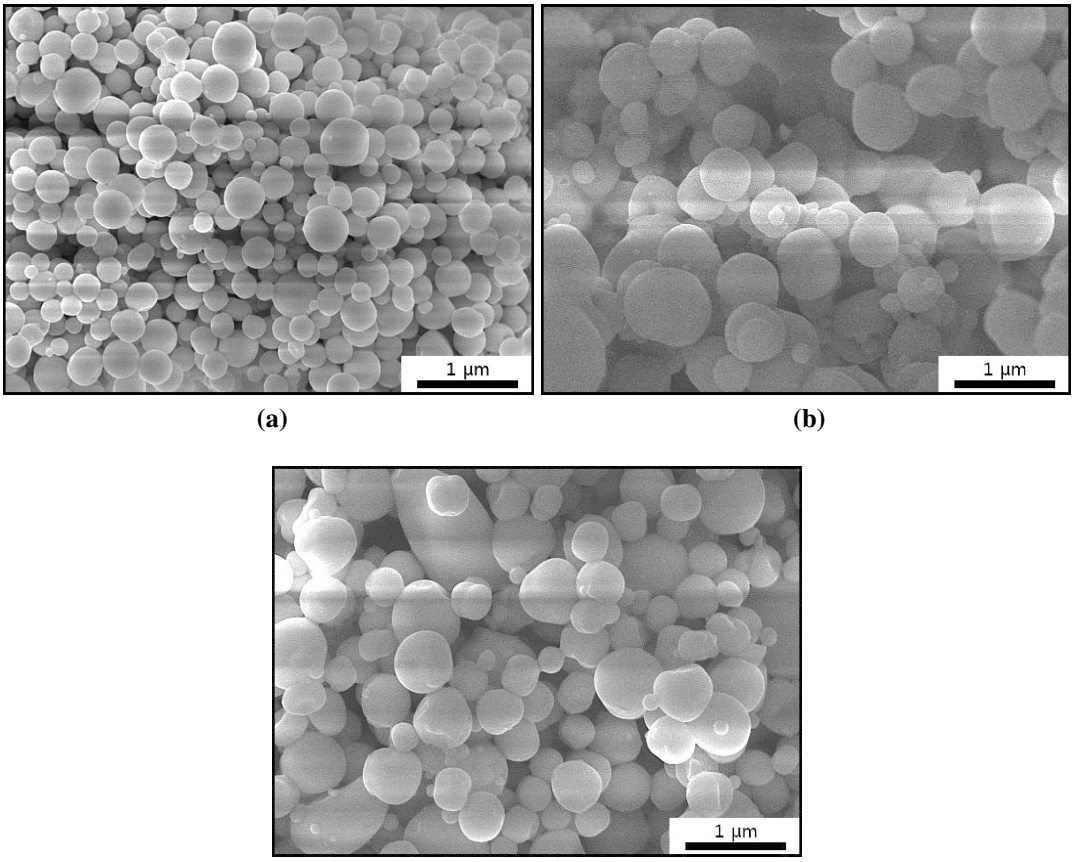

(a) **(b)**

(c)

Figure 4.5: SEM micrographs of the powders synthesised in the gas heating setup at different flow rates: a) 0.2, b) 0.4 and c) 0.6 $ml \cdot h$. Needle-substrate distance, concentration and applied voltage were fixed at 20 *mm,* 0.2 *M* and 5.5 *kV*, respectively.

The data were calculated by multiplying the predicted droplet diameter and the cube root of the sol concentration (0.2 *M*). From figure 4.6 it can be seen that the observed particle diameter trend is in agreement with the predictions. The experimental data lay close to the data calculated by the midfield equation 2.10, while the size calculated by the other equation is much higher. This mismatch can be accounted for by the different ranges of permittivity, viscosity and conductivity that govern the equations. Equation 2.9 is valid for liquids with low values of viscosity, conductivity and permittivity ($\ll$1), while equation 2.10 is valid for liquids with high viscosity, conductivity and permittivity ($\gg$1) [107]. For 0.2 M sol, viscosity and conductivity are low, but ε_r is greater than 1. The experimental data are more in

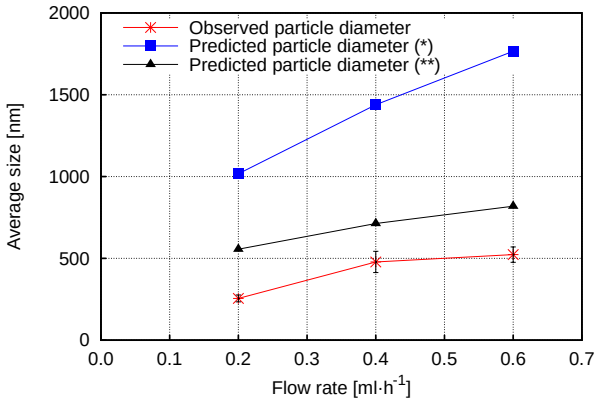

Figure 4.6: Variation of the particle size with the flow rate for powder synthesised in the gas heating setup (observed particle diameter). The symbols * and ** correspond to the predicted particle diameter calculated by using equations 2.9 and 2.10, respectively.

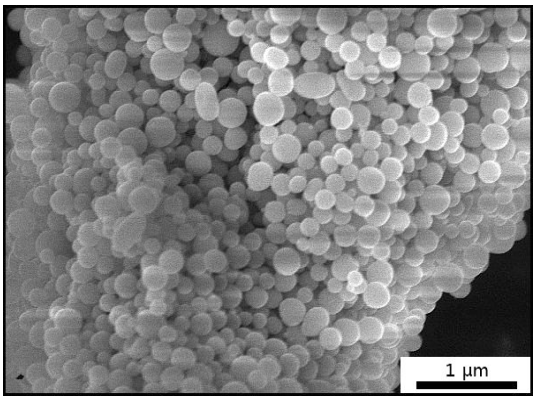

Figure 4.7: SEM micrograph of PZT powder synthesised in the gas heating setup using 0.2 *M* sol. The needle-substrate distance was 20 *mm* and the flow rate was 0.15 $ml\,h^{-1}$.

agreement with the predicted particle diameter trend calculated from equation 2.10, meaning that this equation better represents the effect of flow rate on particle size. A further reduction of the liquid velocity below 0.2 $ml\,h^{-1}$ led to a slight reduction in the particle diameter, as shown in figure 4.7, but it was not adopted for further experiments due to the low yield of synthesised powder.

4.2.3 Effect of heating

To understand the effect of temperature on particle size and shape, 0.2 *M* PZT sol was sprayed at 0.2 $ml\,h^{-1}$ applying a voltage of 5 *kV* at a distance of 20 *mm* and it was dried through the use of a focus lamp. The lamp current was set at 5, 6, 7 or 8 amps in order to increase the temperature of the focus area to approximately 200, 380, 520 and 680^oC, respectively, as show in figure 4.8.

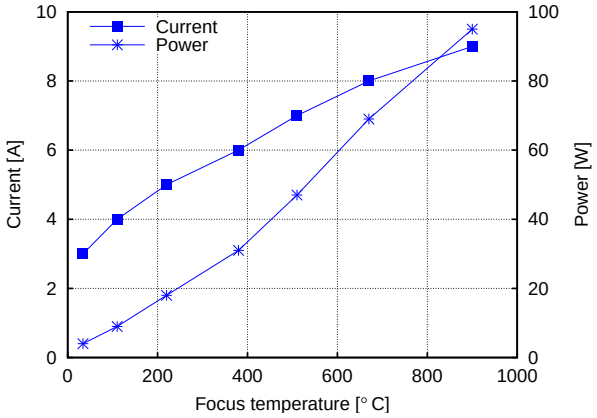

Figure 4.8: Dependence of focus temperature from the applied current or power.

The powders obtained at different temperatures are shown in figure 4.9 and the effect of the focus temperature on particle size is shown in figure 4.10. By comparing the powders dried at 200, 380 and 520^oC (figure 4.9 a, b and c, respectively) it can be seen that the use of lower temperatures results in bigger particles. Increasing the temperature not only led to the formation of smaller particles but also in a mixture of big and irregular particles. At a focal temperature of 680^oC, spherical particles smaller than 200 *nm* and big particles with irregular shapes were created (figure 4.9 d). Due to the presence of these large fragments, the mean particle size was not determined.

The focus area, for all the temperatures, was less than 20 *mm* in diameter, that was smaller than the spray area. This means that the whole spray area was not heated to the same temperature. When the focus temperature was set at 200^oC large and spherical particles were

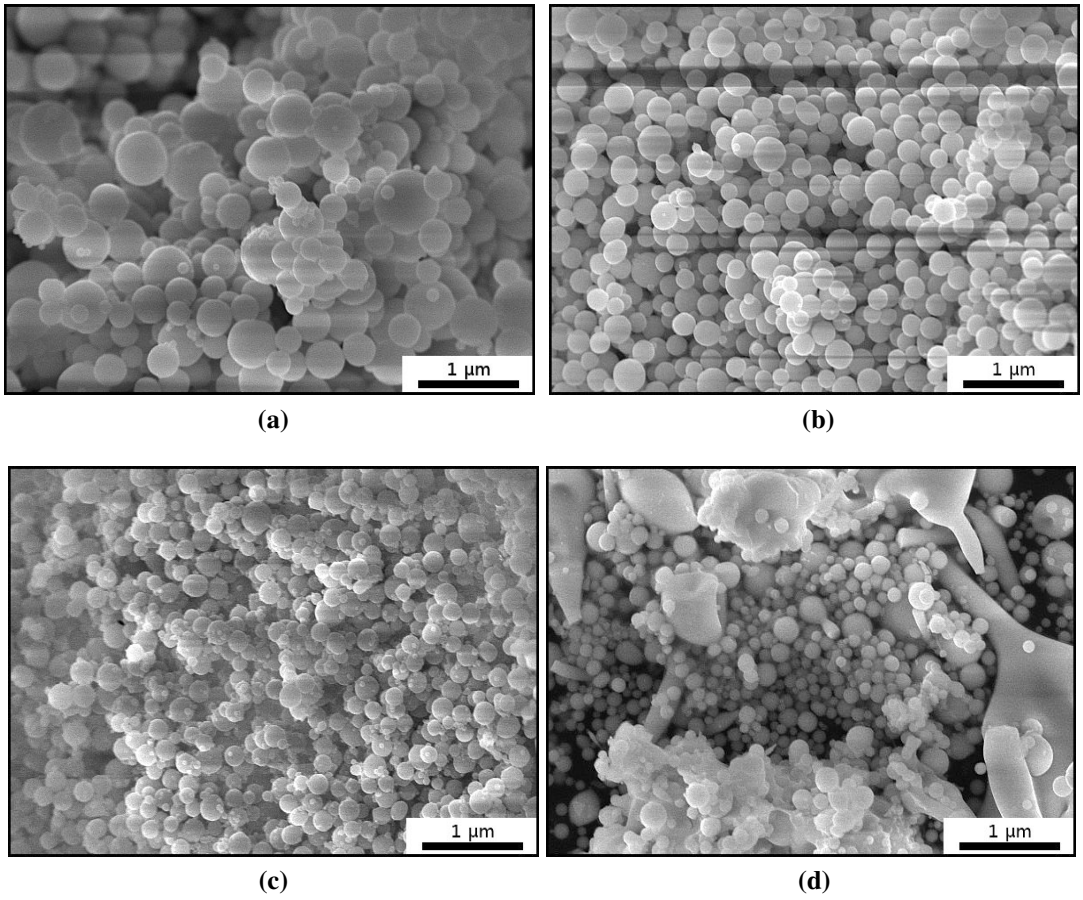

(a) **(b)**

(c) **(d)**

Figure 4.9: SEM micrographs of the powders dried at different focus temperature (direct heating setup): a) 200, b) 380, c) 520 and d) 680^oC. Needle-substrate distance, concentration and liquid flow rate were fixed at 20 *mm*, 0.2 *M* and 0.2 $ml\ h^{-1}$ respectively. The applied voltage was set at 5 *kV*.

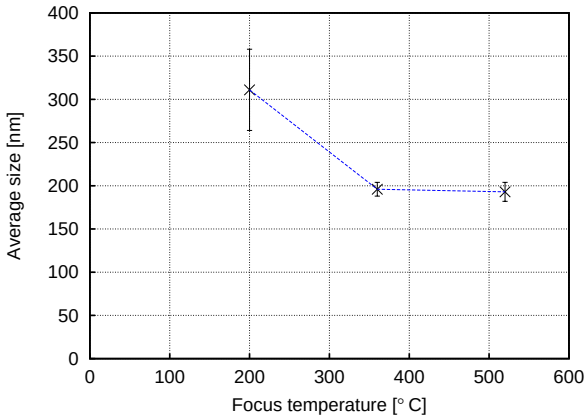

Figure 4.10: Variation of the particle size with the focus temperature. Needle-substrate distance, concentration and liquid flow rate were fixed at 20 *mm*, 0.2 *M* and 0.2 $ml\,h^{-1}$, respectively. The applied voltage was set at 5 *kV*.

formed. But, even if the focus temperature was 200^oC, the surrounding area was at a much lower temperature, namely 50-60^oC, that corresponds to the temperature of the nitrogen flow after its passage through the furnace (in the gas setup). At focus temperatures of 380 and 520^oC, spherical powders were obtained and the particle diameter was reduced from 311 *nm* (focus temperature of 200^oC) to 196 and 193 *nm*, respectively, as shown in figure 4.10. A further increment in the drying temperature did not result in the formation of smaller particles; from figure 4.9 d the presence of big and irregular particles can be seen. Their formation is probably due to the solvent evaporation at the needle mouth. In fact, at this temperature, a strange behaviour was noticed. The stable cone at the apex of the needle was interchanged by the presence of big semi-dried droplets that detached from it causing the formation of large particle with an irregular shape. The cone was reformed after the detachment of the big drop and the process started again. This behaviour can be attributed to the solvent evaporation in the cone at the needle apex. Once the cone was formed the solvent started to dry out due to the temperature and the small distance between the needle and the bottom electrode. It was possible to notice that the cone was drying. This process caused the formation of the semi-dried droplets that resulted in the formation of the big particles on the aluminium foil.

4.2.4 Effect of distance

To increase the flight time of the droplets and the solvent evaporation, the distance between the tip of the needle and the bottom electrode was varied. The distance of 20 to 30 and 40 *mm* in the direct heating configuration (using the focused lamp) were tested. The powders sprayed under these conditions are shown in figure 4.11. The powder obtained at distances of 20, 30 and 40 *mm* were spherical and no big particles were detected when they were dried at 520^oC. The same test was repeated increasing the temperature to 680^oC. At all the distances big and irregular particles were formed as shown in figure 4.11 b, d and f. The particle size of the powder obtained at different needle-bottom electrode distances at 520^oC is reported in figure 4.12. The variation of the particle diameter with needle-electrode distance for the powder dried at 680^oC is not reported due to the presence of the big and irregular particles.

A bigger distance results in larger flight time for the droplet, hence a higher degree of solvent evaporation, that should result in smaller particles. When the spray was dried at 520^oC, the particle size was affected very little by the distance, as shown in figure 4.12. Larger distance and higher temperature should result in a decrease in the particle size, due to the higher flight time and higher degree of solvent evaporation. When the temperature was set at 680^oC and the distance was set at 20 *mm* (see subsection 4.2.3) big and semi-dried droplets were formed due to the high temperature and the small distance between the electrode and the aluminium foil. An increase in the needle-bottom electrode distance should then help in reducing the formation of the big droplets. However their formation occurred even if the needle and the bottom electrode were 40 *mm* apart. This means that to dry the spray at 680^oC, a distance grater than 40 *mm* is needed in order to avoid the formation of the big droplets within the powder.

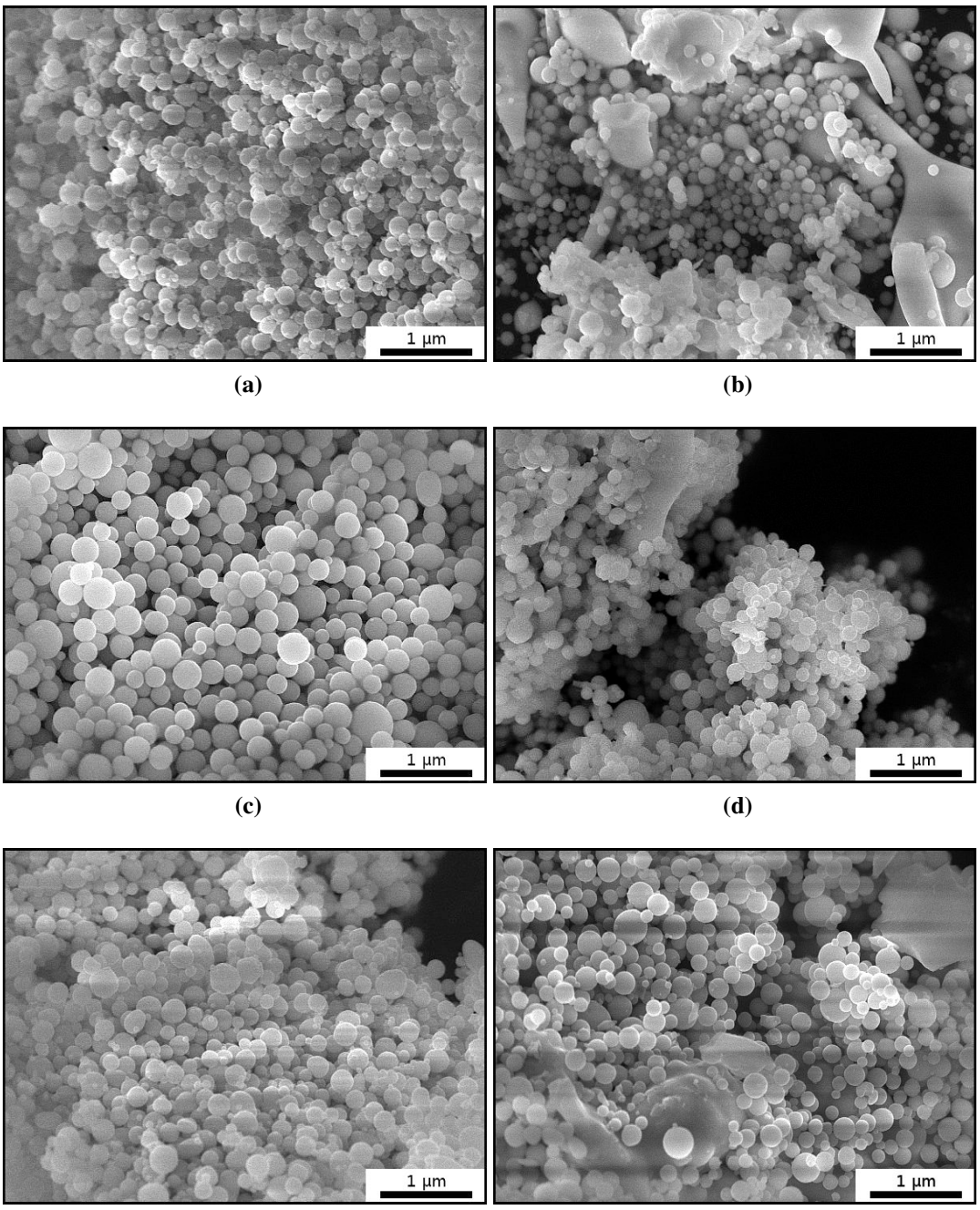

Figure 4.11: SEM micrographs of the powders synthesised in the direct heating setup at different distances and temperatures: a) 20 *mm*, 520^oC, b) 20 *mm*, 680^oC, c) 30 *mm*, 520^oC, d) 30 *mm*, 680^oC, e) 40 *mm*, 520^oC and f) 40 *mm*, 680^oC. The applied voltage was set at 5.5 *kV*.

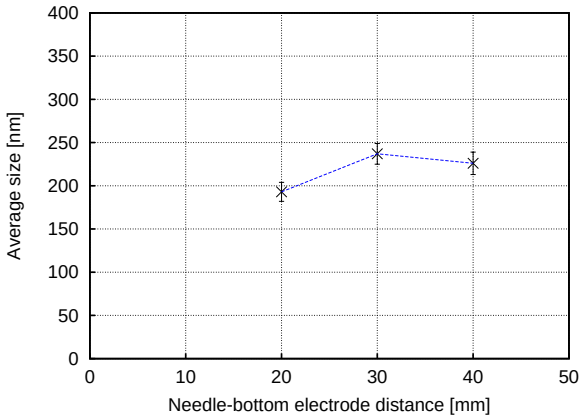

Figure 4.12: Variation of the particle size with the needle-bottom electrode distance for the focus temperature of 520^oC. Concentration, liquid flow rate and applied voltage were fixed at 0.2 *M,* 0.2 $ml\,h^{-1}$ and 5.5 *kV*, respectively.

4.2.5 Yield

To obtain small and spherical PZT particles by EHDA, low sol concentration and flow rate were used, 0.2 *M* and 0.2 $ml\,h^{-1}$, respectively. These conditions led to a small amount of synthesised powder. In 8 hours of deposition the amount of collected powder was less than 0.2 g. In figure 4.13 the theoretical (solid line) and experimental (single points) yields of powder synthesised starting from the sols in the gas heating setup at 0.2 $ml\,h^{-1}$ and with a needle-bottom electrode distance of 20 *mm* are shown. It can be seen that the values are small. The experimental data are in agreement with the theoretical ones, meaning that the sprayed sol was completely converted in powder. At sol concentration of 0.3 *M* a mismatch is noted, attributable to the powder not completely dried.

4.3 EHDA powder ink preparation

PZT powder was synthesised by electrospray with the purpose to obtain small and spherical particles suitable for ink formulation. The target of this research was the development of an ink composed of PZT particles dispersed in PZT sol.

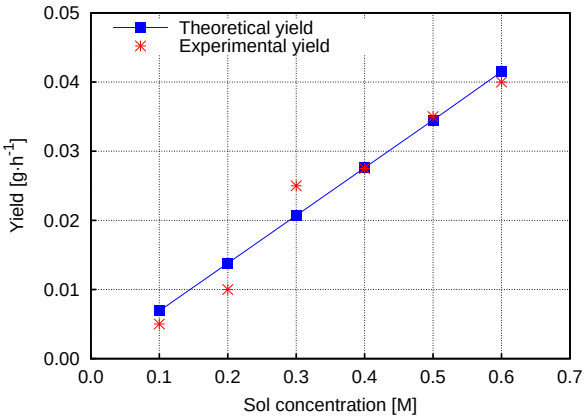

Figure 4.13: Theoretical and experimental yield for the powder synthesised in the gas heating setup.

Since the powder was not subjected to high temperatures during the synthesis, a test to check its stability in the sol was done. The as-prepared powder (dried by the focus lamp) was mixed with PZT sol in order to verify if it was redissolving. It was noticed that the particles dissolved in the sol, indicating an incomplete conversion to ceramic. For this reason a further heat treatment was needed. Small amounts of powder synthesised by EHDA were heated for 20 minutes at different temperatures, from 200 to 650^oC. After the heat treatment the powder was mixed again with the sol to check its dissolution. The powder heat treated at 200^oC redissolved in the sol as the non-heat treated one did. Stable ceramic particles were obtained when the temperature was increased above 250^oC. This means that to avoid the heat treatment step, the spray area should be uniformly dried at a temperature greater than 250^oC. In the direct heating setup the focus area was smaller than the spray area, so even if the focus temperature was set at 520^oC, the surrounding area was at a lower temperature, namely 150-200^oC. This resulted in a non homogeneous drying of the particle, that were not all dried at 520^oC. Therefore a further heat treatment step was needed. An increment in the focus temperature to 680^oC was not considered due to the eventual formation of the big and irregular particles described in subsection 4.2.3.

4.4 Summary

The aim of this chapter was to synthesise spherical PZT particles in the submicron range by electro hydrodynamic atomisation. The effects of several parameters on particle size and shape have been investigated, such as sol concentration, flow rate, drying temperature and needle-bottom electrode distance.

Sols with different concentrations, from 0.1 to 0.6 *M*, have been electrosprayed and dried by the passage of an hot gas flow. Decreasing the sol concentration led to a reduction of the particle size. The dimension of the powder was also reduced by decreasing the liquid flow rate. When the sol was sprayed at 0.6 $ml\,h^{-1}$ the resulting particles were double in size of those obtained with flow rate of 0.2 $ml\,h^{-1}$. In order to dry the powder more efficiently and reduce its diameter, the spray area was heated at different temperatures by the use of a focused lamp. At low temperature (200^oC) the synthesised particles were bigger than the ones dried at higher temperatures, such as 380 and 520^oC. When the focus was set at the highest temperature (680^oC) the presence of big particles within the powder was observed. Finally, to increase the flight time and the solvent evaporation, the distance between the needle and the aluminium foil was increased from 20 to 30 and 40 *mm*. The particle size was found to be affected very little by this parameter. However a distance of 30 *mm* was chosen due to the practicity in its setting.

An amount of powder sufficient for ink formulation was synthesised in the following conditions: sol concentration of 0.2 *M*, liquid flow rate of 0.2 $ml\,h^{-1}$, needle-bottom electrode distance of 30 *mm,* direct heating setup with a focus temperature of 520^oC. The powder needed a further heat treatment at a temperature greater than 250^oC in order to not redissolve in the PZT sol.

Chapter 5

Preparation of PZT micro-nanoparticles by molten salt synthesis

5.1 Introduction

Molten salt synthesis (MSS) is a very versatile process that leads to the formation of large amounts of ceramic material in a short period of time. Compared to solid state synthesis, MSS leads to the formation of ceramics at lower temperature with less aggregates, due to the presence of the molten salt that acts as a solvent enhancing atomic diffusion.

In this synthesis several process parameters have been changed in order to identify their influence on particle size and shape, such as reaction time, temperature and heating ramp rate. Attempts were made in order to synthesise PZT particles in the nano-to-micron range. From the results obtained a formation mechanism for the synthesis of PZT powder by molten salt is proposed.

5.2 Study of MSS parameters on size and shape of PZT particles

5.2.1 Effect of time

As stated in the subsection 2.4.2.2, shorter isothermal time has been reported to lead to the formation of small particles [27, 28, 111]. In figures 5.1, 5.2 and 5.3 examples of the effect of the isothermal time on particle shape are shown. Figure, a, b and c represent the PZT powder heated for 30, 60 and 120 minutes, respectively and d is the XRD pattern of such powders.

Figure 5.1 a, b and c represents the PZT powders synthesised at 750^oC, with a heating ramp rate of $20^oC\,min^{-1}$, for 30, 60 and 120 minutes, respectively. At low isothermal time (30 minutes), the synthesised powder had an irregular shape which became more regular with increasing process time. However, all powders synthesised at this temperature had irregular shape. From the XRD patterns in figure 5.1 d it can be seen that perovskite phase was developed for all the samples. After 30 minutes of reaction, residual PbO and ZrO_2 and PT were found in the mixture. By increasing the isothermal time to 60 and 120 minutes, ZrO_2 and PT peaks were not observed, but PbO was still present within the PZT powder.

In figure 5.2 a, b and c, the powders synthesised at 800^oC for different isothermal times (30, 60 and 120 minutes) and heated at $20^oC\,min^{-1}$ are shown. At this temperature the powders were more spherical, and an increment in the isothermal time did not result in a change in particle shape as in the case of PZT synthesised at 750^oC (figure 5.1). At longer isothermal times bigger particles were obtained. Under these conditions perovskite phase was developed for all the samples, but PbO was still present in the sample heated for 30 minutes at 800^oC, as shown in figure 5.2 d.

In figure 5.3 a, b and c the SEM micrographs of the powders synthesised for different isothermal times at 850^oC, with a temperature ramp rate of $20^oC\,min^{-1}$ are reported. At

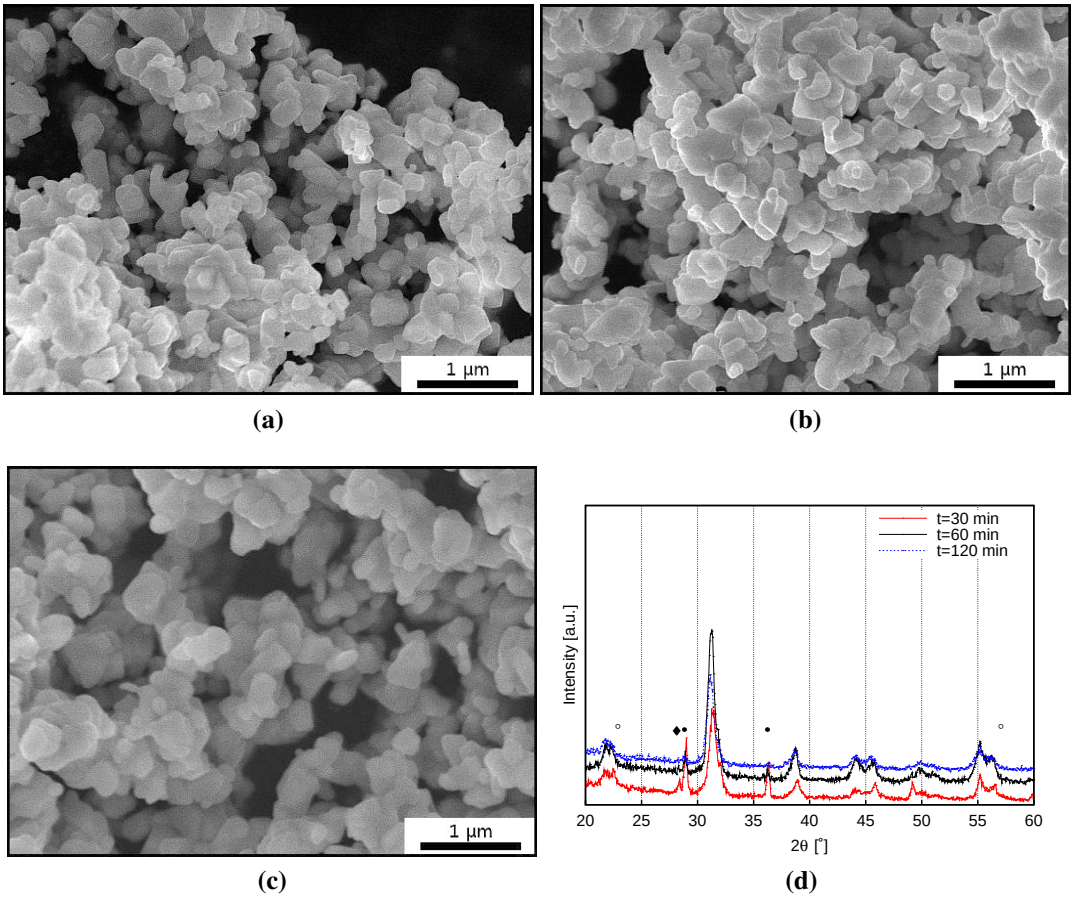

(a) **(b)**

(c) **(d)**

Figure 5.1: SEM micrographs representing PZT powders synthesised at 750^oC with a heating ramp rate of $20^oC\,min^{-1}$ for a) 30, b) 60 and c) 120 minutes. d) represents the XRD patterns of the powders synthesised in these conditions. Symbols •, ♦ and ○ represent PbO, ZrO_2 and $PbTiO_3$ peaks, respectively.

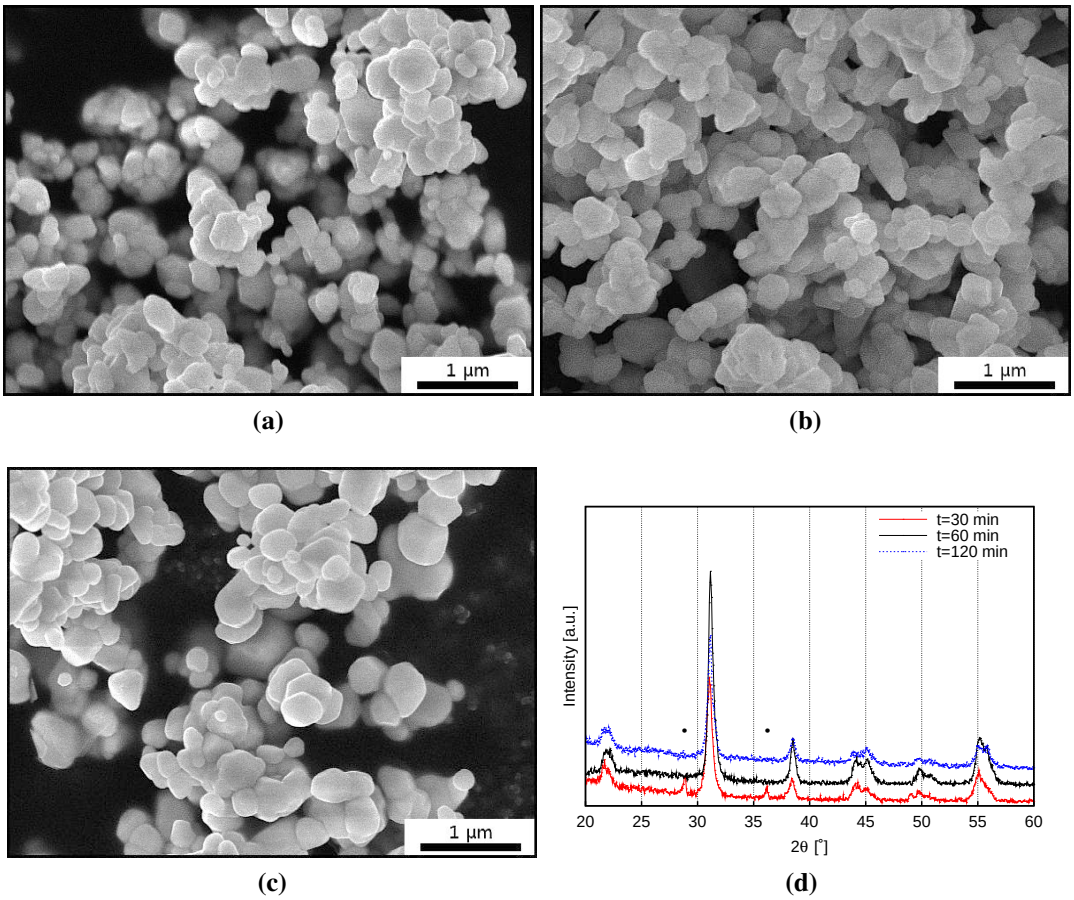

(a) **(b)** **(c)** **(d)**

Figure 5.2: SEM micrographs representing PZT powders synthesised at 800^oC with a heating ramp rate of $20^oC\,min^{-1}$ for a) 30, b) 60 and c) 120 minutes. d) represents the XRD patterns of the powders synthesised in these conditions. Symbol • represents PbO peaks.

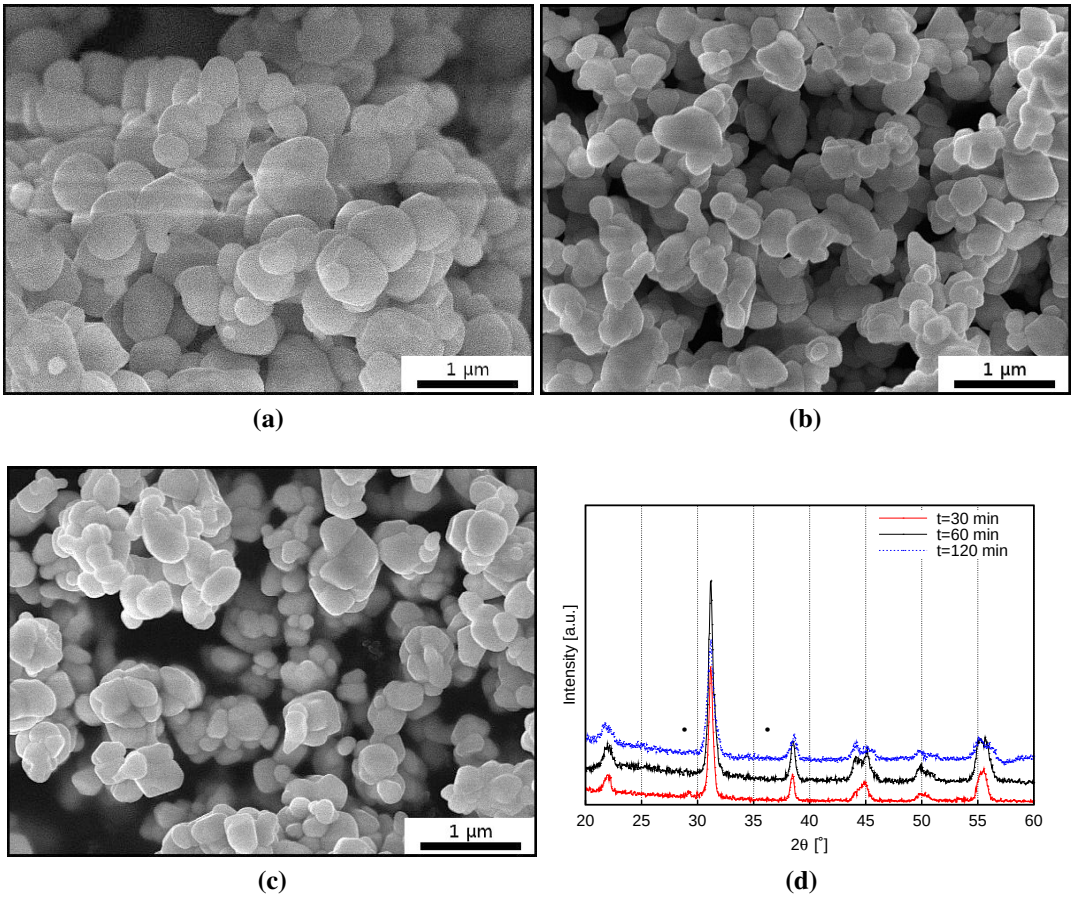

(a) **(b)** **(c)** **(d)**

Figure 5.3: SEM micrographs representing PZT powders synthesised at 850^oC with a heating ramp rate of $20^oC\,min^{-1}$ for a) 30, b) 60 and c) 120 minutes. d) represents the XRD patterns of the powders synthesised in these conditions. Symbol • represents PbO peaks.

this temperature the particles were more spherical than the particles synthesised at lower temperature. Also at 850^oC, the time does not seem to affect the purity of the final product. Perovskite phase was detected for all the samples. However the presence of lead oxide was detected in the sample heated at 850^oC for 30 minutes.

5.2.2 Effect of temperature

To test the effect of temperature on particle size, starting materials were heated at 750, 800 and 850^oC for different periods of time and at different heating rates. Examples that better

show this effect are reported in figures 5.4, 5.5 and 5.6. In each figure, the correspondent XRD patterns are also reported.

In figure 5.4 a, b and c PZT powders heated at $3.3^oC\,min^{-1}$ for 30 minutes at 750, 800 and 850^oC are shown. It can be seen that the powder synthesised at 750^oC shows an irregular shape (figure 5.4 a). ZrO_2 and PbO were found in this final mixture as shown in the XRD pattern in figure 5.4 d. Increasing the reaction temperature to 800^oC (figure 5.4 b) led to a change in the particle morphology into a more regular shape. At this temperature only peaks attributable to PZT were detected in the pattern. The shape changing phenomenon was enhanced by further increment of the temperature: the powder obtained at 850^oC, figure 5.4 c, showed an almost spherical shape and it was larger in size than the powder heated at 750 and 800^oC. Only PZT peaks were detected by XRD analysis as shown in the XRD pattern in figure 5.4 d.

SEM micrographs of the powders synthesised for 60 minutes and heated at $3.3^oC\,min^{-1}$ are reported in figure 5.5. Again, at 750^oC irregular particles were formed (figure 5.5 a) and residual PbO was found within PZT. When the reaction temperature was set at 800 and 850^oC (figure 5.5 b and c) the particle morphology changed to spherical. No PbO, ZrO_2 nor PT were detected in the XRD patterns of these powders.

At fixed isothermal time of 120 minutes perovskite phase PZT powder was obtained for all temperatures between 750 and 850^oC, but at 750^oC PbO peaks were detected in the XRD pattern, as shown in figure 5.6 d. At 750^oC the powder was irregular in shape, that gradually became more spherical by increasing the reaction temperature (from a to c in figure 5.6).

The presence of unreacted PbO, noted in the XRD patter, was confirmed by SEM-EDX analysis, showing large Pb rich particles within the resultant powders, as shown in figure 5.7. The micrograph represents PZT powder synthesised at 750^oC for 30 minutes, with an heating ramp rate of $20^oC\,min^{-1}$. Big particles can be clearly noted within the powder.

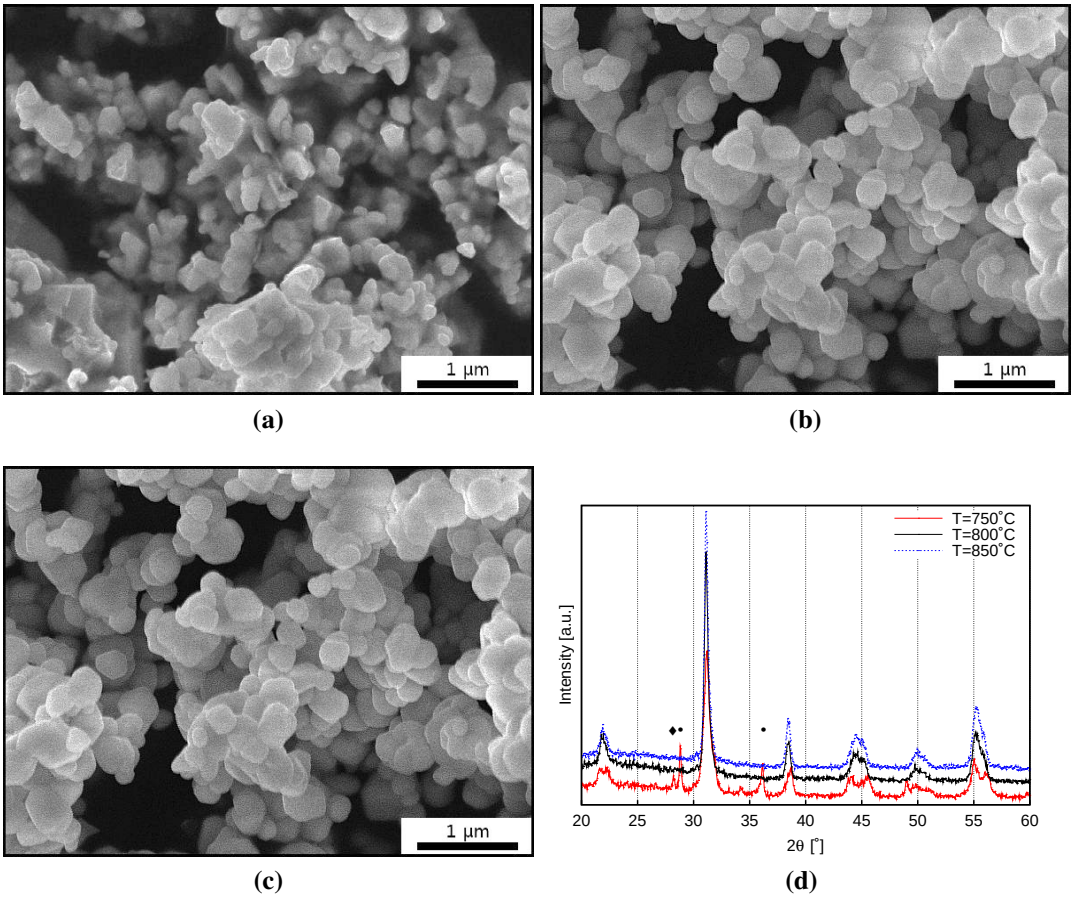

(a) **(b)** **(c)** **(d)**

Figure 5.4: SEM micrographs of the PZT powders synthesised at isothermal time of 30 minutes, with a heating ramp rate of $3.3^{o}C\,min^{-1}$ at a) 750, b) 800 and c) $850^{o}C$. d) represents the XRD patterns of the powders synthesised in these conditions. Symbols • and ♦ represent PbO and ZrO_2 peaks, respectively.

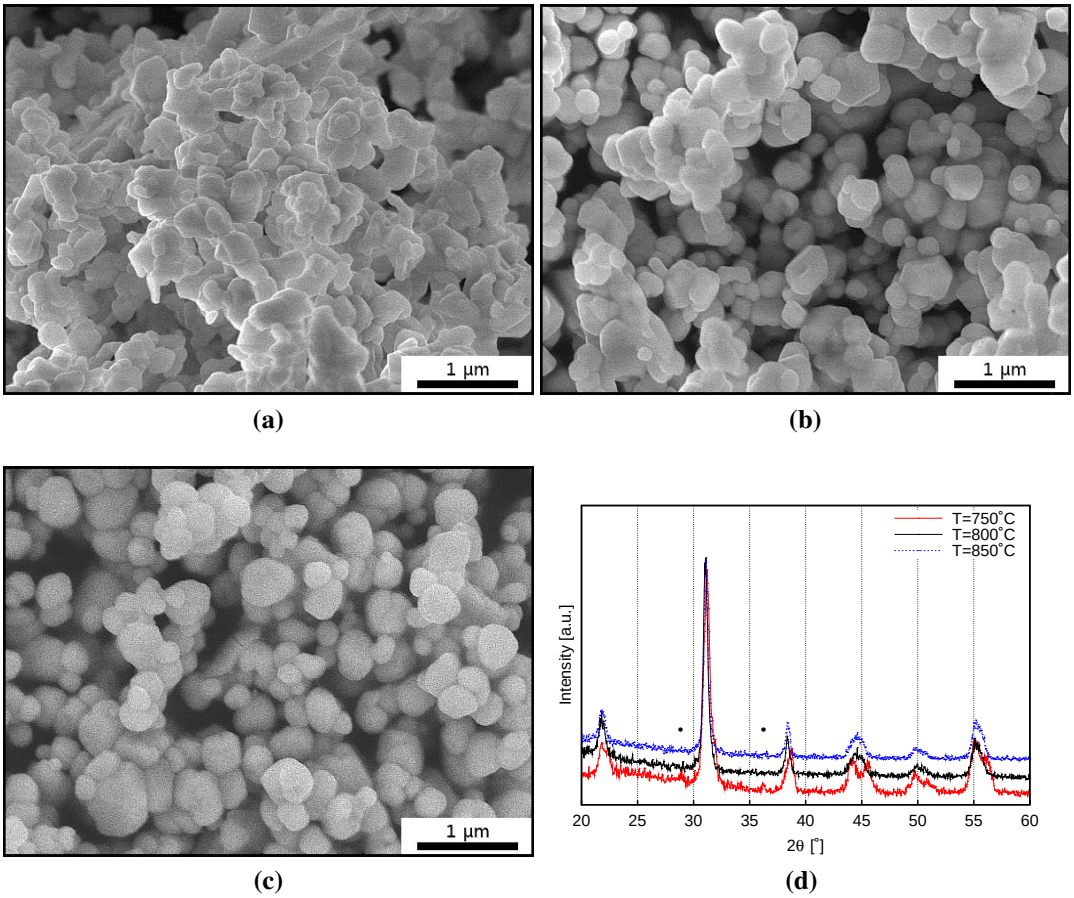

(a) **(b)**

(c) **(d)**

Figure 5.5: SEM micrographs of the PZT powders synthesised at isothermal time of 60 minutes, with a heating ramp rate of $3.3^{o}C\,min^{-1}$ at a) 750, b) 800 and c) $850^{o}C$. d) represents the XRD patterns of the powders synthesised in these conditions. Symbol • represents PbO peaks.

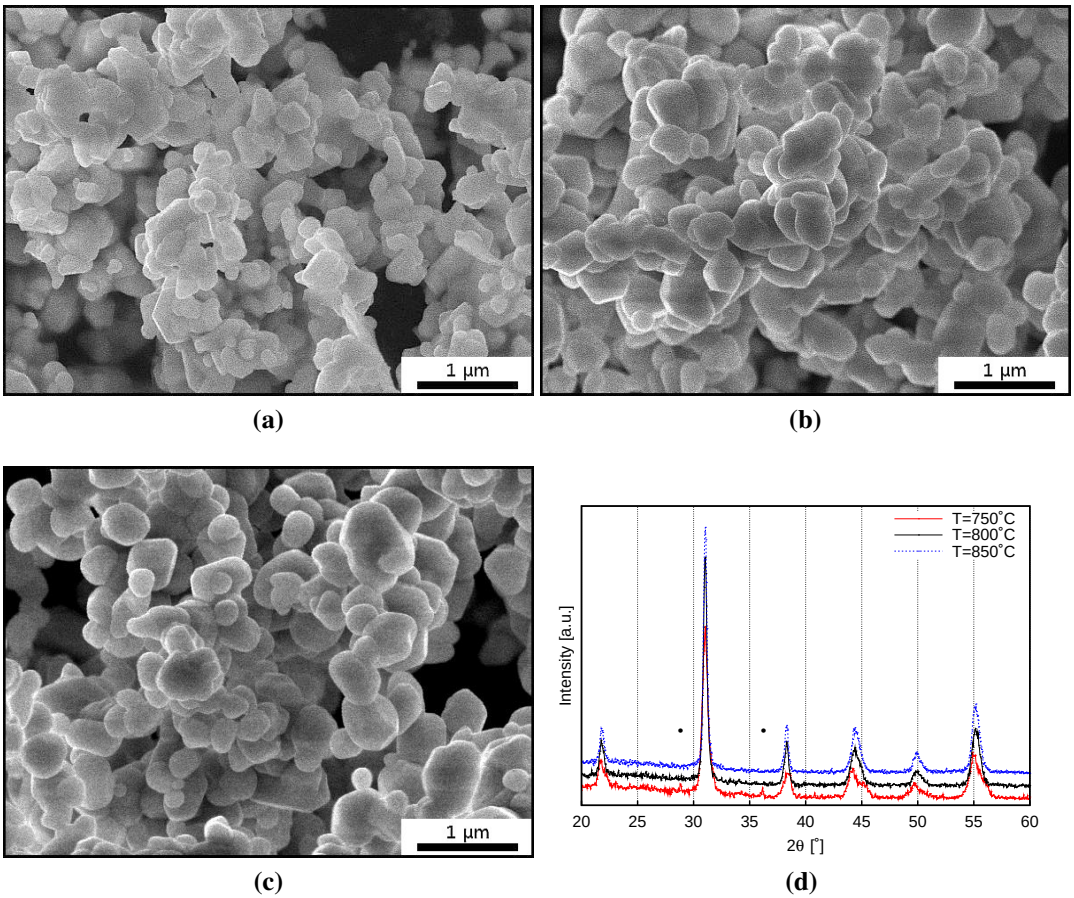

(a) **(b)** **(c)** **(d)**

Figure 5.6: SEM micrographs of the PZT powders synthesised at isothermal time of 120 minutes, with a heating ramp rate of $3.3^oC\,min^{-1}$ at a) 750, b) 800 and c) 850^oC. d) represents the XRD patterns of the powders synthesised in these conditions. Symbol • represents PbO peaks.

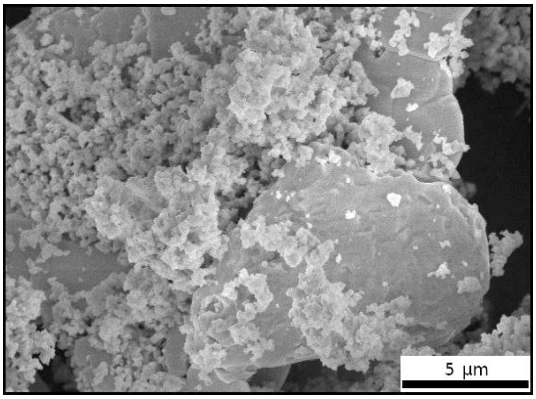

Figure 5.7: SEM micrograph of PZT powders synthesised at 750^oC for 30 minutes with a temperature ramp rate of $20^oC\,min^{-1}$ showing large Pb rich particles.

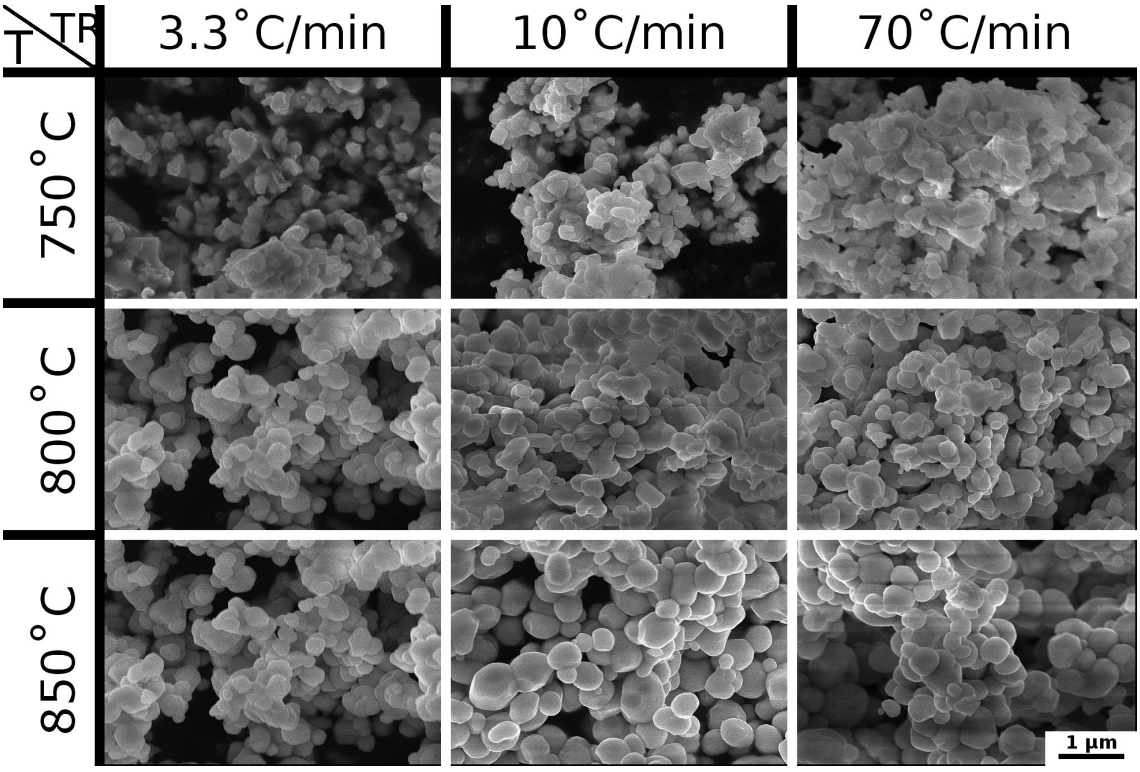

Figure 5.8: SEM micrographs of PZT powders synthesised at different temperatures and for 30 minutes, with heating ramp rates of 3.3, 10 and 70$^oC\,min^{-1}$.

5.2.3 Effect of heating ramp rate and temperature

In order to understand the effect of the temperature ramp rate on particle size and morphology, PZT powder was synthesised at 750, 800 and 850^oC for 30, 60 and 120 minutes under 3.3, 10 and 70$^oC\,min^{-1}$ heating rates. These ramp rates were chosen in order to represent the powder synthesised at the lowest, highest and medium ramp rates. The SEM micrographs of the powders synthesised under these conditions are shown in figures 5.8, 5.10 and 5.12. The correspondent XRD patterns are shown in figures 5.9, 5.11 and 5.13.

Figure 5.8 represents the SEM micrographs of the powders reacted for 30 minutes. It can be seen that at 750^oC (top row) the synthesised powders had an irregular shape independently of the ramp rate used. At this temperature and at all the ramp rates, residual PbO and ZrO_2 were found in the mixture (figure 5.9) by XRD analysis. Moreover when the highest ramp

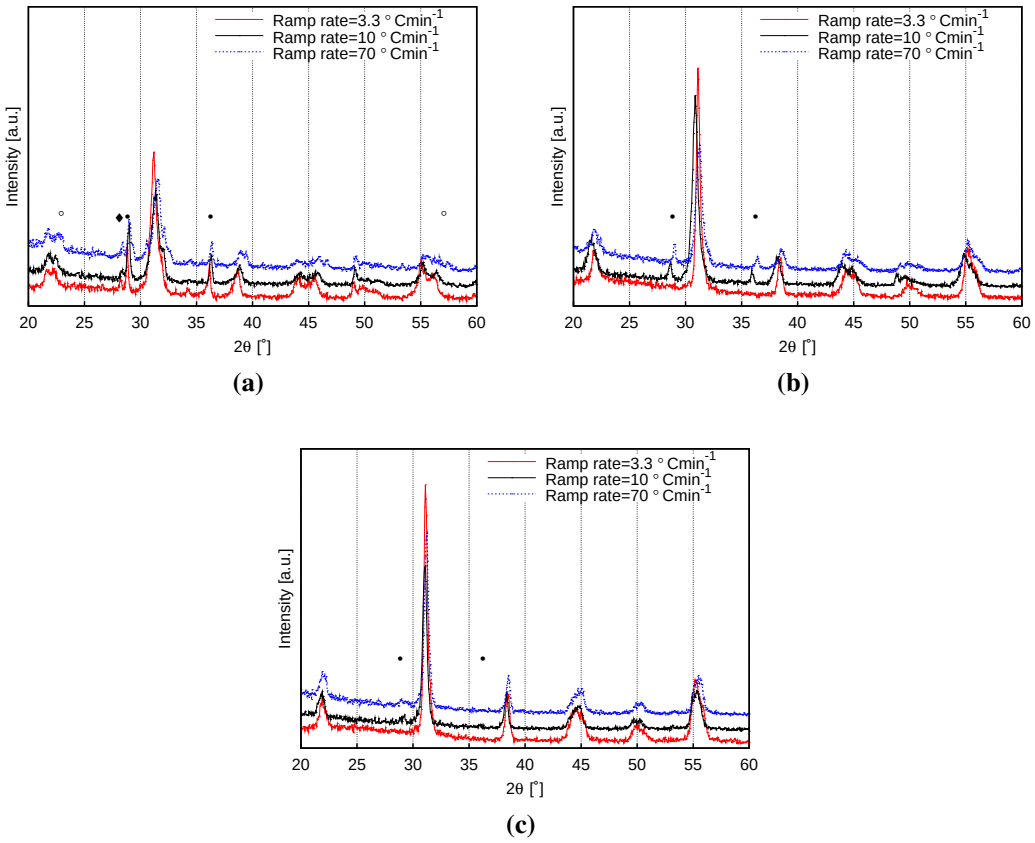

Figure 5.9: XRD patterns of PZT powders heated at 3.3, 10 and 70$^oC\,min^{-1}$ at a) 750, b) 800 and c) 850^oC for 30 minutes. Symbols •, ♦ and ○ represent PbO, ZrO_2 and $PbTiO_3$ peaks, respectively.

rate was adopted to heat the sample, PT traces were also found within the PZT powder.

At 800^oC the particles were more regular, but the powder heated at the fastest rate, 70$^oC\,min^{-1}$, was less spherical than the ones heated at 10 or 3.3$^oC\,min^{-1}$. When the sample was heated at 3.3$^oC\,min^{-1}$ only PZT peaks were detected in the XRD pattern (figure 5.9 b). At the same temperature but at high rates PbO was still present in the final mixture.

Increasing the temperature to 850^oC (bottom row in figure 5.8) led to spherical particles, even at high ramp rate. However, PbO traces were detected in the samples heated at 10 and 70$^oC\,min^{-1}$. When the slowest ramp was used, the final product was pure PZT.

In figure 5.10 the powders that reacted for 60 minutes at 750, 800 and 850^oC, heated

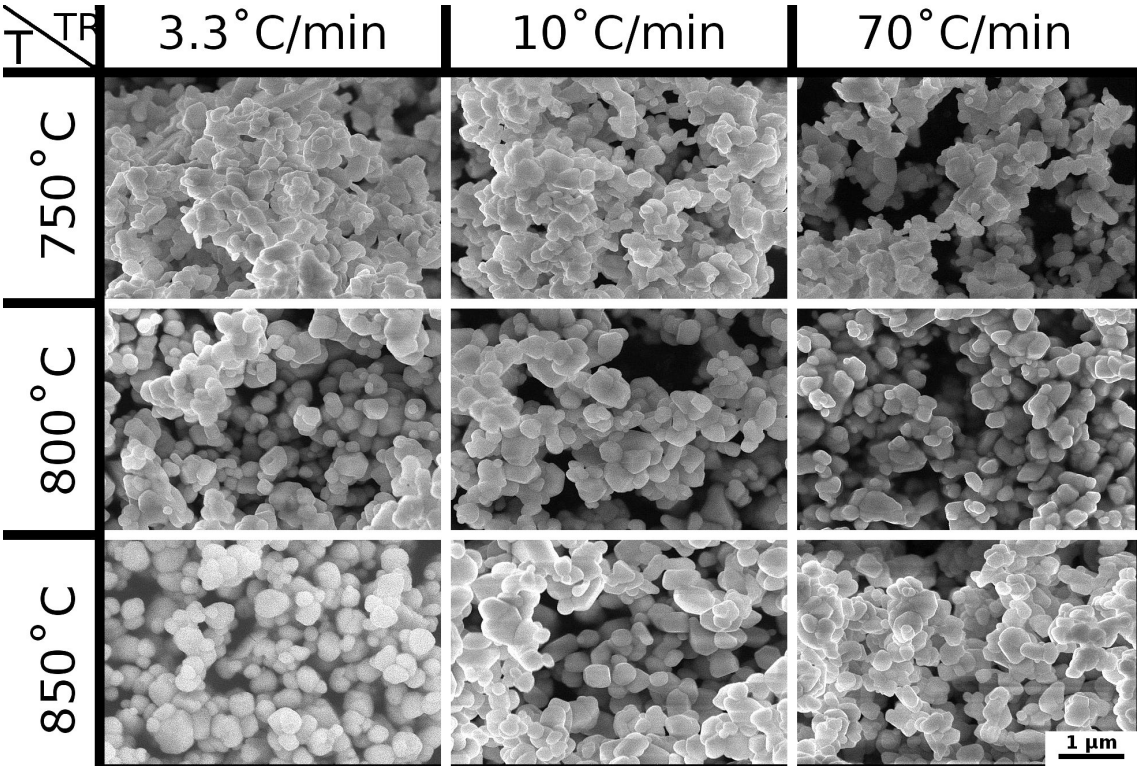

Figure 5.10: SEM micrographs of PZT powders synthesised at different temperatures and for 60 minutes, with heating ramp rates of 3.3, 10 and 70$^oC\,min^{-1}$.

at different rates, are reported. When the starting materials were heated at 750^oC with all the ramp rates (top row), the resulting particle shape was irregular. Increasing the reaction temperature to 800^oC reduced the roughness of the particles, but the oxides heated at the highest ramp rate resulted in more irregular particles than the ones heated slowly. At 850^oC (bottom row) this phenomenon was reduced, but the particles obtained by increasing the temperature at 3.3$^oC\,min^{-1}$ were more spherical than the ones obtained by fast heating. The XRD patterns of the powders synthesised in these conditions are reported in figure 5.11. When the temperature was set at 750^oC, PbO was detected in all the samples. When the fastest ramp rate was used, ZrO_2 was also detected. At 800 and 850^oC no residual oxides were found in the samples, independently from the ramp rate used.

The same experiments were repeated at longer isothermal times (120 minutes) and the SEM micrographs of the powders are reported in figure 5.12. When the starting materials

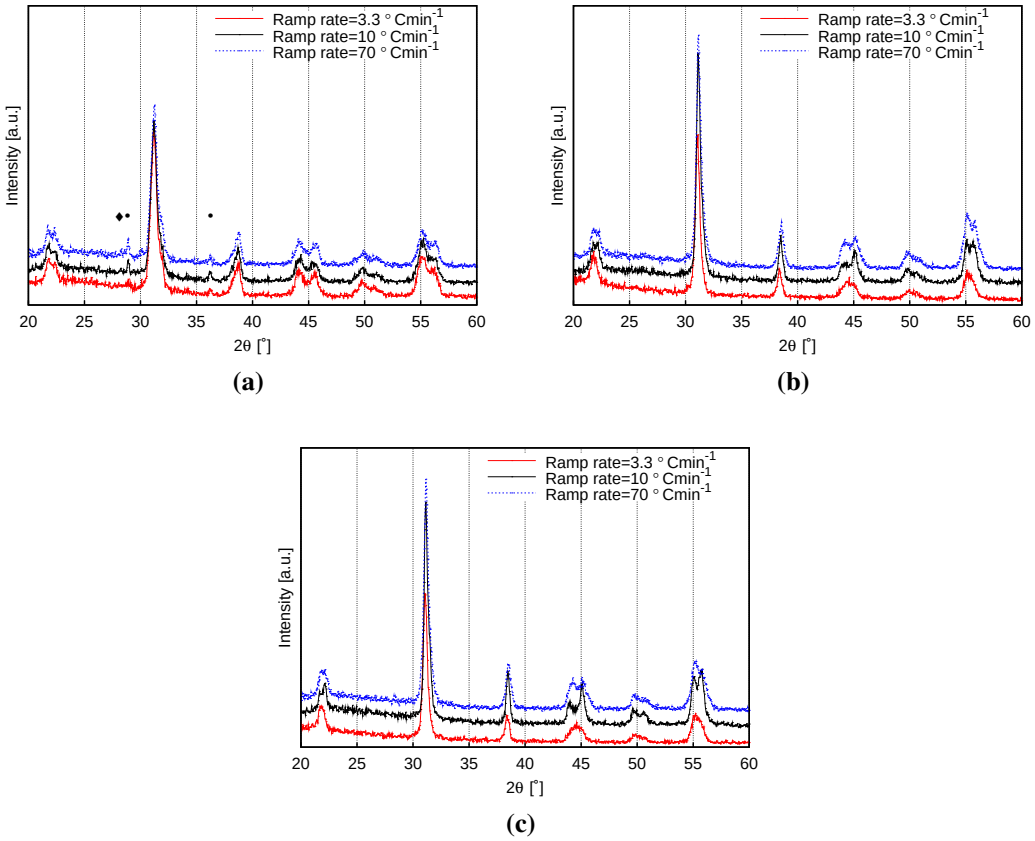

Figure 5.11: XRD patterns of PZT powders heated at 3.3, 10 and 70$^oC\,min^{-1}$ at a) 750, b) 800 and c) 850^oC for 60 minutes. Symbols • and ♦ represent PbO and ZrO_2 peaks, respectively.

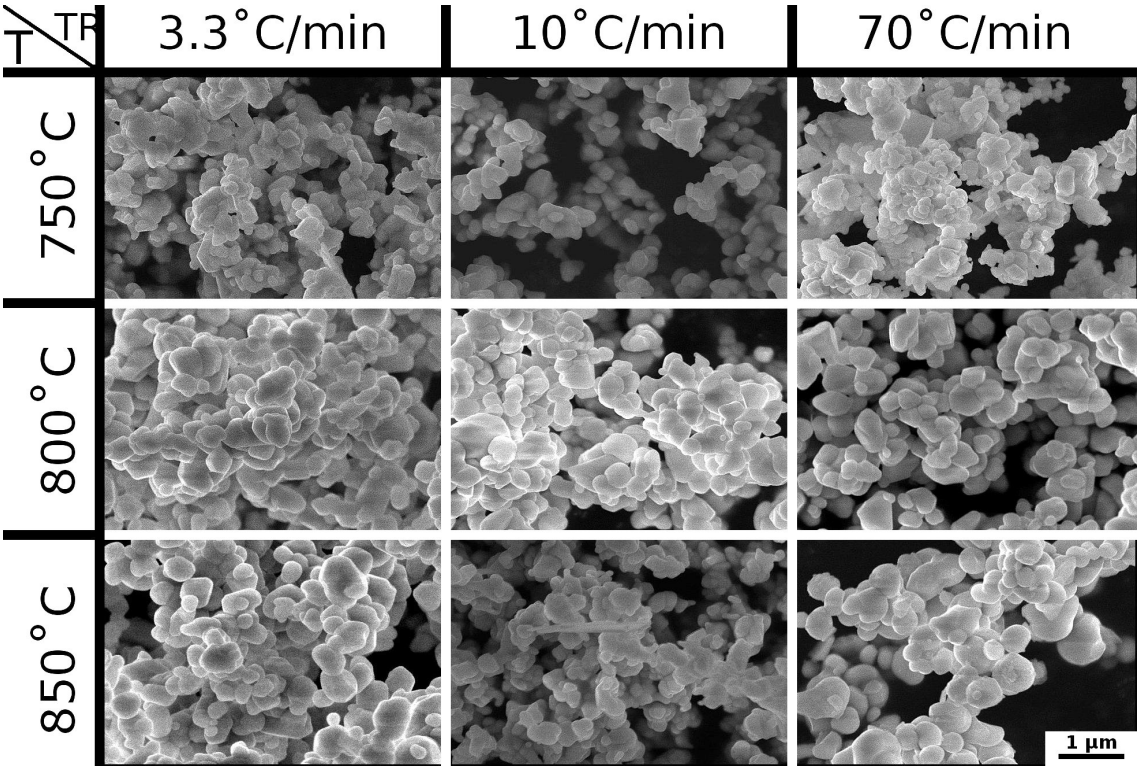

Figure 5.12: SEM micrographs of PZT powders synthesised at different temperatures and for 120 minutes, with heating ramp rates of 3.3, 10 and 70$^oC\,min^{-1}$.

were heated at 70$^oC\,min^{-1}$ to 750^oC (top right), the resultant powder had an irregular shape. Decreasing the ramp rate led to less irregular powder, but no marked difference was observable for the different heating rates used. At higher temperatures (800 and 850^oC) the particle shape was changed from irregular to more spherical even if the oxides were heated at 70$^oC\,min^{-1}$. In figure 5.13 the XRD patterns of the powders reacted for 120 minutes at 750, 800 and 850^oC and heated at different ramp rates are reported. After 2 hours of reaction PbO and ZrO_2 were still present in the final mixture of the sample heated at 70$^oC\,min^{-1}$ to 750^oC (figure 5.13 a). Residual PbO was also detected in the sample heated at 3.3$^oC\,min^{-1}$ to the same temperature. At 800 and 850^oC only PZT peaks were observed in the XRD patterns, except for the sample heated at 70$^oC\,min^{-1}$ to 800^oC, where residual PbO was still present.

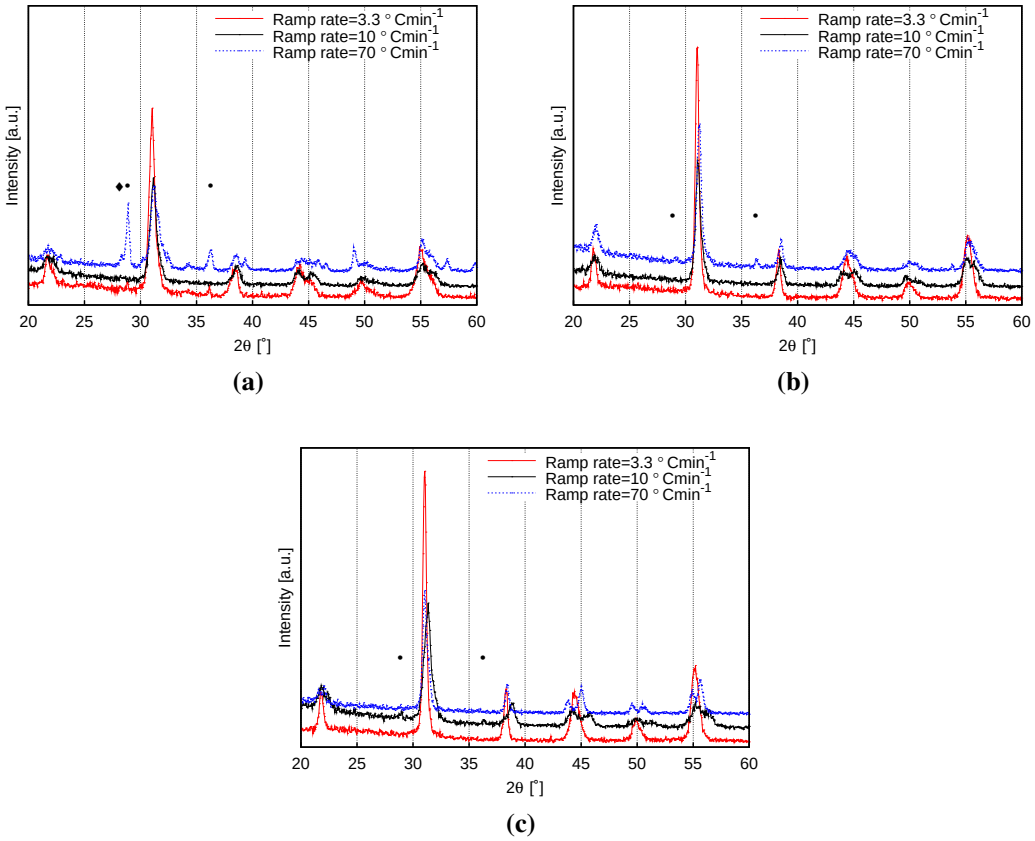

Figure 5.13: XRD patterns of PZT powders heated at 3.3, 10 and 70$^oC\ min^{-1}$ at a) 750, b) 800 and c) 850^oC for 120 minutes. Symbols • and ♦ represent PbO and ZrO_2 peaks, respectively.

5.3 Discussions

5.3.1 Effect of time, temperature and heating ramp rate

The size of particles and morphology are directly correlated. As shown in figures 5.4 and 5.6, bigger particles are also more spherical. Conversely, smaller particles are oddly shaped. Partial conversion, observed in the XRD patterns, is always associated with highly irregular particle shape.

The presence of starting materials, such as PbO and/or ZrO_2, along with PZT was detected in the samples heated at low ramp rates to 750^oC, for short periods of time. Their presence was also noted in the final mixture when the reaction temperature was quickly increased, even at 800 or 850^oC. This behaviour can be explained by considering the overall reaction time (see subsection 2.4.2.2). An increase in temperature also increases the time at which the flux is in the liquid state, meaning a longer overall reaction time. Moreover the mobility of the atomic species in the salt is higher at higher temperatures meaning that they can diffuse more rapidly through the flux and react thereby producing bigger PZT particles. Assuming that at 660^oC the eutectic mixture of NaCl and KCl is in the liquid state, a calculation of the overall reaction time for all the parameters combination can be made and it is shown in table 5.1. It can be seen that at low heating ramp rates, such as 3.3 and 5$^oC\,min^{-1}$, an increment in temperature from 750, to 800, to 850^oC led to an increment of the overall reaction time, even if the isothermal time was kept constant. This means that the powders synthesised using low temperature ramp rates had more time for diffusion to occur in the liquid medium compared to the powders synthesised at higher rates, at the same temperature and isothermal time. This explains the change in morphology for the powders synthesised at constant isothermal time but at different ramp rates. When the starting materials were heated slowly to the required temperature the resultant powder shape was more regular compared to the shape obtained when an high ramp rate was used, as shown in figures 5.8, 5.10 and 5.12.

Table 5.1: Overall reaction time calculation for the synthesis of PZT by MSS at 750, 800 and 850^oC, with heating ramp rates of 3.3, 5, 10, 20 and 70$^oC\,min^{-1}$ at different isothermal times: a) 30, b) 60 and c) 120 minutes.

(a)

30 *min*	Ramp rate ($^oC\,min^{-1}$)				
T (^oC)	3.3	5	10	20	70
750	57	48	39	35	31
800	72	58	44	37	32
850	88	68	49	40	33

(b)

60 *min*	Ramp rate ($^oC\,min^{-1}$)				
T (^oC)	3.3	5	10	20	70
750	87	78	69	65	61
800	102	88	74	67	62
850	118	98	79	70	63

(c)

120 *min*	Ramp rate ($^oC\,min^{-1}$)				
T (^oC)	3.3	5	10	20	70
750	147	138	129	125	121
800	162	148	134	127	122
850	178	158	139	130	123

The effect of temperature and time on particle size and morphology can be explained on the basis of the processes occurring during molten salt synthesis: nucleation and coarsening [122]. Nucleation represents the initial process that occurs in the formation of a solid from in a solution and consists of the generation of nuclei. The coarsening is the subsequent growth to particles. It can follow two mechanisms. In the first one the particles grow by the addition of new material from the solution. With time, the number of particles does not change but they grow in size until they reach a maximum size. At this point (corresponding to a complete conversion) particle growth stops. With increased temperature, the reagent mobility increases leading to a more frequent nucleation. Under this condition the time for coarsening is reduced (due to rapid consumption of reagents) and small particles should be obtained. If this coarsening mechanism is followed, particle size should increase with time (to a steady state size), but decrease with temperature. In the second way (Ostwald ripening) the large particles grow and the small ones dissolve [134], because the system tries to minimise the energy by reducing the interfacial area. Since larger particles have smaller interfacial area

than the same volume of particles with smaller dimension, a longer isothermal time should lead to a fewer number of particles that are larger in size. The particle growth by this mechanism is then limited by atomic diffusion in the molten flux. An increase in the reaction temperature enhances diffusion, leading to the formation of bigger particles. Therefore, if Ostwald ripening occurs, particle size should increase with both time and temperature. PZT formation is nucleation controlled, where it is more difficult to achieve nucleation than particle growth. Thus it is possible to obtain few nuclei that all grow, but it is difficult to have more small particles.

In figure 5.14 the particle size as a function of time is plotted for all the temperatures and ramp rates. In figure 5.14 a the size of the particles synthesised at 750^oC are reported. It can be seen that the data are scattered, without a clear trend. At this temperature the particles shape was irregular, especially if the starting materials were heated at high ramp rates, such as 20 or 70$^oC\,min^{-1}$. Particle dimension was measured manually from a SEM micrograph of each sample. In the case of irregular shape, the maximum length of each particle was measured because the powder have to pass through nozzles while avoiding clogging. The scatter of the data and the big values of particles size at low temperature can be attributed to this measuring process. As the temperature was increased to 800 and 850^oC (figure 5.14 b and c), the average particle dimension slightly increases with time.

The effect of temperature on the average particle size for all the ramp rates used is shown in figure 5.15. At low ramp rate (3.3 and 5$^oC\,min^{-1}$) particle size slight increases with temperature when the isothermal time was set at 30 or 120 minutes. After 60 minutes of reaction instead particle size seems to decrease with temperature. Also at high ramp rates, particle dimension slightly increases when the temperature was increased from 800 to 850^oC. The data scattering at 750^oC can be attributed to the measuring process as stated above.

As stated before, at short reaction time (30 minutes) and low temperature (750^oC) starting PbO and ZrO_2 were detected along with PZT. At slow ramp rates (3.3 and 5$^oC\,min^{-1}$), an

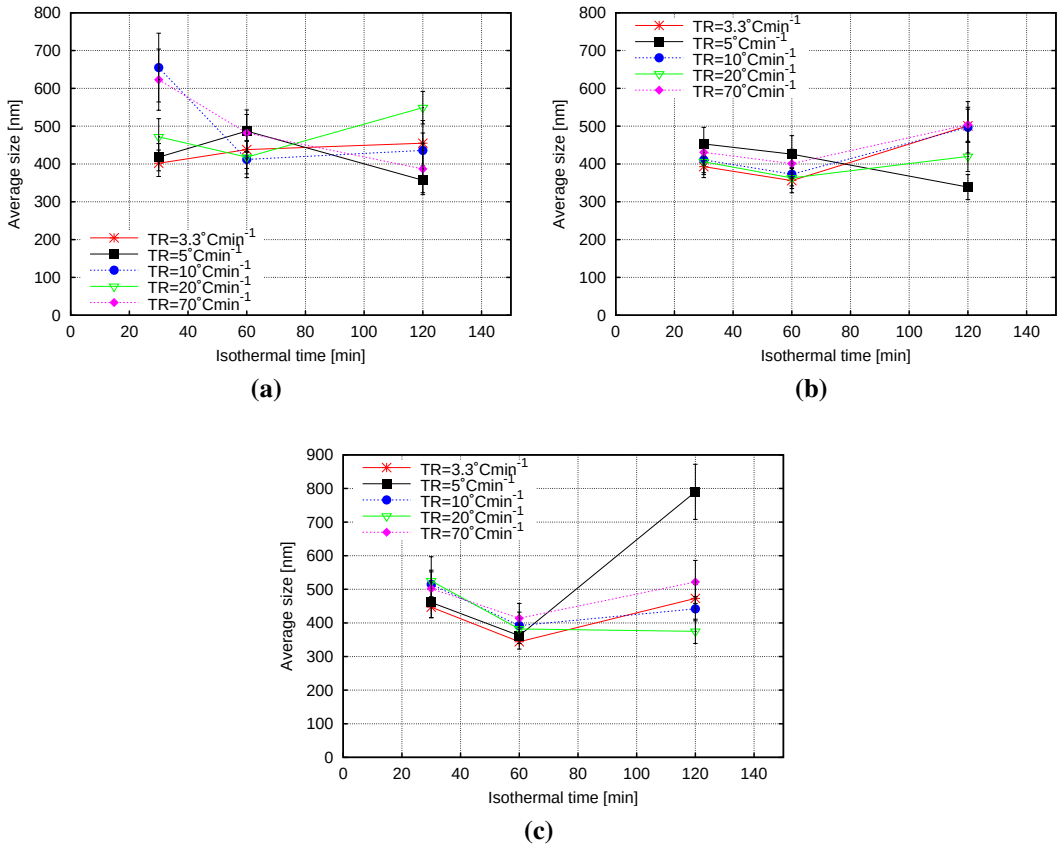

Figure 5.14: Particle size as a function of isothermal time for PZT powder synthesised at a) 750, b) 800 and c) 850^oC.

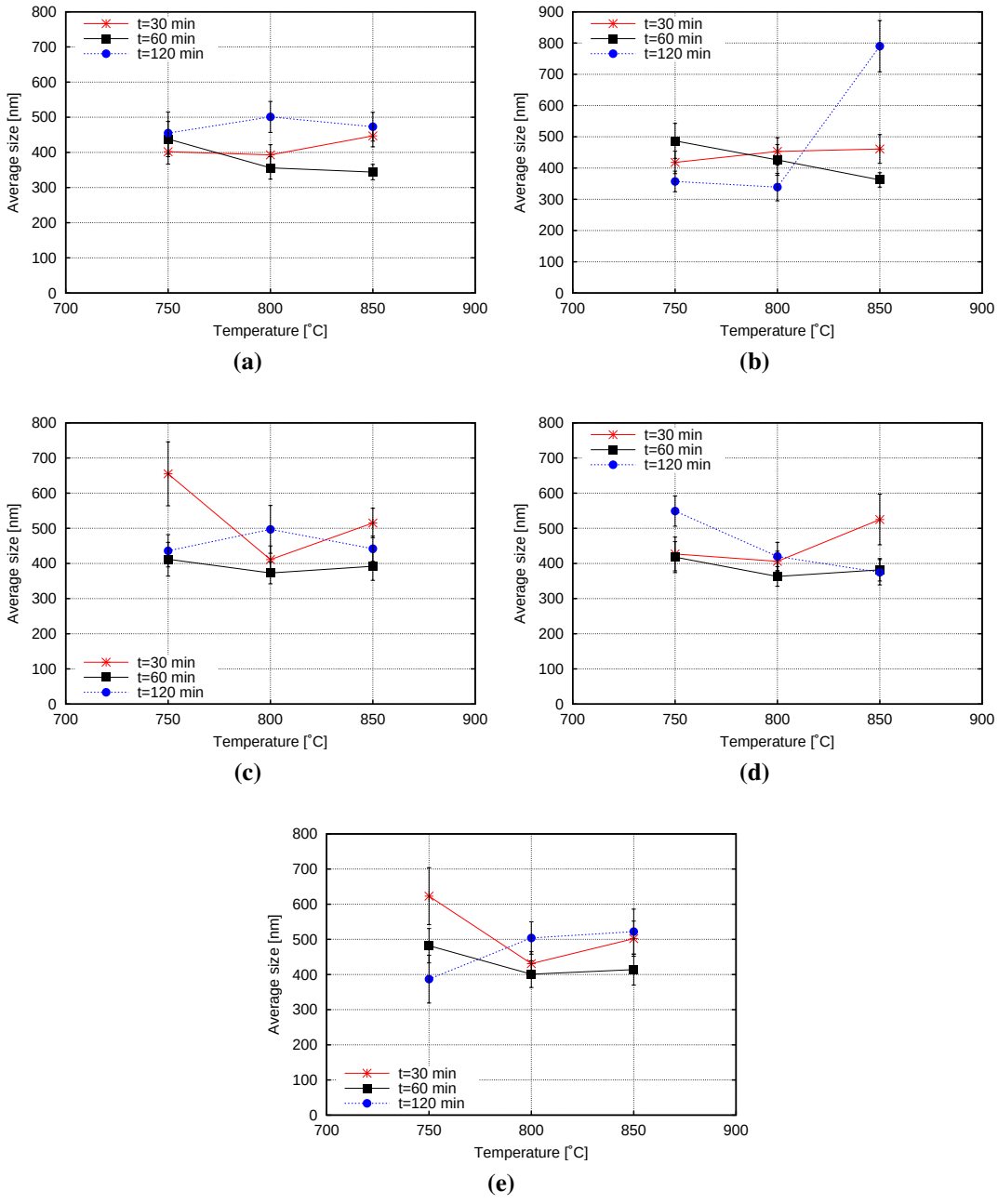

Figure 5.15: Particle size as a function of temperature for all the ramp rates: a) 3.3, b) 5, c) 10, d) 20 and e) $70^{o}C\,min^{-1}$.

increase in temperature and/or in time led to the complete conversion of the oxides into PZT. At higher heating rates PbO was still present at 800^oC after 30 minutes of reaction at rate of 10, 20 and $70^oC\,min^{-1}$. ZrO_2 was instead only detected at 750^oC when the starting materials were heated at $70^oC\,min^{-1}$ for all the isothermal times. This means that after 30 minutes the reaction was not complete, even if a slow rate was used to heat the oxides. An increase in time and/or temperature led to a complete conversion of the starting material into PZT. Therefore it is possible to suppose that after nucleation, the particles first grow by the addition of new material (first coarsening mechanism). When the time and temperature are increase, no more starting materials are available with PZT and the growth proceeds by the slower Ostwald ripening mechanism.

According to Yoon et al. [111], under the same conditions of isothermal time and reaction temperature, higher heating rates should lead to smaller particle size. PMN was synthesised at 750^oC for 10 minutes, heating the starting materials between 5 and $150^oC\,min^{-1}$. The reaction was conducted in a Li_2SO_4-Na_2SO_4 flux, in the eutectic proportion. In the present synthesis of PZT, a reduction of particle size due to an increased ramp rate was not observed. This can be attributed to the different reaction conditions. In this synthesis of PZT, the starting oxides were not heated at such fast rates. Moreover the flux utilised was NaCl-KCl. The size and morphology of the product obtained by MSS is believed to be affected by the solubility of the oxides in the flux [115, 119, 123, 130]. Since PZT was synthesised in molten chlorides and PMN in molten sulphates, it is possible that two different mechanisms occur: template formation in the case of chlorides and dissolution-precipitation mechanism in sulphates (see subsection 2.4.2.5). The difference in product formation can explain why the particle size was not reduced by increasing the ramp rate in the case of PZT synthesis. In this study, a change in the particle morphology was instead observed, from irregular at high rates, to more regular at low ramp rates as shown in figures 5.8, 5.10 and 5.12. Moreover an increment in the heating rate led to a larger particle size distribution, especially for the powders synthesised at

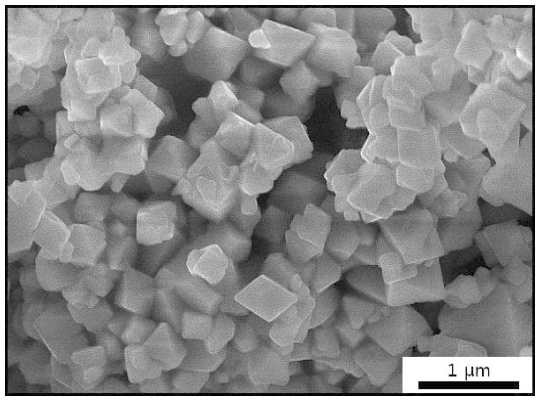

Figure 5.16: SEM micrographs of PZT powder synthesised at 750^oC for 30 minutes, with a temperature ramp rate of 5$^oC\,min^{-1}$.

750^oC, with the presence of big particles in the final PZT powder.

Spherical PZT particles were obtained by heating the starting materials at 3.3$^oC\,min^{-1}$ for 60 minutes at 850^oC. Under these conditions residual PbO or ZrO_2 were not found in the final mixture after washing with deionised water and the average size of the particles was 344$\pm$22 *nm*. The powder synthesised under these conditions was used for further experiments (see Chapter 6).

When the starting materials where heated at 5$^oC\,min^{-1}$ to 750^oC for 30 minutes, the resulting particle morphology was cubic-like, as shown in figure 5.16. By increasing the time and/or temperature, the shape became irregular and eventually spherical.

5.3.2 Possible formation mechanism of PZT by MSS

The mechanisms for the formation of PZT by MSS have not been reported in literature. Reports on the formation of PZT during mixed oxide solid state reaction [135, 136] propose that PbO diffuses into and reacts *in situ* with TiO_2 particles forming $PbTiO_3$ shell around a TiO_2 core. PT then reacts further with PbO and ZrO_2 to form PZT. In the case of MSS of zinc aluminate it was noticed that the reaction steps were the diffusion of the dissolved ZnO on the Al_2O_3 particle surface, the diffusion of the dissolved ZnO to the unreacted core of alumina

with the formation of an $ZnAl_2O_4$ shell and then the reaction between the two oxides [115]. Since in molten salts the diffusion of the ZnO is really quick, it was assumed that the rate controlling step was the diffusion of Zn ions through the $ZnAl_2O_4$ shell.

In MSS the solubility of the oxides in the molten salt plays an important role in the product formation. According to Yoon et al. [111] PbO solubility in chloride salts is higher than that of ZrO_2. Since TiO_2 is not soluble in molten alkali chlorides [119], the final PZT morphology should be similar to the morphology of TiO_2 (template formation mechanism, see subsection 2.4.2.5), or possibly ZrO_2 where its dissolution is incomplete.

In the case of MSS of PZT, Pb is a very mobile species so the formation of PT should be quick. To produce PZT, Zr then has to diffuse into and react with the PT. It is reasonable to suppose that in the case of PZT the rate-controlling stage is therefore the diffusion of the remnant ions (Zr) through the PT shell as with Zn in the case of $ZnAl_2O_4$ synthesis. This reaction system and the template formation mechanism can be used to explain the observed formation of PZT particles in molten salt synthesis. In the early stage of the process residual PbO and ZrO_2, and the intermediate PT should be all detected along side PZT. In the samples synthesised at low temperature, low isothermal time and fast ramp rate, such as 20 and $70^oC\,min^{-1}$, the presence of these oxides was detected (figures 5.1 d and 5.9 a). As the reaction proceeds the TiO_2 should be completely consumed to produce PT, leaving only residual PbO and ZrO_2. When the samples were heated at 750^oC for 30 minutes, residual PbO and ZrO_2 were detected. If fast ramp rates, such as 20 or $70^oC\,min^{-1}$, were used to heat the samples, peaks of PT were also observed in the XRD patterns (see figures 5.1 d and 5.9 a). As the time was increased to 60 minutes (at the same temperature) PbO was detected in all the samples, but ZrO_2 only in the samples heated at 20 and $70^oC\,min^{-1}$. A further increase in the isothermal time led the reaction to proceed and PbO was detected only in the sample heated at $70^oC\,min^{-1}$. However residual PbO was found in the sample heated at $3.3^oC\,min^{-1}$ at the same time and temperature, meaning an incomplete reaction. When the

reaction temperature was increased to 800^oC no more ZrO_2 peaks were observed in the XRD patterns. This means that a reaction had occurred. PbO was still present in the samples heated at 10, 20 and 70$^oC\,min^{-1}$ to 800^oC for 30 minutes or for 120 minutes (only at 70$^oC\,min^{-1}$). PbO was detected again after 30 minutes of reaction at 850^oC in the cases where 5, 10, 20 or 70$^oC\,min^{-1}$ were used as heating ramps. At higher isothermal times PbO was no more found in the final mixture.

The observations indicate that all the TiO_2 has reacted with PbO to form PT (Stage 1) yet residual ZrO_2 and PbO are still present (Stage 2) due to the lower diffusivity of Zr species.

Stage 1 $PbO_{(MSS)} + TiO_{2(S)} \rightarrow PbTiO_{3(S)}$

Stage 2 $PbO_{(MSS)} + ZrO_{2(MSS)} + PbTiO_3 \rightarrow PZT_{(S)}$

The reaction process can be schematically represented by figure 5.17. After mixing, the oxides and the salts are in the solid phase and no reaction occurs (figure 5.17 a). By increasing the temperature above the salt eutectic mixture melting point (657^oC), the salts are in a liquid state. PbO is dissolved in the salts, ZrO_2 is partially dissolved and TiO_2 is not dissolved because of its non-solubility in alkali chlorides. PbO then diffuses to the TiO_2 particles and there reacts *in situ* forming a PT shell (figure 5.17 c). Not all the PbO has reacted, and it is still present dissolved in the mixture along with ZrO_2. By increasing time and/or temperature, Zr ions in the vicinity of the TiO_2/PT particles, diffuse through the PT shell and there react with TiO_2 core and with the addition of further PbO, the reaction proceeds to the formation of PZT (figure 5.17 d and e).

The growth mechanism of PZT can explain the formation of cubic particles at 750^oC, low isothermal time (ramp rate of 5$^oC\,min^{-1}$, figure 5.16). The TiO_2 starting particles are small and mostly consist of single crystallites. In the early stage of growth, incoming material is likely to deposit and react on preferential grow planes, leading to the cuboid shape. As the particles continue to grow, other forces, such as surface energy, will favour the formation of more equiaxed particles.

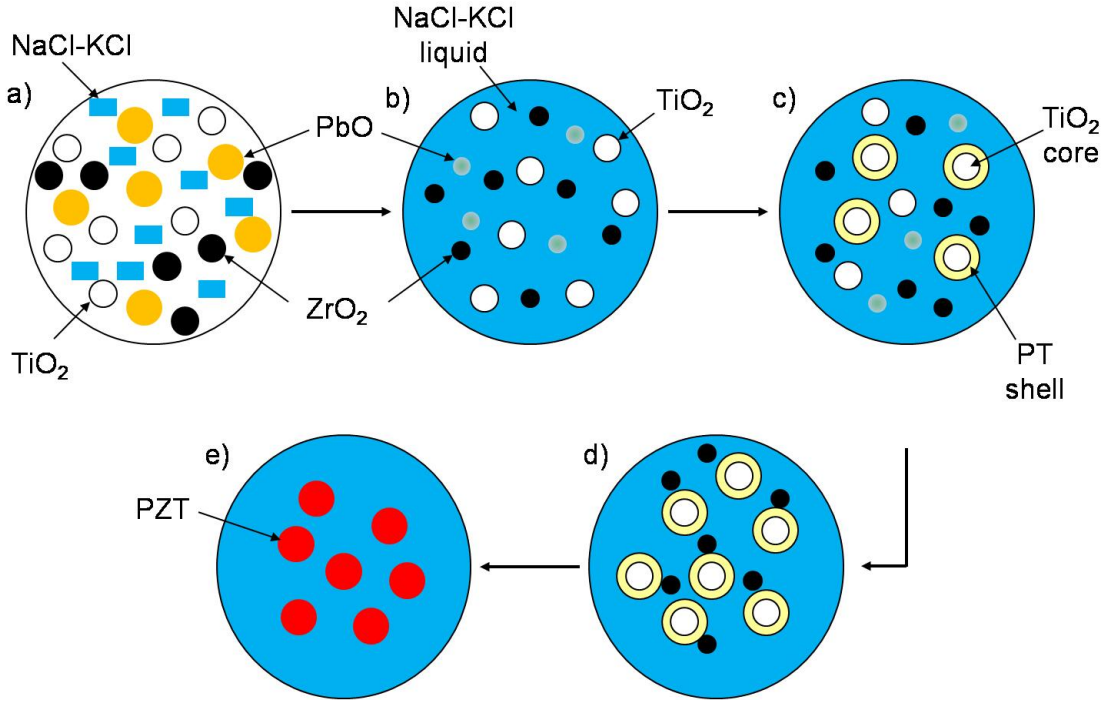

Figure 5.17: Schematic representation of the synthesis of PZT in molten salt: a) PbO, ZrO_2, TiO_2 and solid NaCl-KCl, b) liquid NaCl-KCl, partial dissolution of ZrO_2, c) PT shell formation, d) diffusion of Zr and e) PZT formation.

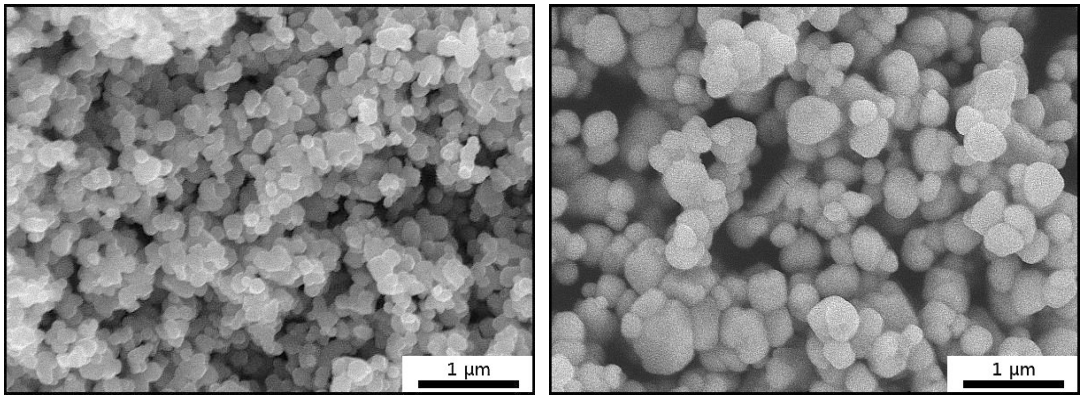

(a) **(b)**

Figure 5.18: SEM micrographs of the starting TiO_2 (a) and PZT powder synthesised at 850^oC for 60 minutes, with a heating ramp rate of 3.3$^oC\,min^{-1}$ (b).

As stated before, if the reaction proceeds by a template formation mechanism, the final PZT powder should be similar in shape to the starting TiO_2 (insoluble in molten chlorides). In figure 5.18 the starting TiO_2 and the final spherical PZT powder obtained by heating the starting oxides and the salt at 3.3$^oC\,min^{-1}$ at 850^oC for 60 minutes are compared. It can be seen that the morphology of the synthesised PZT is similar to that of the TiO_2, with the particles being larger than the original TiO_2. The different size of the particles can be interpreted as a consequence of the addition of ZrO_2 and PbO to form PZT (particle growth). In order to identify if the grains coarse by Oswald ripening, a rough size calculation can be made. In the absence of coarsening, and assuming that the PZT particles will only be larger than the TiO_2 ones due to the addition of Zr and Pb to the initial 160 *nm* TiO_2 particles, the PZT particles should be about 260 *nm* in diameter. Since all the synthesised PZT particles were larger than 260 *nm*, it is possible to assume that coarsening has occurred most importantly by Oswald ripening of particles in close proximity. Figure 5.18 b shows evidence of particles that appear to have fused together during processing.

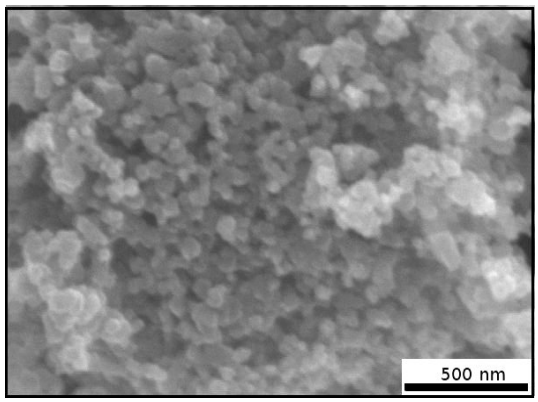

Figure 5.19: SEM micrographs of the synthesised nano-TiO_2. The powder was sintered at 450^oC for 60 minutes, with a temperature ramp rate of $10^oC\,min^{-1}$. Average particle size of 65 ± 4 *nm*.

5.3.3 Particle size reduction

Since the assumptions are that PZT grows from TiO_2 that is not dissolved in the molten salt and the rate limiting step is the diffusion of Zr through PT, several aspects can be considered in order to achieve small PZT particles. Principally the PZT formation mechanism needs to be enhanced relative to the coarsening mechanism. This can be achieved by reducing the diffusion distance. To do so a thinner PT layer and small TiO_2 particles (as they do not dissolve in the molten salt) are needed. Nano-TiO_2 was prepared as described by Chen et al. [137] and its SEM micrograph is shown in figure 5.19. After synthesis the powder was sintered at 450^oC for 60 minutes, with a temperature ramp rate of $10^oC\,min^{-1}$ and the average particle size was 65 ± 4 *nm*. The nano-TiO_2 was used as starting oxide for the molten salt synthesis of PZT, along with ZrO_2 and PbO. The powder was synthesised at 850^oC for 60 minutes with an heating ramp rate of $3.3^oC\,min^{-1}$ and it is shown in figure 5.20 a. The XRD pattern of the same powder is also reported (figure 5.20 b). The resultant PZT powder was not reduced in size as predicted; the average particle size was 412 ± 29 *nm*. No difference in the final PZT powder size was noted. It was instead observed that individual particles were fused together. This indicates that while small particles were produced, the enhanced sintering driving force of the small PZT/nano-TiO_2 also led to enhanced agglomeration and

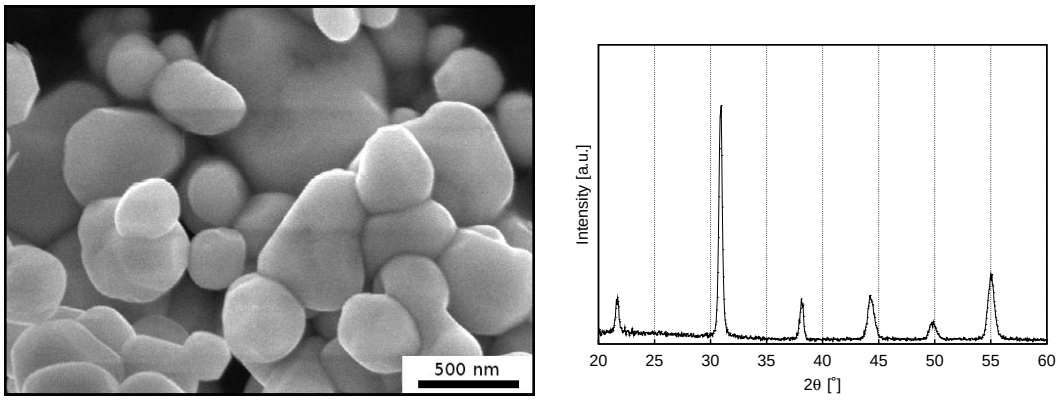

(a) **(b)**

Figure 5.20: SEM micrographs of the PZT powder synthesised starting from nano-TiO_2 (a) and relative XRD pattern (b).

coarsening.

5.4 Powder properties

In order to determine the properties of the synthesised powder PZT films were prepared. An ink with a high solid loading (16 *vol%*) was deposited on platinised silicon wafers by spin coating. The dispersant amount was set at 1.5 *wt%* and the ink was dispersed by the use of the ultrasonic horn. Five different samples were prepared by depositing 1, 2, 3 or 4 layers of PZT ink and 1, 2, 3 or 4 sol infiltrations, as shown in table 5.2. A sample consisting in a single PZT layer was also prepared as reference.

Table 5.2: Composition of the 5 samples prepared by spin coating.

Sample	Ink layers	Sol infiltrations per layer	Mean thickness (μm)
A	1	0	4.5
B	1	1	4.7
C	2	1	7
D	3	1	11
E	4	1	21.8

After sintering at 720^oC for 20 minutes and poling, properties, such as d_{33}, electrical

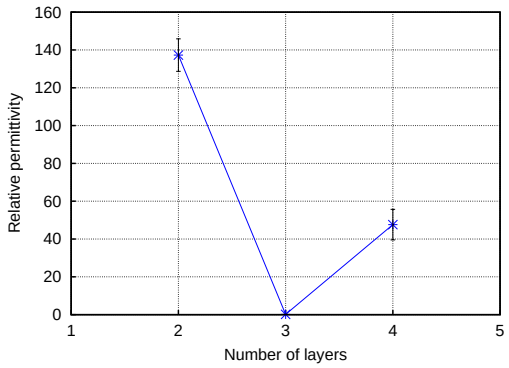

Figure 5.21: Variation of the relative permittivity (at 1 *kHz*) with the number of layers.

permittivity, dielectric losses and ferroelectric hysteresis were measured and the results are reported as follows. For the samples A and B it was not possible to measure such properties due to the presence of through thickness cracks in the films. In this condition top and bottom electrodes were connected and it was not possible to pole the samples and therefore to analyse them.

5.4.1 Dielectric constant

Figures 5.21 and 5.22 represent the variation of relative permittivity and the dielectric loss with the number of sol infiltration. It can be seen that increasing the number of layers from 2 to 3 led to a decrease in the relative permittivity. The value then raised again for the sample E (4 PZT layers and 4 sol infiltrations). This behaviour was not expected. In this study the number of infiltration for each PZT layer was constant to 1. In the work presented by Dorey et al. [48], the infiltration steps for each PZT layer (4 in total) were increased from 0 to 4. Sample E corresponds to the sample 4(c+1s), that represents the sample composed of 4 PZT layers, each of them infiltrated one time. For this sample the authors report a value of relative permittivity of $\sim$350, that is much higher than the value of sample E ($\sim$50). This difference can be attributed to different PZT sol and the presence of dopants. Dielectric loss instead decreases with increasing the number of layers.

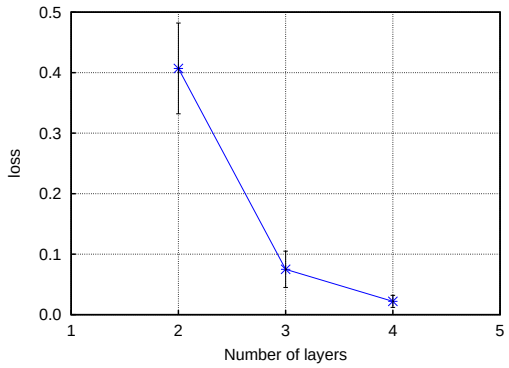

Figure 5.22: Variation of the dielectric loss (at 1 *kHz*) with the number of layers.

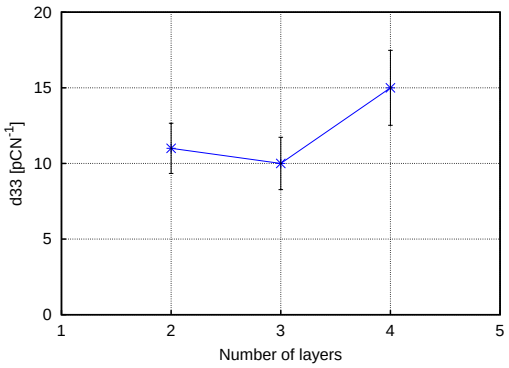

Figure 5.23: Variation of the piezoelectric strain coefficient (d_{33}) with the number of layers.

5.4.2 Piezo and ferroelectric properties

Figure 5.23 shows the variation of the piezoelectric strain coefficient with the number of layers. It can be seen that after a slight decrease, the value of d_{33} increases to 15 $pC \cdot N^{-1}$. In this work no dopants were used in the powder formulation. Since the value of d_{33} is strongly affected by the presence of dopants and their amount [48], it is not possible to compare the the results obtained with the literature. However it seems that the piezoelectric coefficient increases by increasing the number of layers.

An example of the P-E loop is reported in figure 5.24. It represents the changing in the hysteresis loops for the sample D with increasing the voltage applied for each μm of thickness. The remnant polarisation (P_r) obtained after the application of 25 $kV \cdot \mu m^{-1}$ was 2.2 $\mu C \cdot cm^2$. A further increase in the applied voltage was not possible due to instrument

limitation. For sample C the mean P_r was found to be 5.7 (at 30 $kV \cdot \mu m^{-1}$) and for sample E 1.1 $\mu C \cdot cm^2$ (at 15 $kV \cdot \mu m^{-1}$).

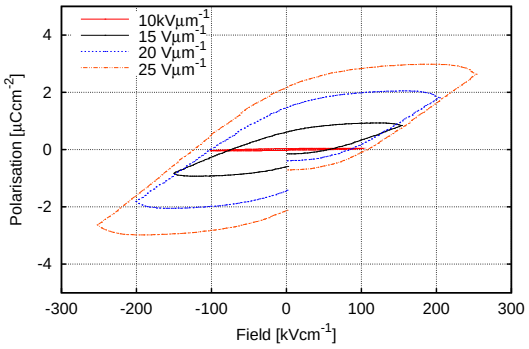

Figure 5.24: Ferroelectric hysteresis loop of sample D.

5.5 Summary

In this chapter the synthesis of PZT powder by molten salt process has been investigated as a means to obtain small and equiaxed particles for use in ink jet printing. The influence of parameters, such as reaction time, temperature and heating ramp rate, on particle composition, size and shape has been studied.

At shorter times (30 minutes) the reaction between the starting materials was not complete. Residual PbO and ZrO_2 and PT were found in the final mixture. The particles obtained at 750^oC and at fast heating rates were less spherical than the same powder treated at higher temperature for the same isothermal time. At high temperatures and long reaction times an excessive particle growth was observed. The smallest particles were obtained by heating the raw materials at 3.3$^oC\,min^{-1}$ up to 850^oC for 60 minutes. A molten salt mechanism for the formation of PZT is proposed whereby molten Pb initially reacts with the insoluble TiO_2 particles to form $PbTiO_3$. Subsequently ZrO_2 diffuses into and reacts with $PbTiO_3$ and the remaining Pb to form PZT. The diffusion of Zr through the PT layer is the rate limiting stage. At the same time as the Zr diffusion, particle coarsening occurs revealing a challenge

to create small particles where two low solubility phases are present.

Chapter 6

PZT ink development and printing

6.1 Introduction

In order to obtain a composite film after printing, PZT inks consisted of PZT powder dispersed in PZT sol were used. Their formulation will be discussed here. The powder used was prepared by both EHDA and molten salt synthesis (chapters 4 and 5).

Inks with different solid loadings were used to print a pattern consisting of 20x20 drops, in order to identify the best combination of printing parameters. A pattern composed of horizontal and vertical lines was also printed on platinised silicon wafers. It was designed to identify the conditions at which the printing quality was enhanced.

6.2 PZT ink formulation

Two different ways were adopted to mix the ink components: ball milling for 24 hours in a glass bottle, and ultrasonication. In the ball mill the powder agglomerates are broken by the constant falling of the balls in the suspension. The ultrasonic horn instead produces high pressured bubbles. Their collapse results in particle size reduction and disaggregation. In

figure 6.1 the effect of 2 minutes of sonication at 60% of amplitude on particle size (MSS powder) is shown. A 100% of amplitude corresponds to the maximum ultrasonic vibrations at the probe tip. The average size of the powder evaluated by image analysis was $\sim$300 *nm*, that corresponds to the first peak maximum. This means that the powder was aggregated after synthesis. The particle size distribution curves reveal that a reduction in the size has been achieved by the use of ultrasound. Before the treatment (figure 6.1 a) a trimodal distribution existed, with particles as big as 9 μm. After the treatment (figure 6.1 b) the distribution is still trimodal, but it is smoother and the maximum size has been reduced to 5 μm. However big particles or agglomerates still exist in the suspension. The particle size and their distribution was not determined for the inks subjected to ball milling due to the non availability of such instrumentation at that time.

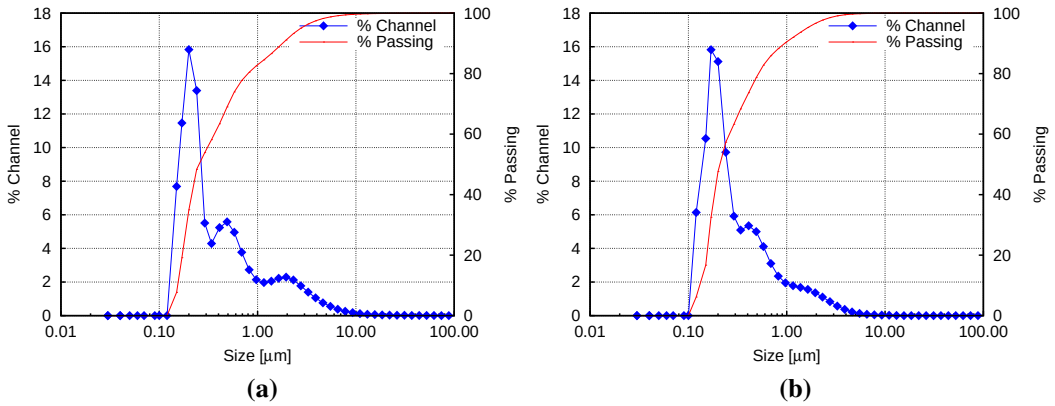

Figure 6.1: Particle size distribution of a 1 vol% PZT suspension in 1-propanol before (a) and after 2 minutes of sonication at 60% of amplitude. The PZT powder was synthesised by MSS.

PZT inks were formulated using powders synthesised by both EHDA and MSS. However, due to the small amount of powder synthesised by electrospray, it was not possible to ball mill or sonicate the suspension. Magnetic stirring was instead applied for 24 hours.

An ink suitable for ink jet printing needs viscosity and surface tension values in determined ranges. For this reason the viscosities of the inks were adjusted by the addition of ethylene glycol (EG). Since the value of viscosity of a solution is principally due to the solvent

Table 6.1: Viscosity values for different combinations of PZT sol and ethylene glycol.

PZT sol (*vol%*)	EG (*vol%*)	Viscosity (*mPa s*)
100	0	5.4
80	20	8.6
65	35	11.3
0	100	17.7

viscosity, PZT sol and ethylene glycol were mixed together in order to reach a viscosity close to 10-12 *mPa s*, as shown in table 6.1. For the inks prepared by ball milling a 80-20 *vol%* mixture of sol and ethylene glycol was used as the liquid media. In the case of ultrasonic treatment the EG amount was increased to 35 *vol%* due to the low values of viscosity reached with the previous mixture. A 5 *vol%* of PZT powder was added to the sol-EG mixture. Dispersant (KR-55) was also combined with the other components (for the dispersant amount determination see subsection 6.2.1).

6.2.1 Dispersant amount optimisation

The optimum amount of dispersant is the quantity needed to obtain a stable suspension where the particles are not aggregated and do not sediment. A right amount of dispersant should cover every particle suspended in the solvent by forming a shell around them. This quantity is related to the size and the surface area of the particle to be covered: smaller particle size means higher surface area and hence higher amount of dispersant.

As the dispersant amount is a function of the particle dimension, it has been determined for inks prepared by both ball milling and ultrasound treatment.

The common method used to determine the optimum amount of dispersant for a suspension is by viscosity measurements. Plotting the viscosity against the quantity of dispersant added to the suspension results in a curve, where the minimum corresponds to the optimum amount of dispersant. In this condition the particles are covered with a layer of dispersant, and therefore stabilised in the liquid media. In figure 6.2, the viscosity is plotted against the

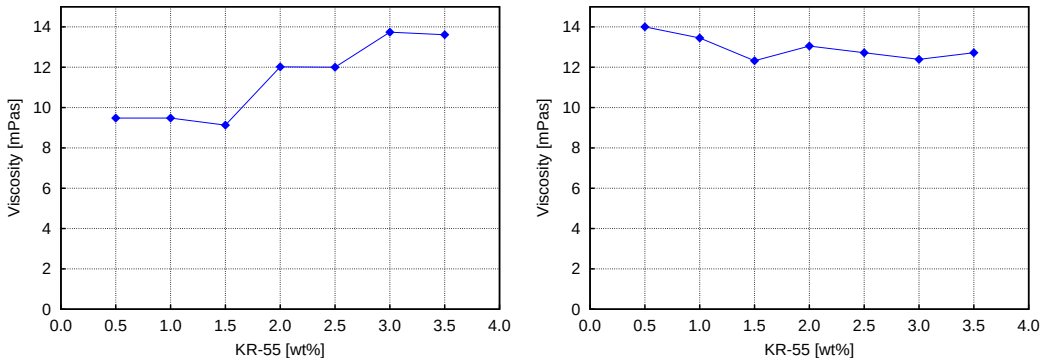

Figure 6.2: Viscosity as a function of KR-55 content in PZT inks prepared by ball milling (a) and ultrasound treatment (b).

amount of KR-55 added to the suspensions for ball milled (a) and ultrasound treated inks (b). It can be seen that for the ball milled inks the viscosity slightly decreased under the addition of KR-55 up to 1.5 *wt%*, and then it increased to higher values. In the case of ultrasonic dispersion the viscosity decreased with the addition of dispersant from 0.5 to 1.5 *wt%* and then the values remained almost constant. In both cases a change in the viscosity appeared with the addition of 1.5 *wt%* of dispersant. This was set as the optimum dispersant amount (KR-55). The difference in the range of viscosity between the two systems is due to the use of different sol-EG mixtures: volume ratio 80/20 for the ball milling system and 65/35 for the ultrasonic system.

It was not possible to determine the amount of dispersant required for inks containing powder synthesised by EHDA due to the low amount of powder produced. When powder synthesised by MSS was used to formulate the ink, 1.5 wt% of KR-55 was used. PZT powder synthesised by EHDA was smaller in size than that prepared by MSS and it was almost perfectly spherical. This means that for the same amount of powder, the surface area produced by the EHDA particles was bigger than the one produced by larger particles. For this reasons a higher amount of dispersant (3.5 *wt%*) was added to the formulation of PZT inks containing powder synthesises by EHDA.

6.2.2 Surface tension determination

The surface tension is another important parameter for an ink suitable for ink jet printing and it should be in the range 28-33 $mN\,m^{-1}$. It was measured by weighting an equal number of water and ink droplets at constant temperature. Knowing the surface tension of deionised water at the operating temperature, it was possible to calculate the sample surface tension by equation 3.1. In table 6.2, the ink compositions and the values of surface tension are reported beside their viscosity. From table 6.2 it can be seen that for the EHDA ink, the values of surface tension and viscosity were not in the right ranges. This was due to the impossibility of determining the best composition due to the small amount of synthesised powder. Surface tension and viscosity of ethylene glycol were 47.7 $mN\,m$ and 16.1 *mPa s*, respectively. The discrepancy between surface tension and viscosity values of the MSS BM-ink and the MSS US-ink is due to different amount of ethylene glycol in the composition, which is higher in the MSS US-ink.

Table 6.2: Compositions and values of surface tension and viscosity for the inks formulated with powder prepared by EHDA and MSS.

Ink	Powder *vol%*	Sol/EG vol%	KR-55 wt%	Surface tension $mN\,m^{-1}$	Viscosity $mPa\,s$
EHDA	5	80/20	3.5	20.9	20.8
MSS ball mill	5	80/20	1.5	24.2	10.9
MSS ultrasound	5	65/35	1.5	28.8	12.3

6.2.3 PZT inks with different solid loading

A high solid loading can compromise the printing process by speeding up the nozzle clogging. In order to determine if the amount of PZT powder has an effect on printing, PZT inks with different solid loadings were prepared. A 65/35 *vol%* mixture of PZT sol and ethylene glycol was used as the liquid media. Quantities, corresponding to 0, 1, 2, 3 and 4 *vol%,* of PZT

powder were added to the mixture along with 1.5 *wt%* (with respect to the powder amount) of dispersant. The 0 *vol%* powder sample corresponds to the pure PZT sol-EG mixture. The inks were dispersed by ultrasonic treatment. Their properties of viscosity, surface tension and density are shown in table 6.3. Values for the 65/35 PZT sol-ethylene glycol mixture and PZT ink with 5 *vol%* of powder loading (MSS US) are also reported.

Table 6.3: Properties of the PZT inks formulated with different solid loadings. Sol/EG corresponds to the 65/35 vol% mixture of sol and ethylene glycol, and MSS US represents the ink with a 5 *vol%* of solid loading.

Ink	Solid loading *vol%*	Viscosity $mPa\,s$	Surface tension $mN\,m$	Density $Kg\,m$	Z
MS1	1	10.9	25.3	1137	2.3
MS2	2	11.5	22.9	1181	2.3
MS3	3	12.2	28.3	1244	2.1
MS4	4	12.1	29.2	1273	2.3
MSS US	5	12.3	28.8	1370	2.3
Sol/EG	0	11.3	27.4	1102	2.4

6.3 Printing of PZT inks

6.3.1 Z calculation

In drop on demand ink jet printing, an ink droplet can be ejected if its "jettability" parameter Z is in the range 1-10 [61, 69]. Z is calculated as described in equation 2.3. At low Z (< 1), the viscous forces dominate and a high pressure is required to eject a droplet. At high Z (> 10) the formation of satellite drops is possible.

From the data in table 6.3 the dimensionless parameter Z was calculated according to equation 2.3 and the values are reported in the same table. It can be seen that the values are in the range 1-10 for all the inks, meaning that droplets can be potentially ejected by the printer. However for some compositions, such as MS1, MS2 and the sol/EG mixture, the values of

surface tension were outside the range 28-33 $mN\,m^{-1}$.

6.3.2 IJP parameters

The printing parameters of the Dimatix DMP-2831 printed (Fujifilm) used for this project were set in determined ranges in order to identify their influence on printing and they will be described in this subsection.

The drop spacing (DS) corresponds to the distance between the centres of two adjacent drops. It was kept constant at 25 μm while the other parameters were changed.

The firing voltage was varied from 15 to 30 *V* and it represents the voltage at which the nozzles eject the droplets. It is related to how much the piezoelectric crystal moves in the fluid chamber in the cartridge (figure 2.10 c). Higher voltages correspond to bigger movement and therefore higher pressures and the ejection of bigger droplets.

In order to reduce the formation of dried ink at the outlet of the nozzles, the tickle control was used. It enables low amplitude pulses to be applied to the nozzles that move the meniscus slightly without droplet ejection. It was set at 23 *kHz*. The nozzles were also kept clean by running a cleaning cycle every 10 passages of the cartridge across the substrate. It was composed of Spit Purge Spit Purge Bolt steps. Spit corresponds to the nozzles firing. In the Purge step the fluid is pushed out of the nozzles with pressure, and in the Blot step, the cartridge touches the cleaning pad to clean the outlet of the nozzles.

The distance between the cartridge and the substrate, namely cartridge print height (CPH), was varied in the range 0.30-0.50 *mm*. A smaller CPH should help to improve the printing quality, by a more precise droplet deposition. As explained by Song and Nur [62], a higher CPH can result in a mismatch in the droplet deposition (see equation 2.6).

The patterns were printed with different number of nozzles: 16, 4 and 1. To verify their functioning, a camera (drop watcher) was used. It consists of a camera that allows the jetting nozzles to be viewed. One or more nozzles can be selected and the printing parameters can

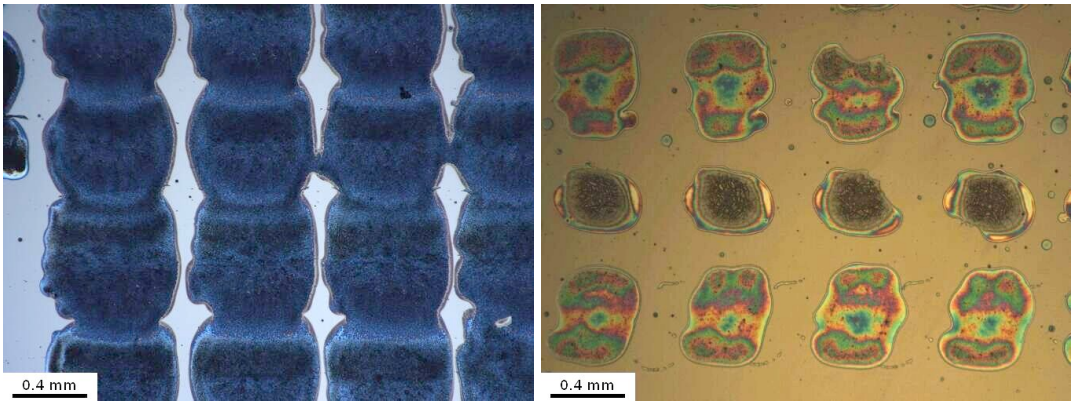

(a) **(b)**

Figure 6.3: Test pattern composed of 10x10 pixels squares printed on platinised silicon wafer with a) MSS BM-ink and b) EHDA-ink. Drop spacing 25 μm, voltage 25 *V* and cartridge printer height 0.35 *mm*.

be changed in order to create the desired printing condition.

6.3.3 Test printing

Initially, MSS BM-ink and EHDA-ink were tested to verify if printing was possible. A test pattern composed of 10x10 pixel squares was printed onto platinised silicon wafer. In figure 6.3 the test patterns printed with MSS BM-ink and EHDA-ink are reported. The distance between the cartridge and the substrate was set at 0.35 *mm*, the drop spacing was fixed at 25 μm and the droplets were ejected at 25 *V*. It can be noted that the behaviour of the inks on the substrate were not similar. In the pattern printed with the MSS BM-ink (figure 6.3 a) the squares touched each other. When the same pattern was printed with the EHDA-ink (figure 6.3 b), single squares were obtained, but their shape was not always the same. This phenomenon was cause by the nozzle blockage. In fact it was not possible to print a great number of patterns with the EHDA-ink because of nozzle clogging. The droplet ejection was checked with the drop watcher camera and none of the 16 nozzles was found to be able to print afterwards. To verify the cause of the clogging, the cartridge print head was analysed by

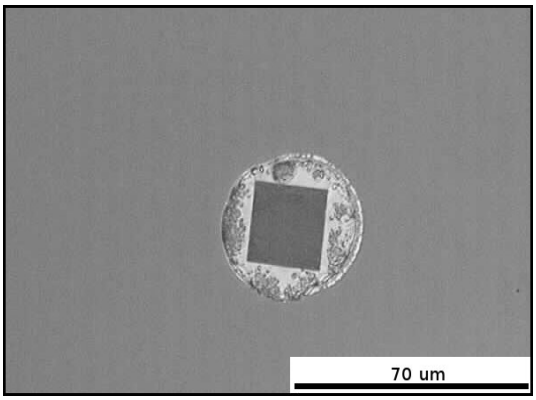

Figure 6.4: Optical micrograph of the external face of a clogged print head nozzle.

optical microscope. A nozzle is shown in figure 6.4. The square in the figure represents the nozzle exit. The circular feature surrounding the nozzle is the ink that has dried after printing. It can be seen that the nozzle orifice is clear. This means that the nozzle has not been blocked on the outside by ink drying in the nozzle exit, but from the inside (reservoir end) by particle sedimentation.

The fact that, with the EHDA-ink, it was not possible to print a great number of patterns and the result of the microscope analysis led to the conclusion that PZT particles in this ink were settling faster than in the MSS MS-ink. The cause of this behaviour was the incorrect ink formulation and agglomerates. In a stable suspension, the particles are suspended in the media without the formation of aggregates or sedimentation. The role of dispersant is to maintain the particles suspended in the solvent creating a layer around them, and hence avoiding their aggregation. In the case of EHDA-ink, the optimum amount of dispersant was not determined due to the small amount of powder available. The KR-55 quantity added to the formulation may have therefore been erroneous: the PZT particles were not all covered or homogeneously covered by the dispersant. This led to particles aggregation that resulted in their sedimentation and hence in nozzle clogging. In addition, the use of magnetic stirring, instead of ultrasound milling or ball milling, may not have been sufficient to break up agglomerates. So, even if the particles synthesised by EHDA were spherical and small in size, the

ink was not formulated correctly or not deagglomerated, that resulted in a non-printability of the ink.

With the MSS BM-ink it was possible to print a greater number of patterns, but the printed squares were not separated from each other due to the spreading of the ink on the substrate. Moreover, nozzle clogging occurred also with this ink. In order to obtain resolved features by IJP, the right printing conditions have to be identify for each ink. This means that for the MSS BM-ink, a drop spacing of 25μm, firing voltage of 25 *V* and a cartridge printer height of 0.35 *mm* was not the best parameters combination.

From the results of this test it was decided to determine the ink behaviour on the substrate surface to improve the quality of the printed area. To do so, a new pattern composed of 20x20 individual drops was printed under different printing conditions with inks with different powder content. The influence of the solid loading on printing will help to identify under which conditions nozzle clogging occurs. The results obtained are shown in section 6.4.

6.4 Relic deposition

A pattern consisting of 20x20 individual droplets was printed with different inks, including the PZT sol-ethylene glycol mixture. The pattern is shown in figure 3.6 a. The printer drop spacing was set at 25 μm, but the droplets in the pattern were positioned 50 μm (2·DS) apart in order to avoid or reduce coalescence between adjacent droplets and be able to determine their diameter. Parameters, such as firing voltage, cartridge print height and number of nozzles, have been changed during printing and their effects on the droplet size will be discussed in the next subsections. The firing nozzles were chosen by the use of the drop watcher function.

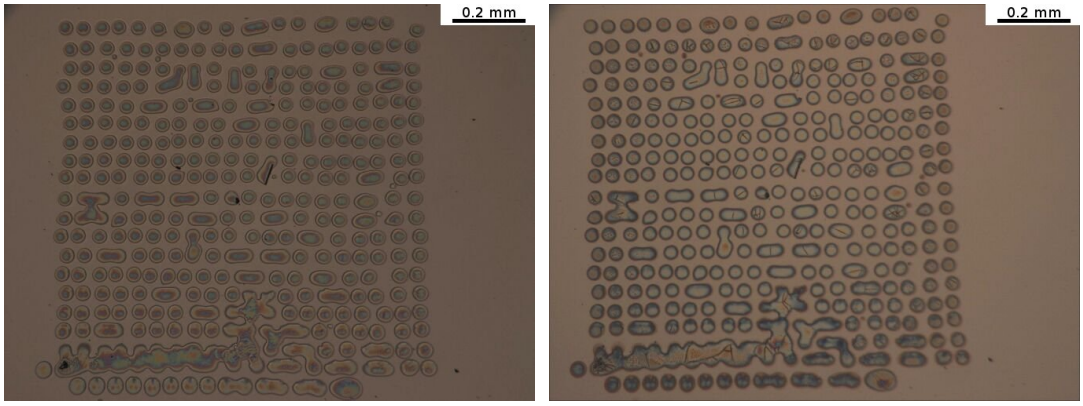

(a) **(b)**

Figure 6.5: Optical micrographs of the 20x20 dots pattern printed with Sol-EG mixture under the following conditions: voltage 15 *V*, CPH 0.30 *mm*, 1 nozzle. a) before sintering and b) after sintering at 720^oC for 20 minutes.

6.4.1 PZT sol - ethylene glycol mixture

The 65/35 *vol%* mixture of sol and EG was firstly utilised to print the pattern with 1, 4 or 16 nozzles. No powder was present in the system.

6.4.1.1 1 nozzle printing

When 1 nozzle was used to print the pattern it was possible to distinguish individual droplets only if they were fired at 15 and 16 *V*. Figure 6.5 represents an example of the pattern printed with 1 nozzle, with a firing voltage of 15 *V* and a CPH of 0.30 *mm*, before and after sintering. It can be seen that not all the droplets are resolved and some have coalesced together. This behaviour reduced the number of valid drops used for size measurement.

In figure 6.6 a the average diameter of the droplets printed under these conditions at different cartridge print heights is shown. A higher voltage leads to the ejection of bigger droplets that should result in larger relics on the substrate. It can be seen that the average dot diameter is around 45 μm. At low firing voltage (15 V) the dimension of the printed droplets was slightly smaller than the droplets ejected at 16 *V*. A further increase in the voltage led to

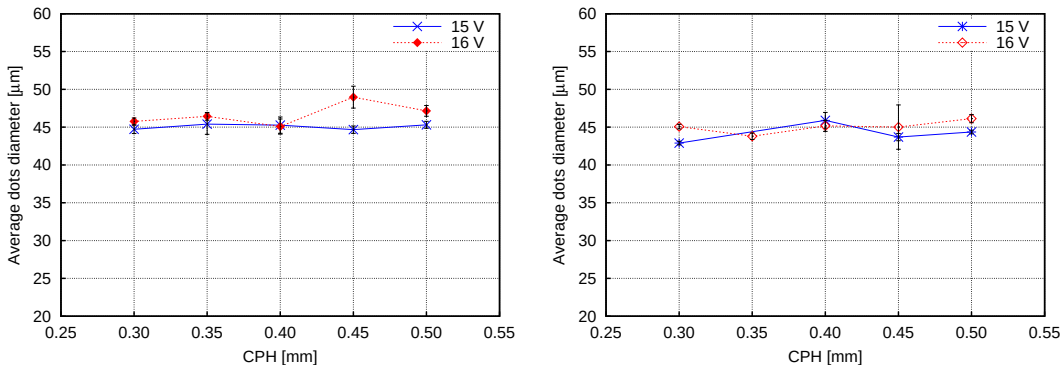

Figure 6.6: Average dimension of PZT sol-EG dots printed with 1 nozzle at different CPH and fired at 15 and 16 V before (a) and after (b) sintering at 720^oC for 20 minutes.

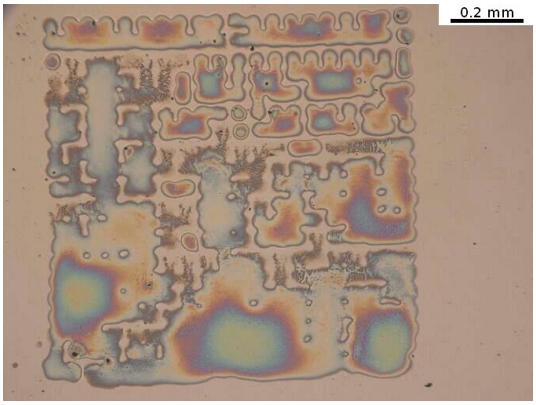

Figure 6.7: Optical micrograph of the 20x20 dots pattern printed with Sol-EG mixture under the following conditions: voltage 20 V, CPH 0.30 mm, 1 nozzle.

the coalescence of the droplets on the substrate, as shown in figure 6.7. The dots were ejected at a distance from the substrate of 0.30 mm and at 20 V. From the optical micrograph it is possible to notice that the resulting printed area is completely different from the one obtained when the voltage was set at 15 V (figure 6.5 a). Very few single droplets can be detected on the substrate. In the remaining area the droplets are coalesced, creating channels of sol instead of dots. This means that under the same conditions of CPH and number of printing nozzles, the voltage at which the droplets are ejected influences the printing quality: higher voltages result in larger relics.

From the graph represented in figure 6.6 a it can be seen that the CPH did not affect the spreading of the dots on the substrate.

After sintering at 720^oC for 20 minutes, the size of the droplets on the substrate was measured again in order to determine if shrinkage has occurred. Figure 6.5 b reports the relics obtained after sintering of the sample represented in figure 6.5 a (voltage 15 *V* and CPH 0.30 *mm*). After the heat treatment, cracks appeared in the printed area due to the shrinkage of the sol during drying, pyrolysis and sintering. The results obtained from the measurement of the relics after sintering are reported in figure 6.6 b. In general the relics on the substrate decreases in size after sintering, meaning that shrinkage has occurred. However the average dot diameter for the pattern printed at a CPH of 0.40 *mm* and fired at 15 *V*, was bigger than the unsintered pattern. This can be attributable to the system used to analyse the data and is not indicative of relic growth.

6.4.1.2 4 nozzle printing

The same pattern was printed by ejecting the mixture from 4 nozzles at the same time. Also under these conditions it was possible to print separate droplets only by firing the mixture at low voltages, such as 15, 16 and 18 *V*. Figure 6.8 a represents the sol/EG mixture printed on the silicon wafer by firing 4 nozzles at 16 *V* and at a distance of 0.50 *mm*. It can be seen that some of the droplets are have coalesced together. The presence of small droplets close to the main droplets can also be detected. Moreover the shape of most of the remaining resolved dots is non circular. The elongated shape of relics and the presence of the small droplets in between the pattern have probably been created by the formation of satellites droplets (see subsections 2.3.5 and 2.3.7.1). This phenomena is characterised by the creation of main drops followed by many other smaller drops and it can be reduced by increasing the ink viscosity [62]. Since the viscosity of the sol/EG mixture was already close to the upper limit (11.30 $mPa \cdot s$) it was not increased further in order not to exceed 12 $mPa\,s$. At higher voltages,

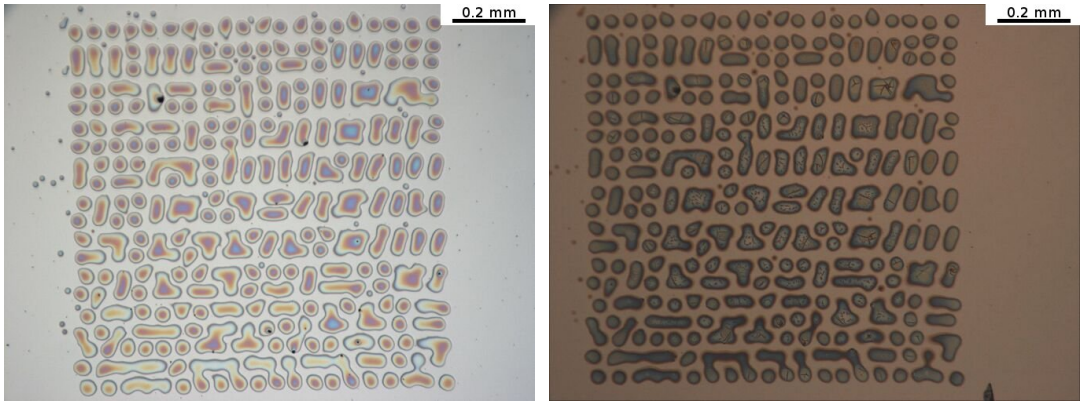

(a) **(b)**

Figure 6.8: Optical micrographs of the 20x20 dots pattern printed with Sol-EG mixture under the following conditions: voltage 16 *V*, CPH 0.50 *mm*, 4 nozzles. a) before sintering and b) after sintering at 720^oC for 20 minutes.

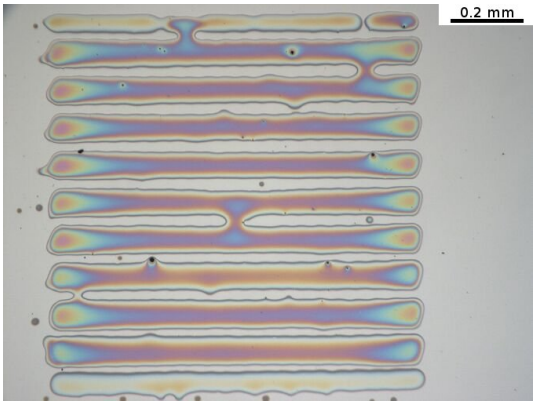

Figure 6.9: Optical micrograph of the 20x20 dots pattern printed with Sol-EG mixture under the following conditions: voltage 25 *V*, CPH 0.35 *mm*, 4 nozzles.

the ejected droplets were bigger in size, resulting in a larger relic size on the substrate. In this way the printed pattern was no longer composed of single droplets but of coalesced droplets. In the example shown in figure 6.9 a pattern printed with a firing voltage of 25 V is shown. Single droplets are no longer detectable on the substrate. They were all coalesced together, which resulted in the formation of lines especially in the printing direction (right to left). Close to the external borders of the pattern, small drops can also be noticed, confirming the formation of satellites drops.

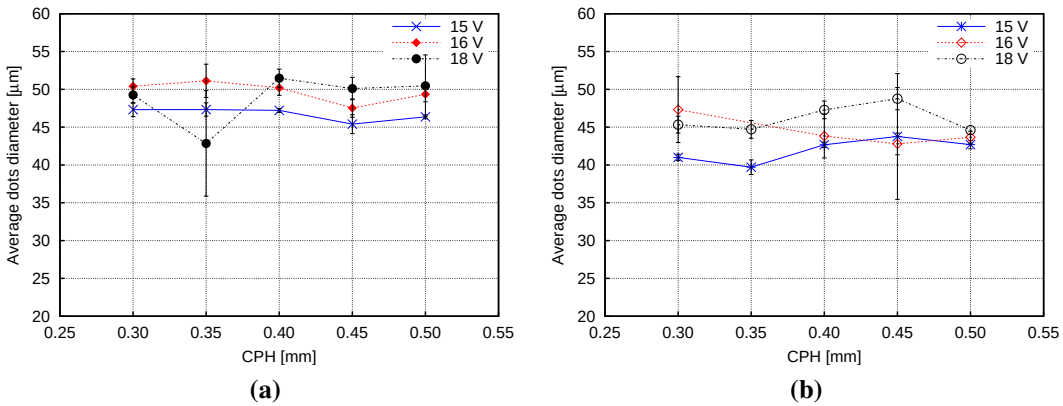

Figure 6.10: Average dimension of PZT sol-EG dots printed with 4 nozzles at different CPH and fired at 15, 16 V and 18 V, before (a) and after (b) sintering at 720^oC for 20 minutes.

In figure 6.10 a the graph representing the average dot dimension under different conditions is shown. The measurement of the droplet size was possible only for patterns printed at low voltages, such as 15, 16 and 18 V, as shown in the graph. The average dimension increases with increasing voltage at which the droplet were ejected. A mismatch can be noted for the droplets printed at a distance of 0.35 *mm* and with a voltage of 18 V. However the error associated to the measurement is relatively large, due to the small number of single droplets detected. For all the trends it can be seen that the average size remained almost constant as seen in figure 6.6 a.

The graph representing the average dots diameter after sintering is reported in figure 6.10 b. It can be seen that the heat treatment led to a reduction of the relics size for all the samples. However cracks appeared on the printed area indicating that the wet film thickness was too high. Figure 6.8 b represents the pattern printed with 4 nozzles, at a CPH of 0.50 *mm* and firing voltage of 16 V after heat treatment.

6.4.1.3 16 nozzle printing

The number of firing nozzles was increased to 16 (maximum number of nozzles) and the 20x20 drop pattern was printed, changing voltages and CPH. Also in this case, the droplets

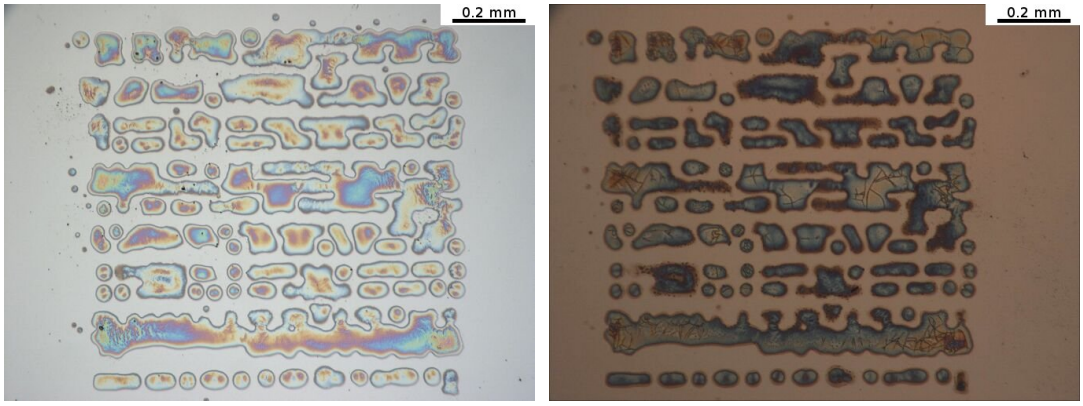

(a) **(b)**

Figure 6.11: Optical micrographs of the 20x20 dots pattern printed with Sol-EG mixture under the following conditions: voltage 16 *V*, CPH 0.50 *mm*, 16 nozzles. a) before sintering and b) after sintering at 720^oC for 20 minutes.

were only resolved when ejected at low voltages. In figure 6.11 a the pattern printed at a cartridge to substrate distance of 0.50 *mm* and at 16 *V* is shown. Small droplets can be detected in the printed area close to the main droplets. Most of the droplets are fused together in different ways, and few single drops can be counted on the substrate. Individual droplets were no longer detectable when the voltage was increased over 16 *V*, as shown in figure 6.12. The figure represents the pattern printed at 28 *V* with a CPH of 0.50 *mm*. It can be seen that no drops are detectable on the substrate: all the drops are coalesced together leading to the formation of distorted lines and rectangles. Small droplets are also visible originating from satellite ejection.

In figure 6.13 a the average diameter of the droplets printed with 16 nozzles is shown. It was only possible to resolve individual drop relics for the pattern printed at 15 and 16 *V*. Moreover the number of resolved droplets was low, meaning that even at low voltages, the droplets tended to coalesce. From the graph it can be seen that the average dimension of the droplets printed at 15 *V* is larger than the droplets printed at 16 *V*. This behaviour was not expected, as an increase in the firing voltage should lead to the ejection of bigger droplets and hence the formation of larger relics on the substrate. This is most likely due to

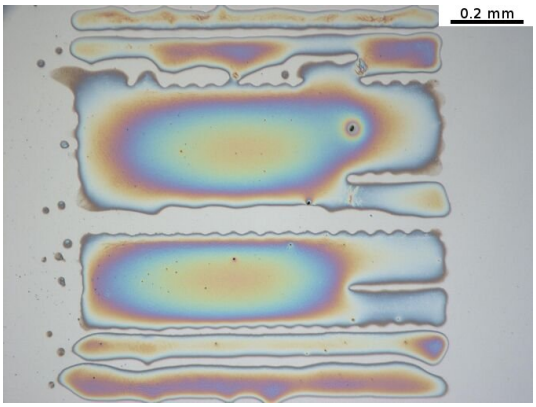

Figure 6.12: Optical micrograph of the 20x20 dots pattern printed with Sol-EG mixture under the following conditions: voltage 28 *V*, CPH 0.50 *mm*, 16 nozzles.

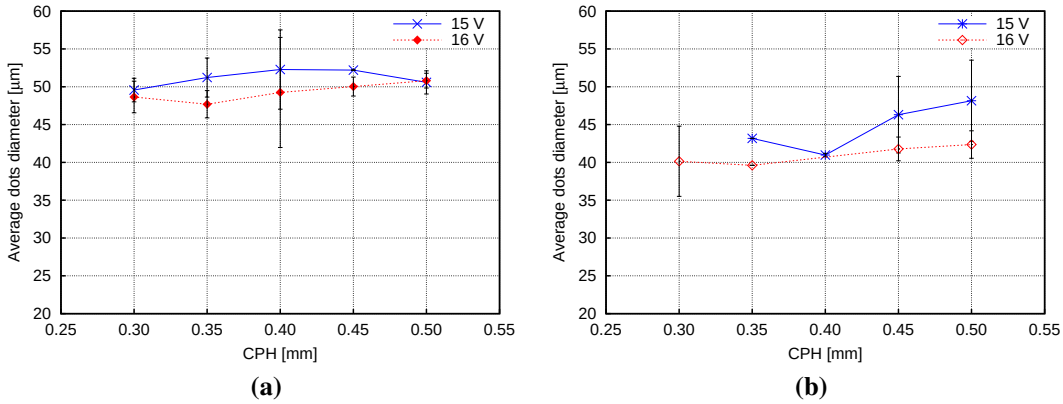

Figure 6.13: Average dimension of PZT sol-EG dots printed with 16 nozzles at different CPH and fired at 15 and 16 *V*, before (a) and after (b) sintering at 720^oC for 20 minutes.

measurement artifacts. In fact the number of valid drops detected on the pattern printed at 16 *V* was smaller that the number of individual drops printed at 15 *V* (effectively removing the larger particles from the distribution). This affected the average dot diameter measurement, resulting in larger droplets at 15 *V*. However when 16 nozzles were used to eject the droplets at 15 *V*, the resulting relics were bigger in size than the relics obtained when 4 or 1 nozzle were used. The same trend is observed when the voltage was increased to 16 *V*, with an exception for the droplets printed with 16 nozzles.

After sintering (figure 6.13 b) the average dimension decreased but the droplets printed

at 15 *V* were still larger in size than the ones printed at 16 *V*. The size of the drops printed at 15 *V* and at 0.30 *mm* of distance from the substrate was not recorded because no circular drops were detectable after sintering. Figure 6.11 b represents the pattern reported in figure 6.11 a, after sintering treatment. Cracks could be noted in the printed area and the dot borders became more jagged after the heat treatment.

6.4.1.4 Summary

Printing of individual droplets of PZT sol-ethylene glycol mixture was possible only at low firing voltages, such as 15, 16 or 18 V. An increase in the voltage led to larger relics on the substrate. At higher voltages no individual drops were detected on the substrate because they coalesced. However a trend can be noted in the way in which drops merge. This coalescing is more likely to happen first in the *X* direction and then in the *Y* direction, due to the movement of the cartridge (along *X* direction) across the substrate during printing. The CPH did not affect the average drop diameter. Increasing the number of active nozzles led to a slight increment in the average dimension. However big errors were associated with the measurements, especially when 16 nozzles were used to print. Finally after sintering a reduction of the relic dimension was noted, with cracks appearing in the features due to shrinkage stresses.

6.4.2 PZT inks

After printing with the PZT sol-ethylene glycol mixture, the 20x20 drops pattern was printed with the inks containing different amounts of PZT powder synthesised by MSS. The solid loading was gradually increased from 1 to 5 *vol%* in order to determine the conditions at which printing was halted due to nozzle clogging.

6.4.2.1 Printing of 1 *vol%* PZT ink

1 nozzle printing The pattern was printed at different CPH and at different voltages, but single drops were detected only when low voltages were adopted, such as 15, 16 and 18 *V*. In figure 6.14 a an example of the printed droplets is reported. It represents the pattern printed at 0.35 *mm* from the substrate, with a firing voltage of 16 *V*. It can be seen that not all the droplets are resolved because some of them are coalesced. At higher voltages the droplets started to

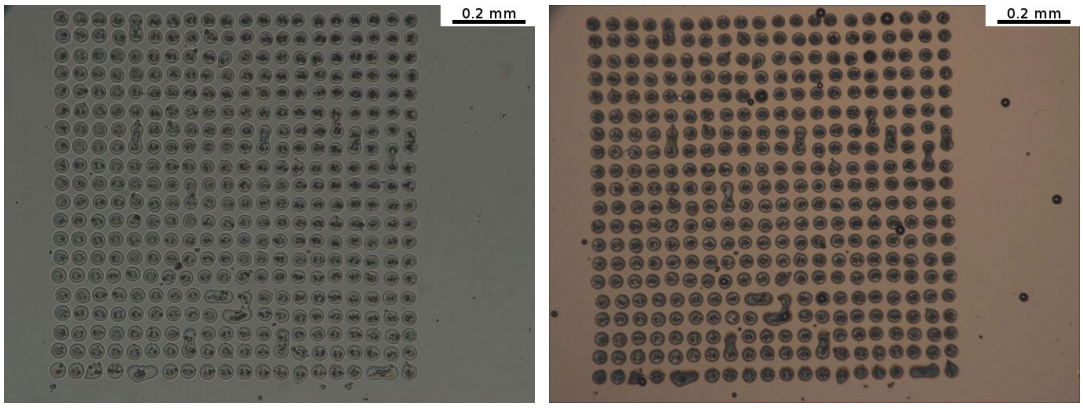

(a) **(b)**

Figure 6.14: Optical micrographs of the 20x20 dots pattern printed with PZT ink MS1 under the following conditions: voltage 16 *V*, CPH 0.35 *mm*, 1 nozzle. a) before sintering and b) after sintering at 720^oC for 20 minutes.

fuse together, as shown in figure 6.15. It can be seen that the droplets were deposited on the substrate and then they coalesced, resulting in the formation of "labyrinth-like" shapes.

The relic size was calculated only for patterns printed at 15, 16 and 18 *V*, as shown in figure 6.16 a. At fixed CPH the dimensions of the printed droplets increased with increasing firing voltage, with an exception at 0.35 *mm*, where the droplets fired at 18 *V* resulted in smaller relics than the droplets fired at 16 *V*. By comparison between figure 6.16 a and figure 6.6 a it can be seen that the droplets printed with PZT ink resulted in smaller relics than the droplets printed with the PZT sol-ethylene glycol mixture. This behaviour is due to the presence of the powder in the ink MS1. The spreading of a droplet on the substrate is

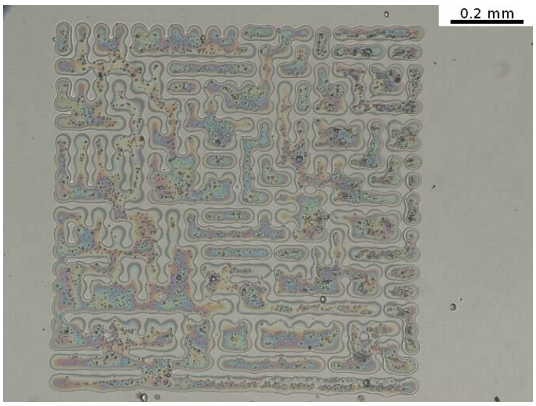

Figure 6.15: Optical micrograph of the 20x20 dots pattern printed with PZT ink MS1 under the following conditions: voltage 23 *V*, CPH 0.30 *mm*, 1 nozzle.

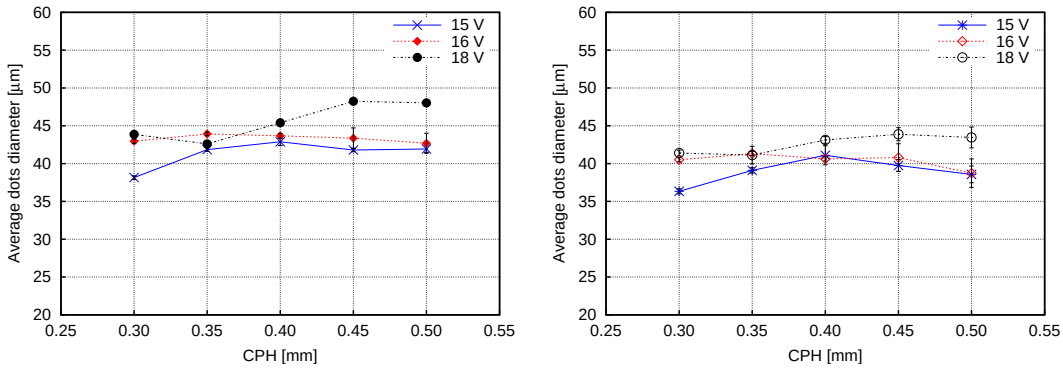

Figure 6.16: Average dimension of MS1 dots printed with 1 nozzle at different CPH and fired at 15, 16 and 18 *V*, before (a) and after (b) sintering at 720^oC for 20 minutes.

controlled by viscosity and surface tension. The first controls the speed of spreading, while the second controls the degree of spreading. Therefore low values of these two physical properties should lead to larger droplets after impact. These values are lower for MS1 than for PZT sol/EG mixture, that should result in larger MS1 drops. However viscosity and surface tension of the two systems are close, meaning that the major effect to spreading was due to the presence of powder in the ink.

After sintering the relic size decreased as shown in figure 6.16 b. All the sintered droplets were smaller in size than the correspondent unsintered ones. Moreover the size of the droplets ejected at 15 and 16 V was smaller than the droplets printed in the same conditions but using the sol-EG mixture. An example of sintered sample is reported in figure 6.14 b. Small cracks have appeared in the drops as in the previous samples.

4 nozzle printing The number of ejecting nozzles was then increased to 4 and an example of the results is shown in figure 6.17 a. Single drops can be detected, but some of the lines of drops are missing from the printed area. This phenomena can be attributed to nozzle clogging and it is confirmed by the presence of fine drops in the surrounding area. These fine drops, or spray are created when the nozzles are partially obstructed by the formation of a dried ink film at their outlets or by the sedimentation of solid in the inlets. In order to avoid the dried ink film formation, the nozzles were kept in movement during the non-printing stage by using the tickle control. Enabling this control applies low amplitude pressure pulses to the ink to move the meniscus slightly but not fire a drop. In this way the formation of the dried ink film at the nozzle outlet is avoided. However, even when the tickle mode was used, the spray formation was not avoided and lines of droplets were still missing, meaning that the nozzles were clogging from the inside due to powder sedimentation. Under these conditions it was possible to determine the relic dimensions for the pattern printed at low voltages, as shown in figure 6.18 a. The average dimension of the relics was found to fluctuate, without a clear

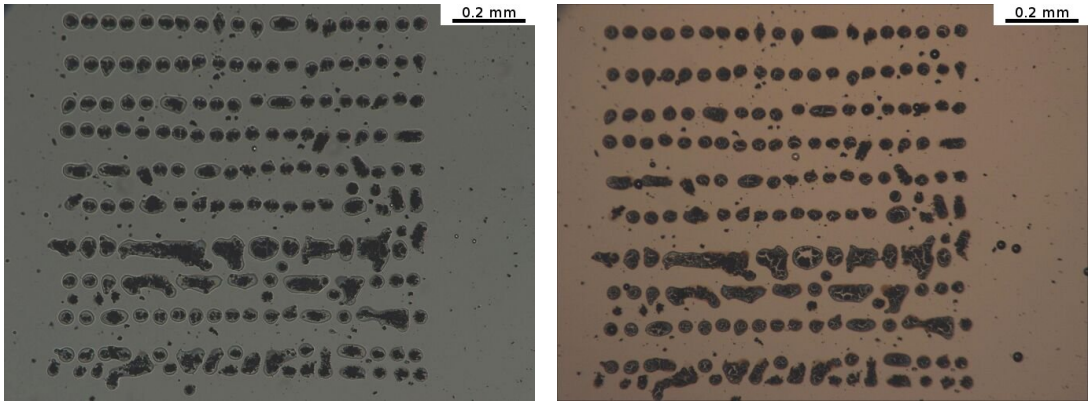

(a) **(b)**

Figure 6.17: Optical micrographs of the 20x20 dots pattern printed with PZT ink MS1 under the following conditions: voltage 18 *V*, CPH 0.35 *mm*, 4 nozzles. a) before sintering and b) after sintering at 720^oC for 20 minutes.

trend due to the changing conditions within the print nozzles. The influence of firing voltage and the cartridge print height on the relic dimensions could not be determined.

At higher voltages the droplets were no longer detectable on the substrate because of their coalescence on the substrate, as shown in figure 6.19. Lines of ink were created in the printing direction. The drops were ejected at 30 *V* and at a distance from the silicon wafer of 0.30 *mm*. Lines of dots were missing and the spray was still visible, confirming the obstruction of the nozzles.

The samples were subjected to the sintering process and the relics were again measured. The results are reported in figure 6.18 b. The average dimension decreased as in the other samples, but under these conditions the error associated with the measurements was higher than in the previous tests, resulting in an almost constant relic size. In figure 6.17 b the pattern represented in figure 6.17 a is shown after heat treatment at 720^oC for 20 minutes. It can be seen that big cracks had appeared on the printed area and in some cases part of the ink was even removed, meaning high stresses and/or a poor ink adhesion on the substrate.

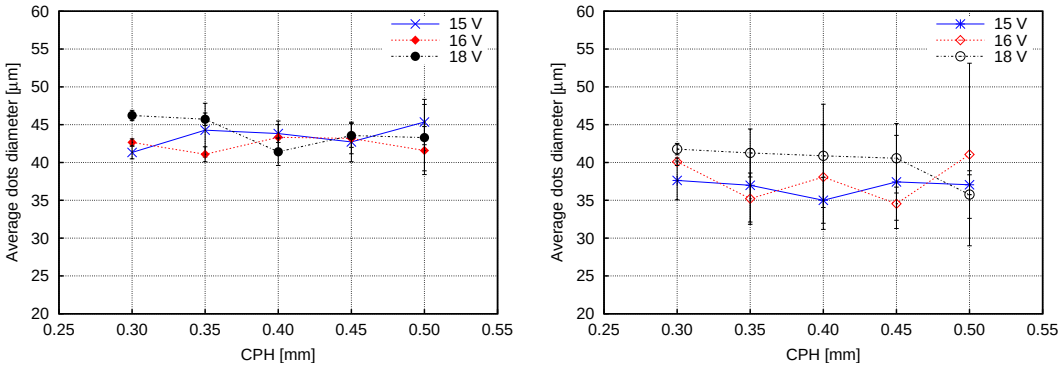

Figure 6.18: Average dimension of MS1 dots printed with 4 nozzles at different CPH and fired at 15, 16 and 18 *V*, before (a) and after (b) sintering at 720^oC for 20 minutes.

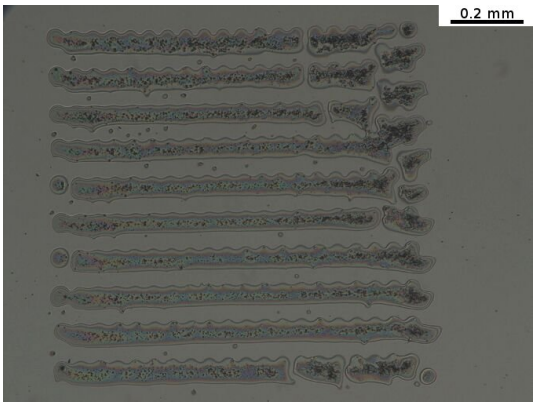

Figure 6.19: Optical micrograph of the 20x20 dots pattern printed with PZT ink MS1 under the following conditions: voltage 30 *V*, CPH 0.30 *mm*, 4 nozzles.

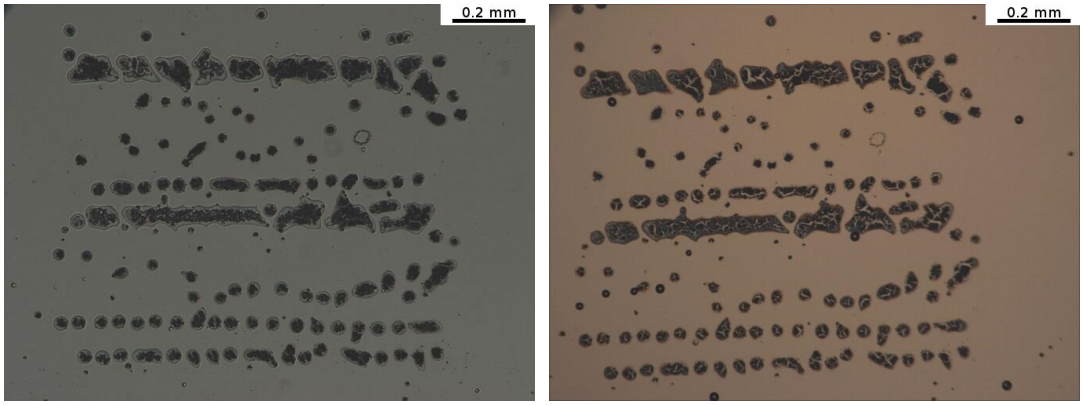

(a) **(b)**

Figure 6.20: Optical micrographs of the 20x20 dots pattern printed with PZT ink MS1 under the following conditions: voltage 18 *V*, CPH 0.40 *mm*, 16 nozzles. a) before sintering and b) after sintering at 720^oC for 20 minutes.

16 nozzle printing When 16 nozzles were used to print, the droplets were separated only at low voltages, but the resulting pattern on the substrate was not composed of 400 dots. As shown in figure 6.20 a, several lines of dots are missing and some are coalesced. Moreover most of the resolved droplets are not aligned but their position on the silicon wafer is out of line. This results from the nozzle blockage due to the sedimentation of the powder in the internal part of the cartridge. It was still possible to determine the relic dimensions for patterns printed at 15, 16 and 18 *V*, even if the number of resolved droplets was low, and the result is shown in figure 6.21 a. When a voltage of 15 *V* was used to eject the droplets, the relic dimension was almost constant with increasing the CPH. At 16 *V*, the curve reached a maximum in correspondence of 0.40 *mm*, and at 18 *V* there was no clear trend of the average dot dimensions. This instability of the measurements is attributable to the low number of valid droplets. The partial nozzle clogging resulted in the ejection of droplets with a size different from the expected one. Therefore, relics with different size were obtained, which resulted in the data scattering. At high voltages very few drops were detected, as shown in figure 6.22. Most of the drops coalesced after the deposition on the substrate and some lines are missing, confirming the nozzles clogging. A further increase in the firing voltage to 28 or

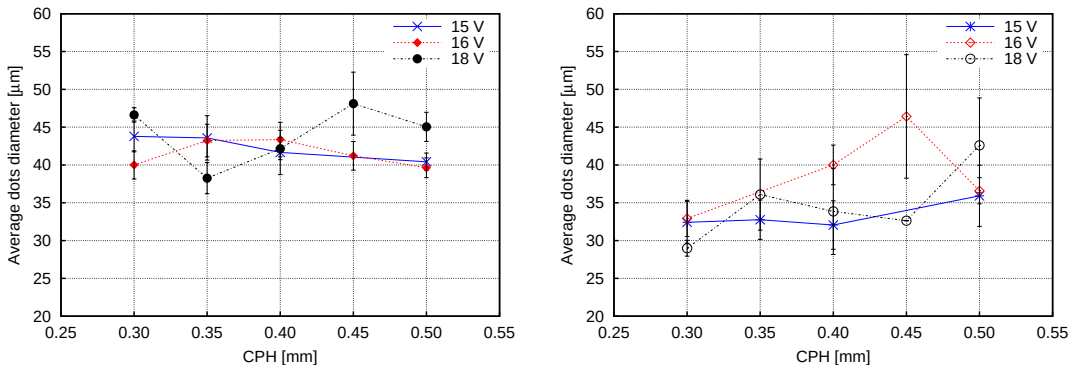

Figure 6.21: Average dimension of MS1 dots printed with 16 nozzles at different CPH and fired at 15, 16 and 18 *V*, before (a) and after (b) sintering at 720^oC for 20 minutes.

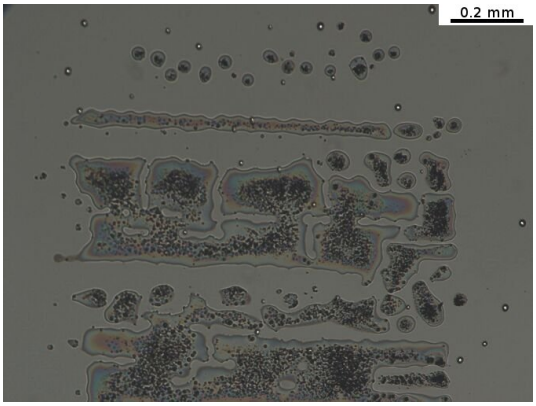

Figure 6.22: Optical micrograph of the 20x20 dots pattern printed with PZT ink MS1 under the following conditions: voltage 25 *V*, CPH 0.35 *mm*, 16 nozzles.

30 *V* led to the total absence of single droplets.

After sintering (figure 6.21 b) the relic dimension of the droplets ejected at 15 and 18 *V* decreased in size, but at 16 *V* a different trend can be noted. In this case the average dimension of the relics created at CPH of 0.45 *mm* was bigger than the correspondent unsintered ones, with a big error bar, due to the very low number of detected droplets after sintering (4). Again after the heat treatment, cracks appeared on the printed area, leading to the transformation of the relics from circular to irregular shapes, as shown in figure 6.20 b.

6.4.2.2 Printing of 2 *vol%* PZT ink

The 20x20 individual drops pattern was then printed with the PZT ink containing 2 *vol%* of powder. When 1 nozzle was used to print no drops were detected on the substrate, due to the quick clogging of the nozzle. With 4 or 16 active nozzles, clogging was still likely to occur, leading to a partial printing of the pattern. However, having a printed pattern leads to the measurement to be done. The same non printing condition was obtained when low voltages were adopted to eject the fluid. Therefore only data obtained at high voltages for 4 and 16 nozzles are reported.

4 nozzle printing No droplets were printed with the PZT ink MS2 at low voltages, such as 15, 16, 20 or 23 *V*. The voltage is related to the drop mass: an increment in the firing voltage led to the formation of bigger drops. At low voltages small drops are then created. However it is possible that the formation of small drops is limited or avoided by the aggregation of the powder contained in the ink. This phenomena explains why with increasing solid loading, the droplet formation at low voltages was not detected. In figure 6.23 the droplets printed with 4 nozzles at a CPH of 0.40 *mm* and at 25, 28 and 30 *V* are shown. The micrographs of the correspondent sintered patterns are also reported. Under these conditions very few drops were ejected from the nozzles, meaning that clogging was occurring. Compared to the relics obtained with PZT ink MS1, with MS2 less cracks appeared after sintering. A higher solid loading means a smaller amount of sol in the ink, that results in less shrinkage [49] and the formation of fewer cracks in the film. (The big circular black spots that appeared after the heat treatment were caused by the deposition of dust during sintering.)

16 nozzle printing When the number of firing nozzles was increased to 16, the printed area was not improved, because nozzles were still blocked by the powder. Also under these conditions no drops were ejected at low voltages. In figure 6.24 the pattern printed at 25,

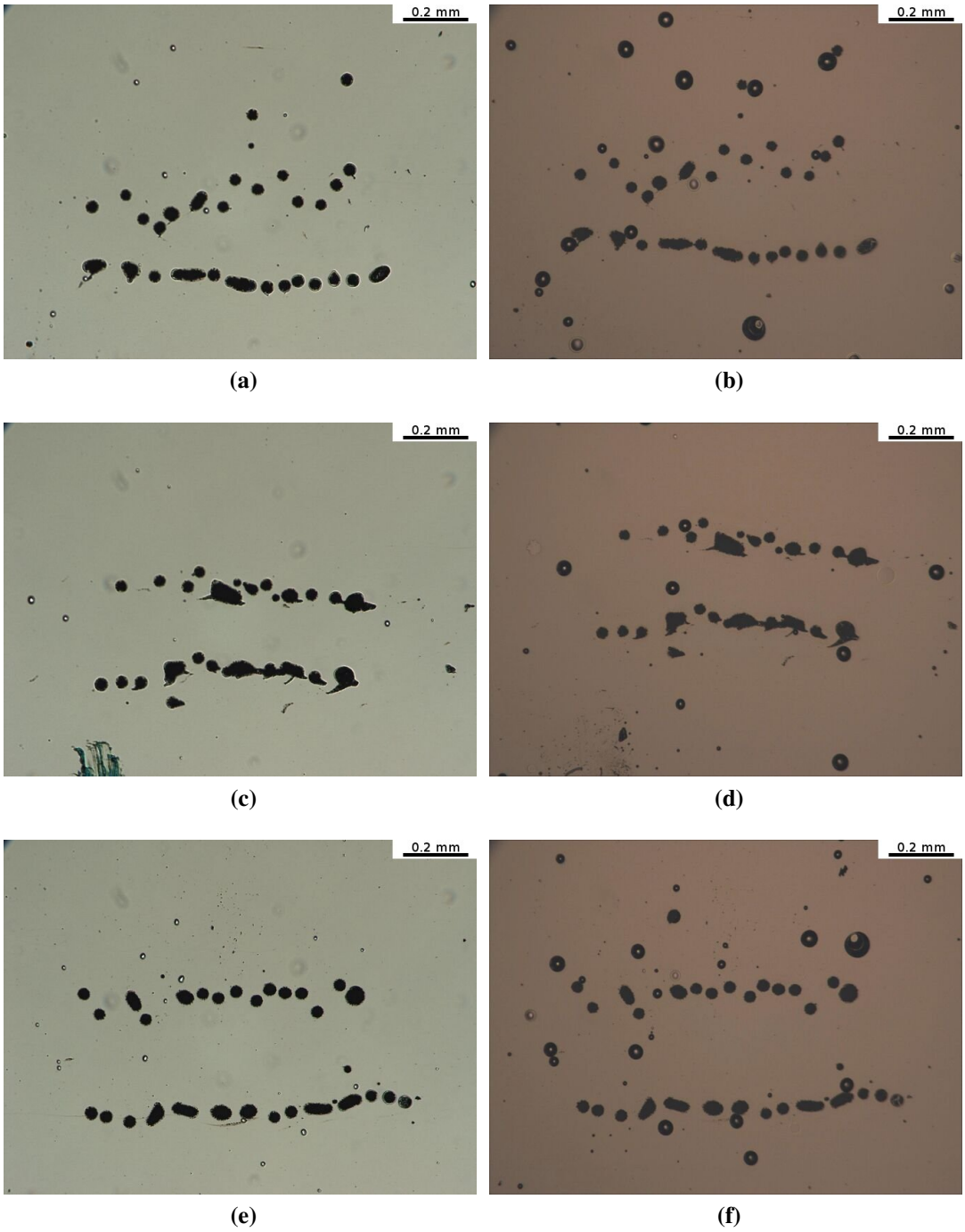

Figure 6.23: Optical micrographs of the 20x20 dots patterns printed with PZT ink MS2 before (a, c and e) and after sintering (b, d and f). a-b) 25 *V*, c-d) 28 *V* and e-f) 30 *V.* CPH and number of firing nozzles were 0.40 *mm* and 4, respectively.

28 and 30 *V* at a CPH of 0.45 *mm* is shown, before and after sintering. It can be seen that few circular drops were deposited on the silicon wafer due to the obstruction of the nozzles. Moreover lines are missing, meaning that some nozzles were completely clogged and they were not able to fire. Again in the sintered samples, less cracks appeared, when compared to the patterns printed with PZT ink MS1.

6.4.2.3 Higher solid loadings

The cartridges were filled with PZT inks formulated with higher solid loadings, namely 3, 4 and 5 *vol%*. They were left undisturbed for 30 minutes with the nozzles facing down, as was done for the previous inks. Unfortunately, it was not possible to print with such inks, because the nozzles clogged during the time the cartridges were left on the bench due to particle sedimentation.

6.4.2.4 Summary

When the pattern was printed with the 1 vol% ink, individual droplets were detected at low firing voltages and with 1 nozzle. Missing lines were detected when more nozzles were used to print because of their clogging. An increment in the powder content in the ink (MS2) led to its "non printability" due to the quick nozzles clogging, caused by the higher amount of particles. Only few drops were printed with this ink. However, the presence of more powder in the ink led to formation of less cracks on the sintered pattern.

6.4.3 Droplet spreading on the substrate

The spreading of a droplet on the substrate can be calculated by equations 2.4 and 2.5. Both the equations give an estimation of the maximum spreading of a drop after the impact with the surface, but only equation 2.5 will be here considered because of the impossibility of determination of the contact angle values (needed for equation 2.4).

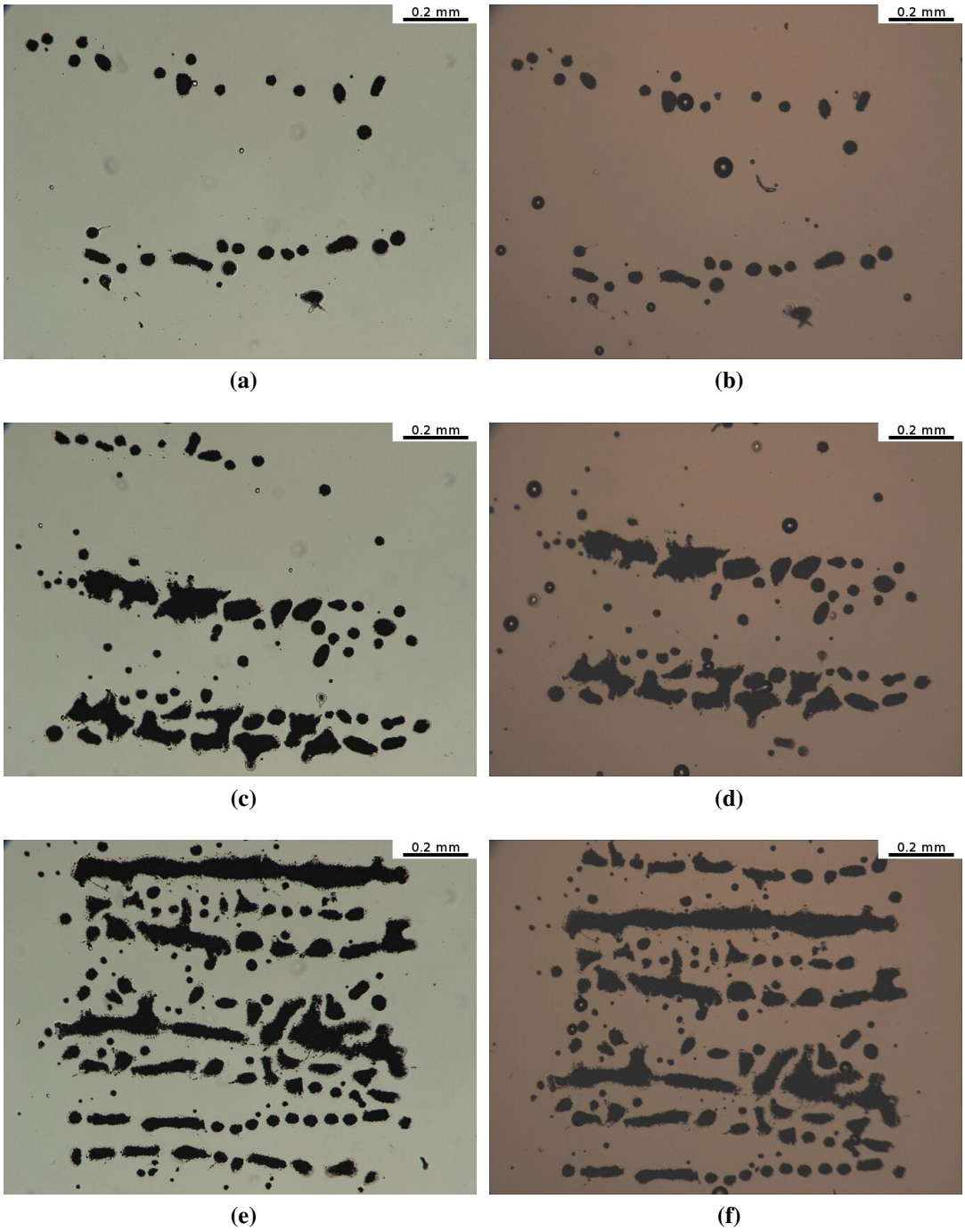

Figure 6.24: Optical micrographs of the 20x20 dots patterns printed with PZT ink MS2 before (a, c and e) and after sintering (b, d and f). a-b) 25 *V*, c-d) 28 *V* and e-f) 30 *V.* CPH and number of firing nozzles were 0.45 *mm* and 16, respectively.

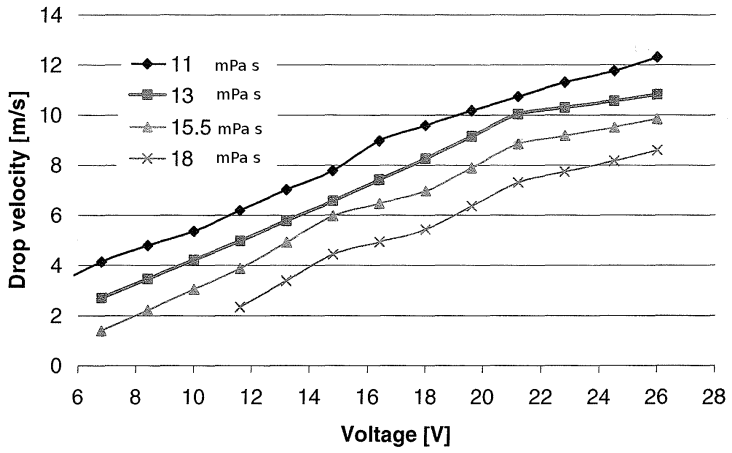

Figure 6.25: Drop velocity as a function of the firing voltage for different liquid viscosities. From [138].

To determine *Re* number, the drop velocity after ejection is needed. From the graph reported in figure 6.25 an estimation of the drop velocity for fluid viscosity of 11 $mPa\,s$ (value close to the viscosity of fluids here considered) can be done. Knowing the value of velocity allows to calculate the maximum spreading diameter. The values are reported in table 6.4. It can be seen that increasing the firing voltage leads to an increase in the drop velocity and hence in the values of β. This means that a drop ejected at higher voltage will spread more than a drop ejected at lower voltage. This confirms what has been determined in the previous sections: higher firing voltage leads to larger relics on the substrate. However the spreading coefficients of the three inks (ejected at the same voltage) are close to each other. This can be attributed to the estimation of the drop velocity through the graph reported in figure 6.25. The velocities were determined from the curve representing a liquid viscosity of 11 $mPa\,s$, while the inks have different viscosity values.

Table 6.4: Maximum spreading values for the inks PZT sol/EG, MS1 and MS2.

Firing voltage V	Drop velocity $m\,s^{-1}$	$\beta_{Sol/EG}$	β_{MS1}	β_{MS2}
15	8.0	1.92	1.94	1.93
16	8.6	1.94	1.96	1.95
18	9.6	1.97	1.98	1.98
20	10.3	1.98	2.00	2.00
23	11.5	2.01	2.03	2.02
25	12.0	2.04	2.04	2.03

6.5 Line array pattern

The line array pattern, shown in figure 3.6 b, was printed in order to identify under which conditions the printing quality was enhanced. The pattern was deposited using 16, 4 and 1 nozzle at three different voltages 15, 20 and 25 *V*. The drop spacing was fixed at 25 μm and the distance between the substrate and the cartridge was varied from 0.30 to 0.50 *mm*. The patter was printed only with the PZT sol-EG mixture and PZT inks MS1 and MS2. Increasing the solid loading resulted in quick nozzle clogging and it was impossible to print the pattern.

6.5.1 PZT sol - ethylene glycol mixture

6.5.1.1 Printing with a firing voltage of 15 V

Figures 6.26, 6.27 and 6.28, represent the line array pattern printed under the same conditions of voltage, CPH and drop spacing, but with 16, 4 and 1 nozzle, respectively. When 16 nozzles were used to print (figure 6.26), it was impossible to distinguish between horizontal and vertical lines. The borders of the pattern were irregular and small drops were deposited close to the pattern.

Decreasing the number of firing nozzles from 16 to 4 (figure 6.27) led to an improvement of the printed area. By comparison between figure 6.26 a and 6.27 a, it is notable that at

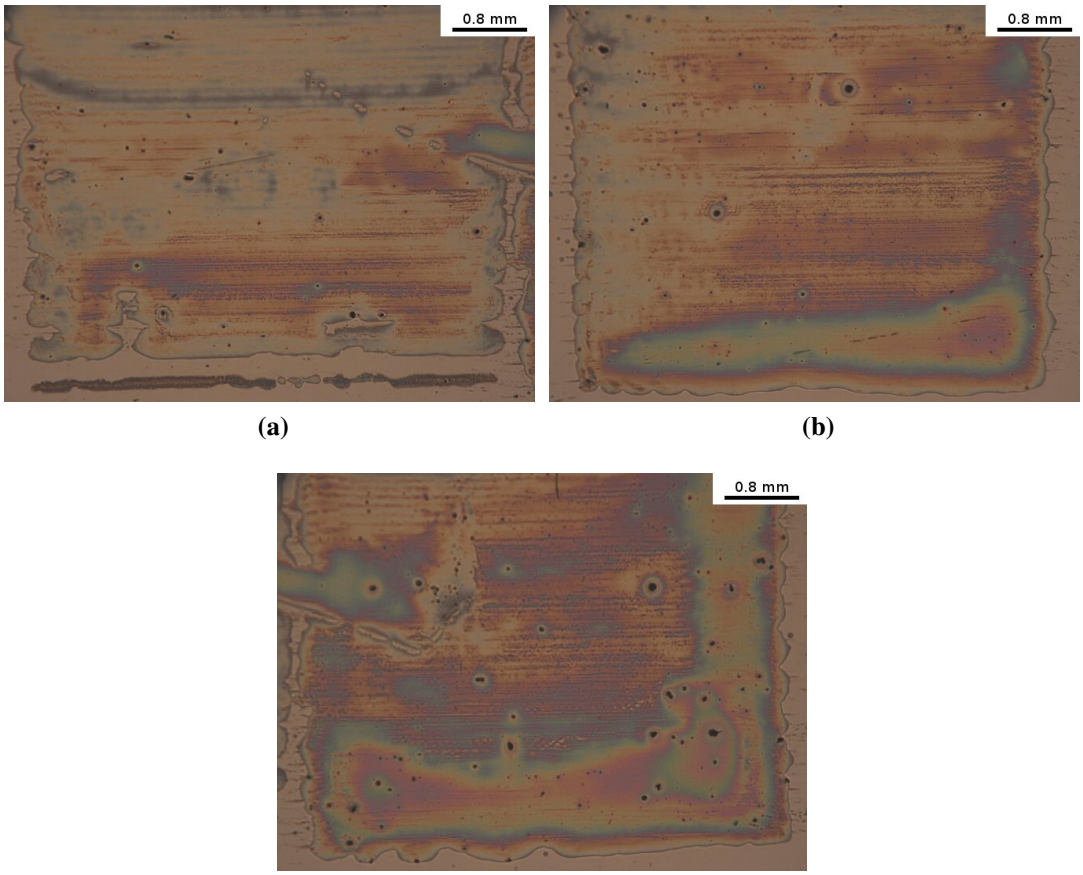

(a) **(b)**

(c)

Figure 6.26: Optical micrographs of the line array pattern printed with Sol-EG mixture at 15 *V* and CPH 0.35 *mm* with 16 nozzles: a) horizontal lines, b) vertical lines and c) square.

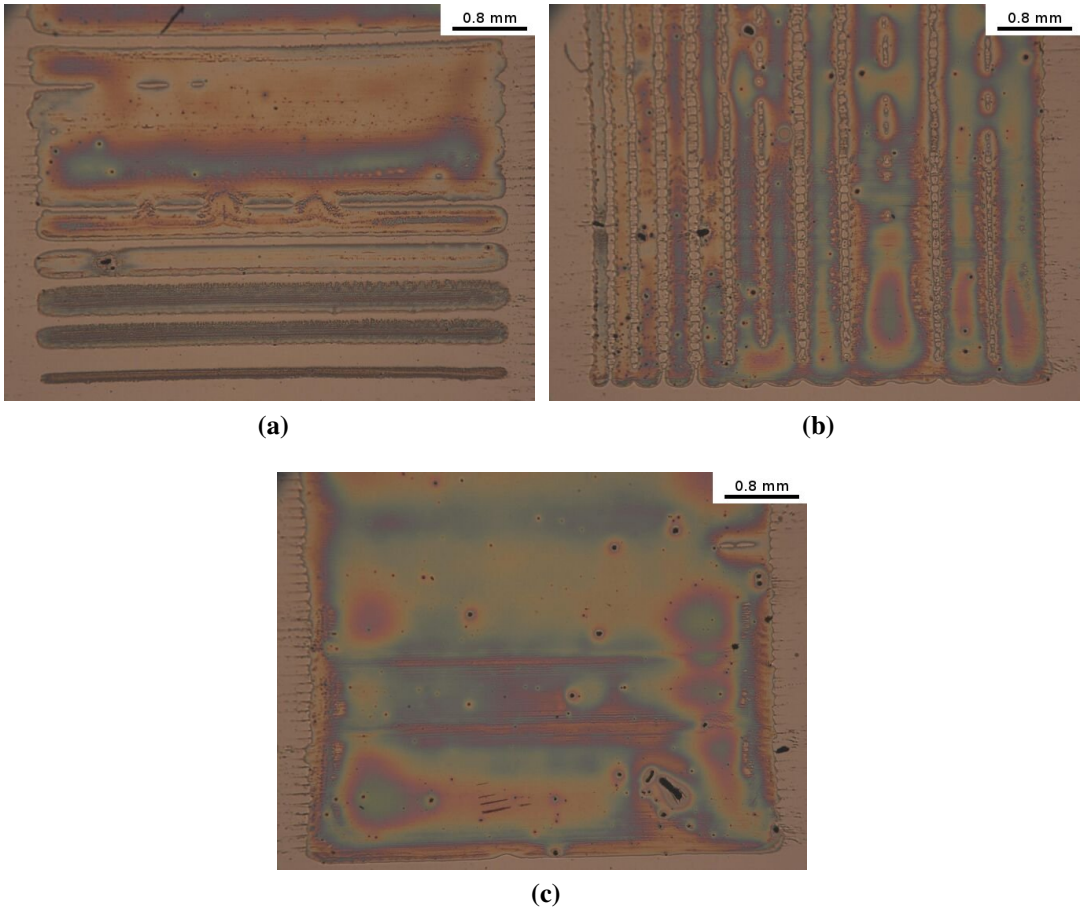

(a) **(b)**

(c)

Figure 6.27: Optical micrographs of the line array pattern printed with Sol-EG mixture at 15 *V* and CPH 0.35 *mm* with 4 nozzles: a) horizontal lines, b) vertical lines and c) square.

reduced number of nozzles, the quality in the printing direction (right to left) has improved. It is possible to detect separate lines, but not all of them are resolved (top part of the figure). The quality has also been enhanced in the transverse direction (figure 6.27 b). Even if they are not completely separated, 12 vertical lines can be recognised on the silicon wafer. However small stripes of ink cover the area between the lines in the printing direction, caused by the coalescence of the droplets or the partial clogging of the active nozzles. This phenomenon is also visible in figure 6.27 c in the left and right sides of the square.

When 1 nozzle was used to deposit the droplets, horizontal and vertical lines were all resolved as shown in figure 6.28. The difference obtained in the quality of the printed area

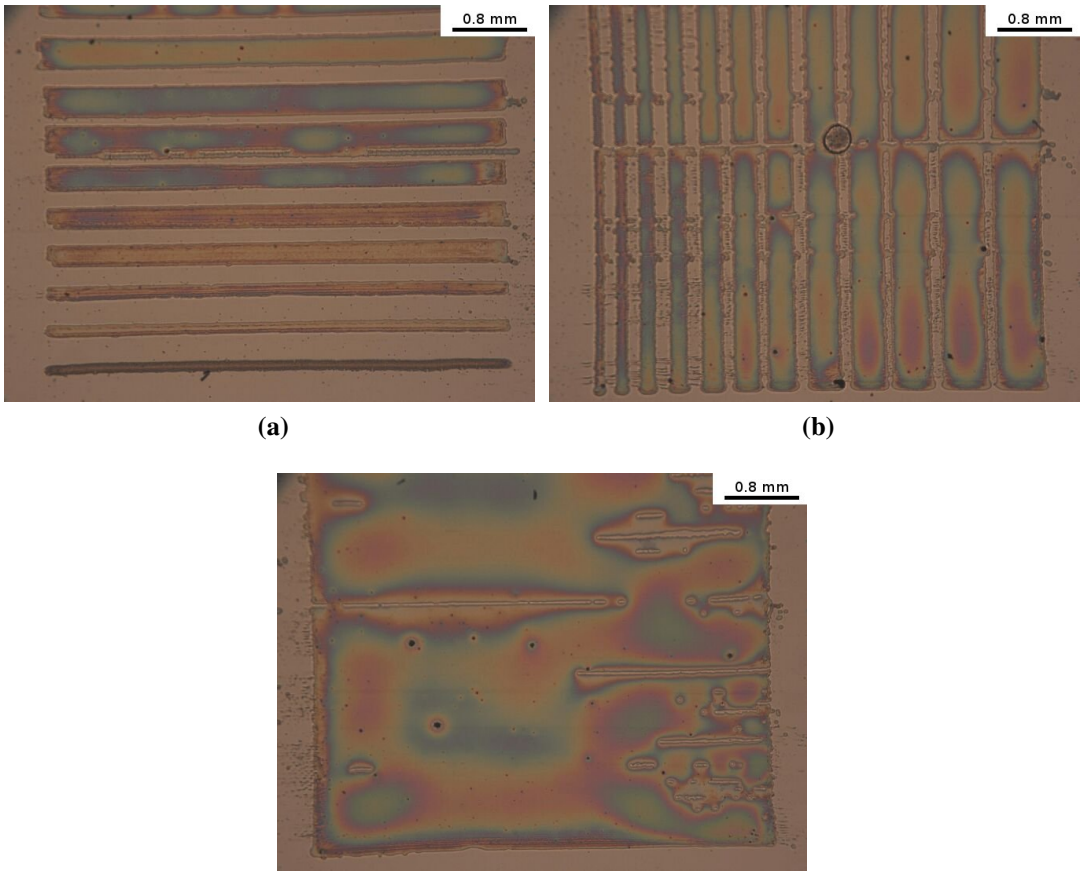

(a) **(b)**

(c)

Figure 6.28: Optical micrographs of the line array pattern printed with Sol-EG mixture at 15 *V* and CPH 0.35 *mm* with 1 nozzle: a) horizontal lines, b) vertical lines and c) square.

by changing the number of active nozzles can be explained by considering the printing time. If the first drop of the first line of drops is deposited at time=0, the first drop of the second line of drops will be deposited at time=x. When 16 nozzles are used, the cartridge passage across the substrate is quick and x is short. Decreasing the number of nozzles leads to an increase in the value of x. Therefore printing with 16 nozzles reduces the printing time, but also reduces the time for single drops to dry before the next drop arrives. In this way when the first droplet of the second line is deposited on the substrate, the first line is still wet and coalescence between the two occurs. This phenomena is reduced by increasing the value of x, namely by reducing the number of active nozzles. Moreover if the previous drop is not hard enough, the impact of the second drop can cause the formation of voids in the film [62].

In figure 6.28 b and c, it can be seen that some lines are missing. This is due to the formation of a dry film of ink at the outlet of the nozzle. The nozzle was recovered thanks to the tickle mode active and the cartridge cleaning after a 10 passages. However a fine spray was deposited in the vicinity of the pattern, due to the partial clogging of the nozzle.

At this voltage, an increase in the CPH (figure 6.29) did not affect the printing quality. However, several parts of the pattern were missing, due to nozzle clogging, caused by the formation of the dry film of ink. It is possible that after a long period of printing, the tickle mode and the cartridge cleaning were not enough to keep the nozzles clean.

6.5.1.2 Printing with a firing voltage of 20 V

As the firing voltage was increased to 20 V it was expected that a printed area similar to the one shown in figure 6.26 would be obtained, because at higher voltages, bigger drops are created and hence bigger relics should result from their impact on the substrate. However this situation was not observed as it can be seen in figure 6.30, that represents the pattern printed with 16 nozzles. Both vertical and horizontal lines were detected, even if some of them had coalesced. This behaviour was not expected and the reason in unknown. Further

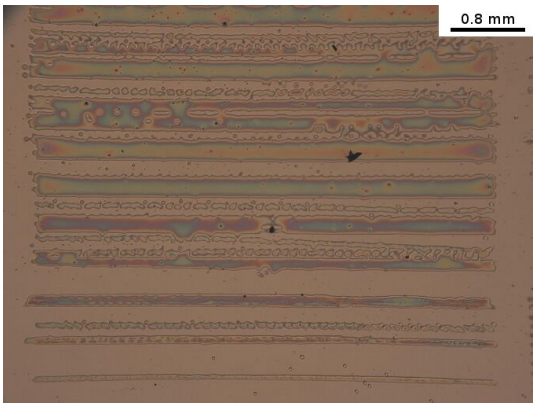

Figure 6.29: Optical micrograph of the line array pattern printed with Sol-EG mixture at 15 *V* and CPH 0.50 *mm* with 4 nozzles.

investigation on this subject will then be necessary. In figure 6.30 c it is possible to notice that some lines were missing, resulting in a non homogeneous printed area.

A decrease in the number of the active nozzles led to an improved quality, as it is shown in figure 6.31. Horizontal and vertical lines were completely separated. However wavy borders of the vertical lines, represented in figure 6.31 b, were detected. This phenomena is also visible in figure 6.31 c and it is caused by the merging between adjacent droplets.

Further improvement was achieved when 1 nozzle was used to print, especially in the printing direction (figure 6.32 a). The lines were resolved and the edges were sharper. The borders waviness was reduced, but some parts were missing, as shown in figure 6.32 c, due to nozzle clogging.

An increase in the cartridge to substrate distance did not lead to an improvement in the printing quality, as shown in figure 6.33. The pattern was printed under the same conditions as figure 6.31 b, but increasing the CPH to 0.50 *mm*. Several drops cover the area between the vertical lines, and some lines are coalesced together, meaning that at 20 *V* an increase in the CPH leads to a reduction of the printing quality because of merging of some lines.

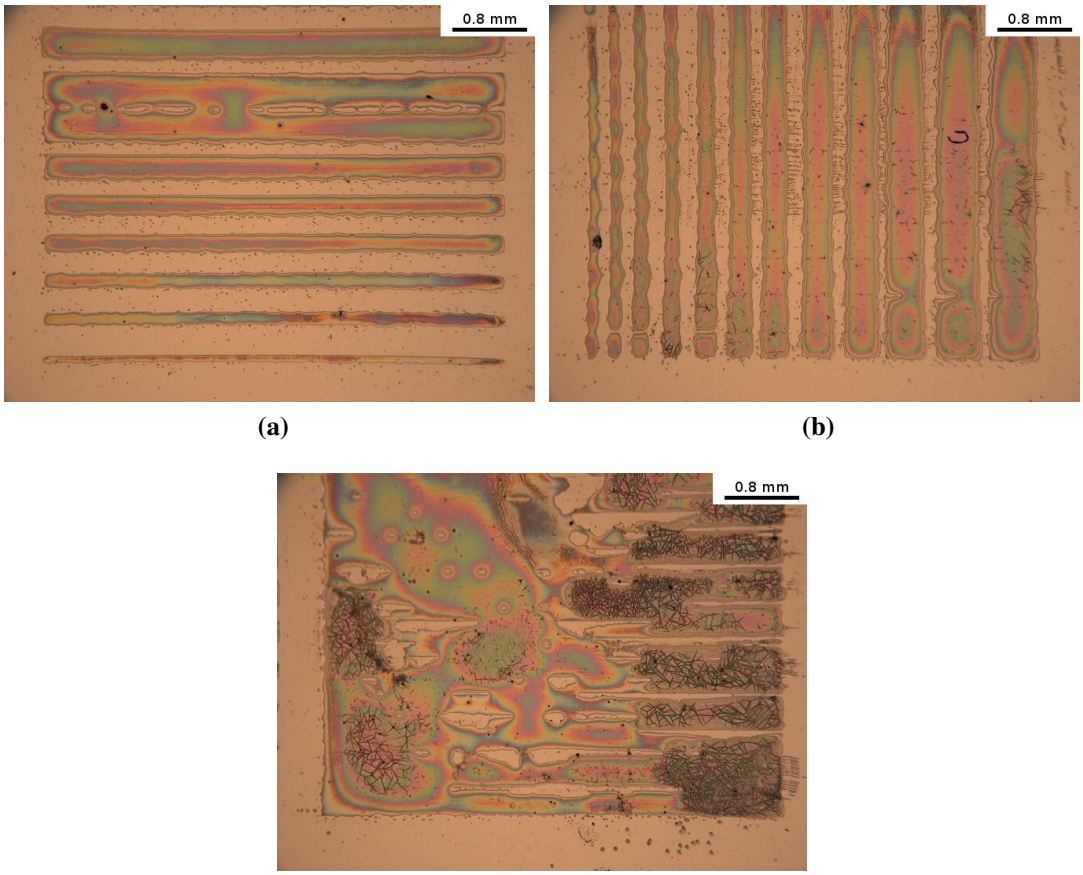

(a) **(b)**

(c)

Figure 6.30: Optical micrographs of the line array pattern printed with Sol-EG mixture at 20 *V* and CPH 0.35 *mm* with 16 nozzles: a) horizontal lines, b) vertical lines and c) square.

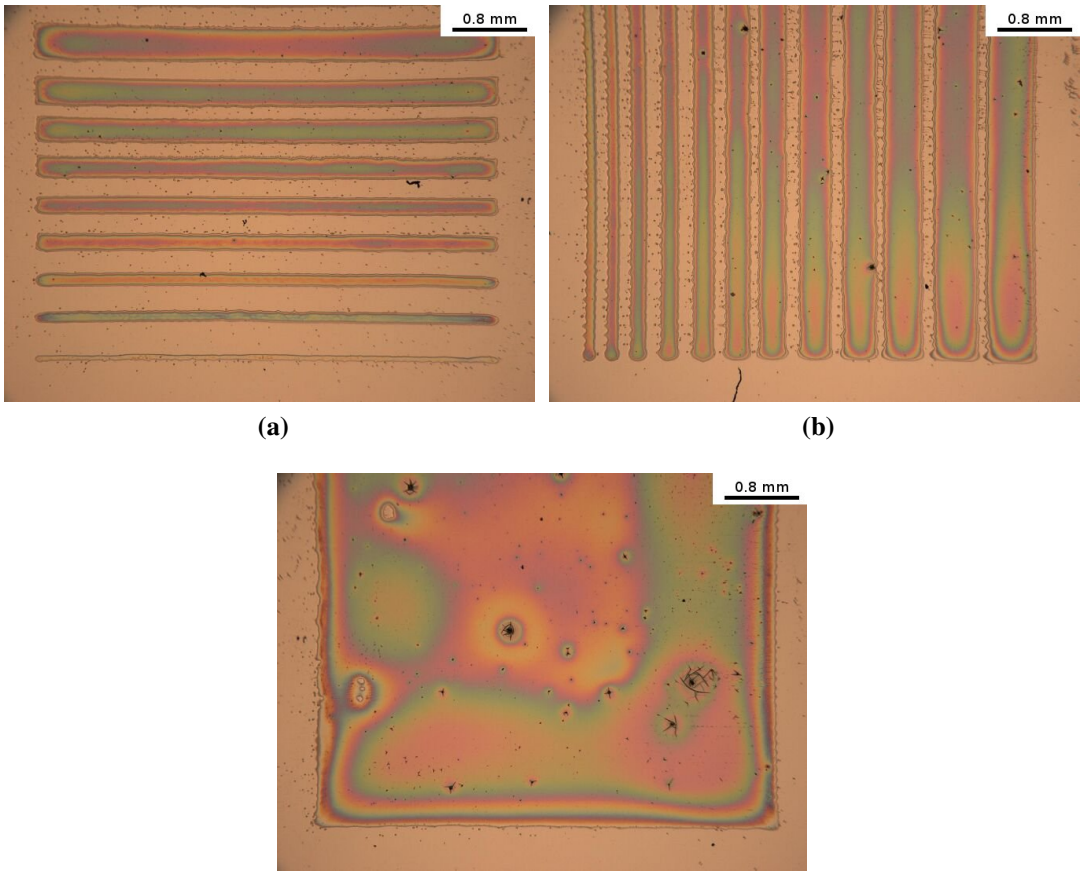

(a) **(b)**

(c)

Figure 6.31: Optical micrographs of the line array pattern printed with Sol-EG mixture at 20 *V* and CPH 0.35 *mm* with 4 nozzles: a) horizontal lines, b) vertical lines and c) square.

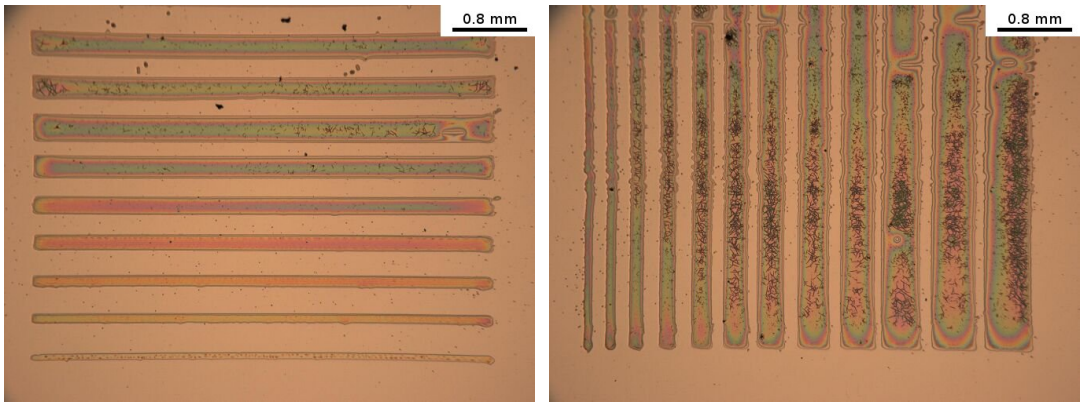

(a) **(b)**

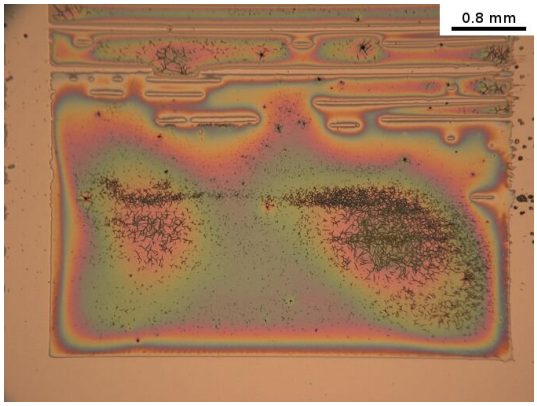

(c)

Figure 6.32: Optical micrographs of the line array pattern printed with Sol-EG mixture at 20 *V* and CPH 0.35 *mm* with 1 nozzle: a) horizontal lines, b) vertical lines and c) square.

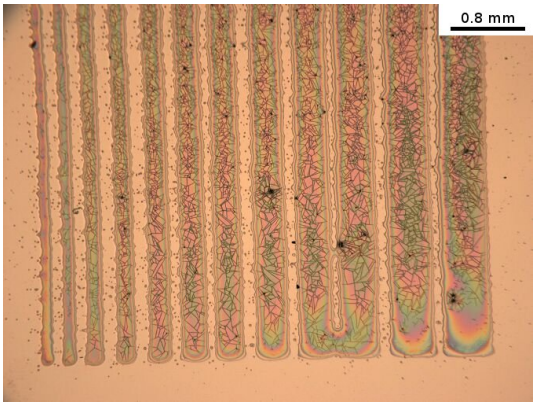

Figure 6.33: Optical micrograph of the line array pattern printed with Sol-EG mixture at 20 *V* and CPH 0.50 *mm* with 4 nozzles.

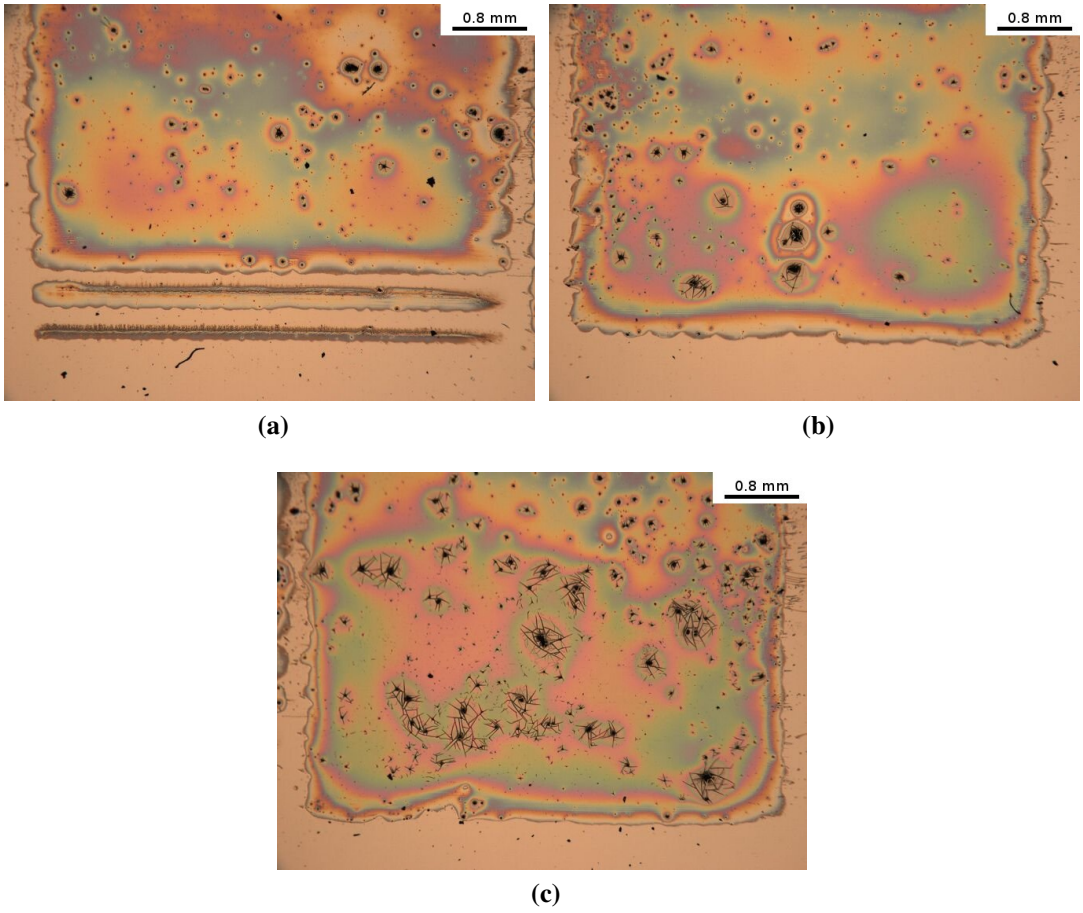

(a) **(b)**

(c)

Figure 6.34: Optical micrographs of the line array pattern printed with Sol-EG mixture at 25 *V* and CPH 0.35 *mm* with 16 nozzles: a) horizontal lines, b) vertical lines and c) square.

6.5.1.3 Printing with a firing voltage of 25 V

The maximum voltage used to print the line array pattern was 25 V. In figures 6.34, 6.35 and 6.36 the patterns printed with 16, 4 and 1 nozzle, respectively, are reported. When 16 nozzles were used it was not possible to detect lines. Only in figure 6.34 a it is possible to notice 2 horizontal lines. Moreover all the borders, even the ones parallel to the printing direction, were irregular, because of the spreading of the droplets on the substrate and on wet droplets previously deposited.

The quality was slightly increased by reducing the number of active nozzles to 4, as shown in figure 6.35. Under these conditions, it was possible to print better separated lines (figure

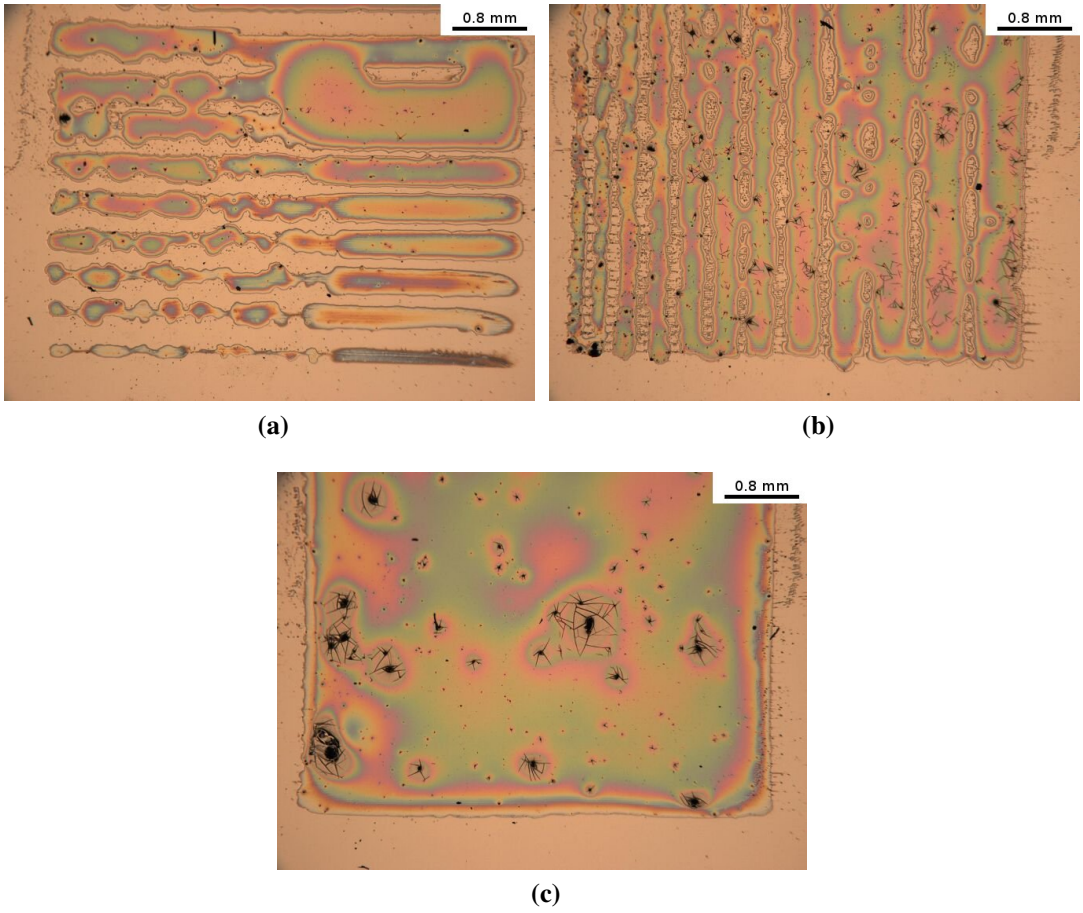

(a) **(b)**

(c)

Figure 6.35: Optical micrographs of the line array pattern printed with Sol-EG mixture at 25 *V* and CPH 0.35 *mm* with 4 nozzles: a) horizontal lines, b) vertical lines and c) square.

6.35 a and b) and the border quality was improved (see figure c).

Well separated lines were printed under the same conditions but using only 1 nozzle (figure 6.36). There are no horizontal or vertical lines touching each other, but a spray surrounds the printed area and covers the area between the lines, probably due to the partial obstruction of the nozzle, caused by the formation of dried ink film.

Figure 6.37 represents the pattern printed with 4 nozzles, at 25 *V* and at a CPH of 0.50 *mm*. By comparing it with figure 6.35 a, it can be seen that more lines are detectable, meaning an slight improvement in the printing quality. This was due to nozzle recovering by the tickle mode and/or by the cleaning cycle. However the borders are still not well defined.

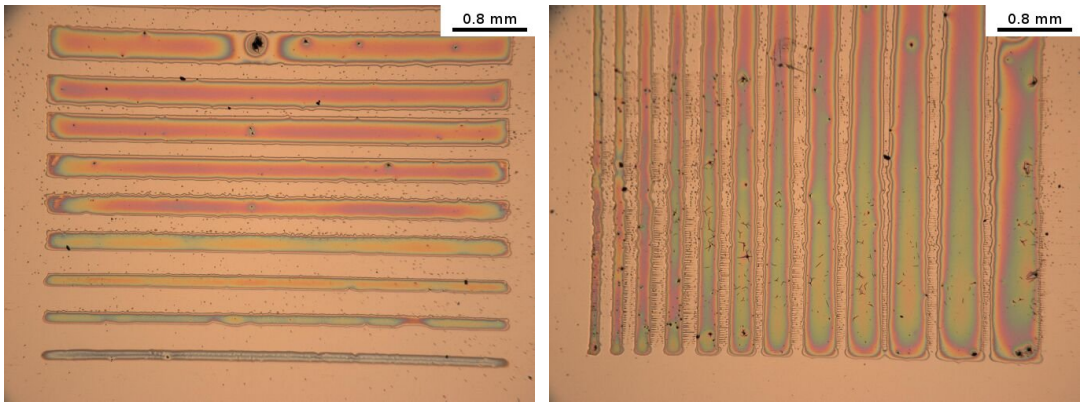

(a) **(b)**

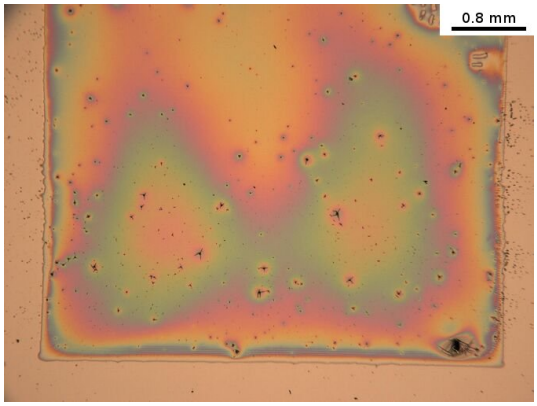

(c)

Figure 6.36: Optical micrographs of the line array pattern printed with Sol-EG mixture at 25 *V* and CPH 0.35 *mm* with 1 nozzle: a) horizontal lines, b) vertical lines and c) square.

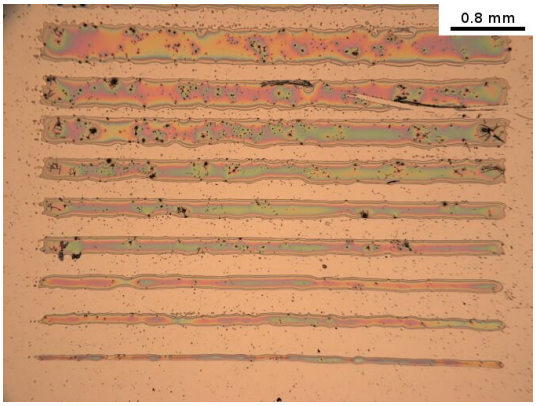

Figure 6.37: Optical micrograph of the line array pattern printed with Sol-EG mixture at 25 *V* and CPH 0.50 *mm* with 4 nozzles.

6.5.1.4 Summary

The purpose of this test was to determine if the printing quality was affected by different printing conditions. It was observed that a decrease in the number of the active nozzles leads to an improvement of the quality in both X and Y directions. This was due to increment in the time between the deposition of subsequent droplets. When 16 nozzles were used to print, the time for a single drop to dry before the arrival of the next one was reduced. Decreasing the number of active nozzle to 1 led to an increment of this time. In this way previous deposited drops were semidried and the coalescence with new drops was reduced, leading to a better printing quality. The quality was also enhanced by reducing the voltage at which the drops are ejected.

6.5.2 PZT inks

The same line array pattern was printed with the PZT inks described in table 6.3. The results obtained for inks MS1 and MS2 are reported in the following subsections. Inks formulated with higher solid loadings, were not suitable for ink jet printing, as the powder quickly blocked the nozzles.

6.5.2.1 Printing of 1 *vol%* PZT ink

Printing with a firing voltage of 15 V Figure 6.38 shows the pattern printed with 16 nozzles at 15 V and at a CPH of 0.35 mm. It can be seen that several lines are missing and the printed area is not clean. Several small drops of ink cover the area between the lines, denoting a partial blockage the nozzles. The missing lines suggest that some nozzles were completely blocked during printing and they were not recovered by the cartridge cleaning process. This means that the nozzles were clogged from the inside by the sedimented powder.

The same result was obtained when 4 nozzle were used to print the pattern, as shown

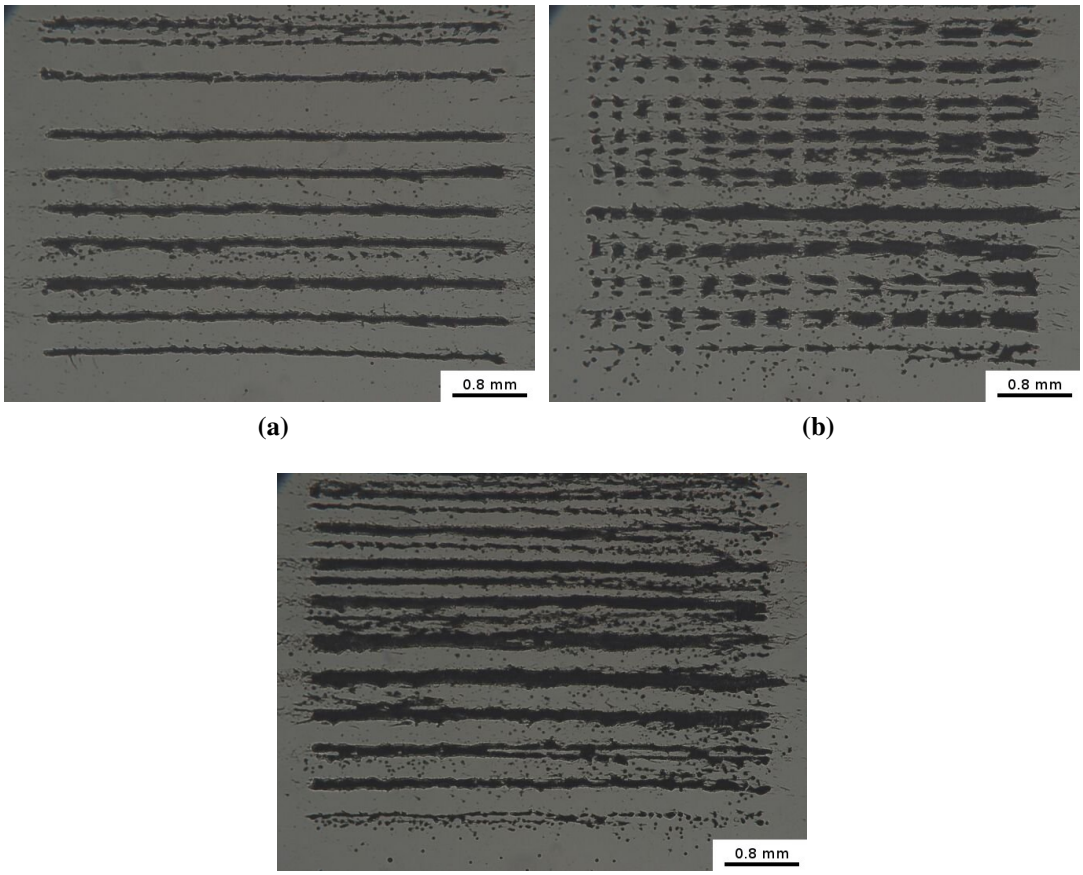

(a) **(b)**

(c)

Figure 6.38: Optical micrographs of the line array pattern printed with PZT ink MS1 at 15 V and CPH 0.35 mm with 16 nozzles: a) horizontal lines, b) vertical lines and c) square.

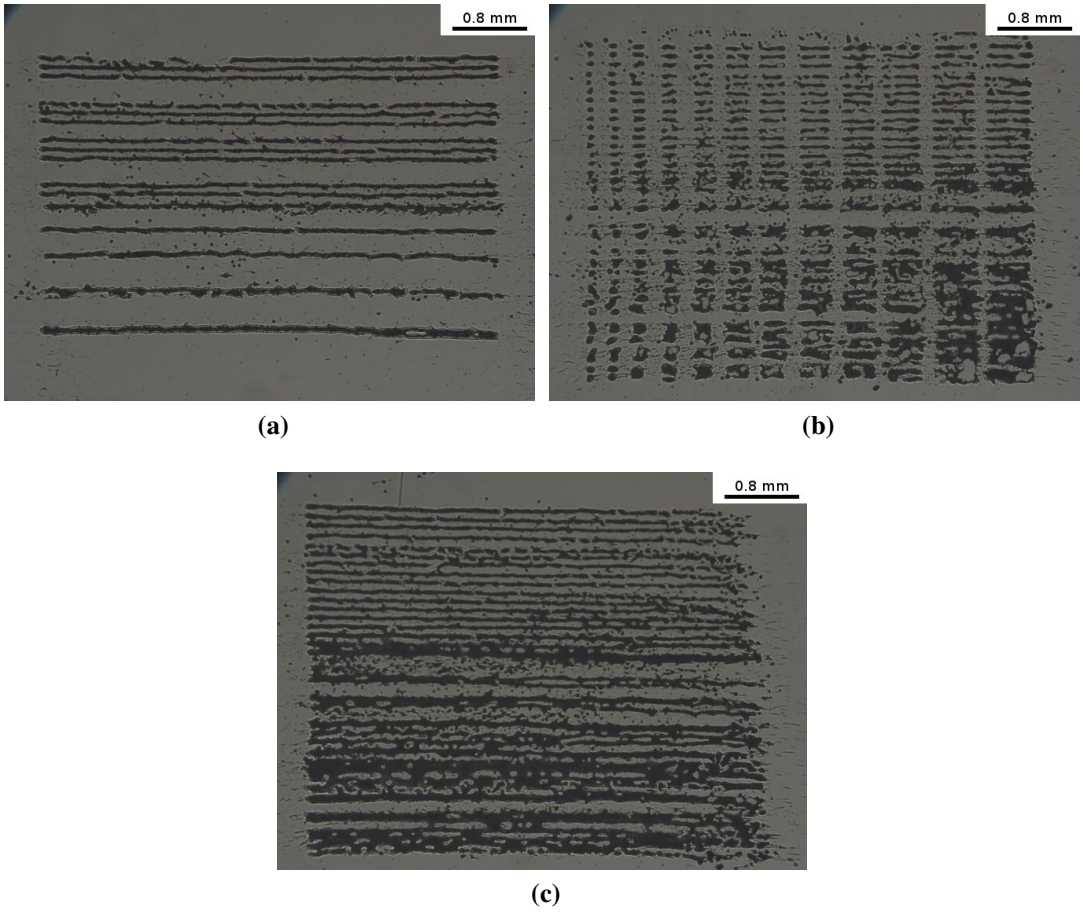

(a) **(b)**

(c)

Figure 6.39: Optical micrographs of the line array pattern printed with PZT ink MS1 at 15 *V* and CPH 0.35 *mm* with 4 nozzles: a) horizontal lines, b) vertical lines and c) square.

in figure 6.39. Again lines were missing, leading to the conclusion that the nozzles were clogged due to the settling of the PZT powder in the cartridge.

The number of active nozzles was reduced to 1, as was done with the PZT sol-EG mixture. The drop watcher function was used to look for an unclogged nozzle, but it was not found and therefore it was not possible to print the pattern.

Printing with a firing voltage of 20 V The pattern was then printed at a voltage of 20 V with 16 and 4 nozzles, figures 6.40 and 6.41, respectively. As in the case of 15 V, the pattern was not printed completely, resulting in line absences. When 4 nozzles were used to print,

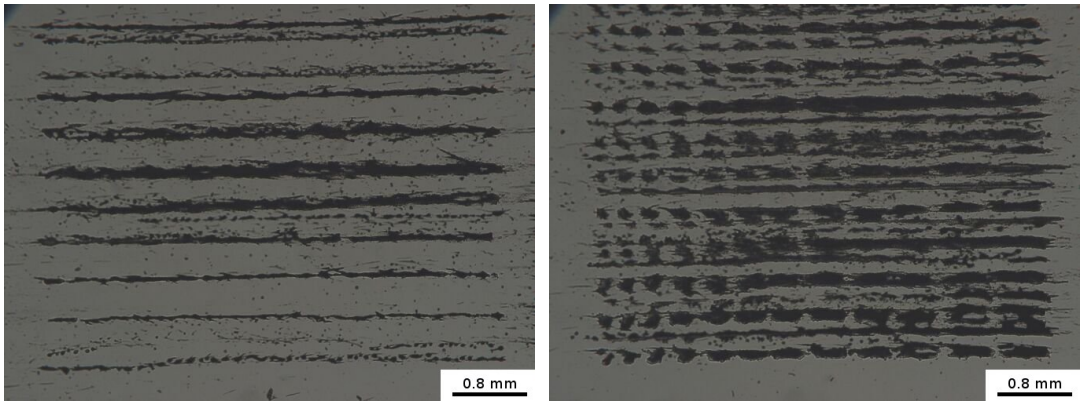

(a) **(b)**

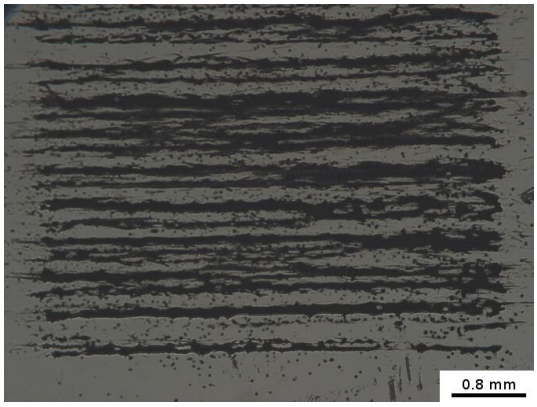

(c)

Figure 6.40: Optical micrographs of the line array pattern printed with PZT ink MS1 at 20 *V* and CPH 0.35 *mm* with 16 nozzles: a) horizontal lines, b) vertical lines and c) square.

the resulting pattern was more complete due to the cleaning cycle of the cartridge, but it was not possible to further reduce the number of the nozzles because of clogging.

Printing with a firing voltage of 25 V In order to be able to print at 25 V, another cartridge was filled with the MS1 ink. At this voltage more complete lines were printed, as shown in figure 6.42 a and b. However small drops of ink were deposited close to the printed area, indicating that the nozzles were partially obstructed. When the pattern was printed with 4 nozzles, figure 6.43, lines of ink were missing from the substrate and the number of small drops was reduced. This was a confirmation of nozzle blockages.

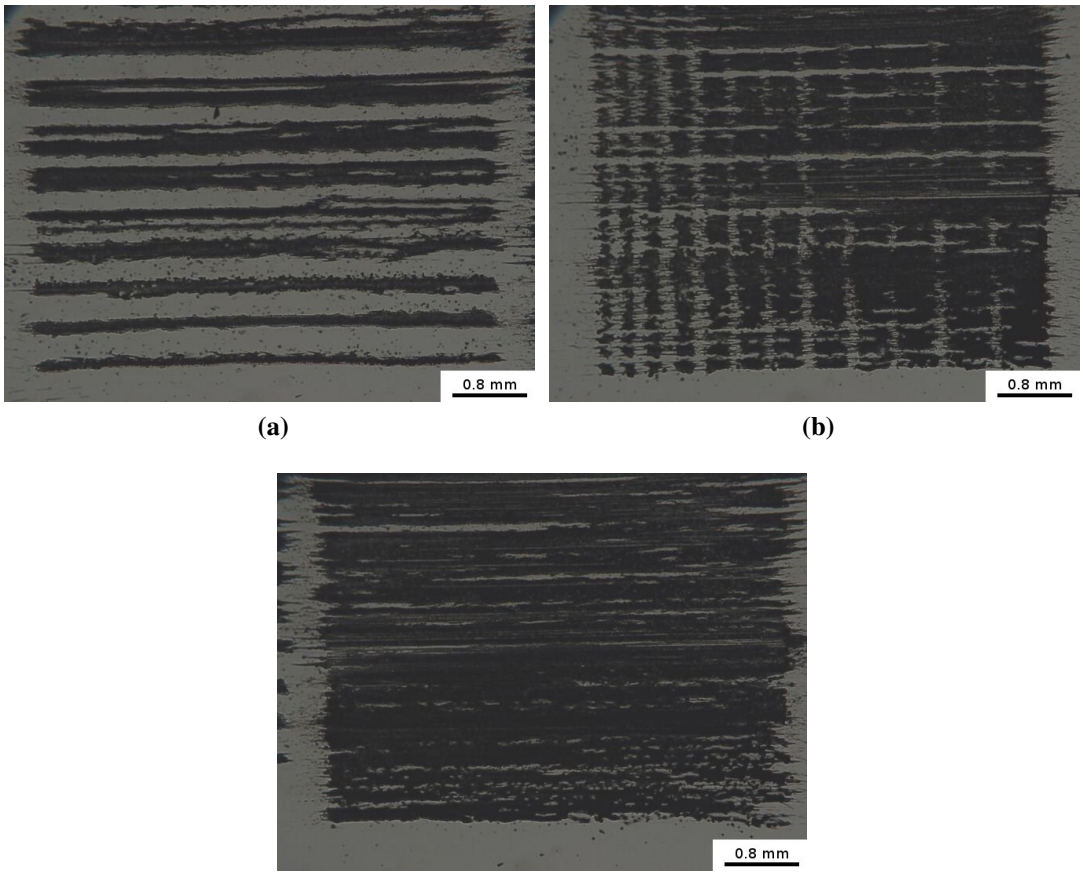

(a) **(b)**

(c)

Figure 6.41: Optical micrographs of the line array pattern printed with PZT ink MS1 at 20 V and CPH 0.35 mm with 4 nozzles: a) horizontal lines, b) vertical lines and c) square.

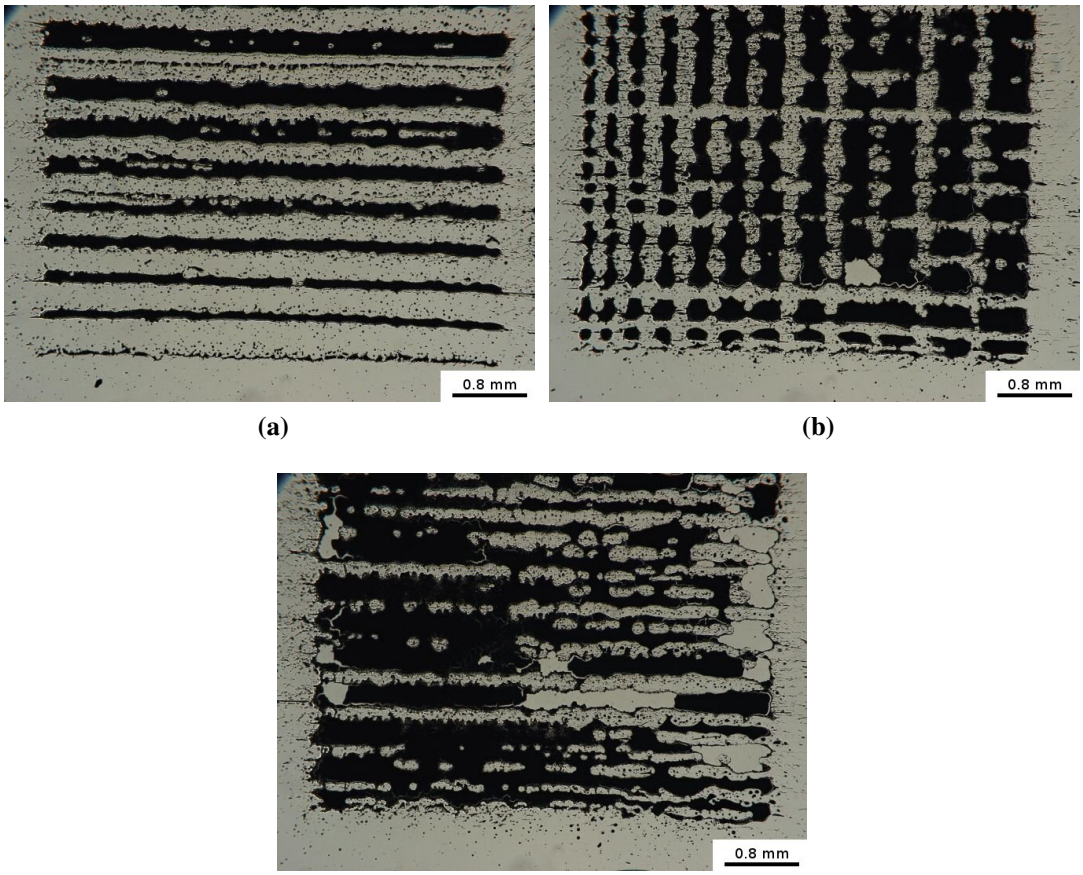

(a) **(b)**

(c)

Figure 6.42: Optical micrographs of the line array pattern printed with PZT ink MS1 at 25 V and CPH 0.35 mm with 16 nozzles: a) horizontal lines, b) vertical lines and c) square.

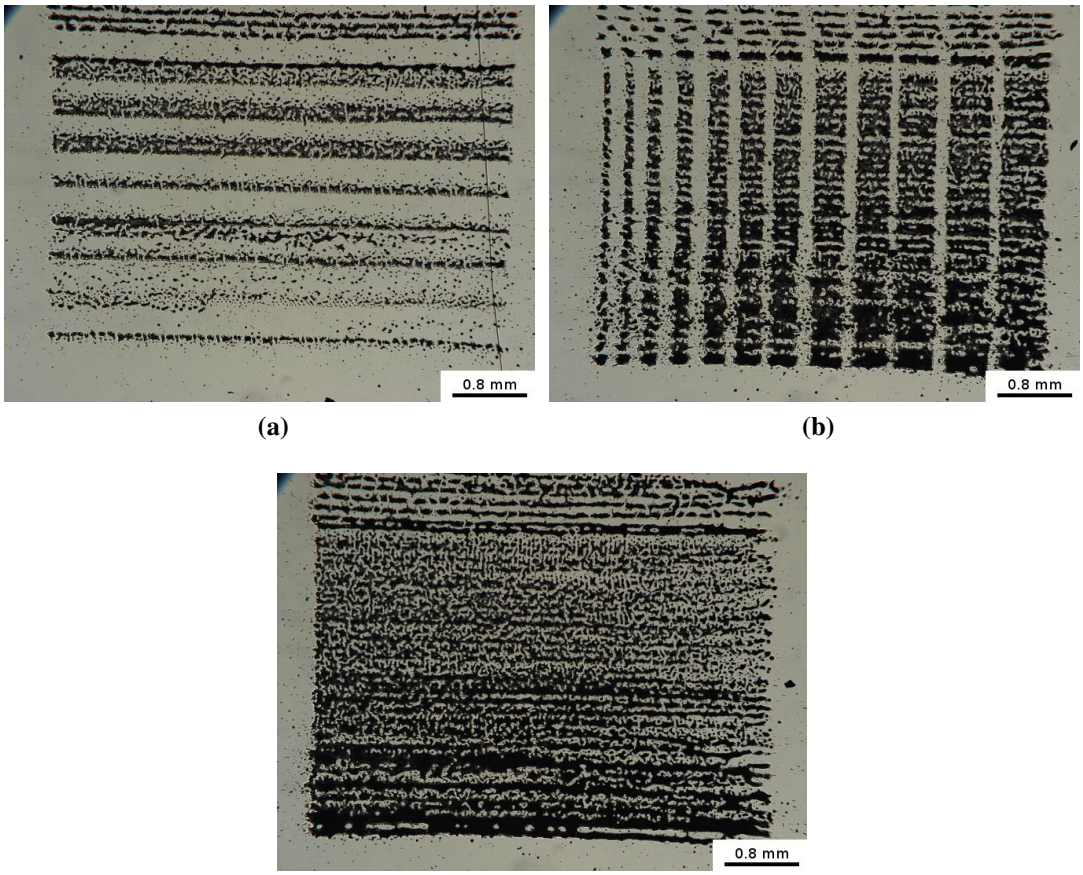

(a) **(b)**

(c)

Figure 6.43: Optical micrographs of the line array pattern printed with PZT ink MS1 at 25 V and CPH 0.35 mm with 4 nozzles: a) horizontal lines, b) vertical lines and c) square.

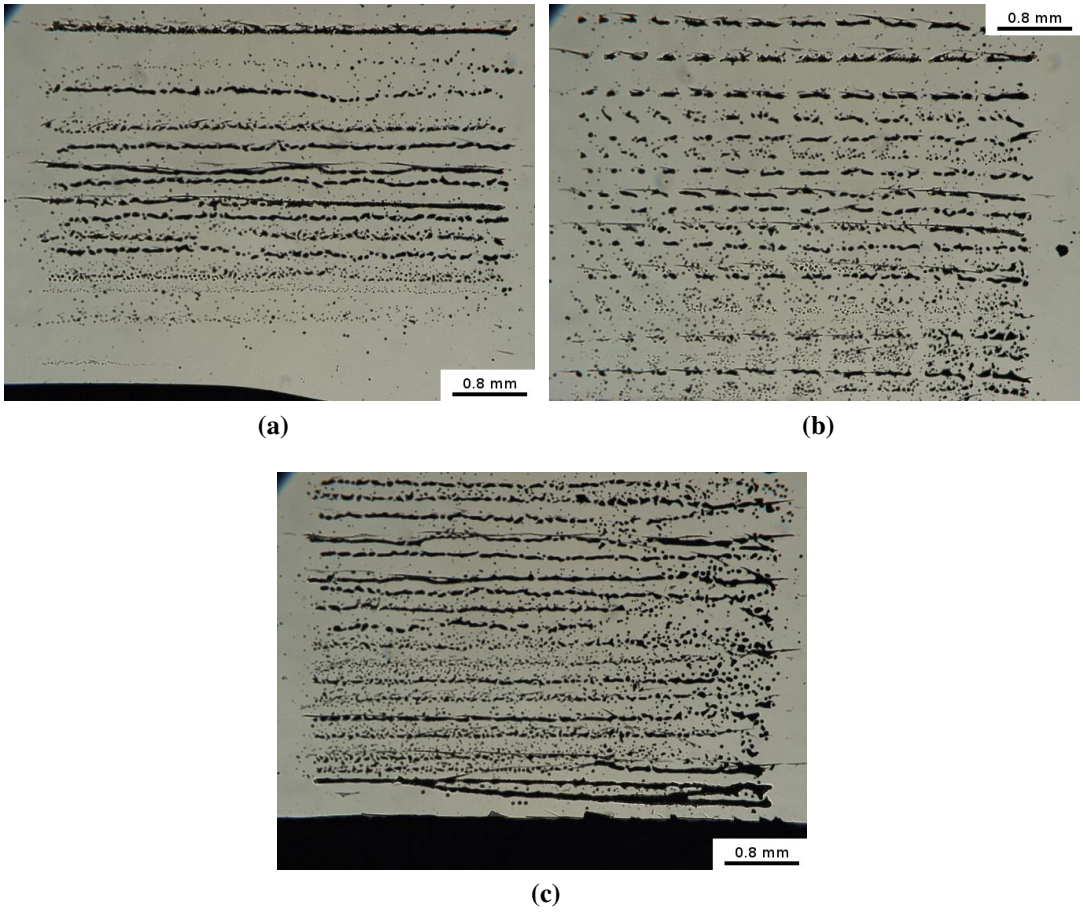

(a) **(b)**

(c)

Figure 6.44: Optical micrographs of the line array pattern printed with PZT ink MS2 at 25 *V* and CPH 0.35 *mm* with 16 nozzles: a) horizontal lines, b) vertical lines and c) square.

6.5.2.2 Printing of 2 *vol%* PZT ink

MS2 (2 *vol%* of PZT powder) was printed. The printing conditions were changed as in the case of MS1, but with the new ink it was possible to print the pattern only at a firing voltage of 25 *V*, as shown in figures 6.44 and 6.45. Moreover, it was not possible to print with 1 nozzle because of clogging. It can be seen that reducing the number of active nozzles from 16 to 4 led to a reduction of the amount of pattern printed on the silicon wafer due to powder sedimentation at the nozzle inlets.

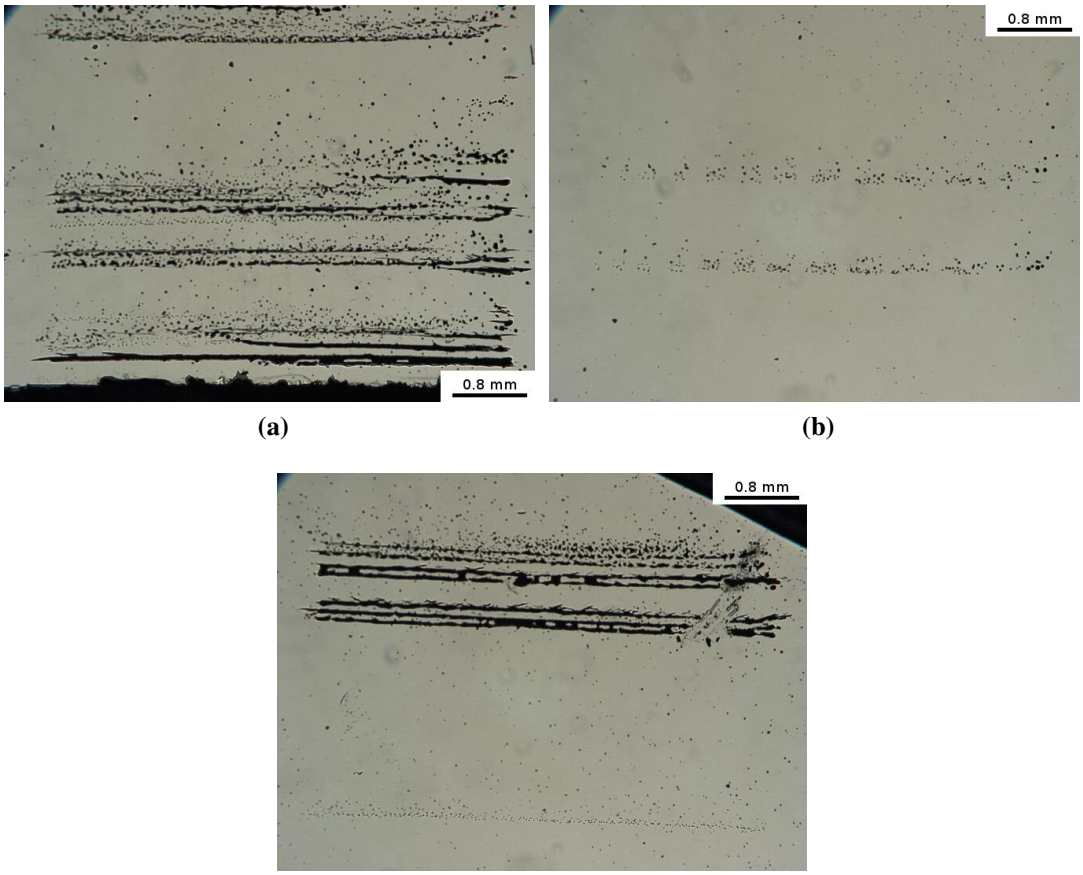

(a) **(b)**

(c)

Figure 6.45: Optical micrographs of the line array pattern printed with PZT ink MS2 at 25 V and CPH 0.35 mm with 4 nozzles: a) horizontal lines, b) vertical lines and c) square.

6.6 Conclusive summary

PZT inks with different solid loading were formulated starting from MSS powder. Two different patterns were printed on silicon wafer in order to determine the influence of printing parameters and powder amount on spreading and printing quality.

- Increasing solid loading:
  - greater sedimentation that led to quick nozzle clogging
  - less pronounced cracks formation
  - shrinkage reduced
- Increasing number of active nozzles:
  - reduced printing quality in X and Y direction
  - enhancement of printing velocity
- Increasing voltage:
  - increment in the droplet size
  - increment in the spreading factor
- Increasing cartridge print height (CPH):
  - not a significant effect.

PZT ink formulated starting from EHDA powder was not successfully printed. Quick nozzle clogging occurred due to a non correct formulation.

Chapter 7

Conclusions and Further work

7.1 Conclusions

- Synthesis of PZT powder in the submicron range
  - EHDA. Spherical particles of $\sim$250 *nm* in diameter were synthesised under the following conditions: 0.2 *M* PZT sol, flow rate of 0.2 $ml \cdot h^{-1}$, needle-bottom electrode distance of 3 *cm* and heating temperature of 520^oC. A further heat treatment was needed to ensure stability of particles in the sol carrier fluid. The process has low yield.
  - MSS. Almost spherical particles with diameter of $\sim$340 *nm* were synthesised at 850^oC for 60 minutes with a ramp rate of 3.3$^oC \cdot min^{-1}$. No further heat treatment was needed to stabilise particles in sol carrier fluid. On the basis of the obtained results, a reaction mechanism for the synthesis of PZT has been proposed, where dissolved Pb reacts with insoluble TiO_2 forming $PbTiO_3$. Then ZrO_2 diffuses into and react with Pb and PT to form PZT. Particle coarsening occurs alongside Zr diffusion, presenting a challenge to obtain small size particles.
- Formulation of stable inks

- EHDA. The EHDA ink was found to be not suitable for ink jet printing application due to a formulation that led to a fast nozzle clogging.
- MSS. Inks with different solid loadings were prepared and tested by IJP.

- Evaluation of inks and films
  - Individual drops were printed on the substrate to understand the ink behaviour. Drop size was reduced by increasing the powder loading from 0 to 1 vol%. It also increases with increasing the firing voltage. CPH did not have a significant effect on droplet dimensions.
  - Printing quality was enhanced by reducing the number of ejecting nozzles and by the use of low voltages.
  - Printing was possible only at low solid content, 0, 1 and 2 vol%. At higher solid loading the powder sedimentation was too fast, that resulted in nozzle clogging, preventing the ejection of droplets. After sintering the appearance of cracks was detected on the relics.
  - Cracking was reduced by increasing powder loading.
  - The particle stability in the sol carrier fluid was poor due to the high density of the powder and due to the inability to produce very small PZT particles.

7.2 Further work

- EHDA is a very promising technique for the synthesis of spherical particles in the nanoscale. The big limit of this process is the low amount of powder producible. This problem can be overcome through the use of multiple EHDA heads. A system composed of parallel multiple needles can be built in order to increase the process productivity.
- To decrease the size of the particles obtained by EHDA, higher voltages can be applied.

In this study only voltages between 4 and 7.5 kV were applied due to instrument limitation. A voltage supply that allows to apply higher voltages can help to reduce droplet size and hence the final particle size.

- Particle stabilisation is really important for obtaining an ink suitable for ink jet printing. For EHDA-ink a new formulation has to be studied to reduce the particle sedimentation rate. To do so, a higher amount of powder is needed. MSS-ink formulation can also be improved to increase the solid loading: a screening of dispersants can be done in order to find the product that best reduces the powder sedimentation rate.
- During the synthesis of PZT by MSS, particle coarsening occurs. This phenomenon leads to the formation of large particles. In MSS, once the product is formed, it leaves the reaction by precipitation from the molten salt. After precipitation it lies on the bottom of the crucible, where coarsening occurs. Stirring the mixture during the reaction could help to reduce the coarsening process by separating particles during critical coarsening stage, leading to the formation of smaller particles.
- The formation of irregular PZT particles was noted during molten salt synthesis. Since the target was the obtainment of small and spherical particles, MSS can be further investigated in order to better understand the influence of process parameters on powder shape.
- The powder synthesised by both EHDA and MSS was pure PZT. In order to maintain the system as simple as possible, no dopants were added to the formulation. However, the properties of the films prepared with a MSS-powder based ink were really poor, due to the absence of dopants. To increase these properties, the addition of dopants can be done in both the processes: in the PZT sol formulation (EHDA) and in the starting mixed oxides (MSS). Moreover, their effect on particle size and shape can be studied.
- Improvements on both powder and ink are needed to reduce the appearance of cracks

in the sintered samples and to enhance the final properties. Once the conditions for a stable ink have been determined, the solid loading can be increased. In this way, the presence of cracks can be eliminated and thick films can be easily obtained by ink jet printing.

- To identify the ink behaviour on the substrate, the evaluation of the contact angle is needed. This will help to determine a more accurate droplet spreading on platinised silicon wafer and hence to improve the printing quality.
- Further investigations have to be done in order to understand the PZT sol-EG mixture behaviour in the line array pattern. In particular the role of surface tension and viscosity, particularly at the length scale present in the droplets and drying features.

Bibliography

[1] A. J. Moulson. *Electroceramics: materials, properties, applications*. John Wiley and Sons, 2003.

[2] N. Setter. *ABC of piezoelectricity and piezoelectric materials*, chapter 1, page 1. Piezoelectric materials in devices : extended reviews on current and emerging piezoelectric materials, technology, and application. 2002.

[3] R. A. Dorey and R. W. Whatmore. Electroceramic thick film fabrication for mems. *Journal of Electroceramics*, 12(1-2):19–32, 2004.

[4] N. Setter. Electroceramics: Looking ahead. *Journal of the European Ceramic Society*, 21(10-11):1279–1293, 2001.

[5] W. Wersing. *Applications of piezoelectric materials: an introductory review*, chapter 2, page 29. Piezoelectric materials in devices: extended reviews on current and emerging piezoelectric materials, technology, and application.

[6] W. W. Wolny. Application driven industrial development of piezoceramics. *Journal of the European Ceramic Society*, 25(12 SPEC. ISS.):1971–1976, 2005.

[7] R. W. Whatmore. Pyroelectric devices and materials. *Reports on progress in physics*, (49):1335–1386, 1986.

[8] R. Maas, M. Koch, N. R. Harris, N. M. White, and A. G. R. Evans. Thick-film printing of PZT onto silicon. *Materials Letters*, 31(1-2):109–112, 1997.

[9] S. LeDren, L. Simon, P. Gonnard, M. Troccaz, and A. Nicolas. Investigation of factors affecting the preparation of (pzt) thick films. *Materials Research Bulletin*, 35(12): 2037–2045, 2000.

[10] M. H Zhao, R. Fu, D. Lu, and T. Y Zhang. Critical thickness for cracking of $Pb(Zr_{0.53}Ti_{0.47})O_3$ thin films deposited on Pt/Ti/Si(100) substrates. *Acta Materialia*, 50(17):4241–4254, 2002.

[11] B. H Chen, C. L Huang, and L. Wu. Crack alleviation processing of lead zirconate titanate thin films deposited by sol-gel method. *Thin Solid Films*, 441(1-2):13–18, 2003.

[12] D. P. J. Cotton, P. H. Chappell, A. Cranny, and N. M. White. A new binderless thick-film piezoelectric paste. *Journal of Materials Science: Materials in Electronics*, 18 (10):1037–1044, 2007.

[13] S. Bonnas and H. Elsenheimer. *Fabrication of ceramic microcomponents by electrophoretic deposition*, page 171. Whittles Publishing, 2009.

[14] D. Wallace, D. Hayes, C. Ting, V. Shah, D. Radulescu, P. Cooley, K. Wachtler, and A. Nallani. Ink-jet as a mems manufacturing tool. In *International Conference on Integration and Commercialization of Micro and Nanosystems 2007*, volume B, pages 1161–1168, 2007.

[15] J. A. Lewis, J. E. Smay, J. Stuecker, and J. CesaranoIII. Direct ink writing of three-dimensional ceramic structures. *Journal of the American Ceramic Society*, 89(12): 3599–3609, 2006.

[16] S. Linardos, Q. Zhang, and J. R. Alcock. Preparation of sub-micron PZT particles with the sol-gel technique. *Journal of the European Ceramic Society*, 26(1-2):117–123, 2006.

[17] S. Linardos, Q. Zhang, and J. R. Alcock. An investigation of the parameters effec-

ting the agglomerate size of a PZT ceramic powder prepared with a sol-gel technique. *Journal of the European Ceramic Society*, 27(1):231–235, 2007.

[18] G. Mu, S. Yang, J. Li, and M. Gu. Synthesis of PZT nanocrystalline powder by a modified sol-gel process using water as primary solvent source. *Journal of Materials Processing Technology*, 182(1-3):382–386, 2007.

[19] Y. Deng, L. Liu, Y. Cheng, C. W Nan, and S. J Zhao. Hydrothermal synthesis and characterization of nanocrystalline (PZT) powders. *Materials Letters*, 57(11):1675–1678, 2003.

[20] A. Wu, I. M. Miranda Salvado, P. M. Vilarinho, and J. L. Baptista. Lead zirconate titanate prepared from different zirconium and titanium precursors by sol-gel. *Journal of the American Ceramic Society*, 81(10):2640–2644, 1998.

[21] R. M. Piticescu, R. R. Piticescu, D. Taloi, and V. Badilita. Hydrothermal synthesis of ceramic nanomaterials for functional applications. *Nanotechnology*, 14(2):312–317, 2003.

[22] A. L. Fernandez-Osorio, A. Vazquez-Olmos, E. Mata-Zamora, and J. M. Saniger. Preparation of free-standing $Pb(Zr_{0.53}Ti_{0.47})O_3$ nanoparticles by sol-gel method. *Journal of Sol-Gel Science and Technology*, 42(2):145–149, 2007.

[23] C. Liu, B. Zou, A. J. Rondinone, and Z. J. Zhang. Sol-gel synthesis of free-standing ferroelectric lead zirconate titanate nanoparticles. *Journal of the American Chemical Society*, 123(18):4344–4345, 2001.

[24] D. Liu, H. Zhang, W. Cai, X. Wu, and L. Zhao. Synthesis of (PZT) nanocrystalline powder by a modified sol-gel process using zirconium oxynitrate as zirconium source. *Materials Chemistry and Physics*, 51(2):186–189, 1997.

[25] J. Van Erven, R. Moerman, and J. C. M. Marijnissen. Platinum nanoparticle production by EHDA. *Aerosol Science and Technology*, 39(10):941–946, 2005.

[26] I. W. Lenggoro, B. Xia, K. Okuyama, and J. F. De la Mora. Sizing of colloidal nanoparticles by electrospray and differential mobility analyzer methods. *Langmuir*, 18 (12):4584–4591, 2002.

[27] H. Zhou, Y. Mao, and S. S. Wong. Probing structure-parameter correlations in the molten salt synthesis of $BaZrO_3$ perovskite submicrometer-sized particles. *Chemistry of Materials*, 19(22):5238–5249, 2007.

[28] H. Zhou, Y. Mao, and S. S. Wong. Shape control and spectroscopy of crystalline $BaZrO_3$ perovskite particles. *Journal of Materials Chemistry*, 17(17):1707–1713, 2007.

[29] F. Bortolani and R. A. Dorey. Synthesis of spherical lead zirconate titanate (PZT) nanoparticles by electrohydrodynamic atomisation. *Advances in Applied Ceramics*, 108(6):332–337, 2009.

[30] C. Kittel. *Introduction to solid state physics*. 1976.

[31] D. Damjanovic. Ferroelectric, dielectric and piezoelectric properties of ferroelectric thin films and ceramics. *Reports on Progress in Physics*, 61(11):1267–1324, 1998.

[32] B. Jaffe, R. S. Roth, and S. Marzullo. Piezoelectric properties of lead zirconate-lead titanate solid-solution ceramics. *Journal of Applied Physics*, 25(6):809–810, 1954.

[33] G. Yi, Z. Wu, and M. Sayer. Preparation of $Pb(Zr,Ti)O_3$ thin films by sol gel processing: Electrical, optical, and electro-optic properties. *Journal of Applied Physics*, 64 (5):2717–2724, 1988.

[34] Ferroperm piezoceramics. High quality components and materials for the electronic industry, www.ferroperm-piezo.com.

[35] R. N. Torah, S. P. Beeby, M. J. Tudor, and N. M. White. Thick-film piezoceramics and devices. *Journal of Electroceramics*, 19(1):95–110, 2007.

[36] A. Hizebry, H. El Attaoui, M. Saadaoui, J. Chevalier, and G. Fantozzi. Effect of Nb and K doping on the crack propagation behaviour of lead zirconate titanate ceramics. *Journal of the European Ceramic Society*, 27(2-3):557–560, 2007.

[37] K. W. Kwok, K. P. Kwok, R. C. W. Tsang, H. L. W. Chan, and C. L. Choy. Preparation and piezoelectric properties of sol-gel-derived Nb-doped (PZT) films for MEMS applications. *Integrated Ferroelectrics*, 80(1):155–162, 2006.

[38] C. Zinck, D. Pinceau, E. Defay, E. Delevoye, and D. Barbier. Development and characterization of membranes actuated by a PZT thin film for mems applications. *Sensors and Actuators, A: Physical*, 115(2-3 SPEC. ISS.):483–489, 2004.

[39] Z. Wang, J. Miao, and W. Zhu. Piezoelectric thick films and their application in MEMS. *Journal of the European Ceramic Society*, 27(13-15):3759–3764, 2007.

[40] Q. Q. Zhang, F. T. Djuth, Q. F. Zhou, C. H. Hu, J. H. Cha, and K. K. Shung. High frequency broadband PZT thick film ultrasonic transducers for medical imaging applications. *Ultrasonics*, 44(SUPPL.), 2006.

[41] P. Marechal, F. Levassort, J. Holc, L. P Tran-Huu-Hue, M. Kosec, and M. Lethiecq. High frequency transducer based on integrated piezoelectric thick films for medical imaging. In *2005 IEEE Ultrasonics Symposium*, volume 4, pages 2223–2226, September 2005 .

[42] M. Lethiecq, F. Levassort, G. Feuillard, and L. P. Tran Huu Hue. *Piezoelectric materials for ultrasonic medical diagnostics*, chapter 11, page 211. Piezoelectric materials in devices : extended reviews on current and emerging piezoelectric materials, technology, and application.

[43] M. Heule, S. Vuillemin, and L. J. Gauckler. Powder-based ceramic meso- and microscale fabrication processes. *Advanced Materials*, 15(15):1237–1245, 2003.

[44] E. S. Thiele and N. Setter. Lead zirconate titanate particle dispersion in thick-film ink

formulations. *Journal of the American Ceramic Society*, 83(6):1407–1412, 2000.

[45] J. Akedo and M. Lebedev. Powder preparation in aerosol deposition method for lead zirconate titanate thick films. *Japanese Journal of Applied Physics, Part 1: Regular Papers and Short Notes and Review Papers*, 41(11 B):6980–6984, 2002.

[46] R. A. Dorey, S. A. Rocks, F. Dauchy, D. Wang, F. Bortolani, and E. Hugo. Integrating functional ceramics into microsystems. *Journal of the European Ceramic Society*, 28 (7):1397–1403, 2008.

[47] A. Wu, P. M. Vilarinho, I. M. M. Salvado, J. L. Baptista, C. M. DeJesus, and M. F. DaSilva. Characterization of seeded sol-gel lead zirconate titanate thin films. *Journal of the European Ceramic Society*, 19(6-7):1403–1407, 1999.

[48] R. A. Dorey, S. B. Stringfellow, and R. W. Whatmore. Effect of sintering aid and repeated sol infiltrations on the dielectric and piezoelectric properties of a PZT composite thick film. *Journal of the European Ceramic Society*, 22(16):2921–2926, 2002.

[49] D. A. Barrow, T. E. Petroff, and M. Sayer. Thick ceramic coatings using a sol gel based ceramic-ceramic 0-3 composite. *Surface and Coatings Technology*, 76-77(1 -3 pt 1):113–118, 1995.

[50] J. Ma and W. Cheng. Electrophoretic deposition of lead zirconate titanate ceramics. *Journal of the American Ceramic Society*, 85(7):1735–1737, 2002.

[51] C. Mack. *Fundamental principles of optical lithography: the science of microfabrication*. Wiley, 2007.

[52] C. J. Brinker, A. J. Hurd, P. R. Schunk, G. C. Frye, and C. S. Ashley. Review of sol-gel thin film formation. *Journal of Non-Crystalline Solids*, 147-148(C):424–436, 1992.

[53] D. B. Mitzi. Solution-processed inorganic semiconductors. *Journal of Materials Chemistry*, 14(15):2355–2365, 2004.

[54] L. Mosher, C. M. Waits, B. Morgan, and R. Ghodssi. Double-exposure grayscale photolithography. *Journal of Microelectromechanical Systems*, 18(2):308–315, 2009.

[55] Y. Zhang, C. Liu, and D. Whalley. Direct-write techniques for maskless production of microelectronics: A review of current state-of-the-art technologies. In *International Conference on Electronic Packaging Technology and High Density Packaging, (ICEPT-HDP '09)*, pages 497–503, August 2009.

[56] J. T. Zeng, K. W. Kwok, and H. L. W. Chan. $K_xNa_{1-x}NbO_3$ powder synthesized by molten-salt process. *Materials Letters*, 61(2):409–411, 2007.

[57] J. Brunahl and A. M. Grishin. Piezoelectric shear mode drop-on-demand inkjet actuator. *Sensors and Actuators, A: Physical*, 101(3):371–382, 2002.

[58] G. D. Martin, S. D. Hoath, and I. M. Hutchings. Inkjet printing - the physics of manipulating liquid jets and drops. *Journal of Physics: Conference Series*, 105(1), 2008.

[59] J. A. Lewis. Direct-write assembly of ceramics from colloidal inks. *Current Opinion in Solid State and Materials Science*, 6(3):245–250, 2002.

[60] J. E. Smay, S. S. Nadkarni, and J. Xu. Direct writing of dielectric ceramics and base metal electrodes. *International Journal of Applied Ceramic Technology*, 4(1):47–52, 2007.

[61] X. Zhao, J. R. G. Evans, M. J. Edirisinghe, and J. H. Song. Formulation of a ceramic ink for a wide-array drop-on-demand ink-jet printer. *Ceramics International*, 29(8): 887–892, 2003.

[62] J. H. Song and H. M. Nur. Defects and prevention in ceramic components fabricated by inkjet printing. *Journal of Materials Processing Technology*, 155-156(1-3):1286–1292, 2004.

[63] D. H. Lee and B. Derby. Preparation of (PZT) suspensions for direct ink jet printing. *Journal of the European Ceramic Society*, 24(6):1069–1072, 2004.

[64] T. Wang and B. Derby. Ink-jet printing and sintering of PZT. *Journal of the American Ceramic Society*, 88(8):2053–2058, 2005.

[65] P. F. Blazdell and J. R. G. Evans. Application of a continuous ink jet printer to solid freeforming of ceramics. *Journal of Materials Processing Technology*, 99(1):94–102, 2000.

[66] V. G. Shah and D. J. Hayes. Trimming and printing of embedded resistors using demand-mode ink jet technology and conductive polymer. Technical report, March 24-28 2002.

[67] M. Ibrahim, T. Otsubo, H. Narahara, H. Koresawa, and H. Suzuki. Inkjet printing resolution study for multi-material rapid prototyping. *JSME International Journal, Series C: Mechanical Systems, Machine Elements and Manufacturing*, 49(2):353–360, 2006.

[68] J. Sumerel, J. Lewis, A. Doraiswamy, L. F. Deravi, S. L. Sewell, A. E. Gerdon, D. W. Wright, and R. J. Narayan. Piezoelectric ink jet processing of materials for medical and biological applications. *Biotechnology journal*, 1(9):976–987, 2006.

[69] J. Windle and B. Derby. Ink jet printing of PZT aqueous ceramic suspensions. *Journal of Materials Science Letters*, 18(2):87–90, 1999.

[70] H. Dong, W. W. Carr, and J. F. Morris. An experimental study of drop-on-demand drop formation. *Physics of Fluids*, 18(7), 2006.

[71] S. Okamura, R. Takeuchi, and T. Shiosaki. Fabrication of ferroelectric Pb(Zr,Ti)O_3 thin films with various Zr/Ti ratios by ink-jet printing. *Japanese Journal of Applied Physics, Part 1: Regular Papers and Short Notes and Review Papers*, 41(11 B):6714–6717, 2002.

[72] S. B. Fuller, E. J. Wilhelm, and J. M. Jacobson. Ink-jet printed nanoparticle microelectromechanical systems. *Journal of Microelectromechanical Systems*, 11(1):54–60, 2002.

[73] J. B. Szczech, C. M. Megaridis, D. R. Gamota, and J. Zhang. Fine-line conductor manufacturing using drop-on-demand PZT printing technology. *IEEE Transactions on Electronics Packaging Manufacturing*, 25(1):26–33, 2002.

[74] N. Reis, C. Ainsley, and B. Derby. Viscosity and acoustic behavior of ceramic suspensions optimized for phase-change ink-jet printing. *Journal of the American Ceramic Society*, 88(4):802–808, 2005.

[75] K. A. M. Seerden, N. Reis, J. R. G. Evans, P. S. Grant, J. W. Halloran, and B. Derby. Ink-jet printing of wax-based alumina suspensions. *Journal of the American Ceramic Society*, 84(11):2514–2520, 2001.

[76] R. Noguera, M. Lejeune, and T. Chartier. 3D fine scale ceramic components formed by ink-jet prototyping process. *Journal of the European Ceramic Society*, 25(12 SPEC. ISS.):2055–2059, 2005.

[77] Air Products. Surfynol CT-324 dispersant datasheet, www.airproducts.com.

[78] P. Calvert. Inkjet printing for materials and devices. *Chemistry of Materials*, 13(10): 3299–3305, 2001.

[79] D. Soltman and V. Subramanian. Inkjet-printed line morphologies and temperature control of the coffee ring effect. *Langmuir*, 24(5):2224–2231, 2008.

[80] S. C Gong. Spreading of droplets impacting on smooth solid surface. *Japanese Journal of Applied Physics, Part 1: Regular Papers and Short Notes and Review Papers*, 44(5 A):3323–3324, 2005.

[81] H. C. Jung, S. H Cho, J. W. Joung, and Y. S Oh. Studies on inkjet-printed conducting

lines for electronic devices. *Journal of Electronic Materials*, 36(9):1211–1218, 2007.

[82] J. Stringer and B. Derby. Limits to feature size and resolution in ink jet printing. *Journal of the European Ceramic Society*, 29(5):913–918, 2009.

[83] M. Lejeune, T. Chartier, C. Dossou-Yovo, and R. Noguera. Ink-jet printing of ceramic micro-pillar arrays. *Journal of the European Ceramic Society*, 29(5):905–911, 2009.

[84] B. Cappi, E. Ozkol, J. Ebert, and R. Telle. Direct inkjet printing of Si_3N_4: Characterization of ink, green bodies and microstructure. *Journal of the European Ceramic Society*, 28(13):2625–2628, 9 2008.

[85] S. Bose and A. Banerjee. Novel synthesis route to make nanocrystalline lead zirconate titanate powder. *Journal of the American Ceramic Society*, 87(3):487–489, 2004.

[86] C. Y. Lee, N. H. Tai, and S. H. Hsieh. Synthesis of nano-sized polycrystalline (PZT) powders using molecular building blocks by designed chemical route. *Journal of Nanoparticle Research*, 8(2):287–292, 2006.

[87] M. H. Kim, A. Golovchanski, S. I. Lee, T. G. Park, and T. K. Song. Synthesis of $Pb(Zr,Ti)O_3$ nanopowders by milling coprecipitation method. *Journal of Electroceramics*, 13(1-3):367–371, 2004.

[88] S. A. Rocks, D. Wang, D. Sun, S. N. Jayasinghe, M. J. Edirisinghe, and R. A. Dorey. Direct writing of lead zirconate titanate piezoelectric structures by electrohydrodynamic atomisation. *Journal of Electroceramics*, 19(4):287–293, 2007.

[89] S. N. Jayasinghe and M. J. Edirisinghe. Electrostatic atomisation of a ceramic suspension. *Journal of the European Ceramic Society*, 24(8):2203–2213, 2004.

[90] D. Sun, S. A. Rocks, M. J. Edirisinghe, R. A. Dorey, and Y. Wang. Electrohydrodynamic deposition of nanostructured lead zirconate titanate. *Journal of Nanoscience and Nanotechnology*, 5(11):1846–1851, 2005.

[91] C. H. Chen, M. H. J. Emond, E. M. Kelder, B. Meester, and J. Schoonman. Electrostatic sol-spray deposition of nanostructured ceramic thin films. *Journal of Aerosol Science*, 30(7):959–967, 1999.

[92] Michel Cloupeau and Bernard Prunet-Foch. Electrohydrodynamic spraying functioning modes: A critical review. *Journal of Aerosol Science*, 25(6):1021–1036, 1994.

[93] A. Jaworek and A. Krupa. Classification of the modes of EHD spraying. *Journal of Aerosol Science*, 30(7):873–893, 1999.

[94] A. Jaworek and A. T. Sobczyk. Electrospraying route to nanotechnology: An overview. *Journal of Electrostatics*, 66(3-4):197–219, 2008.

[95] F. Bortolani, D. Wang, and R. A. Dorey. *Micro direct writing of ceramics*, chapter 21, page 293. Ceramics processing in microtechnology. Whittles Publishing, 2009.

[96] L. Rayleigh. On the equilibrium of liquid conducting masses charged with electricity. *Philosophical Magazine*, 14:184–186, 1882.

[97] A. Jaworek. Micro- and nanoparticle production by electrospraying. *Powder Technology*, 176(1):18–35, 2007.

[98] S. N. Jayasinghe, R. A. Dorey, M. J. Edirisinghe, and Z. B. Luklinska. Preparation of lead zirconate titanate nano-powder by electrohydrodynamic atomization. *Applied Physics A: Materials Science and Processing*, 80(4):723–725, 2005.

[99] S. N. Jayasinghe, M. J. Edirisinghe, and D. Z. Wang. Controlled deposition of nanoparticle clusters by electrohydrodynamic atomization. *Nanotechnology*, 15(11):1519–1523, 2004.

[100] B. Dudout, J. C. M. Marijnissen, and B. Scarlett. Use of EHDA for the production of nanoparticles. *Journal of Aerosol Science*, 30(Suppl. 1), 1999.

[101] H. Widiyandari, C. J. Hogan Jr., K. M. Yun, F. Iskandar, P. Biswas, and K. Okuyama.

Production of narrow-size-distribution polymer-pigment-nanoparticle composites via electrohydrodynamic atomization. *Macromolecular Materials and Engineering*, 292 (4):495–502, 2007.

[102] S. N. Jayasinghe and M. J. Edirisinghe. Effect of viscosity on the size of relics produced by electrostatic atomization. *Journal of Aerosol Science*, 33(10):1379–1388, 2002.

[103] S. N. Jayasinghe and M. J. Edirisinghe. Electric-field driven jetting from dielectric liquids. *Applied Physics Letters*, 85(18):4243–4245, 2004.

[104] M. J. Edirisinghe and S. N. Jayasinghe. Electrohydrodynamic atomization of a concentrated nano-suspension. *International Journal of Applied Ceramic Technology*, 1(3): 140–145, 2004.

[105] J. Rosell Llompart and J. Fernaandez de la Mora. Generation of monodisperse droplets 0.3 to 4 um in diameter from electrified cone-jets of highly conducting and viscous liquids. *Journal of Aerosol Science*, 25(6):1093–1119, 1994.

[106] R. P. A. Hartman, D. J. Brunner, D. M. A. Camelot, J. C. M. Marijnissen, and B. Scarlett. Jet break-up in electrohydrodynamic atomization in the cone-jet mode. *Journal of Aerosol Science*, 31(1):65–95, 2000.

[107] A. M. Ganan-Calvo, J. Davila, and A. Barrero. Current and droplet size in the electrospraying of liquids. Scaling laws. *Journal of Aerosol Science*, 28(2):249–275, 1997.

[108] A. M. Ganan-Calvo. The size and charge of droplets in the electrospraying of polar liquids in cone-jet mode, and the minimum droplet size. *Journal of Aerosol Science*, 25(SUPPL. 1):309–310, 1994.

[109] Z. Cai, X. Xing, L. Li, and Y. Xu. Molten salt synthesis of lead lanthanum zirconate titanate ceramic powders. *Journal of Alloys and Compounds*, 454(1-2):466–470, 2008.

[110] H. H. Nersisyan, J. H. Lee, and C. W. Won. Synthesis of ceramic powders in the fusion salts of alkali metal. *Journal of Ceramic Processing Research*, 6(1):41–47, 2005.

[111] K. H. Yoon, Y. S. Cho, and D. H. Kang. Molten salt synthesis of lead-based relaxors. *Journal of Materials Science*, 33(12):2977–2984, 1998.

[112] R. H. Arendt, J. H. Rosolowski, and J. W. Szymaszek. Lead zirconate titanate ceramics from molten salt solvent synthesized powders. *Materials Research Bulletin*, 14(5): 703–709, 1979.

[113] C. Bedoya, Ch Muller, J. L Baudour, V. Madigou, M. Anne, and M. Roubin. Sr-doped $PbZr_{1-x}Ti_xO_3$ ceramic: Structural study and field-induced reorientation of ferroelectric domains. *Materials Science and Engineering B: Solid-State Materials for Advanced Technology*, 75(1):43–52, 2000.

[114] R. Senthilkumar, K. Sridevi, A. Subramania, and M. S. Vijaya. Preparation and piezoelectric properties of lead zirconate titanate ceramics. *Ferroelectrics*, 332:77–82, 2006.

[115] Z. Li, S. Zhang, and W. E. Lee. Molten salt synthesis of zinc aluminate powder. *Journal of the European Ceramic Society*, 27(12):3407–3412, 2007.

[116] Thermfact and GTT-Technologies. www.factsage.cn/fact/documentation/ftsalt/ftsalt_list.htm.

[117] S. Zhao, Q. Li, L. Wang, and Y. Zhang. Molten salt synthesis of lead lanthanum zirconate titanate stannate powders and ceramics. *Materials Letters*, 60(3):425–430, 2006.

[118] T. Kimura, A. Takenaka, T. Mifune, Y. Hayashi, and T. Yamaguchi. Preparation of needle-like $TiZrO_4$ and (PZT) powders. *Journal of Materials Science*, 27(6):1479–1483, 1992.

[119] Z. Cai, X. Xing, R. Yu, X. Sun, and G. Liu. Morphology-controlled synthesis of lead

titanate powders. *Inorganic Chemistry*, 46(18):7423–7427, 2007.

[120] S. H. Cho and James V. Biggers. Characterization and sintering of lead zirconate-titanate powders. *Journal of the American Ceramic Society*, 66(10):743–746, 1983.

[121] Y. Hayashi, T. Kimura, and T. Yamaguchi. Preparation of rod-shaped $BaTiO_3$ powder. *Journal of Materials Science*, 21(3):757–762, 1986.

[122] B. Roy, S. P. Ahrenkiel, and P. A. Fuierer. Controlling the size and morphology of TiO_2 powder by molten and solid salt synthesis. *Journal of the American Ceramic Society*, 91(8):2455–2463, 2008.

[123] T. Kimura, T. Takahashi, and T. Yamaguchi. Preparation and characteristics of Ni-ferrite powders obtained in the presence of fused salts. *Journal of Materials Science*, 15(6):1491–1497, 1980.

[124] J. Chen, R. Yu, H. Li, C. Sun, T. Zhang, H. Chen, and X. Xing. Structure and shape evolution of $Bi_{1-x}La_xFeO_3$ perovskite microcrystals by molten salt synthesis. *European Journal of Inorganic Chemistry*, (23):3655–3660, 2008.

[125] Z. Yang, Y. Chang, X. Zong, and J. Zhu. Preparation and properties of PZT-PMN-PMS ceramics by molten salt synthesis. *Materials Letters*, 59(22):2790–2793, 2005.

[126] Z. Cai, X. Xing, R. Yu, G. Liu, and Q. Xing. Large-scale synthesis of $Pb_{1-x}La_xTiO_3$ ceramic powders by molten salt method. *Journal of Alloys and Compounds*, 420(1-2): 273–277, 2006.

[127] Chien C. Chiu, Chen C. Li, and Seshu B. Desu. Molten salt synthesis of a complex perovskite, $Pb(Fe_{0.5}Nb_{0.5})O_3$. *Journal of the American Ceramic Society*, 74(1):38–41, 1991.

[128] V. K. Lamer and R. H. Dinegar. Theory, production and mechanism of formation of monodispersed hydrosols. *Journal of the American Chemical Society*, 72(11):4847–

4854, 1950.

[129] C. Destree and J. B.Nagy. Mechanism of formation of inorganic and organic nanoparticles from microemulsions. *Advances in Colloid and Interface Science*, 123-126 (SPEC. ISS.):353–367, 2006.

[130] Z. Li, W. E. Lee, and S. Zhang. Low-temperature synthesis of $CaZrO_3$ powder from molten salts. *Journal of the American Ceramic Society*, 90(2):364–368, 2007.

[131] D. R. Lide. *CRC Handbook Chemistry and Physics, 85th Edition*, page 2656. CRC Press, 2004.

[132] P. I. Karkanas. PhD thesis: Cure modelling and monitoring of epoxy/amine resin systems, 1998. School of Industrial and Manufacturing Science. Cranfield University.

[133] J. Xie, J. C. M. Marijnissen, and C. H Wang. Microparticles developed by electrohydrodynamic atomization for the local delivery of anticancer drug to treat C6 glioma in vitro. *Biomaterials*, 27(17):3321–3332, 2006.

[134] Y. M. Chiang, D. III Birnie, and W. D. Kingery. *Particle coarsening*, page 388. Physical ceramics. Principles for ceramic science and engineering. Wiley and sons Inc, 1997.

[135] S. S. Chandratreya, R. M. Fulrath, and J. A. Pask. Reaction mechanisms in the formation of (PZT) solid solutions. *Journal of the American Ceramic Society*, 64(7): 422–425, 1981.

[136] V. A. Russell and C. H. Spink. The differential thermal analysis behavior of lead zirconate titanate materials. *Thermochimica Acta*, 19(1):45–54, 1977.

[137] J. Chen, L. Gao, J. Huang, and D. Yan. Preparation of nanosized titania powder via the controlled hydrolysis of titanium alkoxide. *Journal of Materials Science*, 31(13): 3497–3500, 1996.

[138] Fujifilm Dimatix. Printer handbook, www.dimatix.com.